Frictional Interaction of Elastomeric Materials

David Stratford Devalba

Queen Mary University of London

School of Engineering and Materials Science

Submitted in partial fulfilment of the requirements of the Degree of Doctor of Philosophy

Abstract

The frictional behaviour of rubber is a topic of great interest and importance due to the invaluable uses of rubber in industry. The very particular behaviour of rubber also makes rubber friction a fascinating subject matter. Despite this it is still a topic not well understood.

Previous studies have attempted to link the fracture mechanics of rubber crack propagation to the adhesive friction of rubber. The feasibility of such an approach to the adhesive friction of a rough rubber against a smooth surface, a configuration which can occur in various situations such as rubber seals or windscreen wipers, has been investigated. Rolling friction, described well by a fracture-like peeling process, is used to evaluate the viscoelastic dependence of sliding friction for various combinations of surfaces.

A novel use of rubber is proposed as a material for particles to be used for jamming based soft robotics applications. This area of soft robotics is comparatively new and the materials that are being used at present are neither well established nor have been examined in great detail. Rubber would offer a material easily manufactured to desired shapes and dimensions with a wide range of moduli allowing modification to suit specific applications. The effect of jammed rubber particles on the response of a jammed packing to an externally applied load is examined. The evolution of inter-particle forces is studied using a rheometer configuration. Finite element techniques and modelling are employed to study the rubber in more detail.

Statement of Originality

I, David Stratford Devalba, confirm that the research included within this thesis is my own work or that where it has been carried out in collaboration with, or supported by others, that this is duly acknowledged below and my contribution indicated. Previously published material is also acknowledged below.

I attest that I have exercised reasonable care to ensure that the work is original, and does not to the best of my knowledge break any UK law, infringe any third party's copyright or other Intellectual Property Right, or contain any confidential material.

I accept that the College has the right to use plagiarism detection software to check the electronic version of the thesis.

I confirm that this thesis has not been previously submitted for the award of a degree by this or any other university.

Signature:

Date:

Acknowledgements

The journey to having a fully-fledged PhD thesis in front of me has not always been smooth and owes a lot to the support and generosity of the people around me.

Firstly, a huge thank you to Professor James Busfield for taking me up into the world renowned Soft Matter research group and for all the help and support he has offered me over more than 4 years. I'd like to thank Alan Thomas for his fruitful input and his necessary patience as I tried to do his ideas justice, and I must thank Lorenzo Botto for his guidance and input.

A special mention must go to the members of the Soft Matter group; Hediyeh, Lewis, Thomas, Chang, Menglong, Yinping, Francesca, Barnabus, Yi, Michele, Hugh, Leihao, and Richard (who only gets a mention because he asked for one). Their help and advice has been invaluable and their fantastic example kept me working hard to live up to the high standards of the Soft Matter group.

I have been lucky enough to meet a lot of special people during the course of my studies and in no particular order I'd like to thank my good friends Ollie and Dan (who helped me immensely by leaving the university), Sheetal, Marta, Kathrin, Asad, Stefania, Servann, Mikhaelis, Artemis, Burcu, Reshma and Maria. Special mention must be made of Anu who chose to spend her Thursday nights in my company for some reason, the company more than made up for the cooking. The PhD would have been a miserable experience without this lot, and they mean the world to me.

Finally, I of course need to thank my parents, Teresa and Marco, who showed unmerited faith in my capabilities, to which I have since strived to live up to, and my brother and sister, Luca and Natalie, for being like family to me.

I also need to acknowledge the Engineering and Physical Sciences Research Council (EPSRC) who provided the funding for my research.

Dedicated to Midge and George

Table of Contents

List of Figures

List of Tables

Nomenclature

Symbol	Base Units	Description
a	m	Contact radius
A	$m^{(1+2\alpha)}(sN\alpha)^{-1}$	Peeling parameter
A_c	m^2	Actual contact area
$\mathrm{A_H}$	-	Hamaker molecular interaction constant
A_s	m^{-2}	Surface area
c	m	Crack length
C	-	Constant coefficient
d	m	Diameter
E	Pa	Young's modulus
E_a	$Jmol^{-1}$	Activation energy
E_A	Jm^{-2}	Adhering energy
E_{loss}	J/Jm^{-1}	Energy loss from peeling
E_n	J/Jm^{-1}	Strain energy at crack length n
E_p	Jm^{-2}	Peeling energy
E_t	J	Elastic energy
E_v	-	Viscoelastic losses
E'	Pa	Storage modulus
E''	Pa	Loss modulus
E^*	Pa	Dynamic modulus
E_0	J/Jm^{-1}	Strain energy at zero shear
f	s^{-1}	Frequency
F_A	N	Adhesion friction component

F_c	N	Force normal to inter-particle contact plane
F_f	N	Friction force
F_g	N	Force due to gravity
F_H	N	Hysteretic friction component
F_N	N	Normal force
F_S	N	Shear force from optical measurements
F_ε	N	Shear force from shear angle
g	ms^{-2}	Earth gravitational constant
G	Pa	Shear modulus
G_r	Pa	Relaxation modulus
h	m	Height
I	-	Strain invariant
J	Pa^{-1}	Compliance
k	Pa^{-1}	Modulus term
k_b	$m^2kgs^{-2}K^{-1}$	Botzmann's constant
K	Pa^{-1}	Relative modulus
K_m	Pa	Bulk modulus
L	m	Length
m, n	-	Fitting parameters
M	kg	Mass
N	m^{-3}	Number of molecular chains per unit volume
p	Pa	Pressure distribution
q	Pa	Traction
Q	N	Tangential force

r	m	Radius
r_e	m	Molecular chain end-to-end distance
R	m	Relative curvature
R_a	m	Mean roughness
R_t	Pa^{-1}	Retardation Spectrum
s	m	Separation
S	JK^{-1}	Entropy
S_a	m	Asperity spacing
t	s	Time
T	K	Temperature
T_E	Jm^{-2}	Tearing energy
T_g	K	Glass transition temperature
u	m	Deformation
U	Jm^{-3}	Energy density
v	ms^{-1}	Velocity
w	m	Width
W_p	Jm^{-2}	Work of adhesion
α		Peeling parameter
β	-	Power constant
γ	Jm^{-2}	Dupre adhesion energy
γ_{12}	Jm^{-2}	Interfacial energy
γ_d	Jm^{-2}	Dispersive surface energy component
γ_L	Jm^{-2}	Liquid surface energy
γ_p	Jm^{-2}	Polar surface energy component

γ_S	Jm^{-2}	Solid surface energy
Γ	-	Gamma function
δ	m	Displacement
δ_d	-	Phase lag
ε	-	Strain
λ	-	Extension ratio
λ_L	Pa	Lame constant
μ	-	Friction coefficient
ν	-	Poisson's ratio
π_e	Jm^{-2}	Equilibrium pressure of vapour absorption
θ	°	Angle
σ	Pa	Stress
σ_f	Pa	Adhesive frictional shear stress
τ	s	Retardation time
ω	s^{-1}	Circular frequency

1 Introduction

Friction is an important property to be considered in engineering applications, and as such lots of resources and studies have focused on understanding and modelling friction. However, while the friction between two rigid solids can be vaguely described by Amonton's and Coulomb's laws, rubber refuses to bow to simplistic material models. The malleability of rubber means that contact with another surface can change greatly with increasing normal loading, altering the interaction between the two surfaces. The straining of the rubber means that friction becomes a viscoelastic response; add to this a strong interfacial adhesion, and interactions quickly become complicated. Recent studies have had some success in modelling friction behaviour with complex models of many parameters. The focus of these models has been on correctly identifying the effects of mathematically characterizable rough rigid surfaces on rubber friction. Success has also been met in the comparison of adhesive friction events to rubber fracture mechanics. In this thesis work is conducted on understanding the friction of a rough rubber surface on a smooth rigid surface as a peeling event and describing it from established fracture mechanics. In the second part of the thesis a potential application of rubber particles to soft robotics is examined. Jamming is a very interesting phenomenon that has been defined to encompass a number of different phase changes in materials affected by various parameters. The jamming of macroscopic particulate matter has seen a growing use in soft robotic applications. The use of rubber particles in such applications is investigated, following which the inter-particle forces between rubber particles subjected to an externally applied force is investigated. Section 4 introduces a new theory to describe friction of rough rubber on smooth rigid surfaces. Section 4.4 describes a novel FEA method for the characterisation of shape-dependent peel energy. Section 5.1 examines the behaviour of monolayer packings of rubber particles in response to an externally applied load. Section 5.2 details experimentation on the forces developed between rubber hemispheres sheared in approximation of two particles in a packing. Section 5.2.3 develops a model to describe the inter-particle interactions observed in section 5.2.

2 Literature Review

2.1 Brief History of Rubber

The discovery of the Americas by Europeans in the 1490s led to their exposure to many novel plant species which have become an indispensable part of modern life. Among these was the latex of a tree, of which the harvesting and coagulation into useful objects was developed by native Americans and demonstrated to explorers such as Columbus (Wolf & Wolf 1936; Warren 1987).

Figure 2-1: Collection of latex from Hevea Brasiliensis trees (Milliken et al. 2009).

Many plants were found to produce various forms of latex however that of the Hevea Brasiliensis tree (Figure 2-1) was found to give the highest purity, elasticity and yield (Warren 1987). The sap, or latex, is mostly made up of long-chain hydrocarbons, the base building block for the remarkable properties displayed by rubbery materials (Bateman 1963).

It was not until much later at the beginning of the 19th century that the exploits of Thomas Hancock and Charles Macintosh began to push the use of rubber for commercial products. Then in 1835 Nathaniel Hayward and Charles Goodyear, by heating raw latex in the presence of sulphur and lead oxide, imagined in Figure 2-2, discovered the cross-linking process of cross-linking the rubber into a permanent set termed vulcanisation by Hancock (Jayasinghe 2002).

Figure 2-2: Charles Goodyear discovering vulcanisation, taken from https://corporate.goodyear.com/en-US/about/history/charles-goodyear-story.html.

The unique viscoelastic and frictional properties of the now stable rubber along with the exponential growth of the automotive industry led to rubber becoming one of the most important engineering materials to this day, encouraging great academic and scientific studies.

2.2 Rubber Properties

2.2.1 Molecular Configuration

Elastomers are composed of long chain hydrocarbons. The typical monomer structure of natural rubber is [-$CH_2CCH_3CHCH_2$-]. The molecular chain is non-planar due to Van der Waals interactions which indicates the flexibility of these long chain molecules (Bateman 1963). The long polymer chains interweave so that the structure of uncross-linked rubber is held together loosely by these entanglements alone and is essentially a very viscous fluid. Cross-links can be introduced into the structure linking neighbouring chains as in Figure 2-3. This micro structure gives rise to unique behaviour which fascinates and intrigues researchers more than 175 years after the discovery of the cross-linking process.

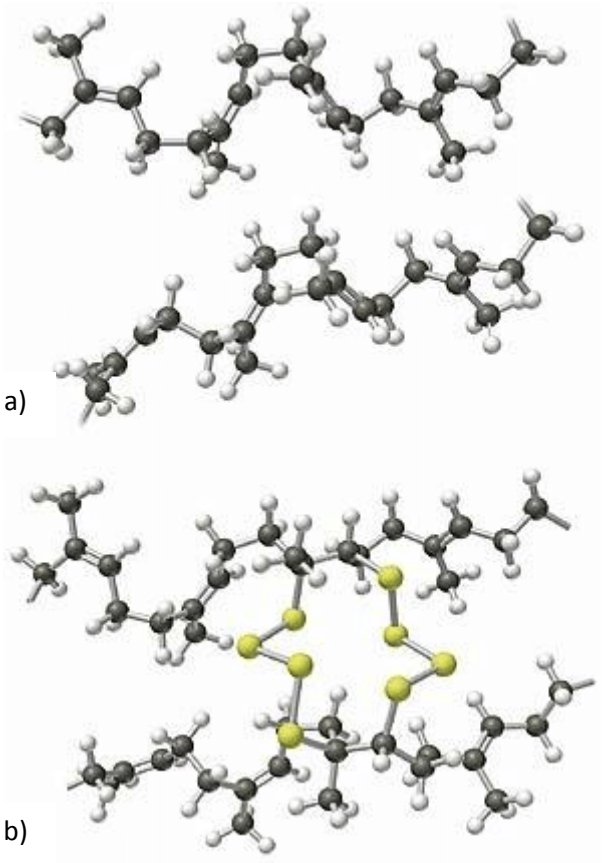

Figure 2-3: Diagram of natural rubber chains, where black and white spheres represent carbon and hydrogen atoms respectively, a) un-crosslinked and b) crosslinked with the yellow spheres denoting sulphur atoms (El-Saftawy 2013).

2.2.2 Vulcanisation

Vulcanisation is the process of cross-linking a raw rubber material so that the hydrocarbon molecules are bonded to one another via these so-called cross-links. The process of vulcanisation was first discovered by a man called Charles Goodyear, and involves heating the rubber in the presence of a cross-linking agent such as sulphur. This is done in the presence of other chemicals that act as activators and accelerators to speed up the vulcanisation to an acceptable rate. This inter-linking of the molecular chains means that the rubber is no longer a fluid and will retain a given shape. The rubber will however also retain its flexibility due to the scarcity of these cross-links, the number of which can be managed to give a required stiffness among other properties.

2.2.3 Glass Transition Temperature

The glass transition temperature (T_g) is the temperature at which polymers undergo a phase change and hence a dramatic change in behaviour. Above the T_g,

the molecular chains of the rubber are free to move and display viscoelastic behaviour. Below this T_g, the elastomer crystalizes and the molecules are no longer free to rearrange themselves in response to an applied force. The behavioural change does not occur in a stepwise fashion at the transition however; as the T_g is approached from above the movement of the hydrocarbon chains becomes ever more restricted, the molecules no longer have thermal motion, the rubber becomes less viscous, and there is less hysteretic energy loss. All this signifies that the properties of rubber are very dependent on the position of their T_g relative to their operating temperatures.

2.3 Rubber Elasticity

The molecular configuration of rubber is such that its behaviour under applied stresses is complicated and strongly dependent on environmental conditions.

Segments of polymer chain between cross-links undergo Brownian motion, a thermally driven rearrangement of the chain within the constraints of the cross-links. Upon deformation, the segments of long-chain molecules are stretched, this limits the amount of freedom the chain had, or the entropy of the segment. Thus, upon extension of the material the entropy of the chains decreases. By thermodynamic principles this must be accompanied by change in energy of the system. The chains release enthalpy to the environment. This can be felt when stretching a rubber band against skin in the heat felt coming from it. On release of the stress, the reverse is observed, as the entropy increases to its original value. The chains essentially form an entropic spring which provides an enthalpy driven restoration force and it shows that this restoration force is not due to stored energy from bond stretching. It has been shown that the work of internal energy is very small (Meyer & Ferri 1935).

2.3.1 Linear Elasticity

At low strains, several assumptions about the nature of an elastomer's elasticity can be made to simplify properties. The main one being that of linear elasticity. This is generally maintained to be a good approximation for strains of up to 10%. Within this region, the Young's Modulus (E) of a material is simply the ratio of stress (σ) to strain (ε).

$$E = \frac{\sigma}{\varepsilon} \quad 2\text{-}1$$

Another common approximation is that of incompressibility. As the Poisson's ratio of elastomers tends to be high (approaching 0.5) it is approximated as equal to 0.5 and this is equivalent to having an infinitely large bulk modulus (K), i.e. that the material is incompressible. Given that the relationship between Young's Modulus and the other moduli can be expressed as:

$$E = \frac{9GK}{(3K+G)} \quad 2\text{-}2$$

Then the shear modulus can be approximated by:

$$G = \frac{E}{3} \quad 2\text{-}3$$

2.3.2 Hyperelasticity

Upwards of around 10% strain the behaviour of rubbers becomes non-linear and hyperelastic models, models based upon a strain energy density function, are typically used to map this behaviour.

The starting point to explaining the deformation behaviour of rubber statistically is to acknowledge the random orientation of the long-chain molecules. Work on using theory of the entropic nature of the molecular rearrangements of elastomeric molecules to estimate the stress strain behaviour of rubber was conducted by Kuhn (1934) and Wall (1942). The discrepancy in the solutions of the two approaches followed by the two authors was reconciled by Treloar, who generalised these results to apply to any homogenous strain behaviour (Treloar 1943a; Treloar 1943b; Bateman 1963):

$$U = \frac{1}{2}Nk_bT(\lambda_1^2 + \lambda_2^2 + \lambda_3^2 - 3) \quad 2\text{-}4$$

Where U is the stored energy density of deformation, N is the chains per unit volume, k_b is Boltzmann's constant, and λ_1, λ_2, λ_3, are the principal extension ratios. Equation 2-4 is also known as a strain energy function. These are the basis of most common hyperelastic models. This model, known as the Neo-Hookean model, represents low strain behaviour quite well. However, deviation from experimental results are seen at larger strains. One reason for this is the finite extensibility of the polymer chains which, at high levels of deformation, leads to an

increase in gradient. Classic models such as the Neo- Hookean or Mooney-Rivlin, (Mooney 1940), models are still used due to their simplicity and ability in spite of this to capture a reasonable range of stress states. More sophisticated hyperelastic models, such as the Ogden model (Ogden 1972) and the extended tube model (Kaliske & Heinrich 1999), seek to cover a wider breadth of stress levels and states at the cost of greater complexity (number of material parameters).

Generally, the lower the strain range of interest the lower the complexity of the model required and therefore the lower number of material parameters needed. For strains of up to $\approx 150\%$ the Neo-Hookean model is sufficient, and the Mooney model is adequate up to $\approx 250\%$ (Marckmann & Verron 2006). This thesis is mainly concerned with low strain phenomena; for the most part linear elasticity can be assumed.

2.3.3 Viscoelasticity

The hyperelastic models ignore the effects of time and history on the stress-strain behaviour of rubber. Elastomers in reality display a combination of properties that are similar to both an elastic solid and a very viscous fluid. As such pronounced hysteresis losses are observed during cyclic tests, stress or strain relaxation occurs, and the material response is temperature and rate dependent.

The delayed elongation of rubber from a fixed stress (creep) is caused by the rearrangement of the long polymer chains and can be expressed as:

$$\lambda = J(t)\sigma \qquad 2\text{-}5$$

Where $J(t)$ is a time dependent compliance. A simplifying assumption is that of linear viscoelasticity; a material is linearly viscoelastic if Boltzmann's superposition principle can be applied to it, i.e. that the net effect of multiple stresses applied to a system at different times is simply the sum of the responses to the individual stresses. The effect of stresses on strain up to a time t_o can be expressed mathematically:

$$\lambda = \int_{-\infty}^{t_o} \frac{d\sigma}{dt}(t_o - t)dt \qquad 2\text{-}6$$

The response of a system can be modelled with a spring and dashpot system; the spring providing the elastic modulus and the dashpot the viscous modulus. There is

a component of the response to applied stress of the system that is delayed due to the damper.

$$\sigma = \lambda + \tau\,\dot{\lambda} \qquad 2\text{-}7$$

The strain is thus found as:

$$\lambda(t) = \sigma\left(1 - e^{-\frac{t}{\tau}}\right) \qquad 2\text{-}8$$

The delay in the strain to applied stress can be seen to be quantified by τ, termed the retardation time. A material can be modelled by a series of these spring dashpot systems, each representing a spectrum of retardation times of the material. This represents the distribution of properties of molecular units of the material. The more spring-dashpot units are used the closer the model is to the elastomer being modelled. A continuous distribution can be assumed such that $R_t(\tau).d(log\tau)$ elements, where $R_t(\tau)$ is the retardation spectrum of the system, have retardation times $\log\tau$ to $\log\tau + d(\log\tau)$ so that the compliance is given by:

$$J(t) = \int_{-\infty}^{\infty} R_t(\tau).\left(1 - e^{-\frac{t}{\tau}}\right) d(\log\tau) \qquad 2\text{-}9$$

In a similar way relaxation may be considered such that a relaxation modulus $G_r(t)$ can be defined as:

$$G_r(t) = \int_{-\infty}^{\infty} H(\tau).\, e^{-\frac{t}{\tau}} d(\log\tau) \qquad 2\text{-}10$$

Where $H(\tau)$ is the relaxation spectrum of the system (Bateman 1963). $H(\tau)$ can be found from the dynamic moduli using the following formula (Ferry et al. 1953):

$$H(\tau) = A_H G'\left(\frac{d(logG')}{d(log\omega)}\right) = BG''\left(1 - \left|\left(\frac{d(logG'')}{d(log\omega)}\right)\right|\right)$$

$$A_H = \left(\frac{2-\rho}{2\Gamma\left(2-\frac{\rho}{2}\right)\Gamma\left(1+\frac{\rho}{2}\right)}\right) \qquad 2\text{-}11$$

Where ρ is the local slope of the spectra, and Γ is the gamma function.

When an elastomer is subjected to an applied stress or strain with sinusoidal wave-form the response lags behind with a phase difference.

$$\varepsilon = \varepsilon_0 \sin(\omega\tau)$$

$$\sigma = \varepsilon_0 sin(\omega\tau + \delta_d) \quad \text{2-12}$$

Where $\omega = 2\pi f$ is a circular frequency (f is the frequency) and δ_d is the phase lag between input and response.

The modulus, called the complex or dynamic modulus (E^*), can be split into an in-phase and out of phase component or real and imaginary parts:

$$E^* = E' + iE'' \quad \text{2-13}$$

Where E' and E'' are the storage and loss modulus respectively.

$$E' = \frac{\sigma_0}{\epsilon_0} \cos \delta_d$$

$$E'' = \frac{\sigma_0}{\epsilon_0} \sin \delta_d \quad \text{2-14}$$

The ratio between the moduli gives a measure of damping, or departure from elasticity, of the system:

$$\frac{E'}{E''} = \tan \delta_d \quad \text{2-15}$$

As mentioned earlier, there is a concomitant effect of temperature and frequency; that the dynamic properties of a rubber can be matched at a high frequency and temperature at a lower frequency by appropriately reducing the temperature. The effect of a change in temperature is to scale the time-dependency of the viscosity moduli, thus, all that is needed is the relationship between this factor (a_t) and temperature. This relation is called the Williams-Landel-Ferry (WLF) transform:

$$log a_t = \frac{C_1(T-T_r)}{(C_2+T-T_r)} \quad \text{2-16}$$

Where T_r is a reference temperature and C_1 and C_2 are fitting parameters which, if T_r is chosen appropriately (approximately $= T_g + 50^0$), are approximately constant regardless of the rubber used (Williams et al. 1955).

Viscoelasticity plays an important role in many of the unique properties of rubber including the frictional behaviour of rubber; thus, it will be important to categorise the viscoelastic moduli of the rubber. The relaxation spectrum is a measure of the

spectrum of response of the rubber molecules to a dynamic event and provides a useful way to link the dynamic moduli to the reaction of the rubber to a velocity dependent event such as friction response.

2.4 Fracture Mechanics

2.4.1 Griffith's Criterion

Despite the unique character of the properties of elastomers the basis for their crack propagation characteristics lie with the well-known Griffith's fracture criterion; that the energy needed to propagate a crack be greater than the surface free energy of the created surface. Cracks are assumed to grow around pre-existing flaws in the material.

Typical energies for crack propagation for elastomers tend to be much higher than surface energies of the cracks. This is due to the viscoelastic dissipative energy losses in the material. These occur primarily at the crack tip; any losses in the material bulk are negligible in comparison (in strain crystallising rubbers crystallisation becomes the dominating source of energy loss at high propagation rates) (Roberts 1990). This means that crack propagation may be characterised by a parameter independent of the shape of the specimen. This energy is known as the tearing energy, strain energy release rate, or fracture energy (T_E). This material parameter can be expressed in terms of the change in the total elastic energy in the sample (E_t) with a change in area of crack surface (A) over a constant sample length (l) so that forces do no work (Rivlin & Thomas 1953).

$$T_E = -\left(\frac{\partial E_t}{\partial A}\right)_l \qquad 2\text{-}17$$

Thus, various tests with different sample geometries and loading conditions can be used to find a common tearing energy.

This tearing energy is independent of geometry and is material dependent. T_E can be thought of as the energy required to propagate a crack of length dc. The extension of the crack tip relaxes the stresses in a region proportional to dc. The energy loss is found by considering the strain energy at the crack tip, therefore, for a crack tip modelled as semi-circular, as in Figure 2-4, T_E is given by:

$$T_E = d\int_0^{\frac{\pi}{2}} U_\theta \cos\theta \, d\theta \qquad 2\text{-}18$$

Where d is the crack diameter and U_θ is the strain energy density at an angle θ from the crack tip centre (Thomas 1955).

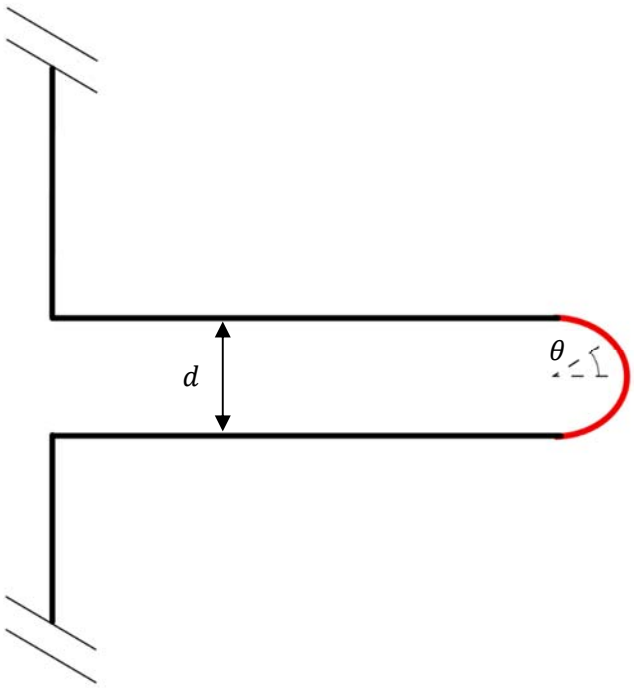

Figure 2-4: Diagram of semi-circular crack tip model.

Equation 2-18 can be approximated by:

$$T_E = \overline{U_t} d \qquad 2\text{-}19$$

With $\overline{U_t}$ being the average crack tip strain energy density (Roberts 1988). This is essentially the same result as equation 2-17. The stresses are concentrated at the crack tip however, for a specific geometry, T_E may be considered in terms of the strain energy released averaged over a volume of rubber dependent on dc and the geometry. Two specific geometries will be briefly discussed.

For pure shear geometry, seen in Figure 2-5, there are four zones in the sample each under different strain energy states. As the crack length (c) increases the volume of zone 3 decreases by the same amount as the volume of 1 increases. Thus, the change in total strain energy can be expressed in terms of the strain energy density in the pure shear region (U) multiplied by the volume of sample released from strain by the propagation of the crack:

$$\partial A = t_0 \partial c$$
$$\partial W = U h_0 t_0 \partial c$$

$$T_E = U h_0 \quad \text{2-20}$$

Where h_0 is the unstrained height of the test piece and t_0 is the unstrained thickness of the sample.

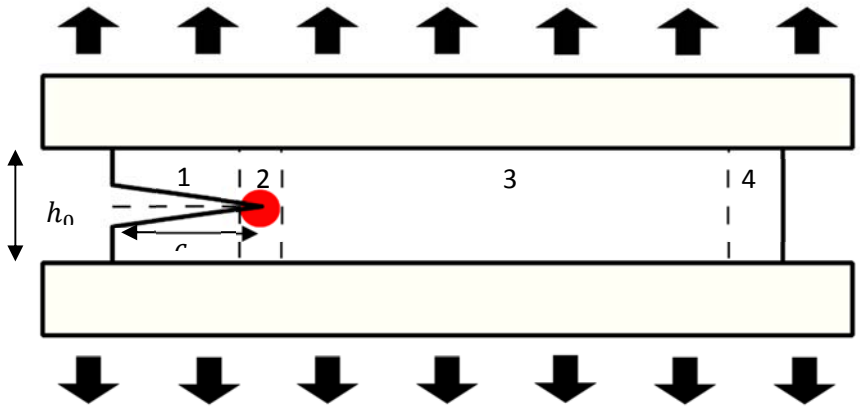

Figure 2-5: Schematic diagram of a pure shear test piece.

It is found that crack propagation in shear occurs in an analogous manner to crack propagation loaded in tension due to local tensile stresses at the crack tip when crack length is suitably big with respect to the sample height (Isaksson & Stahle 2002). At low crack lengths strain gradients at the sample edges affect tearing energy. This occurs for very short crack lengths.

Data for continuous crack growth rate dependence on tearing energy for different test configurations presented by Lake (1995) is shown below in the form of a log graph. This data shows firstly an independence of the tearing energy on test geometry as discussed previously, and also a strong power law relationship on the velocity (v) of crack propagation:

$$\frac{dc}{dt} = C T_E^{\beta} \quad \text{2-21}$$

Where C and β are constants.

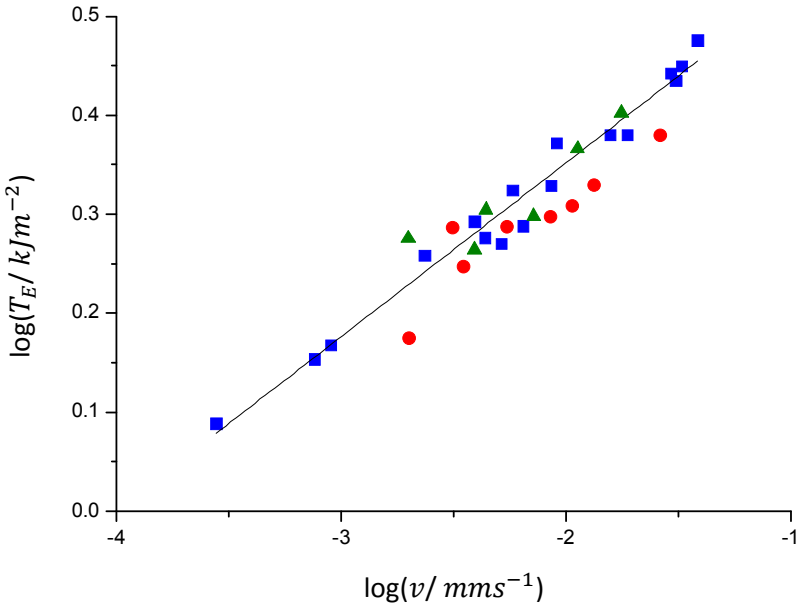

Figure 2-6: Log graph of tearing energy against crack growth rate for various test geometries. Blue squares- split test, red circles- trouser test, green triangles- pure shear test. Adapted from Lake (1995).

Work by Persson and Brener (2005) and Kluppel (Klüppel 2009) have directly linked the fracture mechanics to the viscoelastic properties of the rubber using the relaxation spectrum:

$$\left(\frac{T_E}{T_E^0}\right)^2 = \left(\frac{a_c}{a_c^0}\right)^2 = \left(\frac{a_c^0}{2\pi v}\int_\tau^\infty \frac{H_f(\tau)}{\tau}\mathrm{d}\tau\right)^{-1} \qquad 2\text{-}22$$

Where T_E^0 is the threshold tearing energy to crack propagation, a_c is the crack tip radius and a_c^0 the radius at zero frequency, H_f is a function of the relaxation spectrum, and τ is a characteristic entanglement time. Their work predicts a T_E dependent on v with a transition dependent on the ratio of rubbery to glassy state moduli. Above a low velocity independence and below a critical v a power law is predicted which can be linked to the gradient of the relaxation spectrum (C_H) which embodies this transition in viscoelastic properties between glassy and rubbery states:

$$\beta_H = \frac{(1+C_H)}{(2+C_H)} \qquad 2\text{-}23$$

2.4.2 Cyclic Crack Growth

For non-crystallising rubbers time dependent crack growth is observed under constant loading. If the rubber is capable of strain crystallisation however then there is no time dependent crack growth under constant load below a critical tearing energy (T_c); above this value stick-slip crack growth occurs. Crack growth can be induced with a varying load. Cyclic crack growth is an important example of this, needing consideration in the evaluation of the failure of components. Cyclic crack growth occurs in non-strain crystallising rubber alongside time dependent effects.

Cyclic crack growth is measured in terms of the change in crack length per cycle, which is dependent only on the max tearing energy of the cycle and not on the detailed form of the loading path.

There are three main regimes for cyclic crack growth. Below a critical tearing energy (T_0) the crack is unaffected by the cyclic loading and only crack growth due to ozone attack occurs. Above T_0 for a range of tearing energies there is a linear relationship between crack growth per cycle and max tearing energy (Roberts 1988).

$$\frac{dc}{dn} = C_o + C_a(T - T_0) \qquad 2\text{-}24$$

Where C_0 is a constant due to ozone attack, and C_a is the mechanical crack growth constant. At higher tearing energies there exists a region where crack growth per cycle displays a power law relationship with the max tearing energy analogous to that of equation 2-21 (Thomas 1958; Paris et al. 1961; Klüppel 2009).

$$\frac{dc}{dn} = CT^{\beta} \qquad 2\text{-}25$$

Fracture mechanics, being somewhat important to the engineering application of rubber and especially to the largest user of rubber, is a well explored topic of research and provides a well-established foundation of theory which will be applied to friction mechanics in this thesis.

2.5 Contact Mechanics

2.5.1 Elastic Half-Space

The elastic half-space approximation is an approximation of bodies in contact as semi-infinite bodies fronted by a plane. This is attributed to contact cases where

the contact deformation is sufficiently small as to allow it to be approximated by linear elasticity. This implies the contact radius is significantly less than the radii of curvature of the bodies in contact, meaning that the deformation is not significantly affected by the shape of the bodies away from the contact region, nor by the precise application of stresses away from the contact.

This relatively simple approximation is also a very useful one in that it enables the determination of contact as a function of the stresses in the contact region only and not the stress distribution throughout a complex component. It forms the foundation for modern contact mechanics.

2.5.2 Hertzian Contact

Work conducted by Hertz (1882) produced a method of finding contact properties between two elastic bodies provided they could be approximated as elastic half-spaces (Johnson 1982). This allows the building of the theory on well-established work by Cerruti (1882) and Boussinesque (1885) on elastic half-spaces. A further assumption made was that of zero friction between the contacting bodies, thus the effects of tractions parallel to the contact plane on deformations and stress fields are neglected.

Considering the displacement of two points within two surfaces brought into contact by a normal displacement (δ), the two points in the surface are displaced by the contact deformation relative to points in the bodies far away from the contact that don't experience deformation by an amount u_z.

$$\delta = \delta_1 + \delta_2$$

$$u_z = u_{z1} + u_{z2} \qquad \text{2-26}$$

If these two points are in contact post deformation, then the total deformation of the points is summarised by the expression:

$$u_z + S = \delta \qquad \text{2-27}$$

Where S is the initial separation of the surfaces.

It is assumed the profiles of the two contacting surfaces be smooth, so that both profiles may be adequately described by an expression up to the second order of the principal plane axes in terms of the principal radii of curvature of a surface,

where the axes are as defined in Figure 2-7 For rotationally symmetric surfaces (e.g. spheres) $R_{max} = R_{min} = r$ and the relative curvature:

$$R = \frac{1}{\left(\frac{1}{R_1}+\frac{1}{R_2}\right)}$$

so that equation 2-27 and the expression for the normal elastic deformations can be written:

$$u_z = \delta - \frac{r^2}{2R} \qquad 2\text{-}28$$

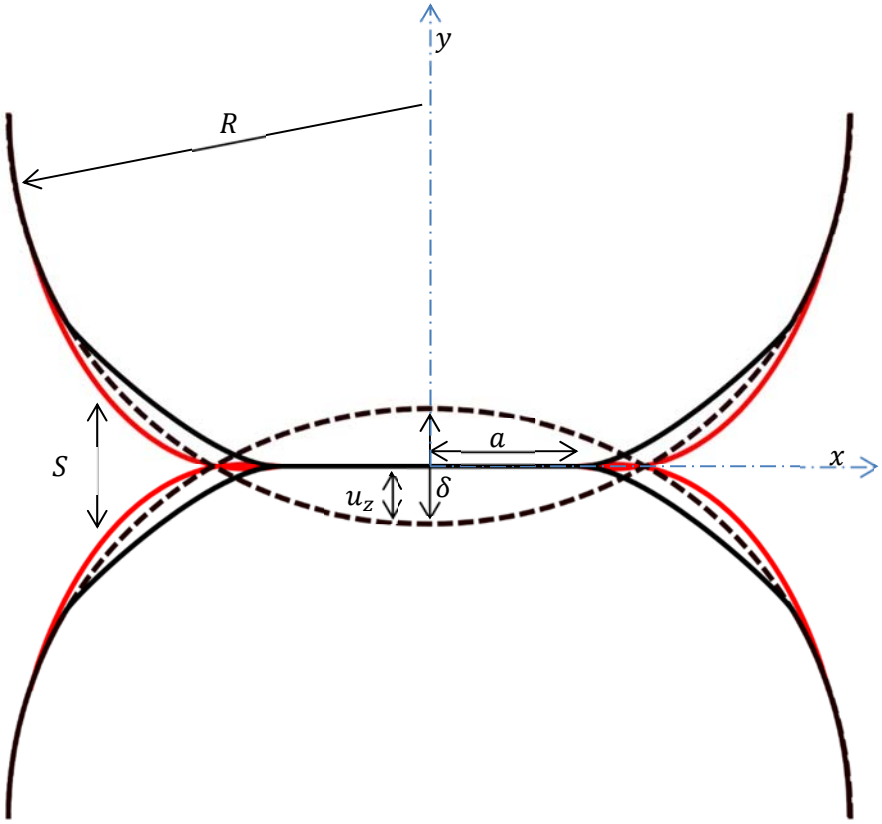

Figure 2-7: Diagram of deforming contacting bodies; dashed line- undeformed profile, solid line- Hertzian deformation, red line- JKR deformation.

Where $r_c^2 = x^2 + z^2$ is the necessarily circular profile of the contact patch.

The pressure distribution which satisfies the conditions of contact is given in terms of the contact radius (a) and the pressure at the centre of the contact (p_0):

$$p = p_0\left(1 - \left(\frac{a}{r_c}\right)^2\right)^{\frac{1}{2}} \quad \text{2-29}$$

The total normal force for this pressure distribution can be found by integrating the pressure over the contact area:

$$F_N = \int_0^a 2p\pi r dr_c$$
$$= \frac{2}{3}\pi p_0 a^2 \quad \text{2-30}$$

Normal displacement (u_{zs}) is given by:

$$u_{zs} = \frac{(1-\nu_s^2)}{E_s}\frac{\pi p_0}{4a}(2a^2 - r_c^2) \quad \text{2-31}$$

Thus equation 2-30 becomes:

$$\frac{\pi p_0}{3Ka}(2a^2 - r_c^2) = \delta - \frac{r_c^2}{2R} \quad \text{2-32}$$

Where the effective modulus K:

$$k_s = \frac{(1-\nu_s^2)}{\pi E_s} \quad \text{2-33}$$

$$K = \frac{1}{\frac{3}{4}\pi(k_1+k_2)} \quad \text{2-34}$$

From this, expressions for the compression and contact radius can be obtained in terms of material properties and the max pressure.

At $r = 0$:

$$\delta = \frac{2}{3}\frac{\pi p_0 a}{K} \quad \text{2-35}$$

At $r = a$:

$$\frac{\pi p_0}{3Ka}(2a^2 - a^2) = \frac{2}{3}\frac{\pi p_0}{K} - \frac{a^2}{2R}$$

$$a^2 = 2R\left(\frac{2}{3}\frac{\pi p_0 a}{K} - \frac{1}{3}\frac{\pi p_0 a}{K}\right)$$

$$a = \frac{2}{3}\frac{\pi p_0 R}{K} \quad \text{2-36}$$

Equation 2-36 can be used to give expressions for a and δ in terms of the applied normal force:

$$a = \left(\frac{RF_N}{K}\right)^{\frac{1}{3}} \quad \text{2-37}$$

$$\delta = \frac{F_N}{aK}$$

$$= \frac{a^2}{R} \quad \text{2-38}$$

These two equations are two important results of the Hertzian contact principle (Johnson 1985; Johnson 1982). They allow for the calculation of the contact size between two elastic bodies from the applied normal force. It can be shown that this solution is unique, no other stress distribution satisfies these conditions. In a similar fashion the solution to the problem of two cylinders in contact is found from approximating to the line loading of an elastic half-space (Johnson 1985):

$$a = \left(\frac{4F_N R}{\pi K}\right)^{\frac{1}{2}} \quad \text{2-39}$$

The Hertzian solution however neglects a few important effects which have quite the influence when dealing with instances where friction is important and rubber is involved. The first of these issues will be partially addressed by the consideration of tangential forces.

2.5.3 Tangential Loading

When considering the effect of a tangential force on the contact between two bodies, if the two bodies share the same elastic material properties, then the normal displacements will be equal and opposite for both bodies meaning that the normal pressure distribution will remain unaffected by the tangential distribution (Mindlin 1949). This is a very useful simplification of the problem and the assumption can be extended to materials of differing elastic constants as the effect

of tangential tractions on the normal pressure distribution is generally low. This means that the contact size and pressure distribution can still be found using Hertzian contact.

For two initially coincident points on the contact plane when there is no slip at the interface their tangential displacements (u_{xs}) will be equal to the lateral displacement of the bulk (δ_{xs}).

$$u_x = u_{x1} - u_{x2} = \delta_{x1} - \delta_{x2} = \delta_x \quad \text{2-40}$$

For spherical bodies, with a circular contact area, the form of the tangential traction distribution (q) and the lateral displacements, from elastic half-space results, will be:

$$q = q_0 \left(1 - \left(\frac{r}{a}\right)^2\right)^{-\frac{1}{2}} \quad \text{2-41}$$

$$u_x = \frac{q_0 \pi a (2-\nu)}{4G} \quad \text{2-42}$$

The total tangential force can be found by integrating the traction over the contact area resulting in the following expression:

$$Q = 2\pi a^2 q_0 \quad \text{2-43}$$

δ_x is given by:

$$\delta_x = \frac{Q}{8a}\left(\frac{(2-\nu_1)}{G_1} + \frac{(2-\nu_2)}{G_2}\right) \quad \text{2-44}$$

This expression gives a relation between the lateral displacement and the tangential force, or friction force, at the contact interface in terms of the elastic properties of the two materials and the contact radius which is determinable from the Hertzian equations. As there is a zero-slip condition, if the value of Q is below a critical value then u_{xs} at the contact will not be equal to δ_{xs} due to slip (s_{xs}) between contact points:

$$s_x = \delta_x - u_x \quad \text{2-45}$$

Equation 2-44 in this instance becomes an expression for u_x with a constant level of friction force Q, determined by a dynamic friction law which is usually taken as Amonton's law (see section 2.6):

$$u_x = \frac{Q}{8a}\left(\frac{(2-\nu_1)}{G_1} + \frac{(2-\nu_2)}{G_2}\right) \quad 2\text{-}46$$

$$Q = \mu N \quad 2\text{-}47$$

The solution to the problem of a normal loaded contact then subjected to a tangential traction was first found by Cattaneo (1939) and independently by Mindlin (1949). It was shown that for the case where zero-slip in the contact is presumed, the traction would increase to an infinite value at the edge of the contact (Mindlin 1949). Thus, it was concluded that there must be some slip in the contact even when the overall contact condition is static. It was supposed that there is present an annulus of slip around the centre of the contact where no slip will occur. For the central stick region, the equations for the displacements will be those seen previously, equations 2-40 and 2-44. Within the slip annulus equation 2-46 comes into play.

The traction with these conditions was found by superimposing two tractions, one corresponding to the contact about to slip and the other describing the traction of a zero-slip inner area. If the contact is on the verge of slipping then only the point at the centre is stuck and, applying Amonton's law, the pressure profile, equation 2-29, can be used to define the traction:

$$q' = \mu p_0 \left(1 - \left(\frac{r}{a}\right)^2\right)^{\frac{1}{2}} \quad 2\text{-}48$$

Defining the stick region as a circle of radius c the traction due to this stick region is given as:

$$q'' = -\frac{c}{a} p_0 \left(1 - \left(\frac{r}{a}\right)^2\right)^{\frac{1}{2}} \quad 2\text{-}49$$

The overall traction is the summation of equations 2-48 and 2-49:

$$q = q' + q'' = \left(\mu - \frac{c}{a}\right) p_0 \left(1 - \left(\frac{r}{a}\right)^2\right)^{\frac{1}{2}} \quad 2\text{-}50$$

As with the traction the overall displacement is found from an addition of the displacements caused by each traction:

$$u_{xs} = \frac{\pi\mu p_0}{8G_s a}(2-\nu)(a^2-c^2) \quad 2\text{-}51$$

When $r \leq c$:

$$\delta_x = u_{x1} - u_{x2} = \frac{3\mu P}{16}\left(\frac{(2-\nu_1)}{G_1} - \frac{(2-\nu_2)}{G_2}\right)\frac{(a^2-c^2)}{a^3} \quad 2\text{-}52$$

The total friction force is found by the difference of the integrals of the two tractions over the respective areas they are applied:

$$Q = \mu P\left(1 - \left(\frac{c}{a}\right)^3\right) \quad 2\text{-}53$$

Within the annulus, $a \gg r \gg c$, slip occurs. This slip follows equation 2-45 so that the slip is found from:

$$s_x = \delta_x - ((u'_{x1} + u''_{x1}) + (u'_{x2} + u''_{x2})) \quad 2\text{-}54$$

This solution isn't exact. The vertical displacements cancel but the vertical slips do not so that the assumption that the lateral force acts parallel to the contact is contradicted. This vertical slip however is very small and can be neglected.

The normal force from Elata (1996) differs slightly from the above, due to the use of a different stress distribution, when describing the results of Mindlin (1949) and Walton (1978). (The normal components of the solutions ought to be Hertzian however as normal and tangential tractions were found to be independent):

$$p = \frac{2}{\pi^2 R B_1}(a^2 - r^2)^{\frac{1}{2}} \quad 2\text{-}55$$

Where B_1 is a function of Lame constants:

$$B_1 = \frac{1}{4\pi}\left(\frac{1}{G} + \frac{1}{(\lambda+G)}\right)$$

$$\lambda = K_m + \frac{2}{3}G \quad 2\text{-}56$$

This results in a contact size dependence of the normal force of the form:

$$P = \frac{2}{\pi^2 R B_1}(a^2 - r^2)^{\frac{1}{2}} \quad 2\text{-}57$$

It is pointed out in a study on the adhesion in contacts that this supposition of infinite stresses at contact edges is unlikely as this would be the case under a

tangential load of any magnitude and the assumption of linear elasticity prevents the exact definition of stresses.

2.5.4 Oblique Contact Loading

The loading paths or loading history has an effect on the resultant contact stress and displacement distributions (Elata 1996). Thus, the application of a normal force followed by the application of a tangential force, as solved by Mindlin (1949) and Cattaneo (1939) before him, is not the same as the unanimous application of both forces even if the forces applied are equal at the culmination of loading. The case where normal and tangential loads are applied simultaneously in proportion to one another, analogous to an off-centre compression, was analysed by Walton (1978). He found that the normal and tangential stress distributions acted independently of one another and thus, retrieved the same normal stress distribution as Mindlin; that of Hertzian contact. The tangential component however took on a different form (Walton 1978).

$$Q = \frac{8R^{\frac{1}{2}}}{3\pi(2B_1+B_2)}\left(\frac{u}{w}\right)w^{\frac{3}{2}} \qquad 2\text{-}58$$

$$B_2 = \frac{1}{4\pi}\left(\frac{1}{G} - \frac{1}{(\lambda+G)}\right) \qquad 2\text{-}59$$

This is related to Mindlin's work by Elata (1996).

While these contact mechanisms form the basis of the approach for a number of different systems such as rock mechanics, geophysics, and seismology, some form of energy dissipation is employed, namely where impacts (velocity of particles is of import) occur; they are used for contact stiffnesses to be used within some effective medium model (Aleshin & Van Den Abeele 2009; Machado et al. 2012). Due to the assumptions made to arrive at these solutions their suitability to applications should be questioned. It has been shown in experimental studies that the fundamental assumptions of an independence of the normal stress distribution to the tangential stresses is not entirely accurate with results showing contact areas increasing after an applied lateral force (McFarlane & Tabor 1950; Ovcharenko et al. 2008; Etsion 2010). These contradictions of the assumptions of independent tractions and interfacial slip however seem to occur in situations where the underlying base assumption to the Hertzian/ Mindlin contact is no longer applicable, that of the purely elastic bodies bounded by a half plane. Clearly care

has to be taken when evaluating the validity of such a simplifying assumption to the case under scrutiny.

2.5.5 Surface Energy

The surface free energy of a material surface is the summary of the attractive potential of the surface atoms. With elastomers, Van der Waal's forces provide an attractive force between surfaces. The Dupre adhesion energy (γ) between two surfaces is defined as the addition of the two surface energies (γ_S) minus the interfacial energy (γ_{12}) which is typically assumed negligible (Dupre 1869; Schrader 1995; Savkoor & Briggs 1977). This energy term introduces tensile stresses outside of the normal pressure field for contacting bodies and thus gives a larger contact area than Hertzian mechanics predict. This is especially important for compliant materials with high surface energies such as elastomers. Peeling energy, or work of adhesion, (E_p) is dependent on this Dupre energy.

Measurement of the surface energy of a solid (γ_S) is complicated by the fact that it cannot be measured directly and that several procedures exist for determining surface energy (Rulison 1999). Established methods exploit known surface tension values of liquids (γ_L) and use contact angle measurements to determine γ_S. Zisman provides the first widely adopted method for determining (γ_S) however, this method categorises the surface energy with a single term whereas surface energy contributions are generally categorised into two main components; a polar (γ_p) and a dispersive (γ_d) component (here written e.g. γ_{Sp} for the polar component of solid surface energy) (Fowkes 1964a). The polar component is a summary of the effects of dipole-dipole, and induced dipole interactions, and hydrogen bonds; and the dispersive component summarises the effects of Van-der-Waals type interactions (Rulison 1999).

Fowkes (1964b) modelled the interfacial tension of a liquid-solid interaction as the addition of their individual surface tensions minus the geometric mean of their dispersion components:

$$\gamma_{LS} = \gamma_L + \gamma_S - 2(\gamma_{Ld}\gamma_{Sd})^{\frac{1}{2}} \quad 2\text{-}60$$

This equation ignores the polar contribution to the interaction. From Young's equation; $\gamma_L \cos\theta = \gamma_S - \gamma_{Ls} - \pi_e$, where π_e is the equilibrium pressure of vapour absorption onto a solid surface:

$$\cos\theta + 1 = \frac{2(\gamma_{Sd}\gamma_{Ld})^{\frac{1}{2}}}{\gamma_L} \quad 2\text{-}61$$

This provides a method of determining the dispersive component of γ_S but doesn't deal with the polar component. The term π_e is assumed zero as the liquid will typically have a higher energy than the solid and that absorption of a higher energy substance will not lower the surface energy of the solid (Fowkes 1964b).

Owens and Wendt (1969) built on Fowkes' work. They assumed an extension to equation 2-60 in the form:

$$\gamma_{LS} = \gamma_L + \gamma_S - 2(\gamma_{Ld}\gamma_{Sd})^{\frac{1}{2}} - 2\left(\gamma_{Lp}\gamma_{Sp}\right)^{\frac{1}{2}} \quad 2\text{-}62$$

Thus, they arrived at a more general form of equation 2-61:

$$1 + \cos\theta = \frac{2}{\gamma_L}\left((\gamma_{Sd}\gamma_{Ld})^{\frac{1}{2}} + \left(\gamma_{Sp}\gamma_{Lp}\right)^{\frac{1}{2}}\right) \quad 2\text{-}63$$

Assuming $\pi_e = 0$. Equation 2-63 can also be expressed as:

$$\frac{\gamma_L(\cos\theta+1)}{2\gamma_{Ld}^{\frac{1}{2}}} = \left(\frac{\gamma_{Sp}\gamma_{Lp}}{\gamma_{Ld}}\right)^{\frac{1}{2}} + \gamma_{Sd}^{\frac{1}{2}} \quad 2\text{-}64$$

In this form, equation 2-64 the expression can be likened to a linear equation of the form $y = Cx + y_0$ where $y = \frac{\gamma_L(\cos\theta+1)}{2\gamma_{Ld}^{\frac{1}{2}}}$ and $x = \left(\frac{\gamma_{Sp}\gamma_{Lp}}{\gamma_{Ld}}\right)^{\frac{1}{2}}$ and thus γ_{Sp} and γ_{Sd} can be found from the gradient and intercept respectively from what is called an Owen-Wendt plot. Multiple liquids of known and differing surface tensions are used to create the plot (Owens & Wendt 1969; Rulison 1999). Alternatively a liquid with no polar contribution ($\gamma_{Lp} = 0$) could be selected to find γ_{Sd} and then another liquid with a non-zero γ_{Lp} could be used to find γ_{Sp} (Rulison 1999). The surface energy is an important surface property in the evaluation of adhesion. The Owens-

Wendt method can be easily adopted using a few solutions with a selection of surface tension parameters.

2.5.6 Adhesive Contact

So far, the contact mechanics have required that the normal stress distributions be compressive throughout the contact, and therefore the effects of adhesion have been ignored. If adhesion were present within a contact, the mutual attraction of the two surfaces would increase the contact area. This has been observed particularly for low normal loading where contact has been seen to deviate from Hertzian theory (Johnson et al. 1971).

This is an effect which should be taken into consideration when considering relatively compliant materials such as rubber. A pioneering paper by Johnson, Kendal, and Roberts, (JKR) (1971) introduced the JKR model which dealt with spherical adhesive contacts.

The method used was from an energy balance consideration, the balance between work done by the normal load (U_w), the stored elastic energy of deformation (U_t), and the surface energy (U_s). The derivation considers the energies involved in the system when the bodies are taken into contact at a supposed normal force P_1 to a contact radius a_1. Then the contact is taken back to a_0 ($a_0 < a_1$) under the same load and the difference in energies is equivalent to the elastic energy of the deformation due to the tensile stresses in the contact. From this the contribution of the surface energy to the contact is found and is expressed as a contribution to F_N which takes it above F_{N0}, the value of the normal force without adhesion effects.

$$F_N = F_{N0} + 3\lambda\pi R + \sqrt{6\lambda\pi R P_0 + (3\lambda\pi R)^2} \quad \text{2-65}$$

The contact radius is then given in the same fashion as the Hertz theory but with the JKR normal force:

$$a^3 = \frac{R}{K}\left(F_{N0} + 3\lambda\pi R + \sqrt{6\lambda\pi R F_{N0} + (3\lambda\pi R)^2}\right) \quad \text{2-66}$$

$$\delta = \frac{2}{3}\frac{F_N}{K a_1} \quad \text{2-67}$$

The comparison of this energy based approach to that of fracture mechanics has been noted by Savkoor and Briggs (1977).

Barquins (1988) adopted a similar approach to that of Johnson et al., by starting from Hertzian contact, in solving for the adhesive contact for a cylindrical body onto an elastic plane. This work produced the following expression for the relation between F_N and the contact half-width (a):

$$\frac{F_N}{L\left(\frac{\pi E\gamma^2 r}{16(1-\nu^2)}\right)^{\left(\frac{1}{3}\right)}} = \left(\frac{a}{\left(\frac{2\gamma r^2(1-\nu^2)}{\pi E}\right)^{\frac{1}{3}}}\right)^2 - 4\left(\frac{a}{\left(\frac{2\gamma r^2(1-\nu^2)}{\pi E}\right)^{\frac{1}{3}}}\right)^{\frac{1}{2}} \quad \text{2-68}$$

Where L is the axial length of the cylinder. The resulting theory was validated experimentally by Barquins (1988) and by Chaudhury et al. (1996) who expressed it in the more general form:

$$\frac{F_N}{L} = \frac{\pi K a^2}{3R} - \left(\frac{8}{3}K\pi a\gamma\right)^{\frac{1}{2}} \quad \text{2-69}$$

Another model was proposed by Derjaguin et al. (1975). This differed from the JKR model in the way the intermolecular forces are considered. Long-distance attractive forces outside the contact range are considered to affect the contact rather than the short-range attraction within the contact considered in the JKR model. The thermodynamic reasoning used leads to an expression for the normal force of contact of a sphere on a flat plane of:

$$F_N = -\frac{Ad}{12z_0^2} + \left(\frac{2(2d)^{\frac{1}{2}}}{3k}\right)\delta^{\frac{3}{2}} \quad \text{2-70}$$

Where A_H is the Hamaker molecular interaction constant, d is the sphere diameter, z_0 is the minimum distance between the sphere and the plane, and δ is the displacement of the sphere towards the plane. It was found that the two theories can be considered applicable to different cases. Work done by Tabor (1977) examined whether the separation outside the contact zone for various materials meant that attractive forces needed to be considered outside the contact area. For soft materials, the separation was large so that attractive forces outside the contact would not come into play, however for harder materials the separation was much less so that that assumption could not be made. Hence, the JKR model would be a good fit in the first instance whereas the DMT model gives a better fit to the latter. It was shown by Tabor that the relevance of one method over another depended

on a parameter that quantified the ratio of elastic deformation with contact force range (Tabor 1977; Adams & Nosonovsky 2000).

$$\mu = \left(\frac{Rw^2}{E^* z_0^3}\right)^{\frac{1}{3}} \quad 2\text{-}71$$

Essentially, this implies that for softer, more compliant materials the JKR model is more correct and as such this is the form of adhesive contact predominantly used throughout.

2.5.7 Tangential Loading of Adhesive Contact

The effects of a tangential load on an adhesive contact were examined in the form of an energy balance approach, in a similar fashion to Johnson et al. (Johnson et al. 1971) and with comparison to fracture mechanics. It was found that an increasing tangential load had the effect of decreasing the contact area. There exists a critical tangential load (Q_c) at which an equilibrium is obtained. This Q_c is dependent on the magnitude of the normal load. It was hypothesised that beyond this value of tangential force the contact would unpeel in an unstable manner. The reduction in contact area was not expected to extend beyond the Hertzian contact as the stress intensity factor reduces to zero at this point. Thus, a change in mechanism may be expected beyond this point. The experimental results seem to corroborate the theory to an extent however stress relieving effects are thought to interfere at high tangential forces.

2.6 Friction

Friction is an omnipresent property of the interaction of any two bodies. It is thus a very important consideration in design and manufacture. Amonton's first law of friction holds that frictional force between two bodies is independent of contact area. Amonton's second law, also attributed to Leonardo Da Vinci, states that the frictional force between two bodies in contact is proportional to the normal force relative to the interface (Amontons 1699). Finally, there is Coulomb's law, which claims that the frictional force is independent of sliding velocity (Gao et al. 2004). These rules mean a simple expression for the friction force (F_f) may be used:

$$F_f = \mu F_N \quad 2\text{-}72$$

Where μ is the coefficient of friction and F_N is the normal force. While these simple laws hold surprisingly well for a majority of material interactions all three are,

however, nearly always inadequate when considering rubber interactions. Rubber friction is readily seen as being a very different prospect to that of typical materials where the simple friction laws are not an adequate descriptor of the interaction of two surfaces where at least one is a rubber. Rubber friction is not independent of contact area. For two typically rigid materials with a few asperities and the quantity of contact points, the actual area of contact will not vary greatly on changing the apparent area of contact. Rubber, however, due to its deformability, has an actual contact area that will vary with apparent area. Similarly, it is the deformation of rubber that gives it a non-linear dependence of the actual contact area on F_N, meaning that F_f is not a linear function of F_N. Finally, it will be shown that friction depends on the viscoelastic properties of rubber and thus is velocity dependent.

The work of Grosch (1963) showed the presence of two distinct sources for the friction. Sliding on smooth substrates displayed a friction term which could be reduced greatly with the introduction of lubricant. Sliding upon rough substrates however displayed a friction term present despite lubrication. A master curve of the friction of both over a wide range of velocity is shown in Figure 2-8. Thus, it was shown that there was an adhesion component to the friction (F_f) due to the interaction of the surfaces (F_A), and an internal friction or hysteretic term from the deformation of the rubber by substrate asperities (F_H).

$$F_f = F_A + F_H \tag{2-73}$$

This is indicative of the complexity of rubber friction with different applications and situations clearly having different contributions of both. This can be seen when comparing a windscreen wiper and a tyre. Rubber friction can be further sub-categorised into: lubrication, which brings with it its own friction mechanics with the interaction between the surfaces and the fluid important, and abrasion, which is the loss of rubber material from asperity interaction.

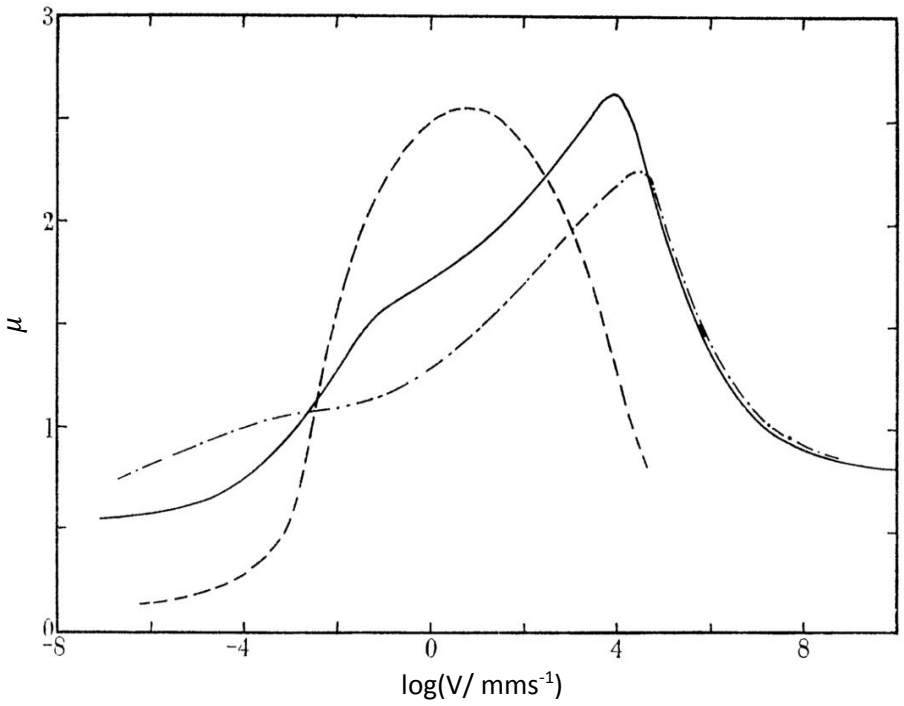

Figure 2-8: Master curves for styrene butadiene rubber against; solid line- silicon carbide, dashed line- wavy glass, dot-dashed line- dusted silicon carbide (1963).

2.6.1 Hysteresis

As there is compelling evidence to suggest both hysteresis and adhesive contributions depend in part on internal energy losses of the rubber, the name is slightly misleading. Here the hysteresis contribution is defined as the contribution to friction due to the energy losses caused by the deformation of the rubber by asperities on the counter-surface, and will be limited to this effect. The contribution to rubber friction from the internal friction of rubber has been shown, again in the work of Grosch (1963), to be highly dependent on temperature and velocity, as seen in Figure 2-9. The velocity of sliding can be considered in terms of a frequency at which the rubber is deformed by the substrate asperities. This frequency change gives a change in the dynamic moduli of the rubber and therefore hysteretic friction is dependent on the viscoelasticity of the rubber. Thus, the friction dependence on temperature and velocity are inextricably linked such that, in similar fashion to what was discussed in part 2.3.3, Williams-Landel-Ferry (WLF) type transforms are applicable to data to change a temperature sweep to an equivalent velocity dependence (Williams et al. 1955). This is demonstrated in the construction of the master curves in Figure 2-8.

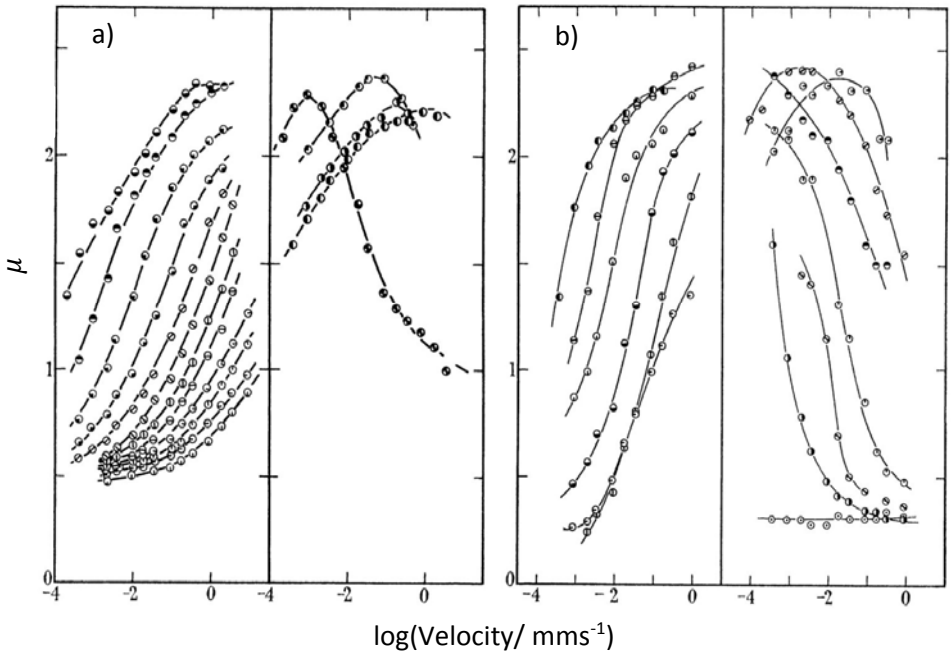

Figure 2-9: Friction data at different temperatures, with lower temperature curves where curves pass a maxima are shown on the right of graphs, for a) isomerised rubber on rough silicon carbide and b) acrylonitrile butadiene rubber on smooth wavy glass, taken from Grosch (1963).

2.6.2 Adhesion

The adhesive component of rubber friction originates from the attractive molecular forces between rubber molecules and a counter-surface, mostly Van-der-Waals interactions. It was originally considered to be simply the energy required to sever these bonds that caused the adhesive contribution to friction. However, values for this quantity were far too low to explain the magnitude of friction observed. The pioneering work of Grosch demonstrated that adhesive friction of rubber was also rate dependent and affected by the viscoelastic properties of the rubber characterised by the applicability of the WLF equation (Grosch 1963). Schallamach proposed that the molecules adhered to a surface were stretched when sliding, and this produced some energy loss. Schallamach developed a theory behind adhesion, whereby particles from the interacting rubber surface enter a trough, a lower energy state, on the surface of the other material. Activation energy is then required to remove the particle from this trough. The application of strain makes an otherwise randomly occurring jumping of particles from one trough to another, to take place in the direction of the strain in order to relieve stress (Schallamach 1953). This is the concept of individual chains in constant thermal motion that, during sliding, form bonds with the other surface. These chains are extended by the relative motion of the two surfaces before the bond is broken; the chain relaxes

and then reforms a new link a molecular distance further along. This cyclic process provides the source of adhesive friction (Moore, 1972).

From these considerations Schallamach developed a relation between the frictional force due to adhesion and the sliding velocity.

$$v = \frac{\lambda}{\tau} \qquad 2\text{-}74$$

Where λ is the distance between bonds and τ is given by the exponential function:

$$\tau = \tau_0 e^{\frac{A}{kT}} \qquad 2\text{-}75$$

Where τ_0 and A are constants.

$$v = \frac{\lambda}{\tau_0 e^{\left(\frac{E_a}{kT}\right)}}$$

$$= Ae^{-\frac{(E_a - BF_f)}{kT}} \qquad 2\text{-}76$$

Where *A* and *B* are constants (Schallamach 1953), (Moore, 1972).

This does not aptly describe the frictional behaviour as it does not predict the maxima. He modified his theory to include a term corresponding to bond formation time dependence, whereby the average number of bonds is affected by the sliding velocity, as well as temperature.

$$F_A = N_0 M v \tau \frac{\left(\frac{\tau}{\bar{t}}\right)^2}{\left(1 - \frac{\bar{t}}{\tau}\right)} \qquad 2\text{-}77$$

Where *M* is a constant.

An expression for the average bond lifespan can be found by consideration of the fraction of bonds present over time and a variable α is defined as follows:

$$\frac{\bar{t}}{\tau} = \phi_1\left(\frac{\alpha\tau}{kT}\right)$$

$$\frac{\left(\frac{\tau}{\bar{t}}\right)^2}{\left(1-\frac{\bar{t}}{\tau}\right)} = \phi_2\left(\frac{\alpha\tau}{kT}\right) \quad 2\text{-}78$$

$$\alpha = BMv \quad 2\text{-}79$$

ϕ_1 and ϕ_2 indicate a functional relationship. The equation for F_A can then be written in the form (Moore, 1972):

$$F_A = \frac{N_0 kT}{B}\left(\frac{\alpha\tau}{kT}\right)\phi_2\left(\frac{\alpha\tau}{kT}\right) \quad 2\text{-}80$$

The derived relation predicts a maximum in the frictional force with respect to the velocity reflecting experimental results. However, it fails to accurately fit the behaviour seen at low or high velocities (Schallamach 1966).

It is thought unlikely that individual chains should deform given the incompressibility of rubber. The similarity between the viscoelastic dependence of the adhesion and that of bulk rubber properties suggests a more global view is necessary. More recent proposals consider the deformation of areas of the rubber surface leading to internal energy losses. This can be physically seen in the form of Schallamach waves.

Persson and Volokitin (2006) conclude that sliding friction is not caused by thermally driven lateral detachments of molecules, however they include forces due to thermal motion in their analysis. They propose a model of the rubber interface with the interface segmented into volumes or stress domains connected to one another and to the bulk of the rubber by viscoelastic springs, shown in Figure 2-10. They describe a theory whereby larger volumes are taken into account rather than individual molecules. These volumes, deemed stress domains, experience an increasing shear stress until a de-pinning stress is reached and then the volume will undergo slip motion. The elastic energy stored in the volume during the stick period is dissipated as heat at the interface and into the rubber.

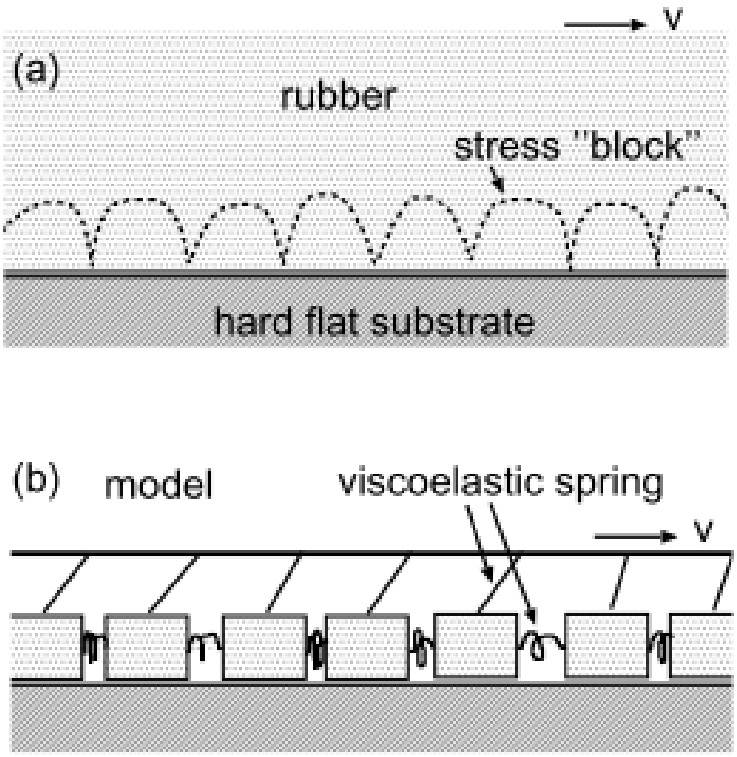

Figure 2-10: Diagram of stress domain model from Persson and Volokitin (2006).

The results obtained from the simulations of this model give a relation between the friction force and the velocity with a peak mirroring experimental results. The model shows a temperature dependence which is comparable to that expected in experiment but only at low velocities. They reason that the significance of the temperature dependence at higher velocities is in the reflection of a decrease in the real contact between the rubber and the track.

2.6.3 Discontinuous Sliding

The sliding of a smooth rubber surface over a likewise smooth counter-surface presents an uninterrupted contact between the two which very quickly reaches large stresses if the whole surface is to slide as one, even at low velocities. Mechanisms of sliding for finite sections of the rubber must be present in order for continuous sliding to occur. At higher velocities, these processes are not able to occur.

2.6.3.1 Schallamach Waves

Schallamach waves, seen in Figure 2-11, form in order to relieve stress build up from sliding of a flat area of rubber against a substrate. They are waves of

detachment progressing from the rear of a contact, with respect to the direction of sliding of the rubber, to the front which facilitate the sliding of a smooth rubber surface over a smooth counter-surface at certain velocities. These waves of detachment are buckling instabilities which form in the rubber due to stress build up and can provide a lower resistance to motion than pure sliding (Schallamach 1971). Schallamach waves are characterised by a critical tangential stress, dependent on the sliding velocity and the modulus of the rubber. This means the waves form above a certain velocity and more readily for softer rubbers. A critical extension exists at which buckling is initiated and Schallamach waves begin to form (Best et al. 1981). Schallamach waves can be thought of as a peeling type process where the waves are waves of detachment between the surfaces (Maegawa & Nakano 2010). The frictional work, given in terms of the friction force and sliding speed (v), is equated to the energy of peeling for the waves to propagate (Roberts & Thomas 1975):

$$F_f v dt = \frac{E_p v_w dt}{d_w}$$

$$F_f = \frac{E_p v_w}{d_w v} \qquad \text{2-81}$$

Where v_w and d_w are the wave speed and distance between waves respectively.

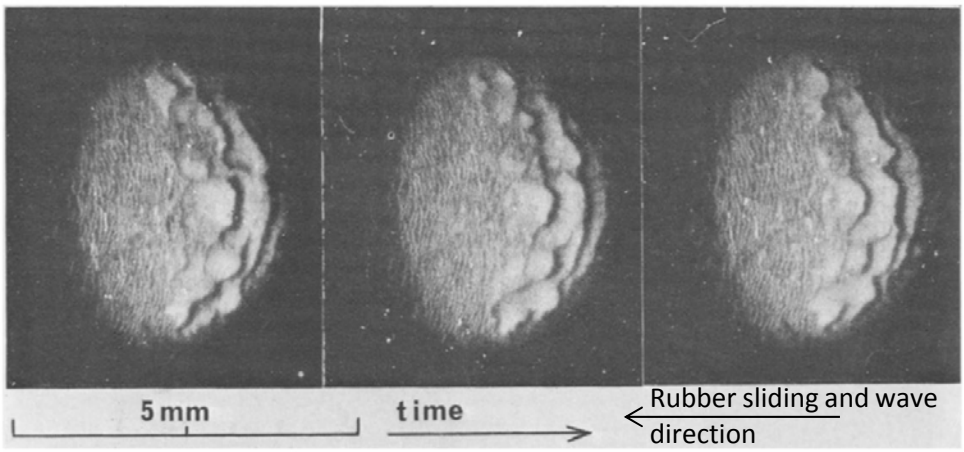

Figure 2-11: Images of Schallamach waves, taken from Schallamach (1971).

2.6.3.2 Stick-Slip

Stick-slip sliding occurs when the entire surface of the rubber suddenly detaches from the counter-surface and jumps forward. This happens when sliding velocity is too fast for Schallamach waves to relieve the stress build-up due to sliding. This

results in a discontinuous wave-form of friction force with peaks and troughs (Maegawa & Nakano 2010). Both Schallamach waves and stick-slip are stress relieving effects which are to be avoided if one is to study the mechanics during pure sliding.

2.6.4 Rough surface Sliding

Work by Persson (2001; 2013; 2015) has focused on rubber friction against self-affine surfaces. Self-affine surfaces are surfaces which display a characteristic wave-form of roughness on many length-scales. Most real surfaces are self-affine. The frictional theory proposed by Persson et al. (2001) highlighted the importance of considering the entire range of the roughness length-scales of the rigid surface. They argue that the energy loss is proportional to the asperity amplitude (A_m) over the wavelength (λ) and thus all wavelengths contribute equally in magnitude to the friction. The contributions will occur at different velocities as determined by $\frac{v}{\lambda}$. Not all length-scales would be in contact however, pressure differences at the top and bottom of larger scale asperities would mean that lower scale asperities would not always be in contact. The main contribution to the friction was determined to be due to the hysteretic losses due to the interaction of the asperities with the rubber. The adhesion between the surfaces, however, affected the cut-off length-scale of the asperities interacting with the rubber.

A similarly complex model was provided by Heinrich and Kluppel. Their approach to the adhesional term was a phenomenological one based on Amonton's law (Heinrich & Klüppel 2008). These models are necessarily awash with descriptive parameters as describing the roughness of surfaces and their effects on friction quickly becomes intricate.

Le Gal et al. (2005) examined the stationary friction of rubber over a rough surface at low velocities (referring to the initial frictional peak). They found a significant contribution to the sliding friction from adhesive effects. This adhesive contribution was greater at lower sliding velocities and was examined against a granite surface of maximum asperity dimensions of 0.2mm and 0.8mm vertically and horizontally respectively, so relatively low level maximum roughness. Their analysis found a correlation between this adhesion and the actual contact between the rubber and the rough substrate. They then analyse the adhesion in terms of the surface free energy (γ) using the following expression:

$$\sigma_f = \gamma / l_c \quad 2\text{-}82$$

Where l_c is a characteristic length-scale and σ_f is the adhesive frictional shear stress given by:

$$\sigma_f = \frac{F_A}{A_c} \quad 2\text{-}83$$

With A_c is the contact area. The surface free energy under dynamic conditions, termed effective surface free energy, is considered dependent on the ratio of the moduli at rest (E) and at frequency (E_ω), in other words the upper value of the effective surface free energy (γ_∞) is ratio of the moduli in the rubber region and glassy region:

$$\gamma_\infty = \gamma \left(\frac{E_\infty}{E}\right) \quad 2\text{-}84$$

This is a similar mechanism to that proposed by Persson and Brener (2005) for crack propagation. The hysteresis component of the adhesive work is essentially amalgamated into the surface free energy term and called the effective surface free energy. The effect of the sliding velocity on the effective modulus of the rubber gives a dependence of the effective surface free energy on the velocity. Thus, beyond an upper velocity limit (v_c) the adhesive friction would be expected to decrease whereas if the velocity range of sliding lies below this, the adhesive friction is expected to increase.

Essentially the adhesion is thought to be affected by the change in the modulus of the interacting rubber at the interface due to the increased frequency of asperity interaction from increasing sliding velocity. The effect of the velocity on the adhesion changes for rubbers with different glass transition temperatures in a manner expected by this description. This indicates that for the examined surfaces and velocities, a fracture mechanics approach is successful in predicting the adhesional friction.

2.6.4.1 Abrasion

Under certain conditions, the sliding of a rubber over a hard counter-surface may result in wear or abrasion of the rubber, the mechanics of which determine the friction observed. Abrasion is a process by which material is lost from a surface due to interaction with another harder material. Generally, abrasion is defined as

specifically referring to the scoring of a surface by hard asperities in a mechanical fracture mechanism (termed abrasive wear for rubber). However, for rubber the definition encompasses all laboratory controlled tests meaning many mechanisms are included (Muhr & Roberts 1992). Abrasive wear of rubber was found to be dependent on viscoelastic properties and occurring due to a tensile failure (Grosch & Schallamach 1966). Wear abrasion occurs due to blunt abrader geometries. This type of abrasion produces abrasion patterns, showing distinct behaviour in initially producing the pattern and then a steady state once the pattern is defined. The steady state behaviour is well described by fatigue crack propagation (Southern & Thomas 1979).

2.6.4.2 Geometric Friction

An additional contribution to the resistance of sliding is observed when a relatively sharp object causing an indent in a rubber is made to slide against the rubber. It has been termed the capstan effect due to its comparison to a rope wrapping round a capstan, in that friction increases exponentially with wrap angle due to the radial component of the friction (Schallamach 1969). The geometric friction is caused primarily by the work done on the rubber by the indenter in pushing the rubber around it and is dependent on the angle of contact and therefore indentation and the geometry of the indenter (Busfield et al. 2010).

These last two categories of friction are briefly introduced chiefly to further illuminate the vast catalogue of mechanisms potentially manifest in rubber friction but are not further examined in the subject matter of this thesis.

2.6.5 Rolling Friction

Rolling friction refers to the resistive force where the relative motion between the two bodies is a rolling motion. For a rubber rolling against a smooth surface the interaction between the surfaces can be seen as the propagation of a crack at the rear and the closing of a crack at the front of the contact (K. Kendall 1975). For an instance of negligible deformation loss in the bulk of the rubber due to asperity interactions, the adhesion of the rubber to the substrate surface can be considered in terms of an energy balance for steady state (constant velocity) rolling (Fuller & Roberts 1981). The potential energy lost as the rubber sample rolls down the surface must be equal to the energy required to peel the rubber. This is almost the case; there is an adhering energy gain of the system from the coming together of

the rubber and substrate at the leading edge of the sample. This has been shown to be negligible in comparison to the peeling energy from pulling the surfaces apart at the rear of the sample (K. Kendall 1975).

The surface free energy (γ), which is defined as an energy per area, from the separation of two surfaces is found as the difference between the surface energies (γ_1 , γ_2) of the materials and the interfacial energy (γ_{12}) (Briggs & Briscoe 1977):

$$\gamma = \gamma_1 + \gamma_2 - \gamma_{12} \quad \text{2-85}$$

The peeling energy (E_p) is the combination of the free energy increase from peeling and viscoelastic losses (E_V) occurring at the peeling edge in the form:

$$E_p \propto \gamma E_V \quad \text{2-86}$$

The viscoelastic term is naturally affected by rolling rate and temperature (Fuller & Roberts 1981). The surface free energy acts as a constant coefficient for a rubber coupling whilst the viscoelastic term is generally more significant (Greenwood et al. 1961; Andrews & Kinloch 1973). The work of adhesion (W_p) is found from the difference between this peeling (E_p) energy term occurring at the peeling rear of the contact and adhering (E_A) energy at the leading edge of the contact:

$$W_A = E_p - E_A \quad \text{2-87}$$

Several simplifying assumptions may be made; that the interfacial energy is negligible with respect to typical surface energy values ($\gamma_{12} \ll \gamma_1$, γ_2), and that the adhering energy is negligible with respect to the peeling energy ($E_A \ll E_P$) so that the work of adhesion is equal to the peeling energy (Fuller & Roberts 1981). This being established it is simple to find the peeling energy from the change in potential energy as the sample rolls down a slope at a constant velocity (K. Kendall 1975; Fuller & Roberts 1981).

Work done to roll a rubber sample over a distance x:

$$W_p = F_f L \quad \text{2-88}$$

Where the force (F_f) is the frictional force resistant to motion.

The energy balance as the sample rolls a length x_R is found from the difference in the peeling energy (E_p) from the crack opening at the front of the contact and the adhering energy (E_A) from the closing crack at the rear of the contact:

$$W_p = x_R w(E_p - E_A) \quad \text{2-89}$$

Where *w* is the width of the sample. As the adhering term can be deemed negligible the frictional force is given entirely in terms of the peeling energy per area. The frictional force will be counteracting the force acting on the sample which is that due to gravity (F_g):

$$W_p = Mgx_R sin\theta_R \quad \text{2-90}$$

Where θ_R is the angle of the incline, M is the mass of the sample and roller, and g is the gravitational constant.

From equations 2-89 and 2-90:

$$E_p = \frac{Mgx_R}{x_R w} sin\theta_R$$

$$= \frac{Mgsin\theta_R}{w} \quad \text{2-91}$$

This well-defined peeling setup gives a simple method of quantifying the adhesive friction between two surfaces. It gives the possibility of measuring the dependence of the adhesion on the velocity of the peeling.

Dwell time may also affect the peeling energy observed in experiments. This can be seen in the study by Kendal (1975), data of which is shown in Figure 2-12. This data shows a second form of velocity dependence apart from the viscoelastic effect on E_p. This effect may become important at low sliding velocities where the dwell time effect on E_p could be significant with respect to the viscoelastic effect.

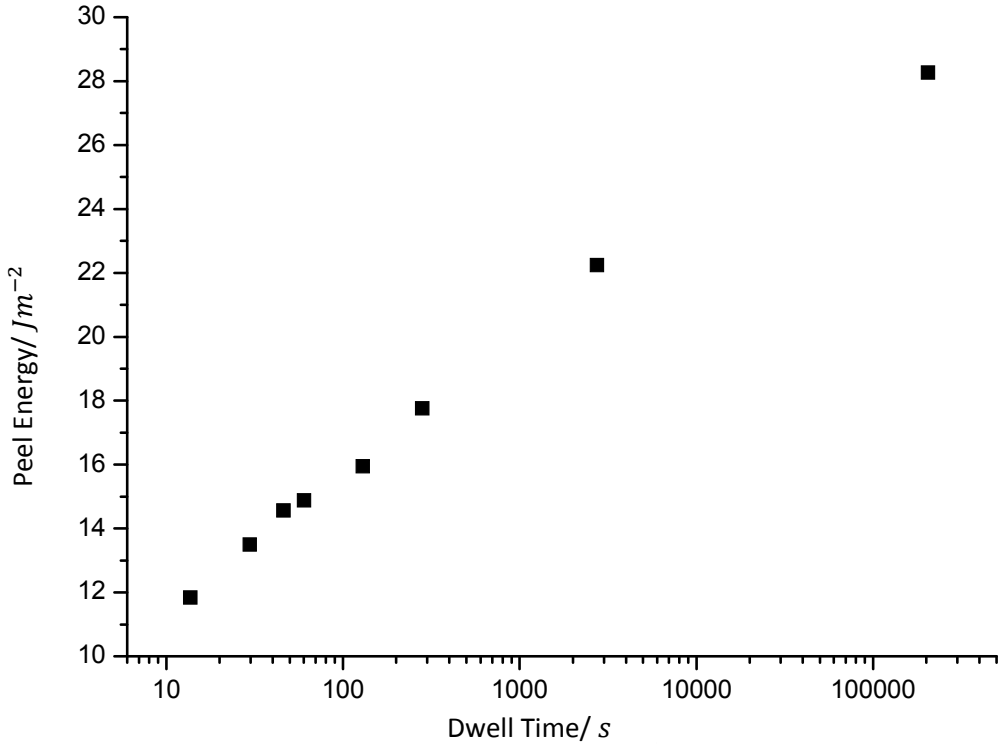

Figure 2-12: The effect of dwell time on peel energy (surface energy at break). Data from Kendall (1975).

2.6.6 Summary

Rubber friction is seen to be strongly dependent on the viscoelastic properties of the rubber. This leads to velocity dependent behaviour which can be broadly split into two distinct contributions. Early adhesive theories approach the problem in terms of individual molecular behaviour whereas recent models describe a process in terms of the stress state of the surface. What is clear is that different situations incur different friction behaviours. The sliding of smooth rubber against a smooth surface displays change from continuous sliding to Schallamach waves to stick-slip sliding behaviours. Work by Arnold et al., 1987, not only shows this for a smooth-smooth interaction, seen in Figure 2-13, but that the frictional behaviour for a rough rubber surface against a smooth rigid surface displays a different behaviour again. Figure 2-13 also shows that at certain velocities the rough rubber friction exceeds that of the smooth. Understanding the mechanism behind the friction for a rough rubber against a smooth surface would be beneficial for applications where friction involving a rubber component and a smooth rigid surface interaction is desired to be minimised or maximised.

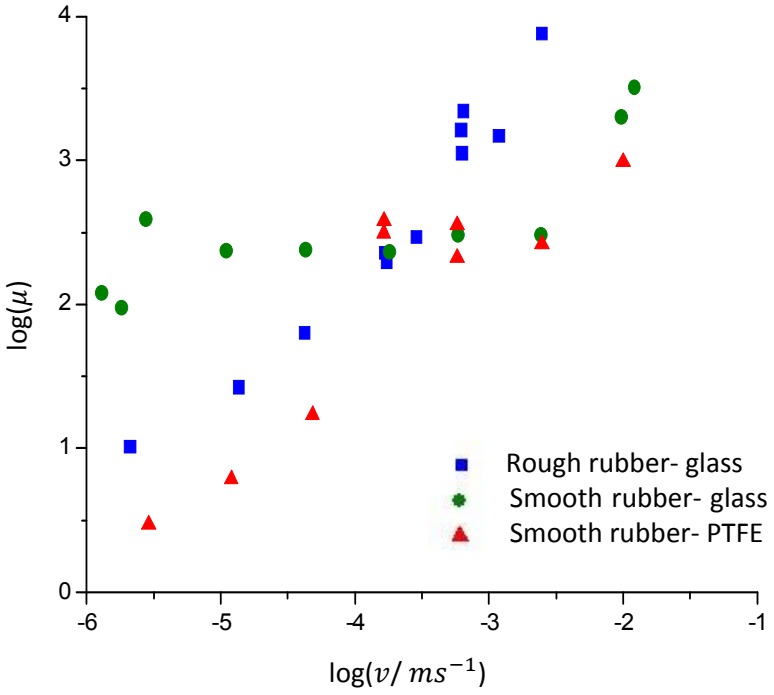

Figure 2-13: Graph of friction data by Arnold et al. (1987) for different combinations of surfaces.

The behaviour of rubber-rubber interactions is also of interest due to the growing field of soft robotics. In particular, robotic systems are being devised that can switch from a free-flowing state to a rigid structure. These systems exploit a process called jamming which is discussed in the following section. In both the rough rubber-rigid surface and rubber-rubber interactions adhesion will be the dominant component of friction.

2.7 Jamming

2.7.1 General Description

Jamming as a concept describes the nature of a system of particles constricted in their ability to move so that structural equilibrium is retained unless an external stimulus is applied to the system. The onset of jamming is determined by the systems conditions. The result of jamming is the transition of a collection of particles from a fluid state to a solid state where movement of particles is inhibited. The point at which the rheology of the system becomes solid is called the jamming transition. Originally applied to describe the change in behaviour of macroscopic repulsive particles under pressure, such as a pile of sand, the definition has been expanded to include many types of systems such as microscopic attractive particles

with density as the controlling parameter, such as colloidal suspensions, or a glassy transition occurring with temperature manipulation (Liu & Nagel 1998). The paper by Liu and Nagel collects all these processes together and proposes a jamming phase diagram. This diagram summarises the effects of temperature, load, and density on the jamming of particles (Liu & Nagel 1998). Attractive interactions were incorporated into the jamming unification by Trappe et al. (2001). They alter the phase diagram to reflect the processes of colloidal suspensions in which the density of the system is described by volume fraction and the temperature effect is dependent on the attractive forces between particles. Focus here is given mainly to macroscopic particulate jamming.

The jamming of granular (macroscopic) media has been observed and manipulated for centuries, such as purportedly in ancient Egyptian construction (Engelbach 1923). Nowadays a need for greater understanding of the phenomenon due to its pertinence to fields such as soil mechanics, architecture and robotics, is encouraging research into the subject (Evesque 2000; Huijben et al. 2009; Höhler & Cohen-Addad 2005). Particularly, extensive work has recently focused on the application of the jamming of granular particles to soft robotics (Jiang et al. 2012; Steltz et al. 2009; Brown et al. 2010; Majidi 2014; Cheng et al. 2010). The growing field of soft robotics reflects the desire for robots to be applied to human interaction and for robots with a wide range of functionality. Human interaction is wanted for medical and orthopaedic applications; conventional robots made out of rigid components are not safe for such as the disparity in rigidity between them and tissue means damage can be caused to the tissue. Biomimetic designs are therefore sought after; components that can alter their stiffness can be used in rehabilitation and to augment or replace natural actuators. Soft robotic systems will be able to adapt to a varying environment, useful for search and rescue applications and surgeries.

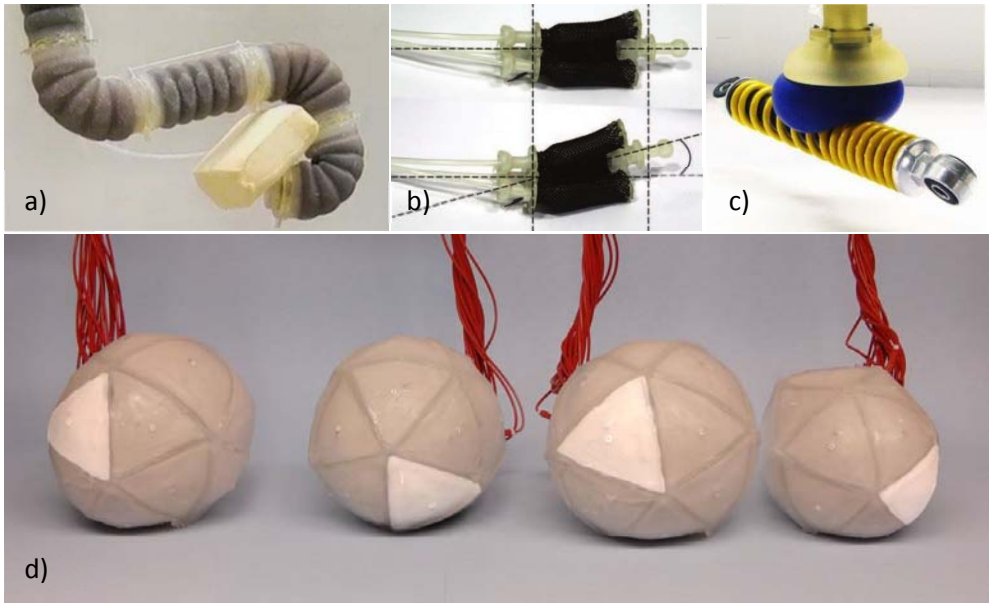

Figure 2-14: Examples of jamming-based soft robotic systems; a) manipulator from Cheng et al. (2010), b) actuator from Jiang et al. (2012), c) gripper from Brown et al. (2010), d) actuator from Steltz et al. (2009).

2.7.2 Behaviour of Jammed Systems

The general behaviour of a jammed system is generally that of a solid material. Under applied external force the jammed particles retain their structure. As external force is increased slippage between particles and local rearrangement of the structure may occur. However, the system is still considered jammed until particle flow is initiated. The structure of a jammed system has an effect on the performance of the system. Various measures are used to assess this structure, such as the average contact number (z) or the jamming density (ϕ).

A paper by Lechernault *et al.* (2007) investigated the behaviour around the jamming transition by studying the response to vibration of a monolayer of cylinders. They enclosed the particles in a rigid square enclosure, one of the walls of which is moveable using a motorised translational stage to enable adjustment of the volume fraction. The vibration was imbued with the base which transferred the vibration to the particles through friction. The base rests on micro-control stands. The movement of a sample of the particles is traced using a camera. This is an interesting system as it allows the isolated study of a single layer of interacting particles. The rigid setup however, does not allow the application of external forces nor does it mirror packings used in soft robotics.

2.7.3 Effect of Particle on Jammed System Properties

Jiang *et al.* (2012), in their work on designing a jamming robotic component, compared several different types of particles in deflection experiments. They found that rigid particles sustained higher levels of force before reaching what they described as a yield limit. This limit more or less increases with a decrease in particle size explained as due to the increase in surface area to volume ratio. However, the results are unclear on this with error bars encompassing a large range. There doesn't seem to be a discernible trend on the deflection at which it takes place which may be counter intuitive. Changing particle shape to cubes decreased the variance in the results dramatically and the maximum force and stiffness was comparable. The curves for rubber cubes maintain the decrease in variance but display a linear relation and therefore a constant stiffness level before reaching a maximum. The composite cubes don't improve much on the yield as might be expected. The general trend of a decrease in vacuum pressure is to increase the stiffness and yield. Cheng *et al.* (2010) compared the compressive stress of packings of different materials. They found a linear elastic region and yield stress for most materials. Glass particles showed a high linear modulus (lower for hollow glass beads), but a low yield stress after which the stress stays relatively constant. In comparison, coffee granules display a lower modulus but a much higher yield stress. This is the reason for its use in many robotic systems (Brown *et al.*, 2010; Cheng et al., 2010; Steltz *et al.*, 2010). This is possibly because of the friction between the rough grains, the irregular shape of the grains that interlock, particle size distribution and possibly oils within the grains contributing capillary action. Steltz et al. (2009) examined the flexural modulus of a range of packing materials, including two sizes of glass beads, at various vacuum levels. Their results for the two supports the volume to surface area effect with the smaller particles giving higher moduli. Their results showed less variation than previously seen with other studies. The material that performed best in terms of flexural modulus was table salt, possibly due to the irregularity of the shape of the grains, not unlike coffee. A paper by Loeve et al. (2010) explores the possibility of using a jamming system to control the rigidity of endoscopes. They conducted a study on the effects of particle size, shape, and hardness on the rigidity of a packing and its ability to resist a force and retain a bend. They found that the change in shape from spherical particles to polygons had a significant effect on the stiffness of the packing, changing from spherical to oval glass did not give significant changes however. This indicates that

having particles with edges and flat faces increases the resistance of the packing to deformation. This can be seen to be due to the fact that particles are able to pack more tightly together reaching a higher packing fraction. The geometric resistances to motion are likely to be higher as well. There is also the potential for greater contact and therefore friction between particles. However, considering the materials involved (steel) this would not likely be a large factor in comparison to geometric considerations. Decreasing size had the effect of increasing the stiffness of the packing up to a certain point. There seems to be an optimal size for which the deflection force is maximal. The stiffness would be expected to increase with a reduction in particle size due to the increase in the surface area to volume ratio, and increase in packing fraction. It is possible that the reduction in particle size has the effect of reducing the yield deformation of the packing so that whilst the modulus is increasing, for the smaller particles, the deformation has surpassed the yield point. The stiffness was examined by comparing different materials. It was seen that steel performed the best; it had a lower stiffness than glass or corundum but higher than polystyrene which were all also used. It was concluded that an optimal stiffness existed. However, the different materials have other differing properties which could have an effect, frictional properties being one example but also polystyrenes low yield stress needs to be considered. Only testing four materials does not present a complete picture. It is clear from the studies conducted that the choice of particle greatly affects the response of the jammed system. To obtain greater packing moduli and yield stresses particles should be chosen to have high interlocking ability and high inter-particle friction decreases variance in response.

The work of Mukhopadhyay and Peixinho (2011) sought to categorise the rheology of hydrogel spheres to give a soft particle system experimental procedure and results. They find a linear relation between strain and normal force at low strains under compression. This then changes to a power law of 1.25 before scaling deviates at high strain. The scaling could only be said to be Hertzian in a narrow range of strains around $\varepsilon \approx 0.1$; the scaling of the surface area followed a 1.4 (Hertzian 1.5) power law with strain. Frictional behaviour was seen between particles at low compression velocities where large packing rearrangements were absent whereas at large velocities the system behaved similarly to hard spheres.

Horizontal laser sheets were used to obtain images of sections through the system and measure surface contact sizes and contact numbers.

It was shown that foams exhibited similar behaviour to granular material, displaying a critical shearing angle despite the differences in flow onset (Lespiat et al. 2011). Although considered frictionless interactions, low shear foam jamming is considered in terms of film thinning between foam bubbles which can form attractive potential between the bubbles (Denkov et al. 2009). This may give analogous examples to that of rubber particulate jamming. The flow of foam has been approximated by 2D models such as the Princen Prud-Homme model (Kraynik & Hansen 1987). This model describes a geometrical change in bubble shape assuming uniform surface tension. Each bubble joint (intersection of walls) connects 3 walls at an equal angle that increases with strain until 4 walls connect. Once 4 is reached flat layers of bubbles are achieved which enable shifting of bubbles. The shape will resume the initial condition and thus a periodic yield stress with strain is predicted. Such behaviour has been experimentally observed (Kraynik 1988). This model approximates the foam structure to a hexagonal repeated pattern, however later models incorporating a disordered arrangement of bubbles compares reasonably well with it. Foam rheology has been studied using rheometers however, typical plate configurations such as parallel plate and cup and bob lead to results affected by wall slip. A vane rheometer configuration moves the shearing plane away from the walls and thus can reduce this factor somewhat (Pernell et al. 2000).

2.7.4 Effect of Membrane on Jammed System Properties

Jiang et al. (2014) studied the lesser effect of the membrane on the response of a jammed packing to an applied force. It was shown that the membrane can distinctly affect the packing deformation in a manner that vaguely follows the scale of the moduli of the membrane material. There are likely to be effects on the packing response from the frictional interaction between membrane and particles as well. The effect of the membrane on a packing could obfuscate observation of particle behaviour.

2.7.5 Response of Jammed Systems

Walton (1987) applied his theory of contact mechanics to predict the modulus of a randomly arranged packing of monodisperse spherical particles. Assumptions in

line with typical contact mechanics of small strain linear elasticity are employed and results are derived for frictionless and no slip cases.

2.8 Finite Element Modelling of Elastomers

Finite element modelling can be an important tool in engineering as it allows the analysis of complex loading and boundary conditions on intricate geometry that would otherwise be mathematically daunting to solve. It is an invaluable instrument when it comes to understanding some of the complexities of rubber behaviour. Finite element modelling is a process where the effects of a force or displacement field on a model of a body or multiple interacting bodies is examined by discretising the bodies into small elements and solving the local stress-strain fields for individual elements. Generally, the process starts with a drawing representing the real-world component(s) it is desired to study, with any simplifying structural assumptions such as planes of symmetry or plane stress. Appropriate material models need to be selected for the objects. Similarly important are the choices of forces and boundary condition applied. The objects are discretised in an (ideally) structured manner to provide elements. Boundary conditions allow the solutions of the force-displacement equations to be solved for some initial elements which in turn enables the solution of others.

FEA techniques are useful not only to model complex geometry and boundary conditions but particularly with rubber to model their non-linear elasticity. Hyperelastic constitutive models, some notable examples of which were discussed in section 2.3, may be implemented. In addition, it may be necessary to include inelastic effects such as creep; and the rubber must be modelled as a viscoelastic material, adding another layer of complexity (Boast & Coveney 1999). The work undertaken in this thesis concerns itself with relatively small strain behaviour; the models assume either linear elasticity or a relatively simple strain energy function. FEA techniques are employed to study multiple geometries.

2.8.1 Contact

The modelling of contact problems can cause severe problems in FE analysis, geometric and boundary non-linearity from contact can cause convergence issues.

Two contact approaches exist, kinematic and penalty. Kinematic attempts to solve contact conditions exactly which makes it simple and more accurate. However, it

can struggle to solve if not all contacting points can be determined. The penalty approach allows the penetration of two surfaces, then applies a restoring force in subsequent iterations. This method involves user determined sensitivity and thus is more forgiving but less accurate than the kinematic method.

The displacement of contacting nodes relative to one another can be simplified by the small sliding assumption. This means that nodes will displace less than an element's width from one another and the model is thus simplified. However, this assumption is often not viable for rubber contact due to large deformations which may require larger sliding in the contact. Thus, finite sliding may need to be used.

When friction is included it results in an antisymmetric stiffness matrix. This means a non-symmetric matrix may need to be used for friction coefficients of value greater than 0.2. This requires more computational resources.

Explicit analysis is typically used for dynamic problems but it can also be usefully applied to contact. There is no stiffness matrix or convergence requirements and contact discontinuities arising from large deformations and material non-linearity are solved automatically. Simulating a static problem as a dynamic one however means that unwanted kinetic energy will be present in the analysis. This can be minimised with very low loading rates. Another problem arises from the determination of the critical timestep used in the analysis. The timestep is found from the dilatational wave speed in the material. For an incompressible material, this is infinite and the timestep would be zero, so the incompressibility assumption cannot be used. The compressibility of the material may still give unreasonable values of the timestep.

In terms of elements, hybrid elements are good for incompressible or nearly incompressible materials. Triangle or tetrahedral elements are useful for meshing complex geometry. However, where possible quadrilateral (quad) elements should be used as they require less computational resources and time with no loss of accuracy. First order elements are generally less accurate than second order but are less affected by distortion.

As elastomers are a relatively soft and deformable material it is possible to describe a material in contact with an elastomer as being relatively rigid with respect to the elastomer. It is therefore possible to assume that this material is rigid in an FE

analysis of contact between the two. The advantages of this is that the size of the model is diminished, contact parameters are easier to determine as only one surface deforms and thus less computational demands and time are needed (Prior & Cadge 1999).

2.8.2 Friction

A finite element model was used to examine the effects of asperity interaction on friction forces by Bui et al. This study specifically looked at the interactions of a rubber asperity with a rigid asperity of similar dimensions. They took into account adhesion forces as a function of normal pressure and a hysteresis contribution by simulating the viscoelasticity of the rubber. They found that their adhesion depended on the viscoelastic properties of the rubber as well, due to the effect of the viscoelasticity on the contact surface area, as velocity is changed. Consequently, they observed peaks in both friction forces with respect to changing velocity, consistent with classic observations (Bui & Ponthot 2002; Grosch 1963).

3 Materials and Methodology

3.1 Rubber Manufacture

3.1.1 Compounding and Vulcanisation

Vulcanisation is required to transform raw rubber latex, with poor mechanical properties, into the useful engineering material seen in everyday life. A rubber compound is typically made up of five main components; the rubber, a cross-linking agent which forms the all-important cross-links, an initiator and an accelerator to expedite the cross-linking reaction, and an antioxidant to protect the rubber from atmospheric ageing. These ingredients are mixed together in the compounding process. A two-roll mill was used to compound the rubber recipe used in experimentation. The recipe can be seen in Table 3-1.

Table 3-1: Rubber recipe.

Chemical	Quantity $pphr$
Stearic Acid (Activator)	2
Sulphur (Cross-linking agent)	2.5
Zinc Oxide (Activator)	5
N-Isopropyl-N-Phenyl-P-Phenylenediamine (IPPD) (antioxidant)	1
N-Tert-Butyl-2-Benzothiazyl-Sulphenamide (TBBS) (Accelerant)	0.5

To allow the chemical cross-links to form, the compound must be held at high temperature and pressure. A sample from the compound was tested using a rheometer to examine its curing rheology, shown in Figure 3-1. The rheometer test and the curing were conducted at 150℃. This gave a value for the time taken for the compound to reach 90% of its maximum viscosity (t_{90}), corresponding to peak cross-link density.

The rubber compound was then put into a mould and placed into a hot-press to cure for a time equal to t_{90}.

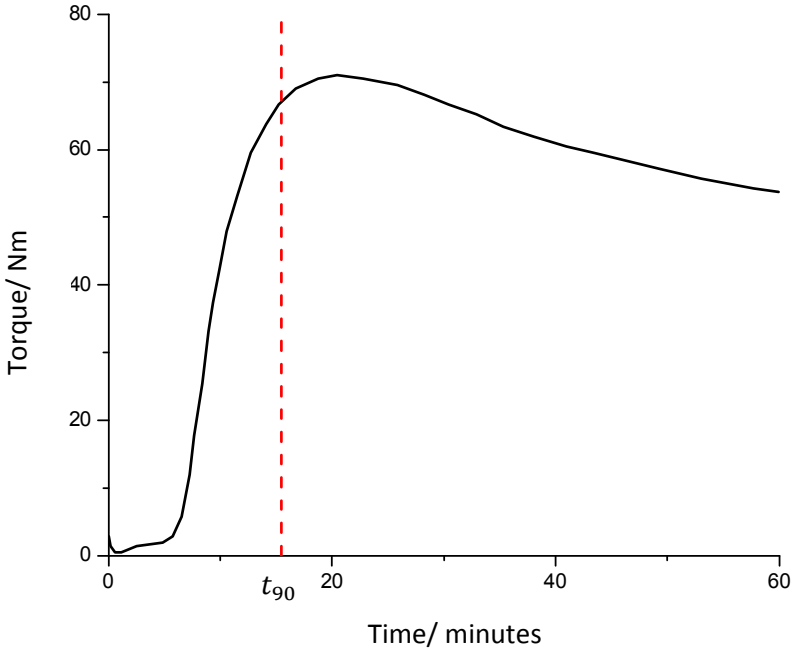

Figure 3-1: Curing curve for NR-0 with t_{90} indicated with the red dashed line.

3.1.2 Methods

1. A quantity of rubber latex was cut and the mass measured.
2. The appropriate mass of each chemical in the recipe were measured out corresponding to the mass of latex.
3. The latex and chemicals were mixed on a two-roll mill using a minimum amount of mixing to produce a homogenous output.
4. The rheometer was set to run for 1hour at 150℃ and allowed to reach operating temperature.
5. Approximately $5g$ of the rubber mixture was tested with the rheometer and the t_{90} cure time was recorded.
6. The required mould was placed into the hot press and the hot press set to 150℃.
7. Once the hot-press had reached operating temperature the mould was removed, the rubber mixture put in the mould, and the mould placed back into the hot-press.
8. The mould was left in the hot-press for time equal to t_{90}, at which point it was removed and the cured rubber removed and left to cool.

3.1.3 Moulding

A variety of rubber moulds were implemented. Smooth mirror-like surfaces were required for rolling experiments whereas different surface finishes were required for the sliding experiments. Moulds to create rubber particles were also needed. A mould surface with an approximately unidirectional roughness was created by machining the surface at specific rates with a 120mm diameter fly cutter. This mould left rubber samples with surfaces as shown in Figure 3-2 a). The dimensions of the large-scale roughness were 50μm in height by 500μm in base length.

Hemispherical asperities were moulded onto samples with a mould surface indented by a 0.5mm diameter ball-nose drill in a controlled pattern seen in Figure 3-2 b). This mould gave hemispherical asperities of 0.5mm diameter and height, spaced 1mm centre to centre.

A similar mould was used to create spherical particles of 5mm diameter for jamming experiments and 2.5mm diameter hemispheres for rheology experiments.

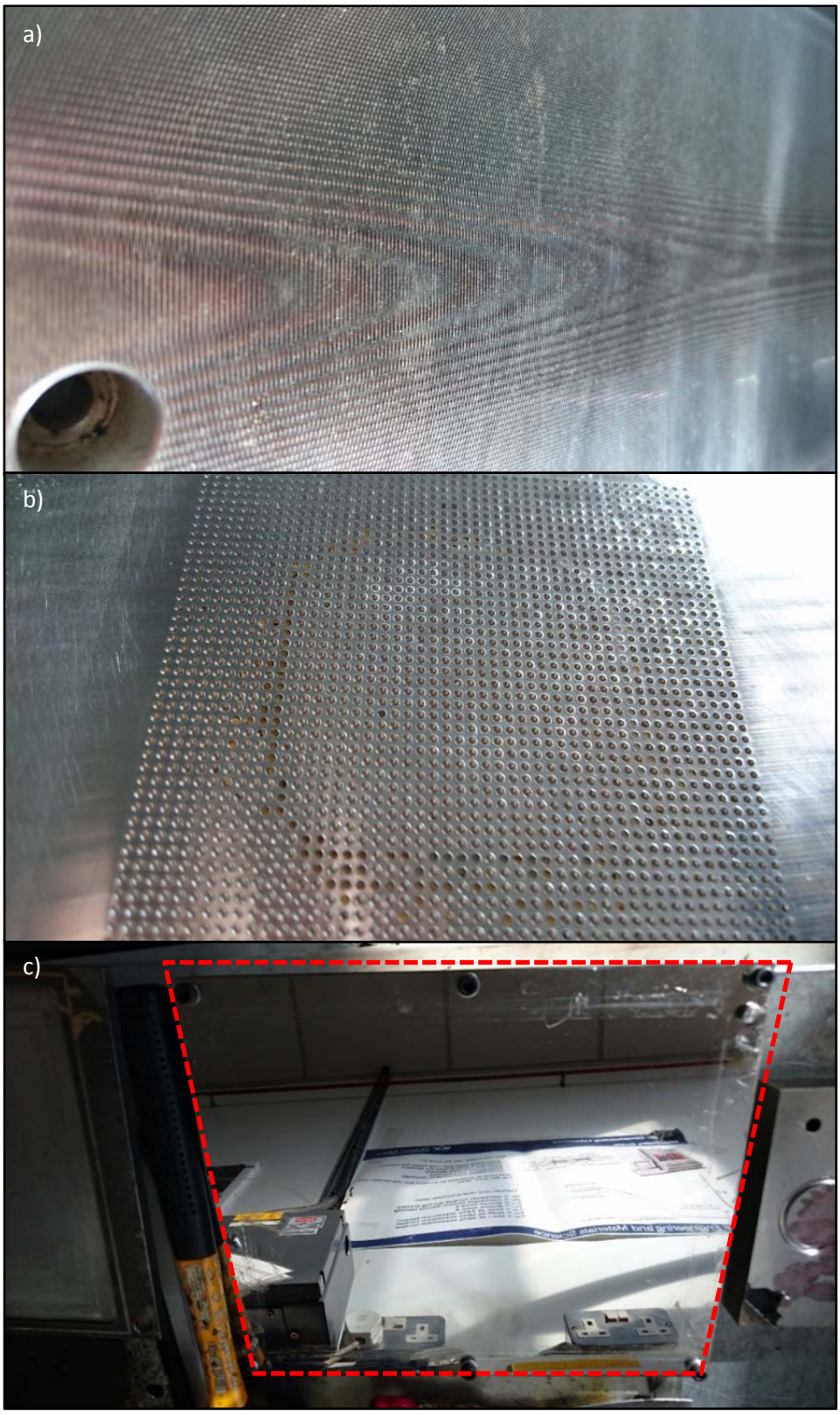

Figure 3-2: Images of moulds used to create specific surfaces; a) cylindrical asperity mould, b) hemispherical asperity mould, c) flat sheet mould.

3.2 Dynamic Mechanical Analysis (DMA)

A DMA is conducted on samples by subjecting a sample to extensions at varying frequencies and temperatures. This is incredibly useful for identifying the dynamic mechanical properties of rubbers, finding the viscoelasticity of samples. Samples used were 2mm thick. Temperature sweeps at a constant low frequency could be used to identify the T_g of a sample.

3.2.1 Methods

1. A rubber sample was cut to dimensions of approximately 5mm by 20mm using a scalpel from an approximately 1mm thick piece.
2. Accurate dimensions of the sample were recorded using a Vernier calliper and a drop gauge.
3. The DMA stand position was calibrated, then the tension film clamp was mounted, and clamp length and compliance were calibrated.
4. A custom method was constructed or loaded as was necessary.
5. The liquid nitrogen was loaded into the liquid nitrogen tank.
6. The sample was loaded loosely onto the clamp and its dimensions inputted, the clamp-to-clamp length read off from the measurements panel.
7. The furnace was closed and the test started.
8. Once minimum temperature had been reached (typically -80℃) the furnace was opened and the clamps tightened on the sample.
9. The furnace was closed and the test was initiated.
10. For testing T_g a constant frequency of 1Hz at a fixed 0.1% strain was applied as the temperature was increased from the initial temperature to a final temperature.
11. For time temperature superposition a frequency sweep up to 100Hz was conducted at the fixed temperature and strain of 0.1%.
12. The temperature was then increased a set amount (≤5℃) and allowed to equilibrate.
13. Steps 11 and 12 were repeated until the final temperature was reached.

The temperature sweeps give a value of T_g of approximately -77°C and -37°C for NR-0 and ENR-0 respectively.

The DMA was also used to produce the relaxation spectra of a rubber sample. The dynamic moduli were needed over a large range of frequencies. The way this was achieved was to run a set frequency sweep at different temperatures then construct a master-curve out of the data using the WLF transform (equation 2-16) with the reference temperature $T_r = Tg + 50^0$. The relaxation spectra ($H(\tau)$) could then be constructed using the formulation suggested by Ferry et al. (1953) (equation 2-11). $H(\tau)$ was found by an iterative process from an initial approximation to A_H using a MATLAB code to iteratively calculate values of the local slope.

3.3 Fourier Transform Infra-Red Spectroscopy (FTIR)

FTIR involves firing an infra-red laser at a sample and analysing the returning signal to identify the absorbed energy bands and thus identify the elements present within the sample. This technique was used to analyse the effect of cleaning the surface of rubber samples with acetone and also to examine oxidative ageing rates of samples.

3.3.1 Methods

1. A sample was cut to a size approximately 5 by 5mm from a 1-2mm piece.
2. Liquid Nitrogen was loaded into the FTIR.
3. A background scan was conducted over the 4000-500cm^{-1}
4. The sample was placed over the scan area and the sample holder pressed firmly into the sample.
5. A scan was conducted over the range of interest.
6. Absorbance peaks were used to determine chemical bonds present in the sample.
7. Steps 3-6 were repeated to analyse multiple samples from a single rubber piece.

3.4 Instron Tensile/ Compression Machine

The Instron tensile/ compression machine was used extensively as part of a sliding friction experimental setup that will be discussed in section 3.8. It was also used to determine the tensile modulus of samples.

3.4.1 Methods

1. A sample was cut from a 2mm thickness piece of rubber using a dumbbell cutter.
2. Sample thickness and width were measured using a drop gauge and a Vernier calliper respectively.
3. The sample was loaded into tension clamps attached to the Instron machine.
4. A small preload was applied to remove slack from the sample.
5. The length from clamp to clamp was measured.
6. A tensile extension was applied to the sample.

3.5 Profilometry

A profilometer maps out a surface, either by the detection of the reflection of a laser off the surface or the displacement of a stylus in light contact with the surface. Both types were used however, due to the low reflection afforded by rubber, a Dektak contact-style profilometer was primarily used. The surfaces of both rubber samples and counter-surfaces used in experimentation were analysed in this way, an example of which is shown in Figure 3-3.

3.5.1 Methods

1. A sample of a surface of approximately 50 by 50mm is cut from the main piece of material.
2. The sample is placed into the profilometer and the area to be scanned is selected.
3. The surface is cleaned with acetone and allowed to dry for 10 minutes.
4. Several quick scans are performed to remove any large gradient.
5. A scan of the selected area is performed.
6. Image analysis software is used to remove any gradients or anomalous peaks due to dust.

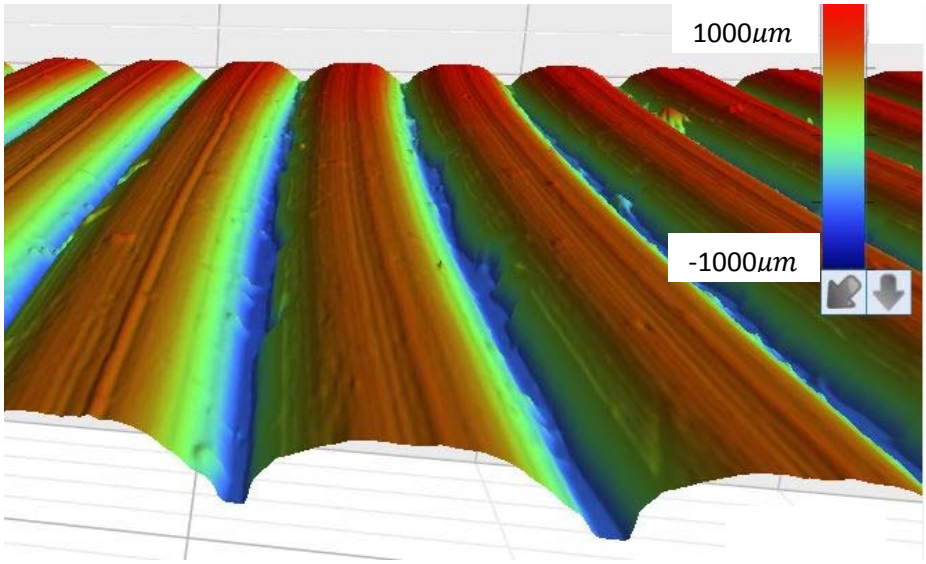

Figure 3-3: 3D profile of cylinder asperity sample taken using Dektak profilometer.

3.6 Contact Angle

The surface energy of the solids used in experimentation was examined via contact angle measurements using a Kruss DSA100. Surface energy of the solids is found by measuring the angle of incident of a droplet of a range of liquids on the solid surfaces.

3.6.1 Methods

1. The sample was placed on the stage and the position of the stage adjusted to align it with the camera.
2. The sample was cleaned with acetone and left 10minutes to dry.
3. A pipette (2-27μl) was used to apply a droplet of 7μl volume to the surface.
4. The camera image of the droplet was frozen and the contact angle was measured using either 2nd tangent or Wendt analyses depending on accuracy to the droplet outline.
5. A further droplet of 7μl was added to the first and step 4 repeated.
6. Step 5 was repeated until the droplet was at least 21μl in volume or the size of the contact was not changing by more than 0.5^0.
7. Steps 3-6 were repeated a minimum of 5 times.
8. Steps 2-7 were repeated using different liquids each time.

3.7 Rolling Friction Tests

3.7.1 Introduction

Rolling friction tests were necessary to evaluate the peeling behaviour of various couplings of rubber and counter-surface. The tests were conducted with a sheet of flat rubber sample attached to a rigid cylinder and a counter-surface of specific material inclined at an angle to the horizontal. Changing the gradient of the incline results in altering the rolling velocity and the peeling energy (E_p). As has been previously discussed E_p is found from the change in gravitational potential energy E_g of the system using equation 2-91.

3.7.2 Apparatus

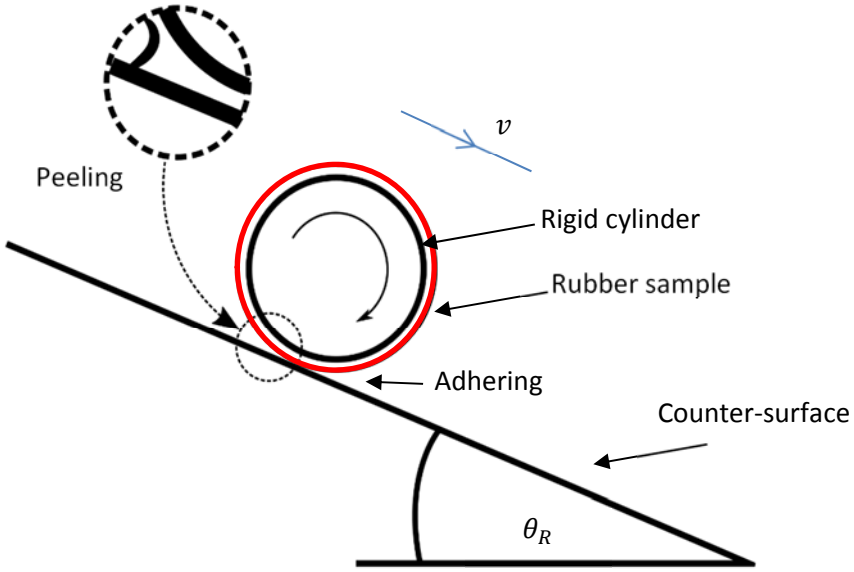

Figure 3-4: Diagram of rolling tests.

The setup for these tests was relatively simple. The requirements were for an interchangeable substrate with a variable incline angle, and interchangeable rubber samples. It matters little whether a cylindrical rubber sample rolls down a flat sheet of material or a rubber sheet is used with a cylinder of a specific material rolling. It was decided to use a rubber sample attached to a rigid cylinder and flat sheets of various rigid materials, as shown in Figure 3-4, as then the same flat sheets could be used in sliding friction tests ensuring that surface properties and bulk material properties were constant for both experiments. A lab-jack was used to alter the incline angle.

3.7.3 Sample Preparation

Samples of rubber were produced in sheets of 200 by 250 by 2mm. These sheets were then cut into strips of 50mm width to then be applied to a Perspex cylinder via double sided tape. The substrates were purchased in sheets. The most important factor in coupling these tests to the sliding friction experiments was that the surfaces were identical, as the peeling parameters that define the peeling of the rubber from the counter-surface may be influenced by factors such as surface imperfections.

Rubber samples of unfilled natural rubber (NR-0) and 50% epoxidised unfilled natural rubber (ENR-0) were created. The substrates used were polymethylmethacrylate (PMMA), polyethylene (PE), polypropylene (PP), glass, and steel.

3.7.4 Methods

1. The substrate was set to the required angle.
2. Both the substrate and the rubber sample were cleaned with acetone and left for 10 minutes to dry.
3. The rubber sample was placed at a point towards the top end of the substrate.
4. The rubber sample was allowed to roll for 50mm before a timer was started.
5. The timer was stopped once the rubber sample had rolled another 5-10mm depending on the angle being used.
6. Steps 2-4 were repeated 10-20 times depending on the rolling velocity.
7. Steps 1-5 were repeated over a range of angles

3.8 Sliding friction tests

3.8.1 Introduction

Testing was done to evaluate the friction of rough rubber samples with controlled, standardised asperities patterned to the surfaces, against different surfaces with different surface energies. Two asperity geometries were tested, cylindrical and hemispherical asperities, with five different surfaces; PMMA, PP, PE, glass, and steel. Results are obtained for NR-0 against all surfaces, and for ENR-0 against glass and steel.

3.8.2 Apparatus

Preliminary tests were conducted using a unislide with a pivoting arm attached as shown in Figure 3-5. A sample was attached to the height-adjustable base and a counter-surface to the arm. The velocity of the sliding was controlled using a Digiplan controller. Later testing was done using a rig designed to attach to an Instron machine.

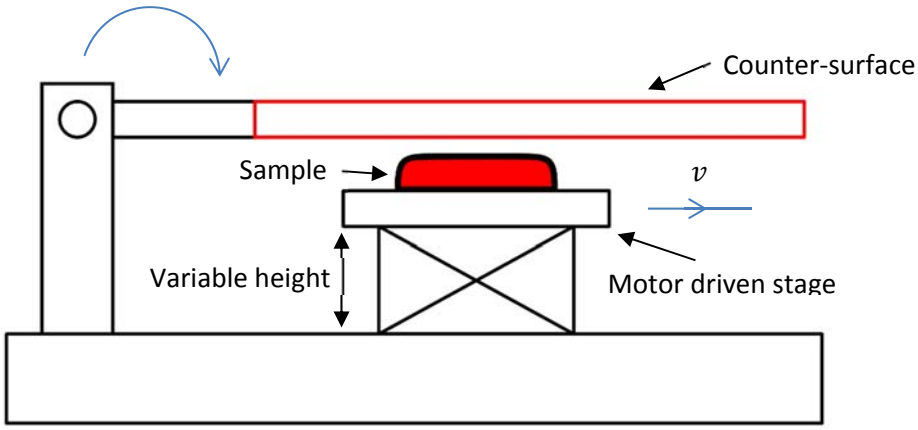

Figure 3-5: schematic diagram of unislide friction apparatus.

3.8.3 Sample Preparation

The rubber samples used were made with two different types of patterned asperities, one with a pattern of grooves extending across the entire sample surface. These samples will be referred to as cylindrical asperity samples. The dimensions of the asperities were approximately 50μm in height by 500μm in base length. A repeating pattern of semi-circular asperities was also tested with; these samples are henceforth referred to as hemispherical asperity samples. The asperities had a diameter 0.5mm.

Rubber samples of both unfilled natural rubber (NR-0) and 50% epoxidised unfilled natural rubber (ENR-0) were used against substrates of PMMA, PE, PP, glass, and steel.

3.8.4 Methods

3.8.4.1 Unislide rig

1. A rubber sample was affixed to an aluminium sheet.
2. The aluminium sheet was fastened to the laboratory jack.

3. The track was connected to the pivoting arm and the arm put at rest away from the sample.
4. The sample and track were cleaned with acetone.
5. The load cell was connected if needed and the software opened and set to the required settings.
6. The Digiplan was switched on if off and set to the desired settings, the acceleration was always maintained at a minimum of ten times the velocity in magnitude.
7. The moving base was positioned to the standard home position using the Digiplan.
8. The track was put into contact with the sample. This step was taken 20 minutes after step 4.
9. The laboratory jack height was adjusted to give a highest possible level of contact between track and sample.
10. The Unislide was set into motion using the Digiplan.
11. Recordings of the force detected by the load cell and the velocity set in the Digiplan were recorded.
12. The track was taken out of contact with the sample
13. Steps 7-12 were repeated to get multiple readings.
14. Steps 4-13 were repeated for different velocities.

3.8.4.2 Instron rig

1. A counter-surface was attached to the base-plate.
2. The level of the counter-surface was measured using a spirit-level and adjusted by changing the height of the base-plate at the corners.
3. A rubber sample was attached to the sled and the chord connected to the load cell.
4. The height of the pulley was adjusted to ensure that the chord was parallel to the counter-surface when taut.
5. The Bluehill software was set to the appropriate settings with the appropriate constant velocity.
6. Both rubber sample and counter-surface were cleaned with acetone and left to dry for ten minutes.
7. With the sample set on the counter-surface the test was initialised and allowed to run for 200mm.

8. The load cell and sled were returned to their initial position.
9. Steps 6-8 were repeated a minimum of 5 times
10. Steps 5-9 were repeated to give results at different velocities.

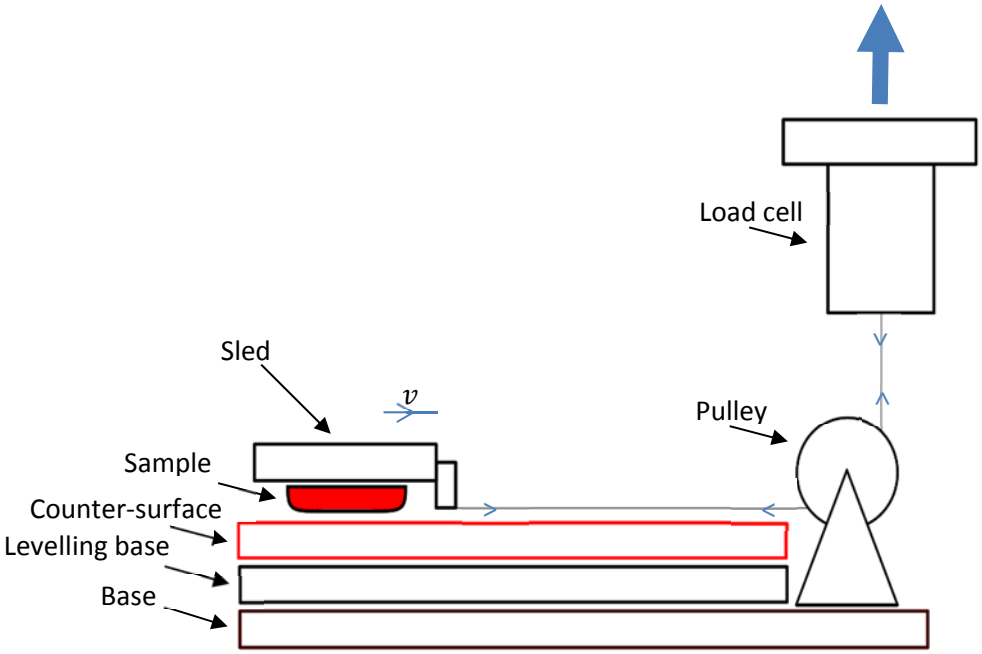

Figure 3-6: Instron sliding friction test setup.

The Unislide setup suffered from a few problems; it was difficult to control the normal load on a sample, which indeed would vary slightly during testing, it was difficult to ensure the sample and counter-surface remained level throughout a test, and it failed to adequately protect the load cell used to measure frictional force, mostly due to the varying levels of moments about the pivoting arm which changed with movement of the motor driven stage. For these main reasons the Instron setup was developed, however the data gathered from early testing on the Unislide was useful in informing the development of an improved friction setup. The Instron setup, shown in Figure 3-6, consisted of a sled, to which rubber samples are attached, which is pulled over a base to which counter-surfaces are affixed by a cord attached to the load cell via a pulley. The cord was kept close to the counter-surface to minimise moments about the frictional interaction between sample and counter-surface, and the position of the counter-surface and height of the pulley could be adjusted to ensure the counter-surface and cord were level. Sliding data presented in later sections will be obtained from the Instron setup.

3.9 Monolayer Jamming Tests

3.9.1 Introduction

The behaviour of jammed macroscopic rubber particles was examined in a controlled manner as a single layer of particles enclosed in a flexible membrane. An external force was applied to the packing to test the response of the packing to applied loading. Tests were done with three types of $10mm$ diameter monodisperse spherical particles; NR-0, acrylonitrile butadiene rubber (NBR), and steel. Three types of force application were examined; bending, shear, and cyclic shear tests.

3.9.2 Apparatus

The packing itself was constructed of a membrane, secured to a specially made nozzle, filled with particles. This nozzle could be attached to a base which sat underneath the packing. This base was made with steel with a layer of PTFE over the top to limit friction of the packing with the base. A PMMA top was attached to the base. This could be adjusted in height to accommodate different sized particles. The purpose of the top was to limit out of plane buckling of the monolayer. PMMA was chosen to allow observation of the packing during tests. To the nozzle a rubber tube was attached which connected to a vacuum pump. Lateral force was applied to the packing using a Unislide to which an indenter and a load cell in series was attached. The setup is shown schematically in Figure 3-7. Depending on the test type an attachment could be applied to the end of the packing to allow for an approximately pure shear deformation of the packing. Two types of test were conducted; a bending and a pure shear test. Cyclic shear tests were also conducted.

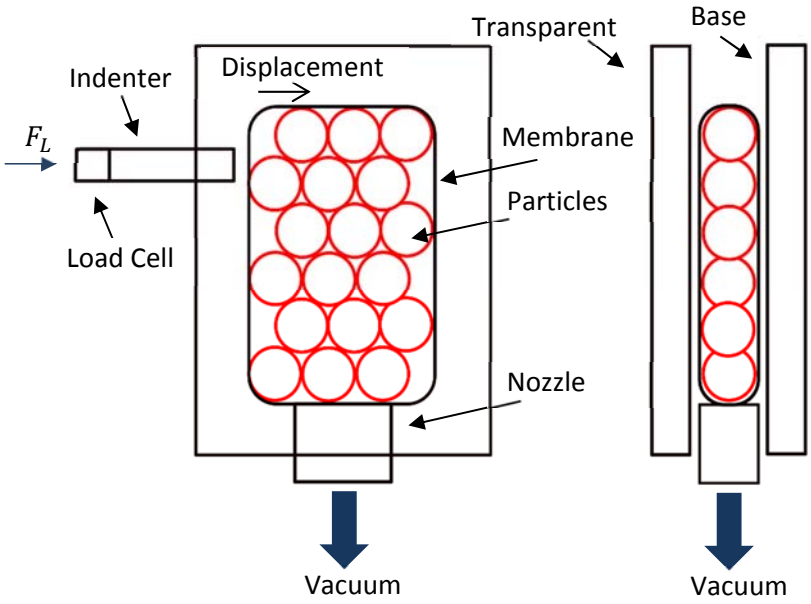

Figure 3-7: Monolayer test setup diagram.

3.9.3 Sample Preparation

A mould was constructed consisting of an array of hemispheres on both sides to enable the production of rubber particles. Two sizes were made; 10mm and 5mm diameters. Samples used were 10mm diameter steel spheres, 10mm diameter NBR spheres, and 10mm diameter NR-0 spheres.

3.9.4 Methods

1. The membrane was filled with the required particles then attached to the nozzle.
2. The nozzle was attached to the base and the particles arranged into a monolayer. The arrangement of the particles was left random or arranged into a hexagonal packing depending on the test.
3. The nozzle was attached to the pump and, depending on test type, an attachment could be attached to the end of the packing.
4. The top was positioned so that it sat with a clearance of approximately 1mm above the packing.
5. The indenter was brought into position; for bending- so that it was minimal distance from the side of the packing 10mm from the end of the packing, for shearing- so that it inserted into the attachment to the end of the packing.

6. The indexer was set to 0.1mms^{-1} and the test initiated to a maximum displacement of ~50mm.
7. The indenter was brought back to initial position.
8. Steps 5-7 were repeated with minimal rest time in between for cyclic tests.

Issues with this testing setup concerned the friction between the packing and the base, and the effects of the membrane on results. The membrane is known to affect the force response of a packing as was discussed in section 2.7.4, and this will be particularly prominent with the monolayer test setup as the ratio of inter-particle contact to particle-membrane contact will be quite low. For detailed examination of the development of inter-particulate forces a rheological test method was developed. In an attempt to mitigate the influence of the membrane a vertical monolayer experimental setup was constructed. This setup would employ a belt-like membrane surrounding a collection of cylindrical particles so that a theoretically plane strain geometry could be studied. The setup was designed to sit with its strain plane vertical to minimise contact with restraining walls, providing the same function as the base and cover in the original setup, and also so that the setup could be mounted onto an instron machine. The friction between the walls and particles however tended to pull particles out of the packing configuration and plane strain conditions were not easy to maintain; thus, the vertical setup was quickly abandoned. The membrane may have a greater effect per particle in the monolayer setup than in a typical packing system as all particles within the monolayer interact with the membrane unlike in a typical packing. For this reason, the number of particles per packing was maintained constant throughout testing.

3.10 Rheological Inter-Particulate Force Testing

3.10.1 Introduction

To observe the development of inter-particle forces upon deformation of particles into one another, a few particles are isolated and sheared with respect to one another on a rheometer. Tests were done on 5mm diameter hemispheres of NR-0.

3.10.2 Apparatus

The rheometer used was an AR2000 rheometer. The plate geometry used was a 60mm diameter top plate and a bottom plate of corresponding diameter was designed to fit onto the base. This, the largest plate accessory for the rheometer,

was used to give the closest approximation to lateral shearing of the hemispheres. Hemispheres were attached to the plates at a distance of 27.5mm from the centre, two attached next to one another on one plate and one on the other plate, as shown in Figure 3-8.

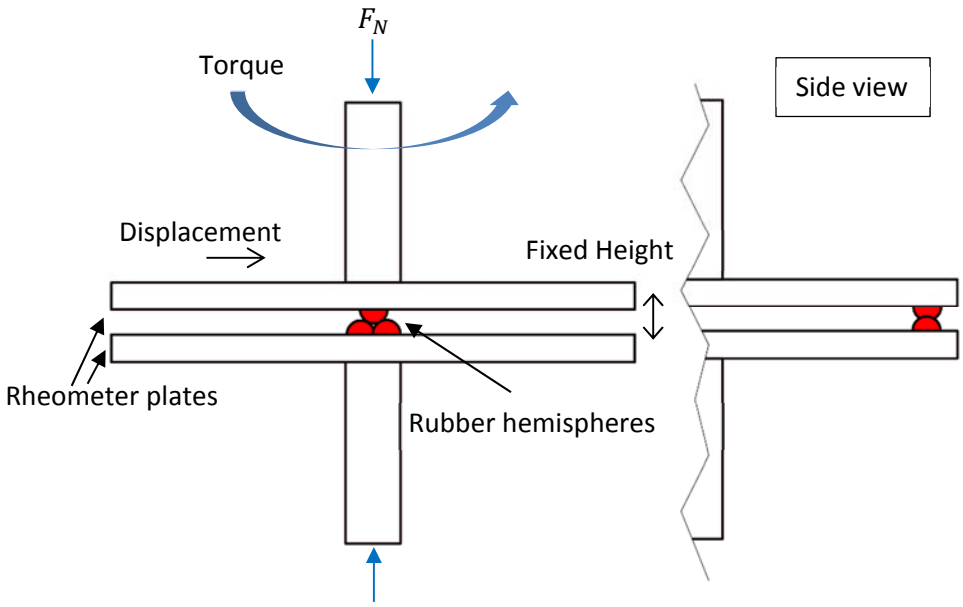

Figure 3-8: Diagram of rheometer test setup.

3.10.3 Sample Preparation

The samples were created using a mould with multiple 2.5mm radius hemispherical indents in it. The rubber samples used were NR-0, some are shown in Figure 3-9 attached to the rheometer plates.

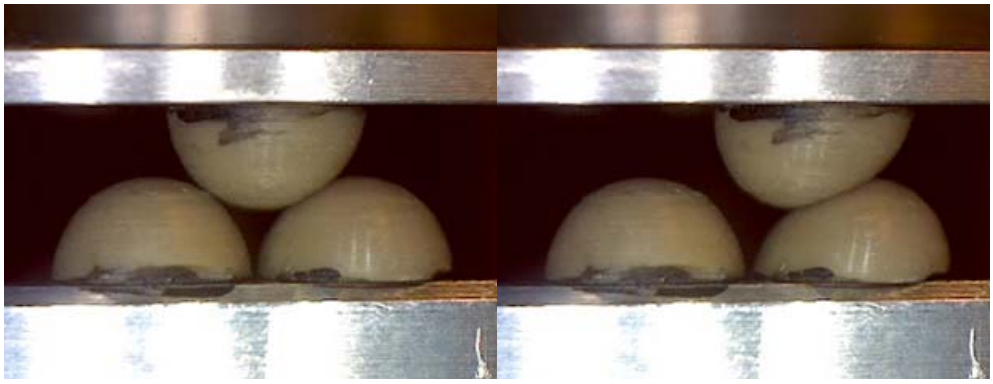

Figure 3-9: Images of the rubber samples during rheometer testing.

3.10.4 Methods

1. The samples were attached to the plates using a stencil and Loctite 480 instant adhesive.

2. The plates were mounted to the rheometer and the test process, a torque ramp, was loaded on the console.
3. The hemispheres were cleaned with acetone and left for ten minutes.
4. The top plate was brought down until the top particle rested in between the two bottom particles and the registered normal force was at the required value.
5. The test was initiated and repeated 6 times. Unless the torque high enough that the top hemisphere completely cleared the bottom two the hemispheres were allowed to come back to initial positioning uninterrupted.
6. The plates were separated again after the set of tests were finished.
7. Steps 3-5 were repeated for different normal force values.

One drawback of these tests was the inability for the rheometer to maintain constant normal force (by altering the separation of the plates) during tests. A packing subjecting the particles it contains to a constant pressure via the membrane would be expected to thus exert a largely constant force from this pressure onto an individual particle. Thus, as a particle is pushed past other particles within the packing, the packing must dilate to accommodate this in order for the pressure of the membrane to remain constant. Modelling of the interactions will not therefore, be of the exact same behaviour as that in a jammed system in a flexible membrane. Once validated against such experimental results however, the model can be easily modified to allow dilation and a constant normal force to mimic jamming robotic systems.

The test provides the best method of studying evolution of force in a particle interaction by isolating a desired part of the system. The test is only an approximation to the interactions within a packing however, with the approximately linear displacement but also with the constant normal distance rather than a constant normal force and changing normal displacement as would be expected in a packing under constant pressure. This test is also limited in the maximum force(torque) to which it can be run. This limits the amount of deformation that can be observed primarily at high normal loads; to obtain a greater range of deformation low initial normal forces must be employed.

4 Sliding Friction of Rough Rubber on Smooth Surfaces

4.1 Introduction

The role of adhesion in sliding friction has been somewhat overlooked in more recent studies as for a lot of common practical purposes its contribution to the overall friction is negligible in comparison to the hysteretic contribution. When one considers that 70% of the rubber industry is concerned with tyre manufacture this isn't too much of a surprise. As such there is still work to be done in linking the adhesive origin on a molecular level with macroscopic observations and a lack of mechanical models to describe the variety of potential situations where a large adhesion force may be present. Adhesive friction can be significant where contacting surfaces have smooth surfaces or where they are pressed into contact by a large pressure in applications such as seals. As has been discussed, stress relieving effects inhibit the adhesional frictions upper confines. This is not always seen as being the case however, as in the work by Arnold et al., where a rough rubber surface does not display the same levelling off of friction as the smooth rubber surface. This indicates a behavioural regime change between the two instances.

4.2 Theory

The data by Arnold et al., (Arnold et al. 1987), can be presented in a logarithmic plot of frictional shear stress against sliding velocity, shown in Figure 4-1. The frictional shear stress is approximated by the sample size quoted in the paper.

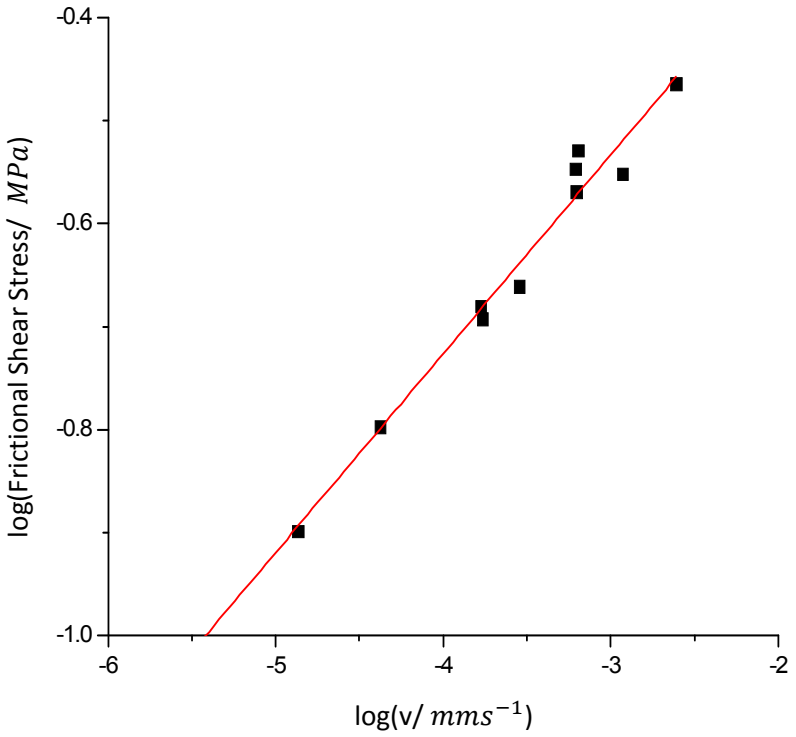

Figure 4-1: Graph adapted from frictional data of Arnold *et al.* modified to show shear stress against sliding rate for rubber with an R_a value of 4μm against smooth Perspex (Arnold et al. 1987)**.**

A power law trend is seen between the frictional shear stress and the sliding velocity. A comparable dependence for rubber peeling energy on peeling velocity has been previously observed (Fuller & Roberts 1981). It was hypothesised therefore that a similar peeling behaviour attributed there was making a significant contribution to the frictional behaviour observed in Figure 4-1. This could allow a new framework for the understanding of the friction behaviour of this instance to be developed based upon a peeling energy mechanism. The reason why this same behaviour is not seen for a smooth rubber surface is due to the onset of buckling effects such as Schallamach waves. Their absence from the rough rubber sliding may be due to the distinct points and areas of the asperity contact areas over which

peeling occurs which means continuous sliding can occur without needing a mechanism such as Schallamach waves.

Similarity between crack growth mechanics and adhesion has been pointed out previously and comparable mechanisms applied in understanding adhesive contact among other things (Pollock et al. 1978; Maugis 1992; Sundaram et al. 2012; Persson & Volokitin 2006). A theory well supported by experimental observation describes the peeling process of rolling friction of smooth rubber on a smooth rigid surface in terms of a crack closing between the two surfaces in front of the rolling and one opening at the rear (K. Kendall 1975). The adhesion is defined as an energetic discrepancy between crack opening and closure at the rear and front of the rolling sample respectively. The peeling process is characterised by an energy loss from detachment of surfaces which far outweighs the attachment energy as the two surfaces combine so that the work of adhesion is equal to this detachment peel energy (G. Briggs, B. Briscoe, 2001; Kendall, 1975). A power law relationship between rolling velocity and peeling energy is found, similar to that seen for the shear stress against velocity in Figure 4-1.

A similar mechanism is proposed to account for the adhesional friction for the case of rough rubber on a smooth surface. The friction behaviour could be supposed to predominantly arise from the adhesional attachment and peeling of the rubber asperities to and from the hard surface. The peeling of the asperities can be seen as a crack growing between the two surfaces with the energy needed to peel the rubber equivalent to the energy required to create two new surfaces. In this investigation, both rolling and sliding tests were conducted with the same rubber against various counter-surfaces to examine how the mechanisms compare. The

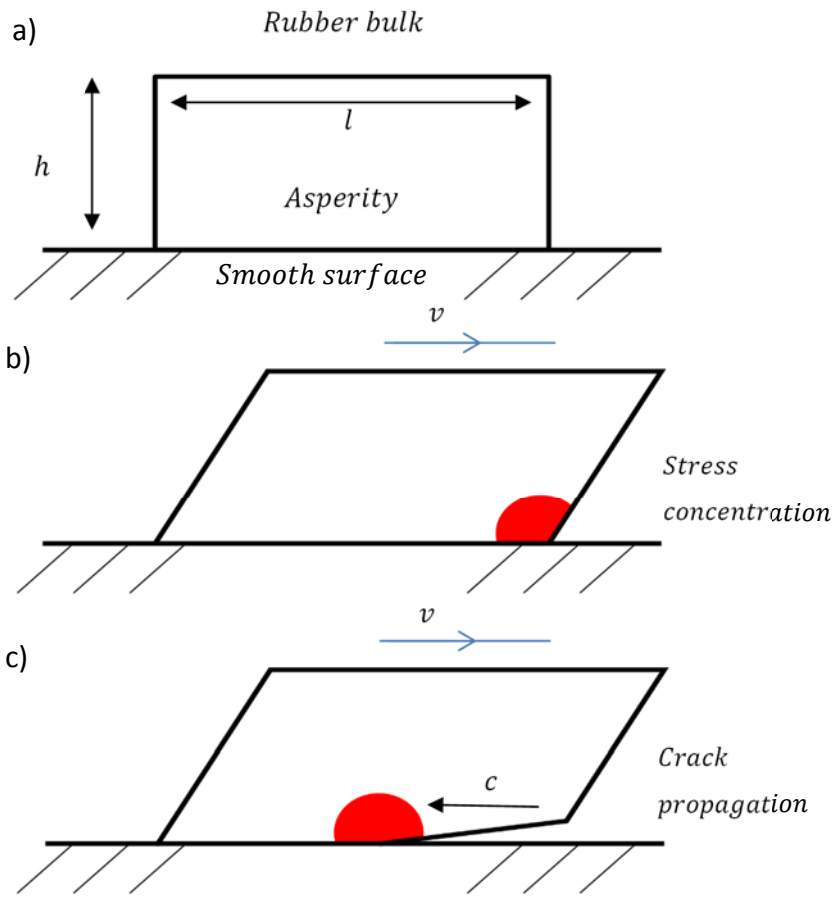

Figure 4-2: Model diagram of a square shaped asperity in 2D peeling. a) Asperity at rest, b) velocity is applied to the rubber and the asperity deforms, c) a crack initiates and propagates between the surface of the asperity and the smooth counter-surface.

well-established rolling mechanism will give coupling specific peeling parameters.

A single simple square shaped asperity on a rubber surface is considered in plane strain (Figure 4-2). With a velocity applied to the rubber the asperity is expected to deform. As the asperity deforms the contact between the surface of the asperity and the smooth counter-surface will start to diminish as the asperity peels away from the opposing surface. This can be thought of in terms of a crack developing between the two surfaces. Comparison of adhesive peeling to crack propagation mechanics has been done before (Pollock et al. 1978; Maugis 1992; Sundaram et al. 2012; Persson & Volokitin 2006). The goal in this instance would be to derive an expression for the friction caused by the energetics of propagating a crack between the adhered asperity and the counter-surface with the geometrical constraints of the asperity. Crack propagation in simple shear, to which the peeling of the model

asperity can be equivalated to, is given by equation 2-20. The energy required to peel the asperity and therefore propagate the crack is the peeling energy (E_p):

$$E_p = T_E = Uh \tag{4-1}$$

The strain energy density of the asperity can be found by considering the deformation of the asperity;

$$U = \frac{1}{2}\sigma\varepsilon = \frac{1}{2}G\varepsilon^2 = \frac{1}{2}G\left(\frac{vt}{h}\right)^2 \tag{4-2}$$

For simplicity, the rubber here is assumed to deform within the small strain linear region. Thus, an expression for E_p is found in terms of the rubber modulus, sliding velocity, and asperity dimensions:

$$E_p = \frac{1}{2}G\frac{(vt)^2}{h} \tag{4-3}$$

The peeling rate characteristics of the rubber become important. Rate of peel is given by the following expression:

$$\frac{dc}{dt} = AE_p^{\alpha} \tag{4-4}$$

Where *A* and α are characteristic material properties. The parameter α defines the dependence of peeling energy on peel rate. Peeling, as with tearing, is considered to be a viscoelastically dominated mechanism which implies that α is dependent on the viscoelastic behaviour of the two materials interacting; i.e. of the rubber (Greensmith & Thomas 1956; K Kendall 1975).

As alluded to earlier, this peeling rate dependence of the peeling energy has been previously observed, notably in rolling adhesion (Barquins 1988; K. Kendall 1975). Rolling experiments are a well-defined, simple configuration which, for negligible hysteresis friction contribution, is entirely dependent on adhesive behaviour. Similarly to the problem considered here, the adhesion is seen as an energetic discrepancy between crack opening and closure at the rear and front of the rolling sample respectively. In this case it is quite easy to see that the energy loss to friction must match that of the change in potential energy as the sample rolls down a slope (K. Kendall 1975; Fuller & Roberts 1981). This configuration gives a simple way of finding the velocity dependence of the peeling energy.

Substituting equation 4-3 into equation 4-4 gives the following expression for the rate of peel:

$$\frac{dc}{dt} = A\left(\frac{1}{2}G\frac{(vt)^2}{h}\right)^{\alpha} \quad 4\text{-}5$$

Integrating with respect to t an expression for the time for the asperity to peel (t_1), at which point the crack has traversed the length of the asperity.

$$t_1 = \left((1+2\alpha)\frac{l}{A}\left(\frac{2h}{Gv^2}\right)^{\alpha}\right)^{\frac{1}{(1+2\alpha)}} \quad 4\text{-}6$$

The work done, W_p, to unpeel the asperity with width *w* can be written as:

$$W_p = w\int_0^l E_p dc \quad 4\text{-}7$$

The work done can also be expressed in terms of the asperity width (*w*), length, velocity and peel time and the average shear stress over the peeling process (σ_f):

$$W_p = \sigma_f wlvt_1 \quad 4\text{-}8$$

Equating the two expressions for the work done and assuming the stored elastic energy involved is zero and that there is no sudden discontinuous relaxation an expression for shear stress is found:

$$\sigma_f = \frac{1}{lvt_1}\int_0^l E_p dc \quad 4\text{-}9$$

Substituting for the various parameters and integrating with respect to t an expression for σ_f is derived in terms of the asperity dimensions, bulk properties of the rubber, and the sliding velocity:

$$\sigma_f = \frac{(2\alpha+1)^{\frac{2(\alpha+1)}{(2\alpha+1)}}}{(2\alpha+3)}\left(\frac{l}{A}\right)^{\frac{1}{(2\alpha+1)}}\left(\frac{1}{2}\frac{G}{h}\right)^{\frac{(\alpha+1)}{(2\alpha+1)}} v^{\frac{1}{(2\alpha+1)}} \quad 4\text{-}10$$

This indicates that a specific rubber of known roughness sliding against a smooth surface would exhibit a frictional shear stress increasing with velocity, as would be expected, within a range governed by the viscoelastic behaviour of the rubber. The derived expression will be henceforth referred to as the box asperity model. No surface is perfectly smooth however the theory should hold provided that the level of roughness of the 'smooth' surface does not give a significant level of hysteresis

and that the contact between asperities on the rubber surface and the counter-surface is approximately continuous (also dependent on normal force). In effect the rubber asperities need to be significantly greater than asperities on the counter-surface.

The theory suggests that a power law relationship should be expected between σ_f and sliding velocity, a characteristic observed in the experimental data of Arnold, Roberts and Taylor (1987). Taking the gradient of the line of best fit, using the theoretical equation, the peeling parameter α can be predicted for the rubber to surface configuration used. The value derived is about 2, which is a similar magnitude to that obtained from fracture mechanics from the crack propagation data by Lake (1995) from Figure 2-6, albeit with SBR rubber, of $\alpha = 2.3$.

The effect of various parameters on the derived theoretical model is examined by altering each of the parameters in turn. When not being varied the parameters are kept at the values: $v = 0.01 mms^{-1}$, $h = l = 1mm$, $\alpha = 2$, $A = 1\times 10^{-6} m^{(1+2\alpha)}(sN\alpha)^{-1}$, for a rubber sample of $10mm$ width and $G = 0.433MPa$.

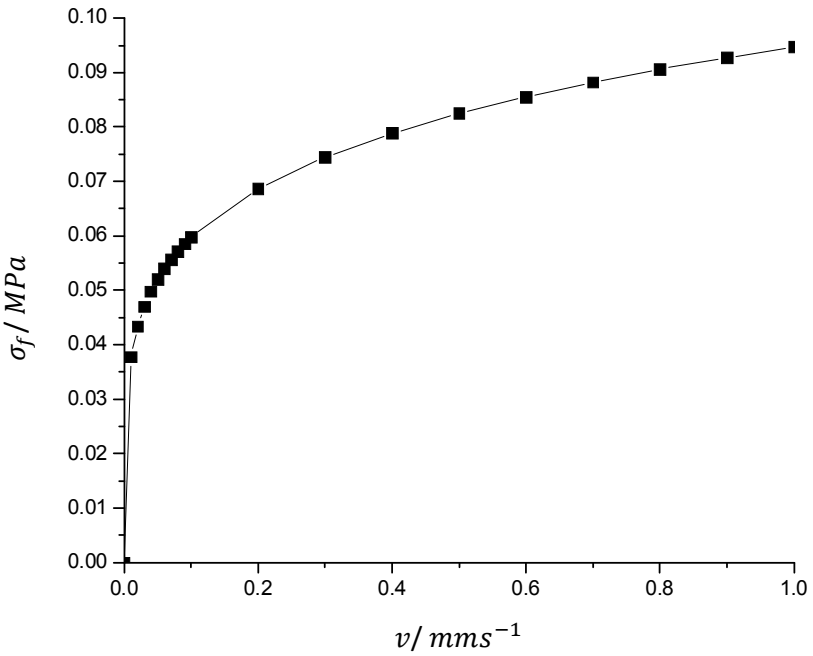

Figure 4-3: Velocity dependence of frictional shear stress predicted by the theoretical model represented by equation 4-10.

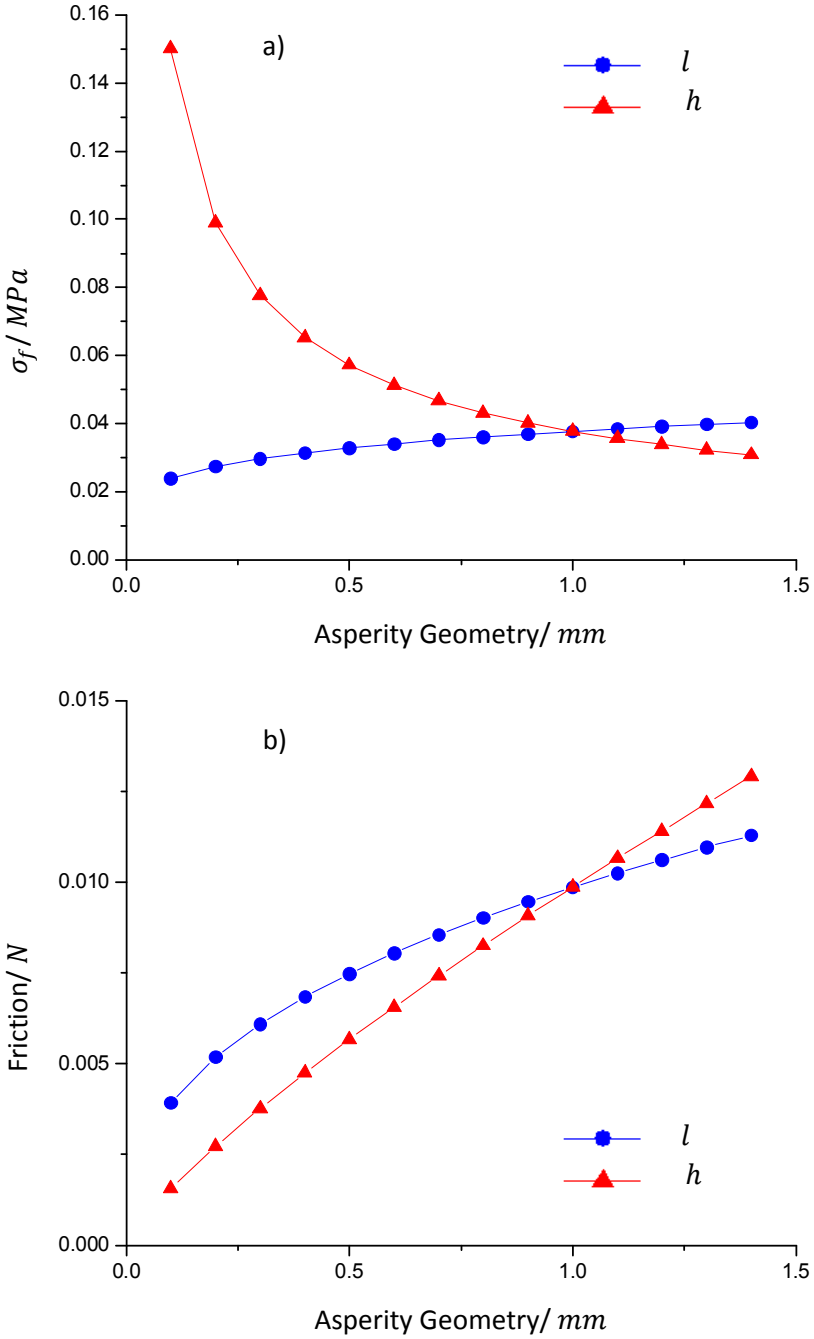

Figure 4-4: Dependence of a) frictional shear stress, and b) friction on asperity geometry predicted by the theoretical model represented by equation 4-10.

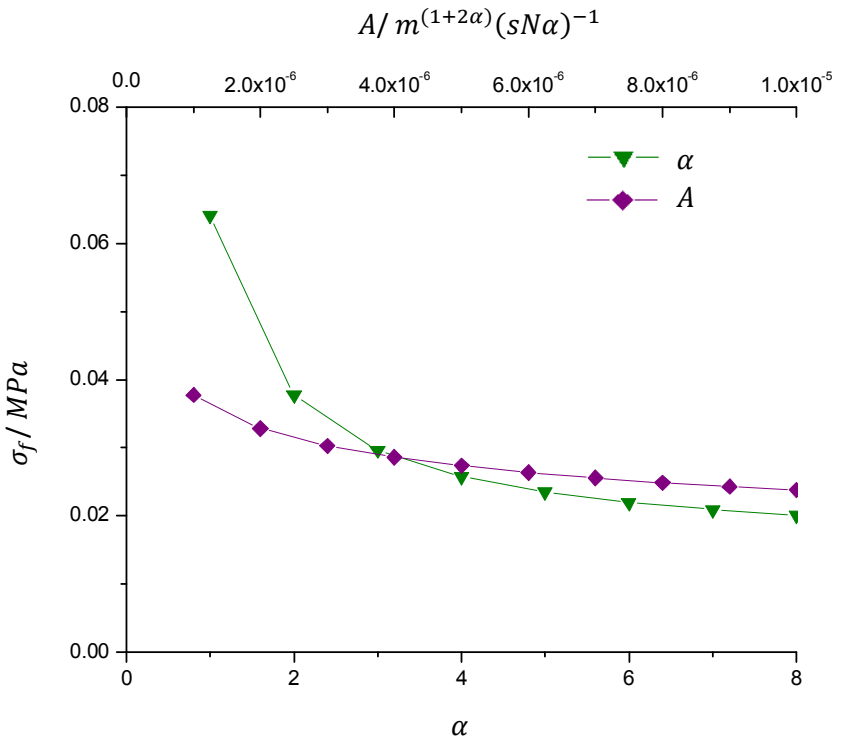

Figure 4-5: Dependence of frictional shear stress on peeling parameters of the rubber-substrate combination predicted by the theoretical model represented by equation 4-10.

It is seen that σ_f increases with increasing speed reflecting an increasing frictional force, Figure 4-3, as would be expected and is observed experimentally (Arnold et al. 1987; Grosch 1963; Heinrich & Klüppel 2008; Persson & Volokitin 2006). It should be noted that although the effect of increased velocity on σ_f diminishes as higher velocities are reached, the change in behaviour of the rubber at very high velocities to a low viscosity glassy material and the subsequent change in frictional behaviour will not be captured by the model which considers a consistent viscoelastic behaviour valid for a large range of velocities. The validity of this behavioural supposition is examined in the results and discussion section (section 4.3.1). Figure 4.4 a) shows the effects of altering the geometric parameters (l and h) of the simple box-shaped asperity used in the theoretical derivation. As asperity length is increased and asperity height is decreased σ_f increases; this can be thought of as the rubber surface becoming less rough and σ_f increasing with increasing smoothness of the surface. While this may be expected when not considering stress relieving effects (Arnold et al. 1987), Figure 4.4 b) shows that the friction increases with increases asperity length and height; this should be expected as the amount of deformation and therefore strain energy of deformation before the asperity

unpeels should increase with increasing asperity volume. This indicates that even with small scale roughness on the rubber surface, provided the normal force and the stiffness of the rubber are such that the asperities maintain independent contact points, the friction exhibited will be very different from that of a smooth surface. The peeling parameters are also seen to influence σ_f (Figure 4-5); with increasing A and α the frictional shear stress is decreased with α having a stronger influence than A over the range of values which are expected to cover experimental conditions.

4.3 Results & Discussion

The theory gives a solid hypothesis to test when keeping a consistent rubber sample. It can be seen whether the model predicts the frictional shear force correctly. The power law relationship between shear stress and the sliding velocity can be examined through experimentation by measuring the frictional force at varying rates.

4.3.1 Rubber Properties

Figure 4-6 shows results for a tensile test on a rubber sample. As can be seen the sample begins to slip from the clamps towards the end of the extension however, only the small strain behaviour is of interest, so this does not impact the modulus value of the rubber that is taken from this data. The modulus, as can be seen in Figure 4-6, is non-linear. The assumption of linear elasticity at low strains is typically taken to 10% strain. It is seen from Figure 4-7 that this is an acceptable assumption for this NR-0. The linear fit provides a value for the low strain modulus of 1.20MPa (2dp) which is at the low end of the range quoted by the CES EduPack 2017 materials selection software database.

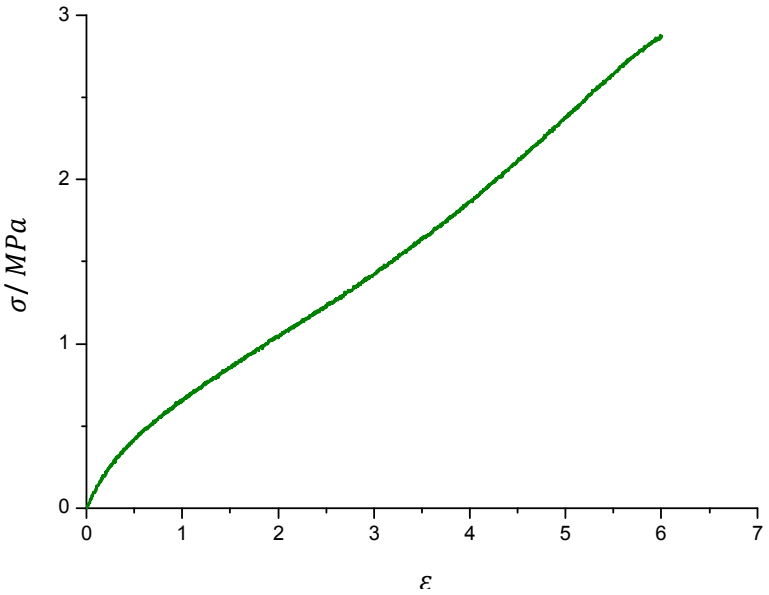

Figure 4-6: Tensile stress-strain curve for NR-0.

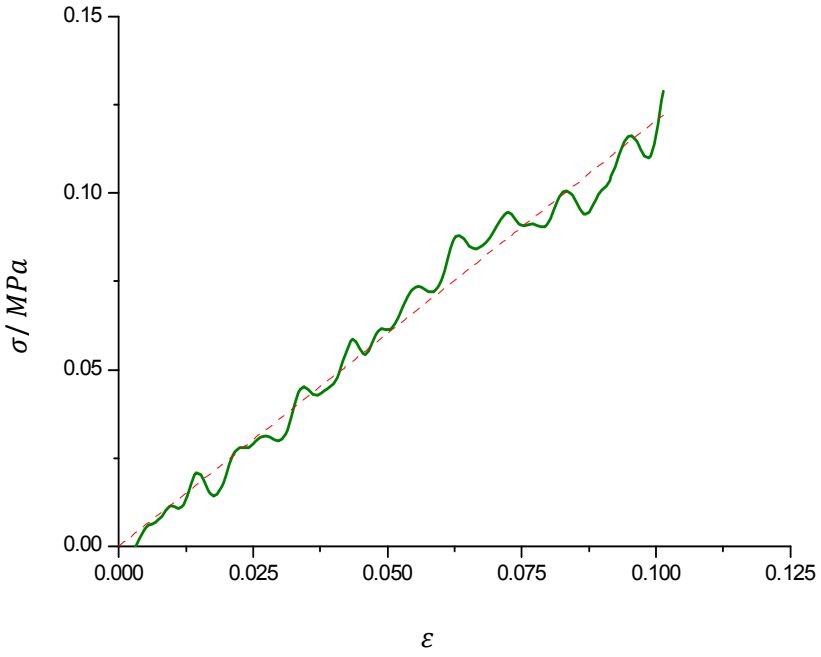

Figure 4-7: Low strain (up to 10%) stress- strain curve for NR-0 (green line). A linear fit is applied (red dashed line).

While it may be the case that the overall modulus of the rubber can be assumed to be approximately constant at low strains the viscoelastic properties of the rubber are subject to change and this affects the behaviour of the rubber. As such, the dynamic properties of the rubber, the storage modulus (G'), the loss modulus (G''),

and the ratio of the two ($\tan\delta$), are important in understanding the behaviour observed in experiment. Figure 4-8 and Figure 4-9 show the viscoelastic behaviour of two rubbers, NR-0 and ENR-0, over a range of temperatures, obtained from DMA. The graphs show the different glass transition temperatures (T_g) of the two rubbers, indicated by a dramatic change in the viscoelastic terms. The different T_g values indicate the different viscoelastic behaviours of the two rubbers.

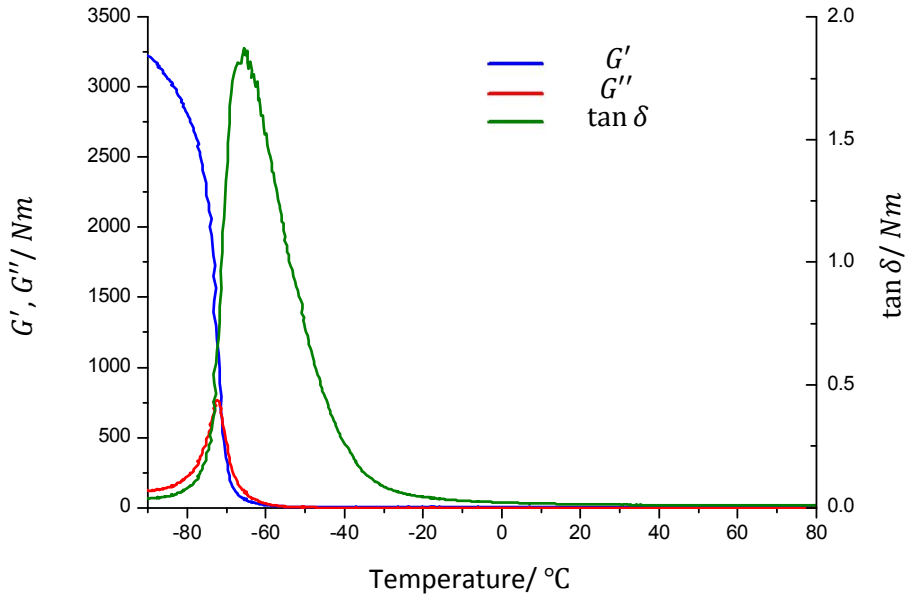

Figure 4-8: Dynamic properties of NR-0 found uing a DMA temperature sweep.

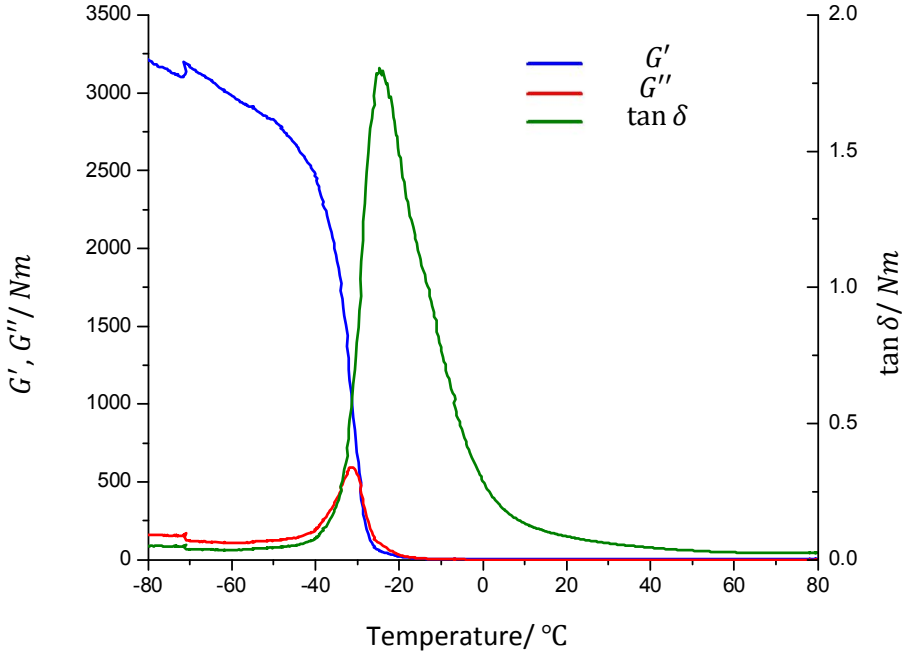

Figure 4-9: Dynamic properties of ENR-0 found uing a DMA temperature sweep.

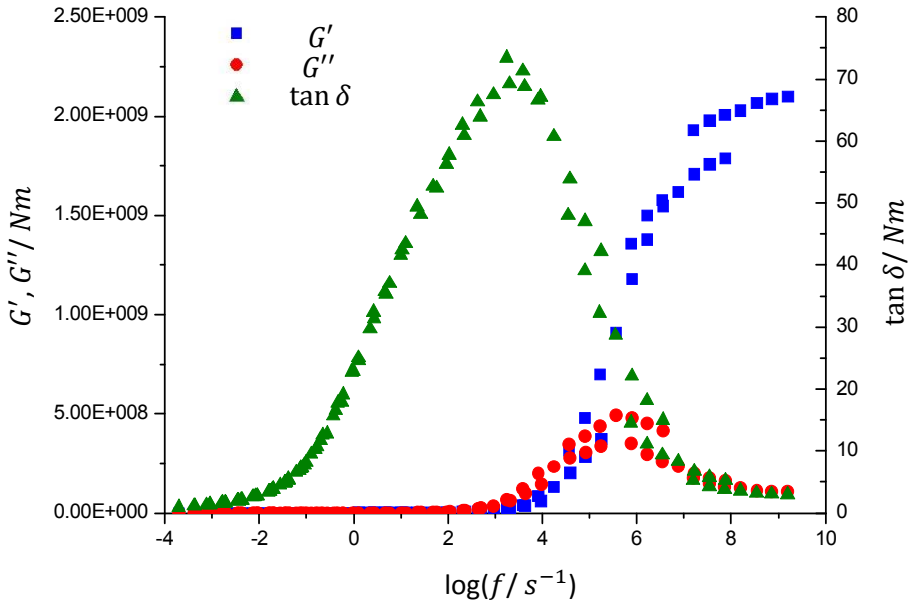

Figure 4-10: Mastercurve of viscoelastic properties for NR-0 using DMA data superpositioned by WLF transform.

The temperature sweeps give a value of T_g (taken at the coincident temperature of the inversion in behaviour of the dynamic moduli) of approximately -77°C and -30°C

for NR-0 and ENR-0 respectively, values which are appreciably similar to those found in literature (Whelan & Lee 1979; Thomas et al. 2014).

The DMA was also used to produce the relaxation spectra of a rubber sample. The dynamic moduli were needed over a large range of frequencies. The way this was achieved was to run a set frequency sweep at different temperatures then construct a master-curve, such as Figure 4-10, out of the data using the WLF transform (equation 2-16) with the reference temperature $T_r = Tg + 50^0$. The relaxation spectra ($H(\tau)$) could then be constructed using the formulation suggested by Ferry et al. (1953) (equation 2-11). $H(\tau)$ was found by an iterative process from an initial approximation to A_H using a MATLAB code to iteratively calculate values of the local slope. The relaxation spectrum for both NR-0 and ENR-0 are shown in Figure 4-11 and Figure 4-12 respectively.

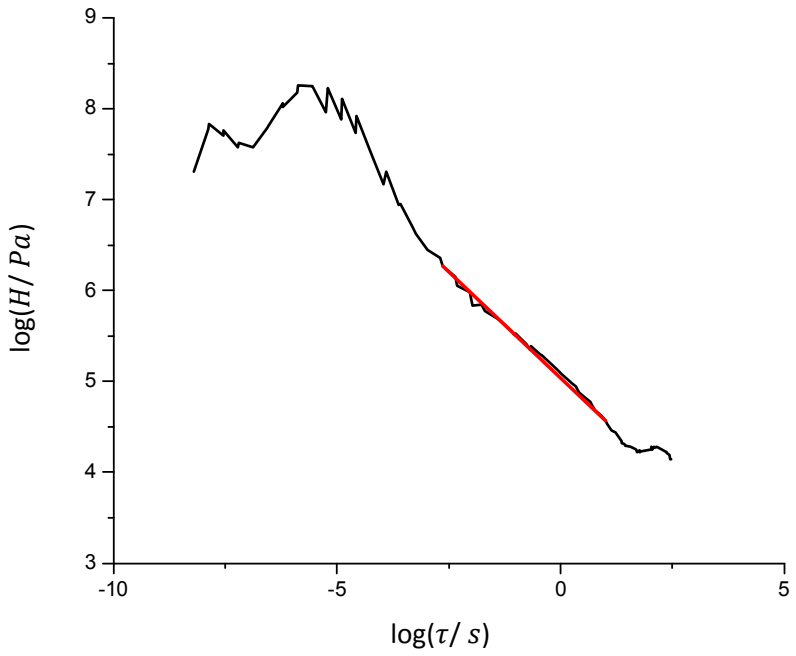

Figure 4-11: Relaxation spectra for NR-0 with a linear fit applied to part of the curve.

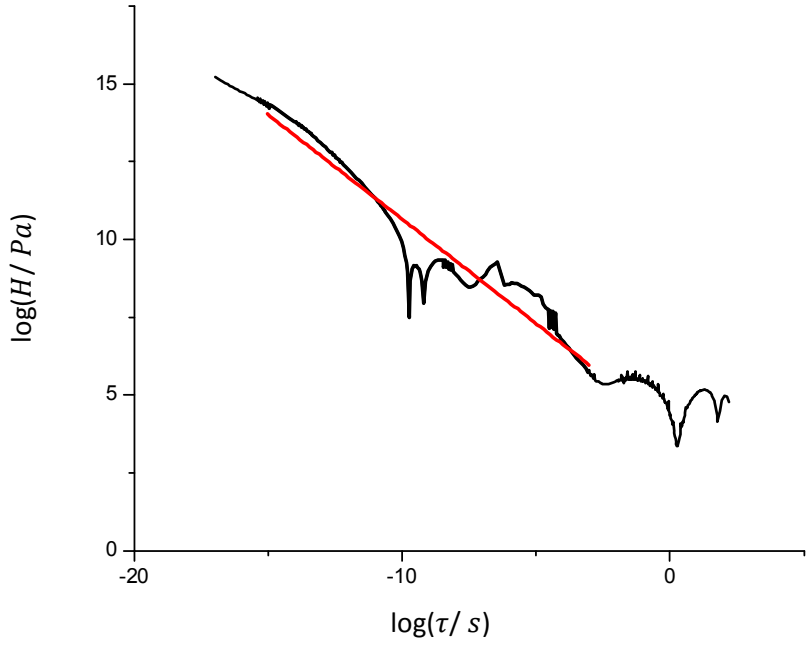

Figure 4-12: Relaxation spectra for ENR-0 with a linear fit applied to part of the curve.

For ENR-0, the relaxation curve produced is not as smooth as would be desired, the rubber was very sensitive to the DMA technique and so unfortunately an adequate curve was not obtained. This makes using the relaxation curve to evaluate ENR-0 impractical and so only the NR-0 relaxation spectrum was used in analysis.

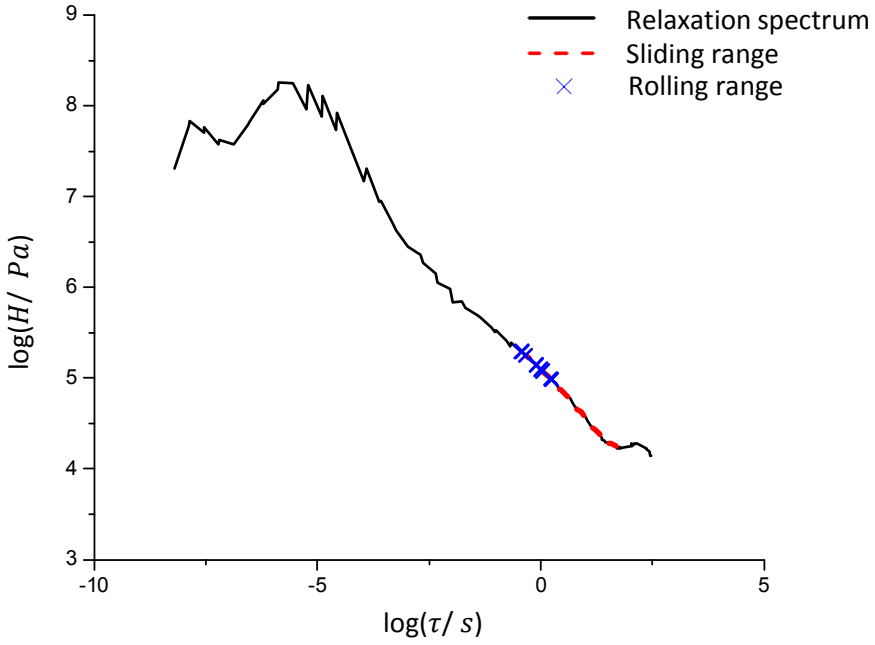

Figure 4-13: Relaxation spectra for NR-0 with approximate frequency ranges of rolling and sliding tests included.

The velocity range of friction tests and where they lie with respect to the range of the relaxation spectrum of NR-0 of the friction tests was examined in Figure 4-13. The velocity ranges (0.01-1mms^{-1} for sliding and 0.01-10mms^{-1} for rolling) were converted into approximate frequencies of the peeling taking place by using a characteristic length; for both rolling and sliding this was taken as the length of the contact patch. The graph shows that the velocity range of rolling tests overlapped with the sliding tests. Both occur along the relatively linear region of the relaxation spectrum.

The relaxation spectrum has been correlated to crack propagation rate in a theory by Perrson et al. (Persson & Brener 2005). A similar method is also used by Kluppel et al. (2000; 2009) on fracture mechanics as well as work conducted on the friction of rubber against self-affine surfaces.

The process of crack propagation and adhesion are dependent on the viscoelastic nature of the rubber and the relaxation spectrum enables the link between the two and shows the effect of the behaviour of the rubber molecules on the friction observed. The tearing energy (T_E) is given by the equation (Klüppel 2009):

$$T_E = \left(\frac{dc}{dt}\right)^{\beta}$$

$$\beta = \frac{(1+C)}{(2+C)} \qquad 4\text{-}11$$

Where C is the coefficient of the linear transition region of the relaxation spectrum. For the case of peel propagation, it is a simple comparison that leads to the definition of the peeling parameter α in terms of the co-efficient of the linear fit to the relaxation spectrum m. Comparison between this equation, specifically the power dependence of the peel energy to velocity, and that used in the derivation outlined in this paper gives:

$$\alpha = \beta^{-1}$$

$$\alpha = \frac{(2+k)}{(1+k)} \qquad 4\text{-}12$$

A linear fit is applied as seen in Figure 4-11. This lead to the calculation of α from this linear fit giving a value of 3.00(2dp), similar to the values obtained from rolling tests. This suggests that whilst peel rate and energy are affected by the substrate the rubber is paired with the dependence of one to the other is almost entirely dependent on the viscoelastic properties of the rubber.

4.3.2 Surface Properties

Of particular interest were the properties of the surfaces of the materials to be used in experimentation with clear influence on frictional properties. Two measures were used to categorise a surface, a measure of surface roughness and a measure of surface energy. The rubber samples were manufactured to retain a specific repeated pattern of surface roughness such as that shown in Figure 4-14. The counter-surfaces used in friction experiments were nominally flat however, it would be impossible to obtain a perfectly flat surface; surface roughness depends on manufacturing processes and so different materials can have significant differences in surface roughness. This could affect results. The surface roughness of counter-surfaces used over a significant distance is shown in Figure 4-15.

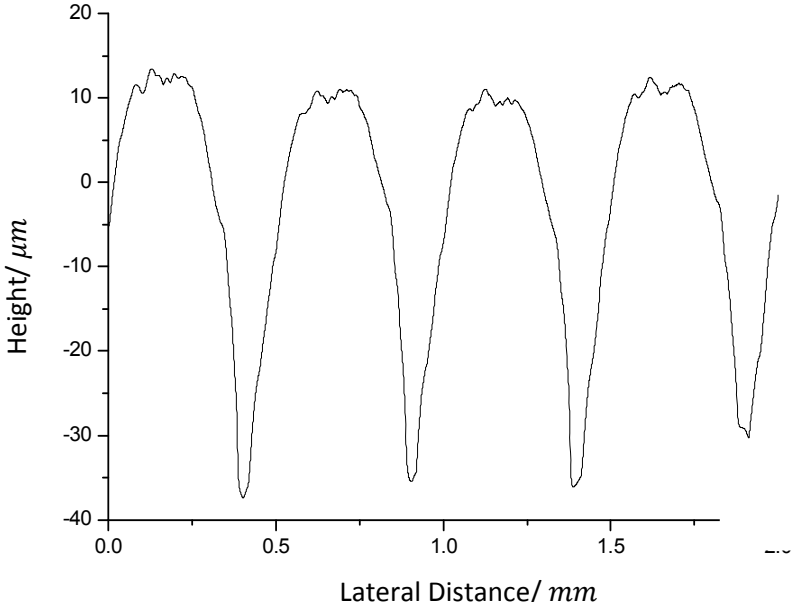

Figure 4-14: Top- 3D profile of cylinder asperity sample. Bottom- 2D profile of cylinder asperity sample.

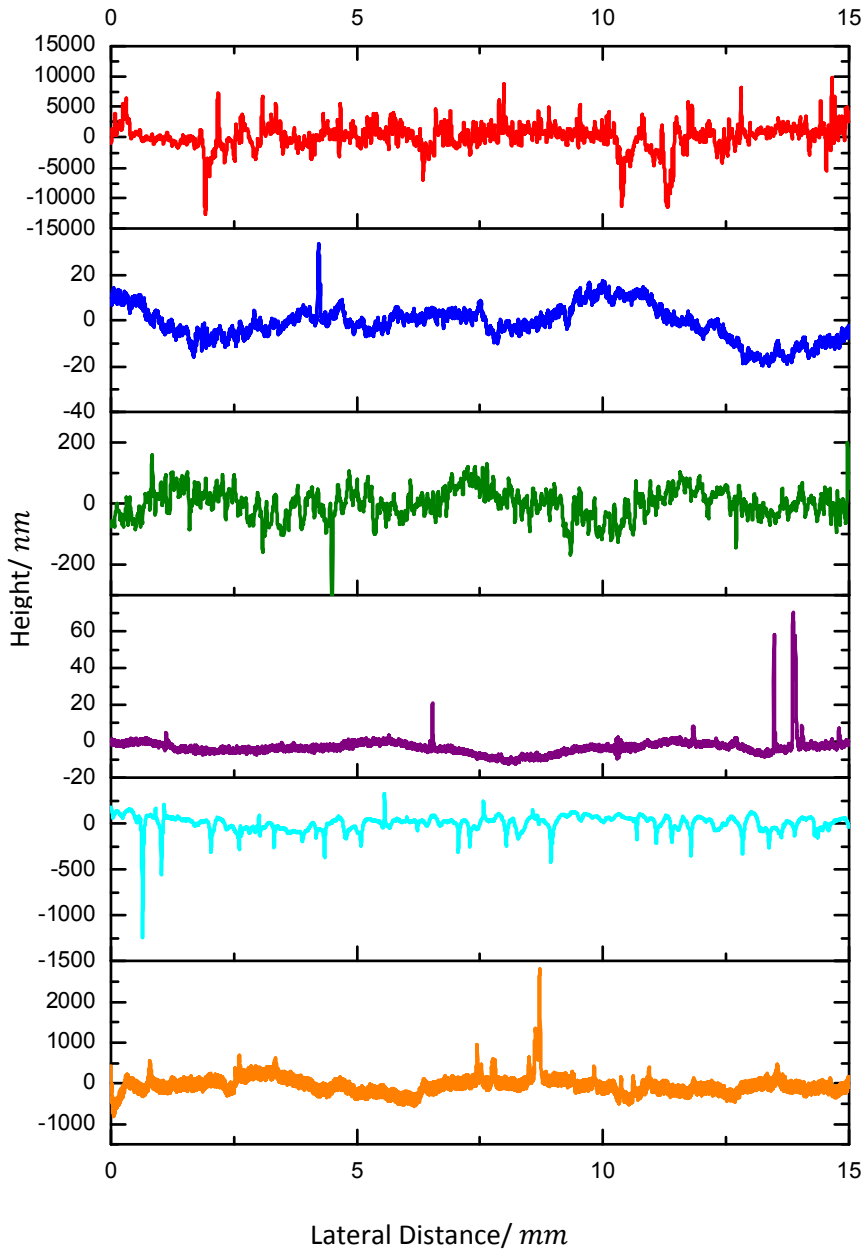

Figure 4-15: Surface scans of: red- PE, blue- PMMA, green- PP, purple- glass, light blue- steel, orange- flat-sheet moulded rubber.

Table 4-1: Surface roughness values (R_A) of various surfaces.

Surface	Average Roughness R_A nm (2dp)
Flat Sheet Rubber	206.00
Glass	5.88
PMMA	8.39
PE	1577.50
PP	48.38
Steel	6.91

Table 4-1 summarises the average roughness values for the counter-surfaces. Glass, steel, and PMMA all have a very low level of roughness which corroborates with their visually mirror-like finishes. The roughness of the PP used is an order of magnitude greater than these and the PE has a much higher roughness than all of the others. This means that the glass, steel, and PMMA surfaces will be most faithful to theoretical conditions whereas the roughness of the PE may cause differences to be seen in results involving this surface. The flat sheet rubber has a level of roughness greater than those of the mirror-like surfaces however, due to the low modulus of the rubber, this will not prevent good contact from being made in rolling experiments and should not be expected therefore to affect results significantly.

Surface energies were assessed using liquids of known surface tensions, summarised in Table 4-2. Four liquids were used so that an Owens-Wendt plot could be constructed for each solid (Owens & Wendt 1969). The liquids used were water and acetone and mixtures by volume of water and ethylene glycol (EG) of 50:50 and 25:75 respectively. 7μl droplets were used as this was the largest size that would enable deposition of more or less the entire droplet at once onto a surface. The droplet diameter tended to be in the range of 3-5mm and therefore should be far greater in magnitude than any surface defects, examined in section 3.5 (Drelich 2013).

Table 4-2: Values of the surface tensions of the liquids used in the contact angle measurements.

Test Liquid Water:EG	γ_L Nm^{-1} (1dp)	γ_{Ld} mNm^{-1} (1dp)	γ_{Lp} mNm^{-1} (1dp)
100:0	72.8	26.3	46.5
50:50	60.3	28.6	31.7
25:75	54.0	28.1	25.9
0:100	47.7	26.4	21.3

The Owens-Wendt plots were constructed using contact angles measured on the various solids with the four liquids and equation 2-64, from which the X and Y parameters were determined:

$$Y = \frac{\gamma_L(\cos\theta+1)}{2\gamma_{Ld}^{\frac{1}{2}}}$$

$$X = \left(\frac{\gamma_{Sp}\gamma_{Lp}}{\gamma_{Ld}}\right)^{\frac{1}{2}} \qquad 4\text{-}13$$

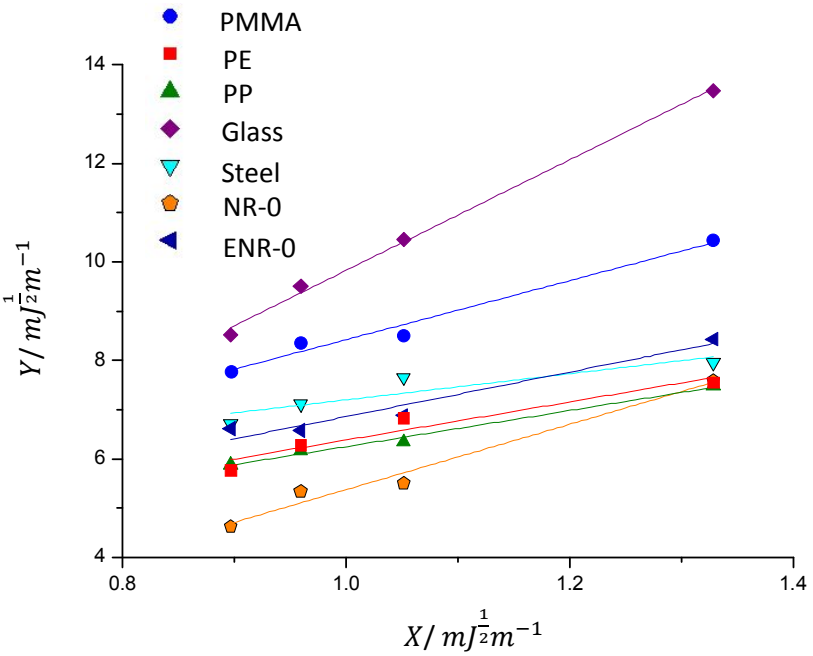

Figure 4-16: Owens-Wendt plot for different materials used in experiments using average 1st droplet contact angles.

Table 4-3: Best fit values from Figure 4-16 and surface tensions derived therefrom.

	Surface	m (2dp)	c (2dp)	γ_{Sp} mJm^{-2} (2dp)	γ_{Sd} mJm^{-2} (2dp)	γ_S mJm^{-2} (2dp)
1st Angle	PE	4.52	2.34	20.46	5.45	25.91
	PP	3.66	2.59	13.40	6.70	20.10
	PMMA	6.00	2.42	36.00	5.90	41.80
	NR-0	6.64	1.26	44.00	1.60	45.60
	Glass	11.24	-1.41	126.30	2.00	128.3
	Steel	6.05	1.29	36.58	1.67	38.25
	ENR-0	3.87	2.51	14.98	6.31	21.29

There is not a clearly defined procedure to follow when using contact angle measurements to determine γ_S; contact angle hysteresis is widely acknowledged and thus it is advised to measure advancing and receding angles however, it is not clear what value of contact angle would be most appropriate to use in γ_S calculations. Here, three different contact angles have been used. The surface areas used will be those given by the 1st droplet angle average, shown in Figure 4-16, as that measurement gave the best fit for the majority of surfaces; although it is noted that for steel the fit is not as good as other surfaces with any contact angle used; in this instance, the contact angle with water droplets was omitted in calculating the surface energy as a strong linear fit could be applied to the rest of the points.

Surface energies are summarised in Table 4-3 and Figure 4-17. It can be seen that the surface energy of the glass surface is much higher than that of other surfaces. This value is lower than values given in literature however these values are taken at high temperatures (Shartsis & Smock 1947). a similar value is seen when standard atmospheric conditions are employed, this is explained as the effect of the presence of some water absorption on the surface of the glass (Rhee 1977). Similarly, the value obtained for steel is seen to be within a range of values found by the same method. It is seen that, just as with glass, surface contaminants affect the surface energy value found and as such cleaning procedure has an effect on the surface energy. As the cleaning procedure used is the same as that for friction

experiments it is assumed that the values obtained are a good representation of the surface energy during the friction tests. The surface energy value for the PMMA measured is very similar to that found in literature (Lee 1999). The values for PP and PE are slightly lower than given values in literature (Pocius 2007). This may again be due to surface absorption or it could be due to the relatively high surface roughness of these two surfaces.

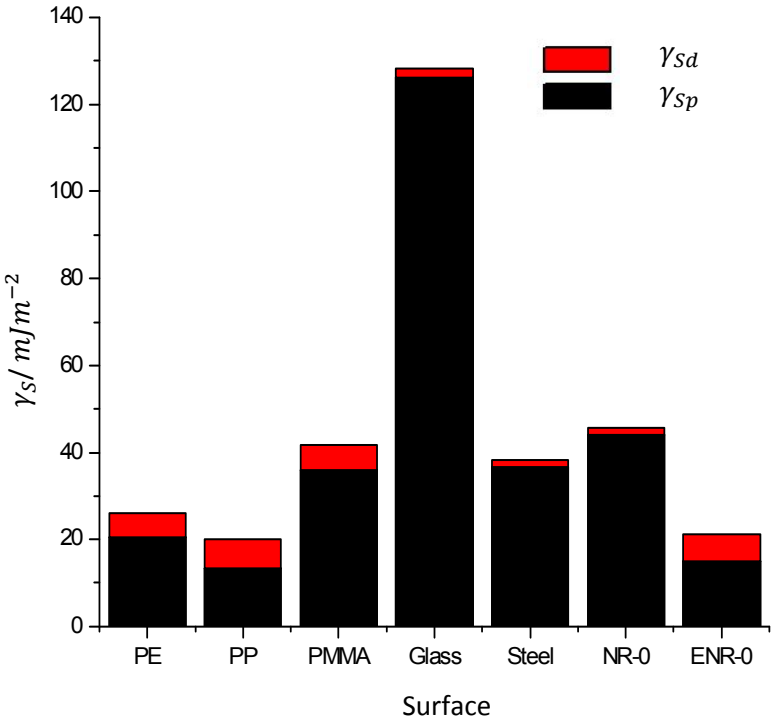

Figure 4-17: Components of γ_S.

The effect of the cleaning process on the surface of the rubber was examined using FTIR. Figure 4-18 shows the results from scanning the surface of a rubber sample before and at various times after it was cleaned with acetone. Major peaks are identified relating to carbon oxygen bonds and a specific alkane bond straight after application of the acetone. These peaks can be attributed to the presence of acetone on the rubber surface. It was seen that any acetone on the surface of the sample was negligible in little time. By 4 minutes these peaks have reduced considerably; it is clear that the acetone is volatile and little remains on the surface beyond this time. The acetone cleaning has the effect of reducing all other peaks which mostly correspond to carbon hydrogen bonds; this could be due in part to

removal of some anti-oxidant from the surface but the peaks recover relatively quickly indicating that it is more likely that the acetone on the surface is reducing some absorbance from the rubber. From this investigation it was determined that a ten minute dwell time was sufficient to allow sample surfaces to dry following cleaning with acetone.

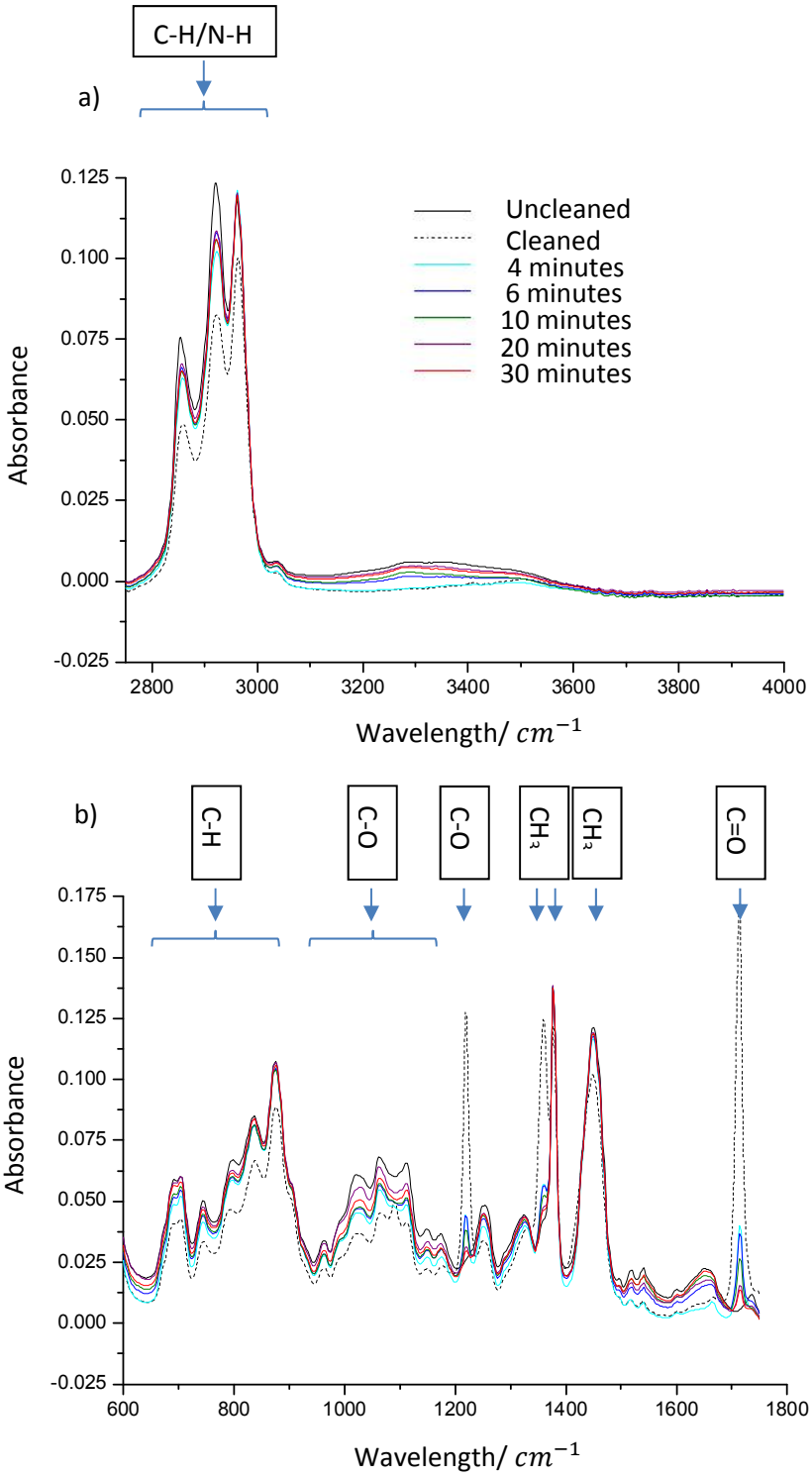

Figure 4-18: FTIR scan of ENR-0 at various times after being cleaned by acetone, a) 2750-4000cm^{-1}, b) 600- 1800 cm^{-1}.

It was considered that perhaps the cyclic stressing of rubber surfaces during testing could promote mechano-oxidative ageing of the samples. This was examined using FTIR. Figure 4-19 shows the results of scans to examine the ageing of samples during testing. The samples examined were used in rolling tests and compared to

samples that had not been used but had been cleaned with acetone at the same time as those rolled. Figure 4-19 shows the unrolled sample scans, with scans both of the side facing air and the side facing down not in contact with air. It is clear that the effect of oxidative ageing was to enlarge the almost non-existent peak at 3300cm^{-1}. This peak corresponds to carbon-oxygen bonds. Minimal change was seen in other peaks. It can be seen that the used sample has a lower peak than the unused sample. This result indicates that rather than accelerating ageing the testing slows ageing of the rubber. It was found that ageing of unused samples could become significant beyond around 3 weeks so samples were not used beyond this point unless appropriately stored.

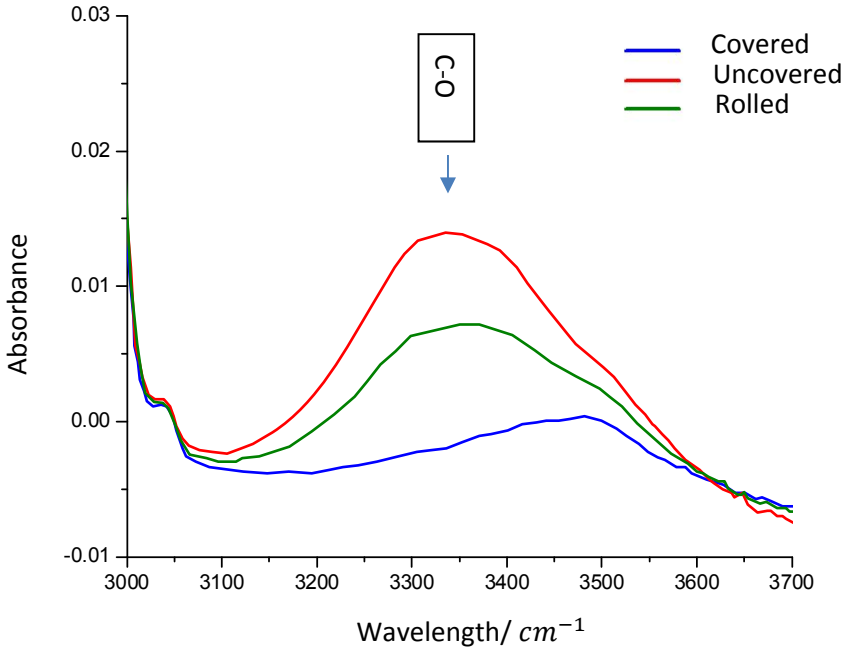

Figure 4-19: FTIR scan of an ENR-0 rolled sample compared to unrolled surfaces.

4.3.3 Rolling Experiment Results

The peeling parameters are predicted by the developed theory to play an important role in determining the level of shear stress that develops during sliding. The peeling behaviour of the various combinations of surfaces that were selected for the study were examined using rolling tests (described in section 3.7).

On the face of it this testing method is a simple and straight forward method to obtain some important material characteristics. The tests were, however, seen to be strongly affected by environmental conditions, as may be expected. Ideally testing would be conducted under strictly controlled conditions however, the testing environment was susceptible to fluctuations in temperature and humidity. Testing was conducted under conditions of $21.5 \leq T \leq 22.5$. Another environmental factor is dust. Tests were conducted in closed laboratory space and the surfaces were cleaned with acetone prior to each test to try and minimise dust effects. The large amount of variation in the results shows that fluctuations in test conditions were not entirely avoided. Moreover, it was observed that rolling velocity decreased with number of tests conducted (some results for this are shown in Figure 4-20). Cleaning the surfaces between tests mostly removed this effect but not entirely. Starting tests again the next day the rolling times would be high, then decrease exponentially. This was not very evident with most surfaces except for the steel surface which showed a remarkable level of this effect. Times were taken from the third test onwards; from when the times typically reached a reasonable level of consistency. This is a result not reported in literature studies of rolling so it is unclear as to the exact nature of the phenomenon. Clearly the rubber has a rest state of surface properties which change from the rolling interaction. This could be analogous to the static friction peak observed from sliding tests in that it takes a certain displacement before the friction levels drop to a consistent level as the sliding behaviour stabilises to a constant state across the surface.

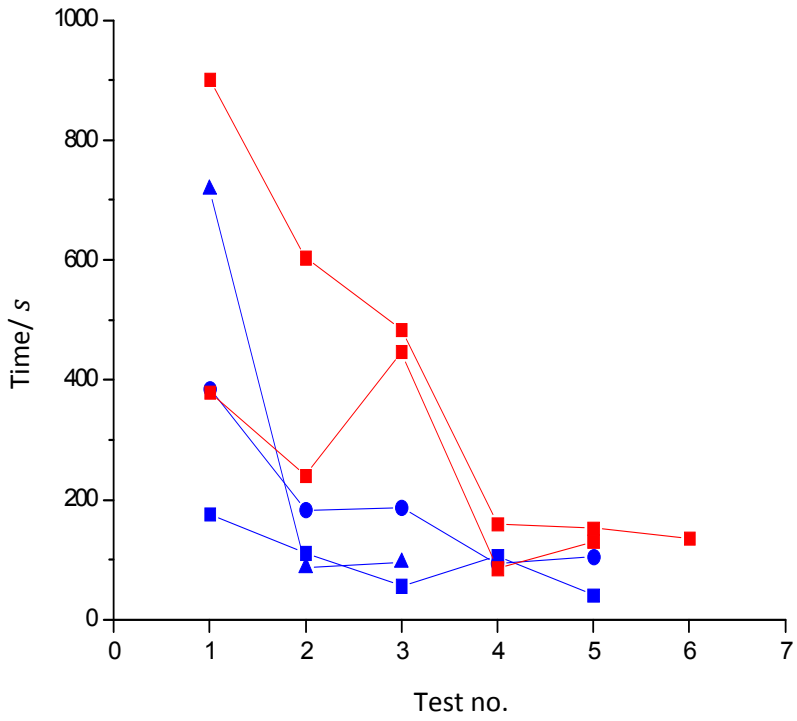

Figure 4-20: Rolling times against number of tests conducted since testing started on a day. Different colours represent two different inclination angles and different shapes represent individual sequence of tests.

The graphs below show the results for various sliding tests conducted. The peeling energy is calculated using equation 2-91. Figure 4-21 shows results using NR-0 flat sheet samples and Figure 4-22 shows results for ENR-0 against the smoothest two counter-surfaces, glass and steel.

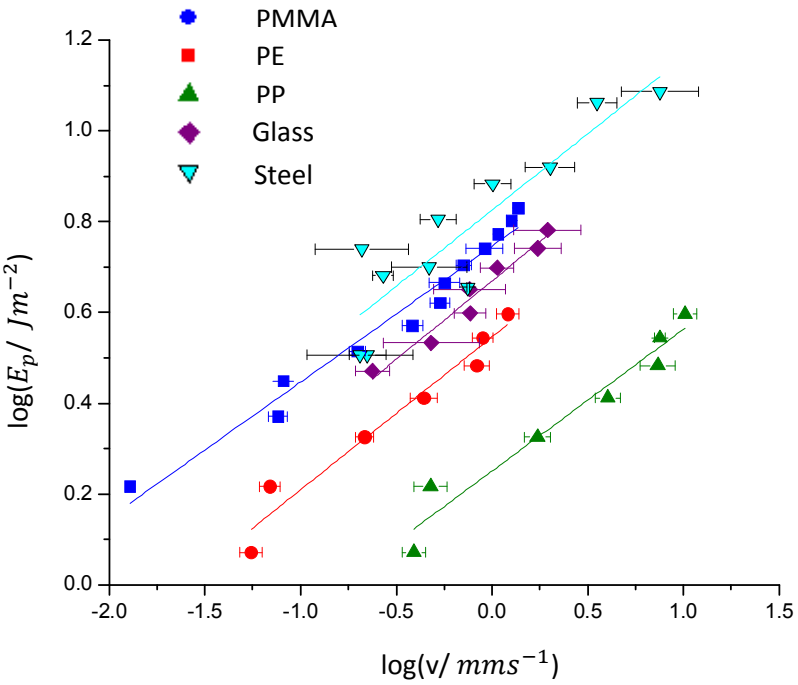

Figure 4-21: Log graph showing rolling results for NR-0 against various surfaces.

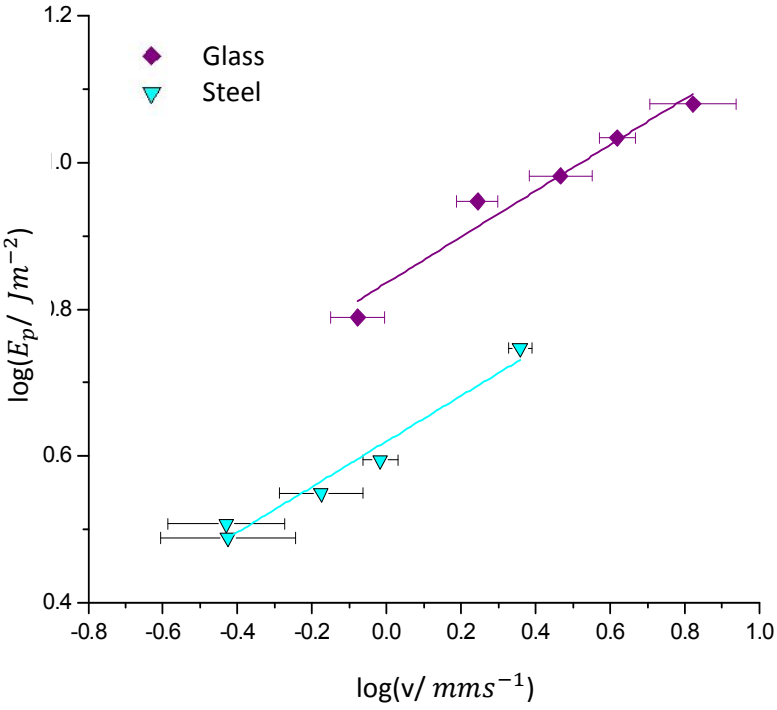

Figure 4-22: Log graph showing rolling results for ENR-0 against glass and steel.

The results reveal a logarithmic dependence of the peeling energy on the rolling velocity; this shows that a power law relationship exists between the two.

Table 4-4: Summary of fits to NR-0 curves in figures 4-21 and 4-22, and peeling parameters derived from them.

	Surface	m (2dp)	c (2dp)	α (2dp)	$\frac{A}{m^{(1+2\alpha)}(sN\alpha)^{-1}}$ (2dp)
NR-0	PMMA	0.30	1.64	3.34	$3.22E^{-6}$
	PE	0.34	1.56	2.97	$2.38E^{-5}$
	PP	0.31	1.19	3.21	$1.57E^{-4}$
	Glass	0.35	1.76	2.89	$8.04E^{-6}$
	Steel	0.34	1.83	2.98	$3.47E^{-6}$
ENR-0	Glass	0.36	1.78	3.18	$2.18E^{-6}$
	Steel	0.31	1.55	3.22	$1.00E^{-5}$

Best fit lines of the form $y = Cx + y_0$ are applied to the data. The lines of best fit are summarised in Table 4-4. The first thing that may be noted in looking at the best fit equations is the similarity between the co-efficients, especially for the ENR-0 tests. The magnitude of E_p between tests using different rubbers varies, with a higher value for the ENR-0 tests however, the two set of tests show different surfaces as having the greater E_p out of glass and steel. This suggests that, while the modulus of the curves may be in good agreement, the scaling of E_p values between surfaces is not well defined.

As has been discussed in section 2.4, the peeling of the rear of the rolling has been successfully compared to fracture mechanics, where the rolling velocity is the crack propagation velocity and the energy of rupture is the peeling energy, thus, an equation analogous to equation 2-21 can be implemented. Here the constants C and y_0 will be called A and α and be deemed peeling parameters:

$$v = AE_p^{\alpha} \qquad 4\text{-}14$$

The peeling parameters A and α can be seen to be found from the line of best fits from the negative of the exponential of the intercept over the gradient and the inverse of the gradient respectively. The peeling parameter values are summarised in Table 4-4. Following the fact that a similar trend is seen with all surfaces a similar

α values are obtained. This suggests that the value of α is strongly dependent on the properties of the rubber, irrespective of the rigid coupled surface. With the comparable behaviour to the fracture mechanics of rubber it is not unexpected that the peeling energy should be dependent on the viscoelastic properties of the rubber. The A term, which offsets the curve of each surface, ought to be dependent on the coupled surface energies of the two materials however, it is seen not to be solely dependent on this in Figure 4-23.

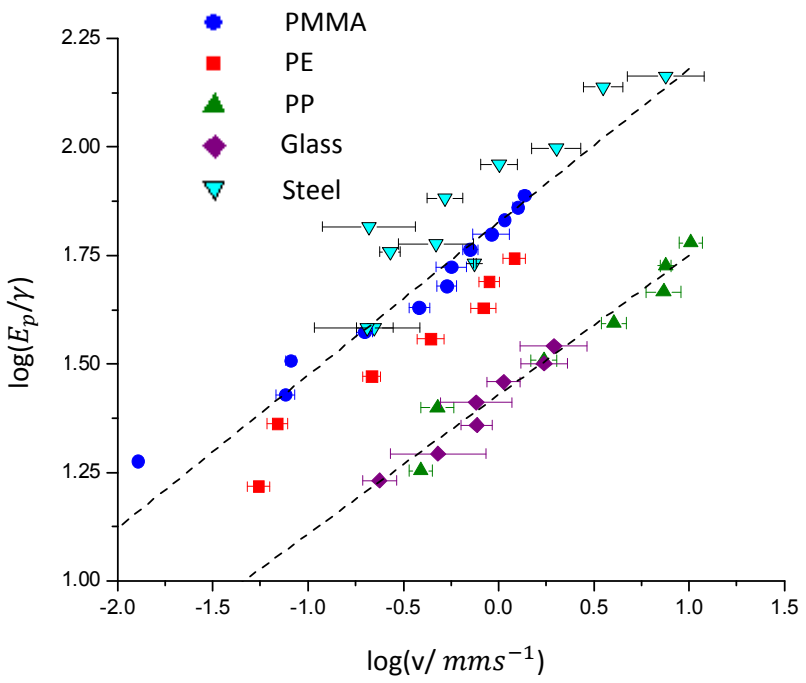

Figure 4-23: Rolling data normalised by the Dupre energy of adhesion, γ, for NR-0 against various surfaces.

The data is normalised by the Dupre energy (γ) (Figure 4-23). The normalised data shows that the magnitude of the peeling energies observed do not simply rank with magnitude of γ_S. The materials can be split broadly into two distinct groups by the normalised data. Figure 4-18 shows the components of γ_S; there is no clear differentiation of the surfaces along the lines shown in Figure 4-23. The high γ_S of the glass gives it a low normalised stress alongside that of PP which has a low frictional shear stress to begin with. The two surfaces represent the two extremes in terms of surface energy.

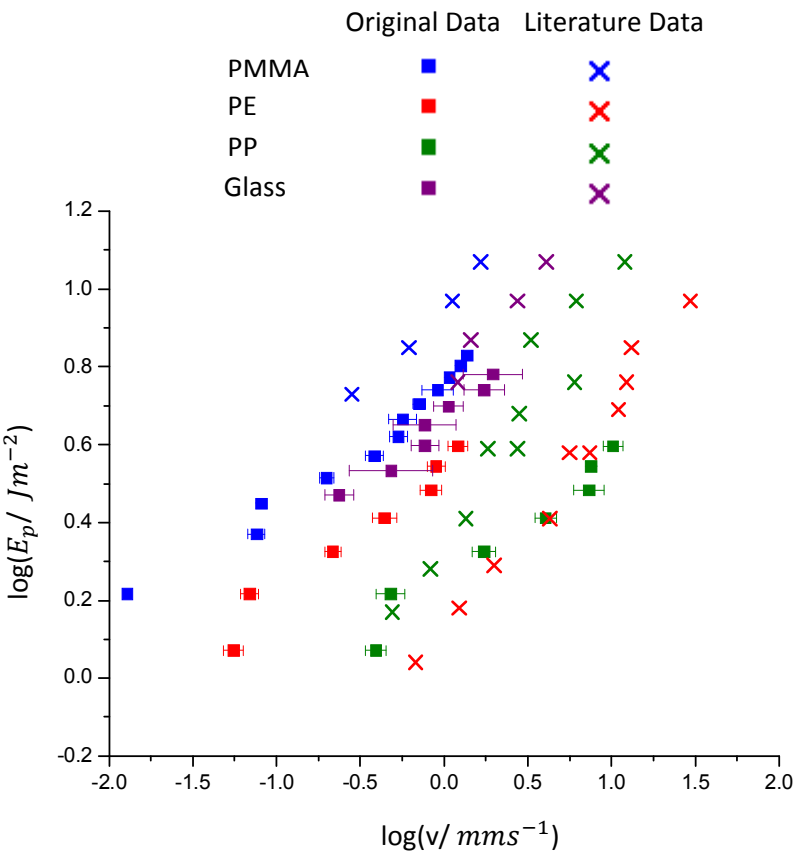

Figure 4-24: Comparison of rolling results to results from Arnold et al. (1987).

In Figure 4-24 experimental results are compared to results from Arnold et al. (1987) which used an unfilled NR-0 (it is unclear which of two samples of moduli of 1.72 and 1.64MPa were used) against some of the same material surfaces examined in this work. Detail of the roughness or surface energies of these surfaces is not given. The values are in the same range as the results obtained although the relatively greater peel energies are found to be greater on the PP surface than PE. This difference is likely due to surface properties; with the roughness of the PP surface used to obtain results in this thesis much larger than that of the PE surface it will have affected adhesion. The two materials used both here and in Arnold et al. (1987) may differ in manufacturing method as well and several different grades of PE and glass and PP exist. As has been discussed, surface treatment also strongly affects surface energy therefore surface energies are likely not the same between the two experiments. The rubber used by Arnold et al. (1987) has a different modulus which likely also affects the results curves. The gradient of the curves is expected to be affected by the viscoelastic properties of the rubber and not by opposing surfaces and it is found from the curves of the data of Arnold et al. (1987)

that a similar value of gradient of about 2.2 is found for all curves, similar to the value obtained from their sliding data. A paper by Fuller and Roberts (1981) gives data for rolling tests on PMMA for two rubbers with different amounts of peroxide. The data is within a similar range as in Figure 4-24 but shows a clear difference in gradient between the two curves.

4.3.4 Contact Measurements

Contact parameters for asperities against a surface were calculated using contact mechanics to give the asperity dimensions for use in the box asperity approximation and to give a value for the actual contact area between the sample and counter-surface. For cylindrical asperities equation 2-69 for the adhesive contact of cylinders, giving the normal load per axial length ($\frac{F_N}{L}$) in terms of the contact half-width (a), was solved iteratively using a MATLAB code for a specific F_N. Hertzian contact is used to approximate the height of the asperities. Similarly, for hemispherical asperities, contact is found using equation 2-68 for adhesive JKR contact and the indentation found from equation 2-66, Hertzian contact at the same normal load to give a value of asperity height. Images of contact of NR-0 asperities on glass were taken with a digital microscope, examples shown in Figure 4-25 and Figure 4-26. contact parameters were then measured using ImageJ software; these measurements are compared with calculated contact dimensions in Figure 4-27 and Figure 4-28 for the two different asperity geometries.

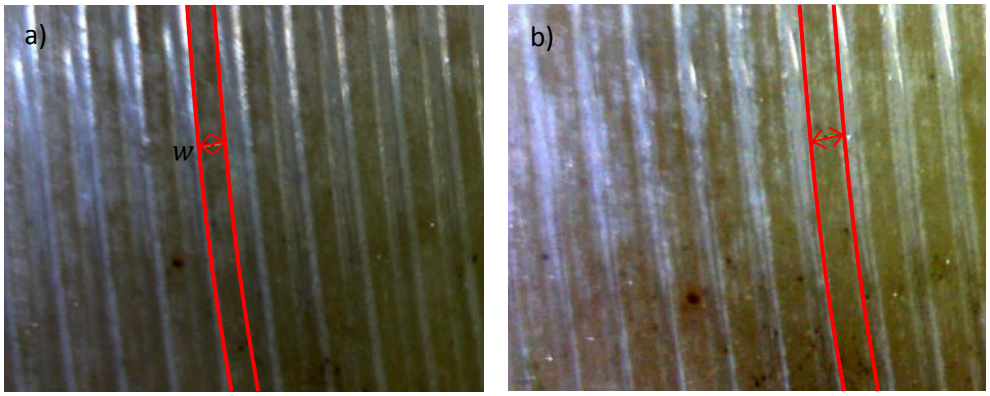

Figure 4-25: Images of ENR-0 cylindrical asperities contacting with glass at; a) 1.41kg and b) 3.41kg.

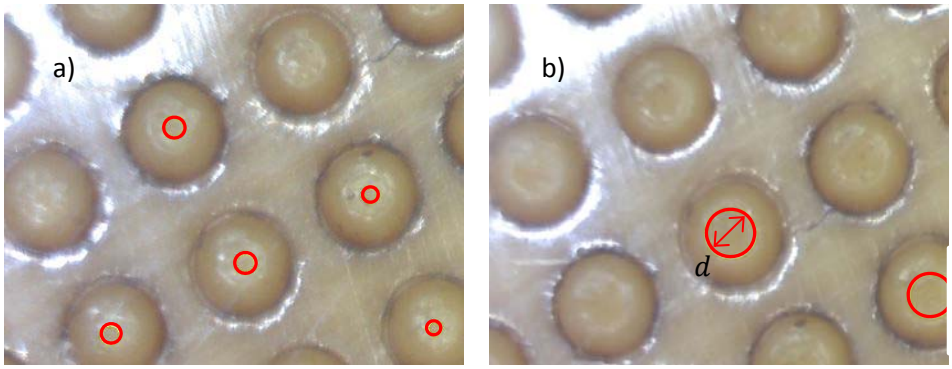

Figure 4-26: Images of ENR-0 hemispherical asperities contacting with glass at; a) 0.43kg and b) 3.41kg

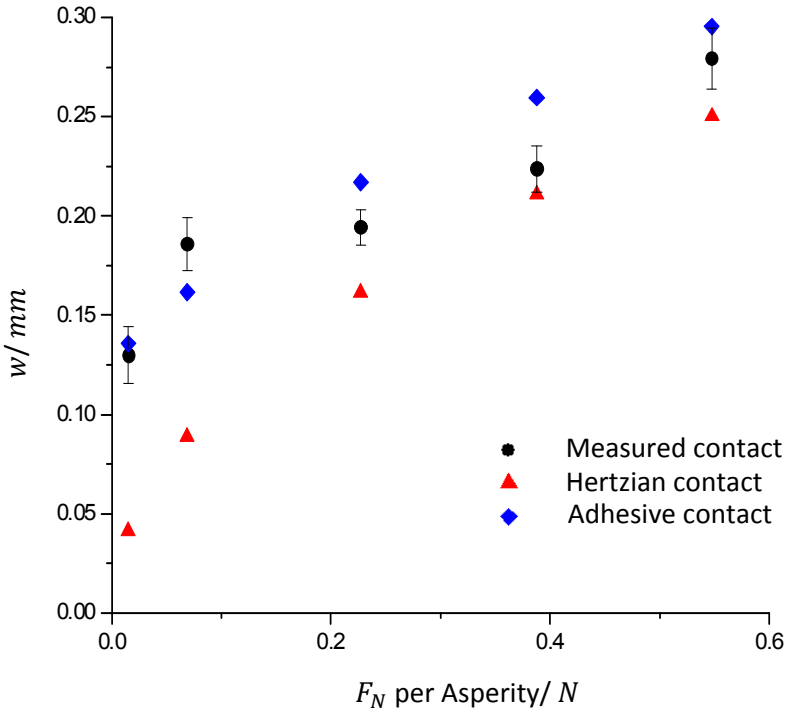

Figure 4-27: Measured contact width compared to calculated contact for NR-0 cylindrical asperities on glass.

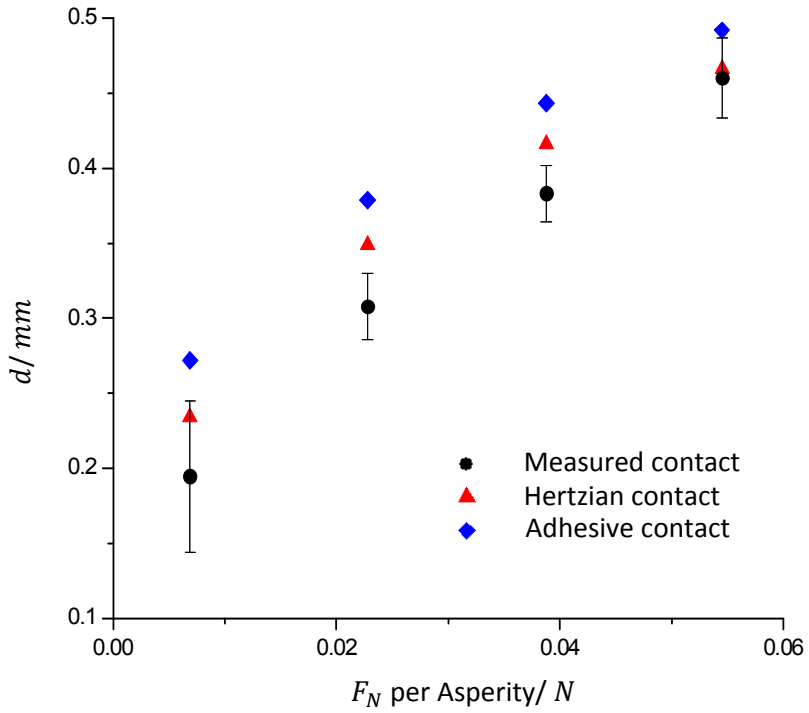

Figure 4-28: Comparison of measured contact with calculated contact for ENR-0 hemispherical asperities on glass.

The calculations seem to compare well to the measured values in both cases, despite the large error involved in measuring the contact. There seems to be less difference between adhesive and non-adhesive hemispherical contact than cylinder contact. Although measurements suggest a contact length lower than Hertzian for the hemispherical asperities this is likely due to human error in measurement and JKR contact was assumed regardless.

4.3.5 Sliding Experiment Results

Experiments were conducted to determine the validity of the theory established in section 4.2, describing the friction behaviour of a rough rubber sliding against a smooth surface.

4.3.5.1 Cylindrical Asperities

The sliding friction of NR-0 samples with a surface comprising of cylindrical asperities was measured against smooth rigid counter-surfaces of PMMA, PE, PP, glass and steel. Figure 4-29 gives sliding results for NR-0 with cylindrical asperities (details of which are described in section 3.1.3). Results are shown in terms of frictional shear stress using the calculated actual area of contact.

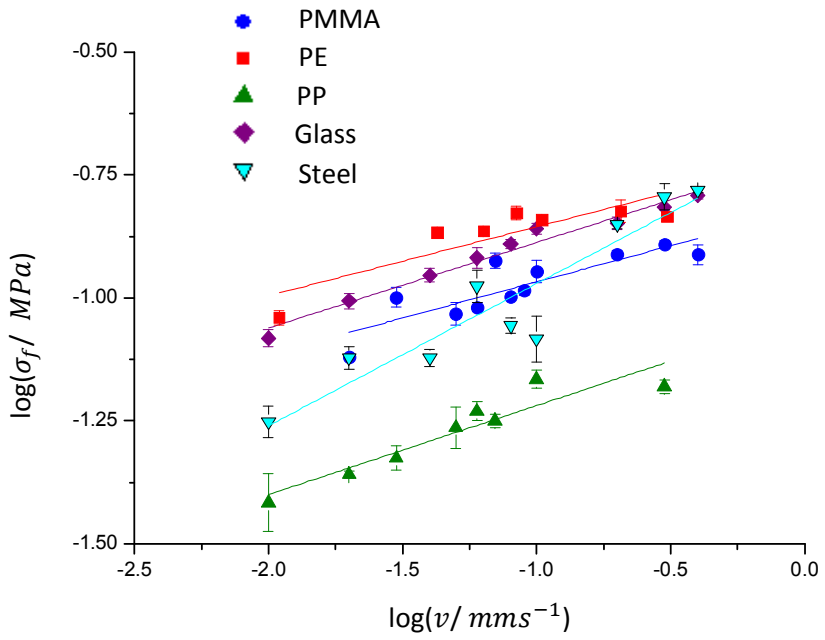

Figure 4-29: Sliding shear stress for cylindrical asperities for NR-0 against various smooth rigid surfaces.

The results of the cylindrical asperity sliding tests indicate that a power law relationship between the sliding velocity and frictional shear stress is present and that, similar to rolling results, the curves display similar gradients for each surface in the log graph, with the exception of steel. The data is corrected for the presence of a small amount of hysteresis contribution by subtracting the force measured over the surfaces having applied lubricant in the form of soapy water. The magnitude of the force measured, seen in Figure 4-30, is relatively small for all surfaces and ranks roughly with the surface roughness of the surfaces (see section 3.5). The frictional force increases slightly with velocity for PP and for all other surfaces does not change significantly therefore an average over the velocities measured was taken as the correcting factor. Figure 4-31 shows the cylindrical asperity sliding data with σ_f normalised by γ multiplied by a characteristic length, here taken as the contact length of an asperity at rest. The graph shows a far less clear distinction into two sets of surfaces, however they show a similar positioning relative to one another.

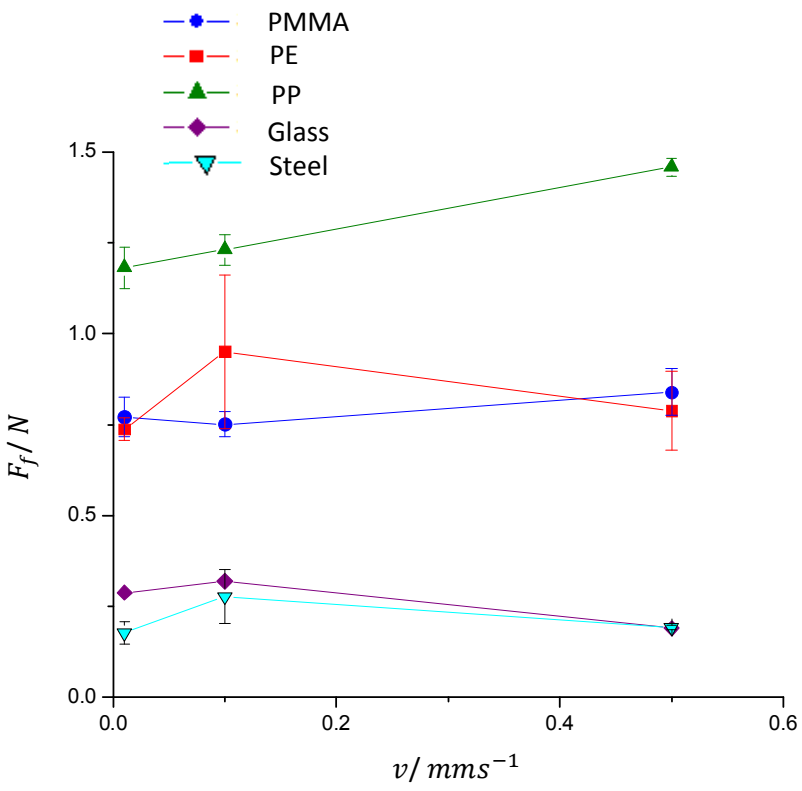

Figure 4-30: Friction of cylindrical asperity NR-0 on Lubricated surfaces.

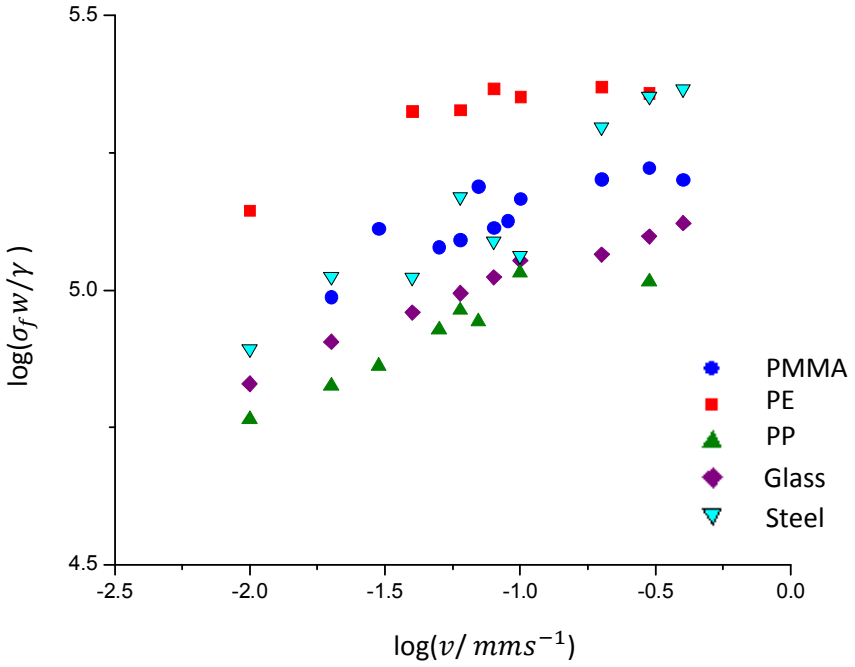

Figure 4-31: Cylinder asperity sliding without hysteretic friction contribution and normalised for NR-0 against smooth rigid surfaces.

4.3.5.2 Hemispherical Asperities

Results shown in Figure 4-32 are for 40mm^2 samples with surfaces patterned with hemispherical asperities 0.5mm in diameter under normal loads 0f 400-500g. It can be seen that, as with the cylindrical asperity results, a similar trend exists between sliding velocity and shear stress for all surfaces; the linear nature of the curves in the log graph once again indicate a power law relationship.

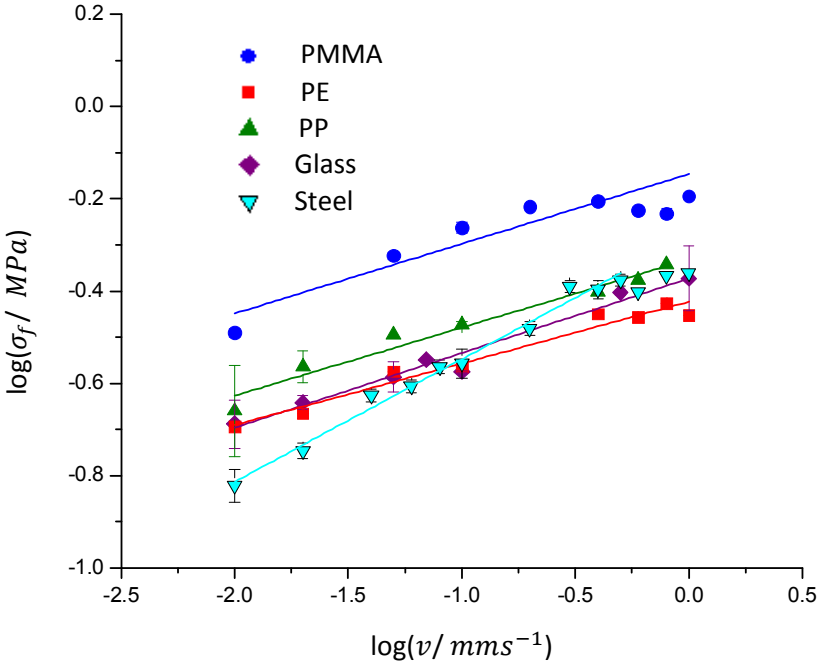

Figure 4-32: Sliding shear stress for hemispherical asperities for NR-0 against smooth rigid surfaces.

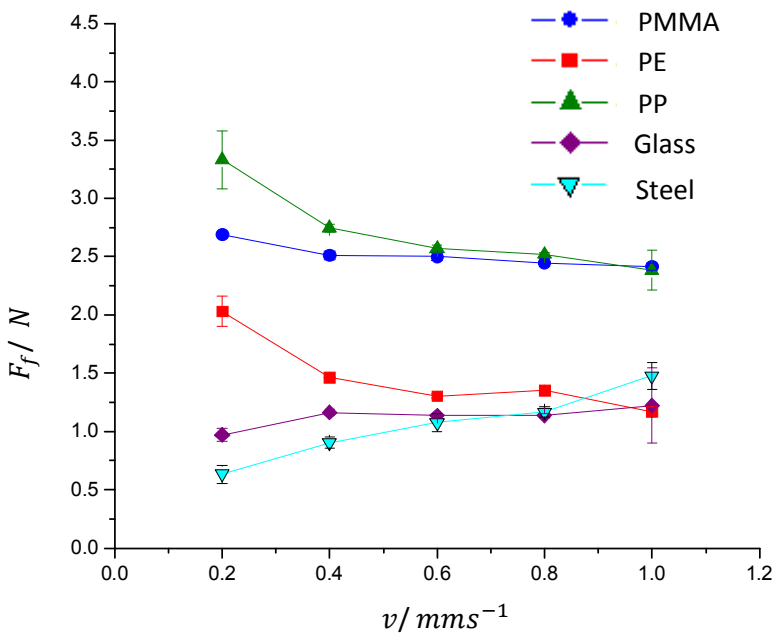

Figure 4-33: F_f of NR-0 on lubricated surfaces.

The lubricated friction is taken, as with other friction measurements, as an average over a distance, and is shown in Figure 4-33. In these tests, stick slip was seen in most, with large fluctuations in the forces measured. This occurrence is due to the relatively large normal load used with respect to the cylindrical asperities. The presence of stick-slip sliding may lend increased error to the result. None-the-less, the friction force on lubricated surfaces for the hemispherical asperities shows a similar ranking of materials as with cylindrical asperities; the two lowest being glass and steel, then PMMA and PE, although the two are closer in magnitude with cylindrical asperities, with PP registering the largest frictional force. All the surfaces show a vaguely independent trend with velocity, as with the cylindrical asperities, with the exception of steel which shows a steady increase with velocity. Unfortunately, stick-slip behaviour is observed which could alter the actual hysteresis contribution to the total force registered during sliding tests. The results suggest that the roughness of the PMMA surface in both instances is greater than that measured with profilometry. The hysteresis contribution was taken as the average of the forces over the velocity range. Figure 4-34 shows the sliding data for the hemispherical asperity samples having subtracted the lubricated friction contribution and normalised it using asperity contact length at rest (L) and γ.

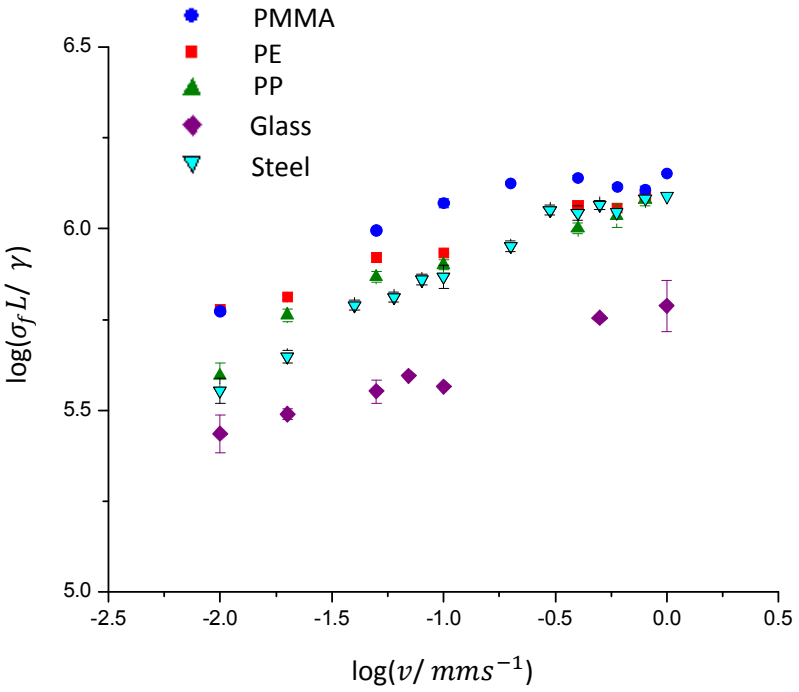

Figure 4-34: Sliding results for hemispherical asperities minus hysteretic friction contribution and normalised for NR-0.

The normalising of the data separates the glass friction from the rest of the surfaces which is similar to rolling friction, except that PP is grouped with the other surfaces here. The data gives a similar fit line co-efficient for all the surfaces which, with the exception of steel, is similar to the cylindrical asperity results.

Tests on glass and steel were repeated with ENR-0 hemispherical asperities. Raw sliding results are shown in Figure 4-35, lubricated friction results in Figure 4-36. And the normalised results having subtracted the lubricated friction levels are shown in Figure 4-37.

The lubricated sliding results show some variation with speed, with a particularly dramatic difference between the data gathered at 0.1mms^{-1} and 0.4 mms^{-1}. The difference could be due to a resonance in the frequency of deformation and the frequency of the roughness on the steel surface however, considering the large difference in the time taken for the measurements to be made at the two different velocities it is likely that the difference is caused by the effect this may have on the conditions of the lubricated testing; drying (to some degree) of the lubricant may affect the surface interaction properties. Irrespective of this, the magnitude of the friction measured at all velocities remains small relative to unlubricated

measurements thus, as before, it was considered adequate to take an average value over the velocity range tested.

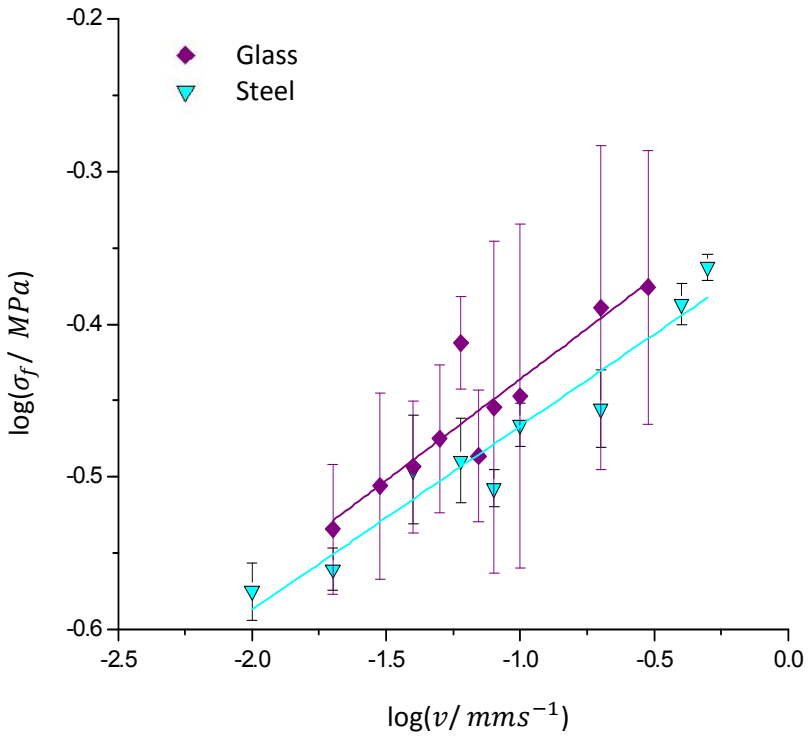

Figure 4-35: Sliding friction of ENR-0 against glass and steel surfaces.

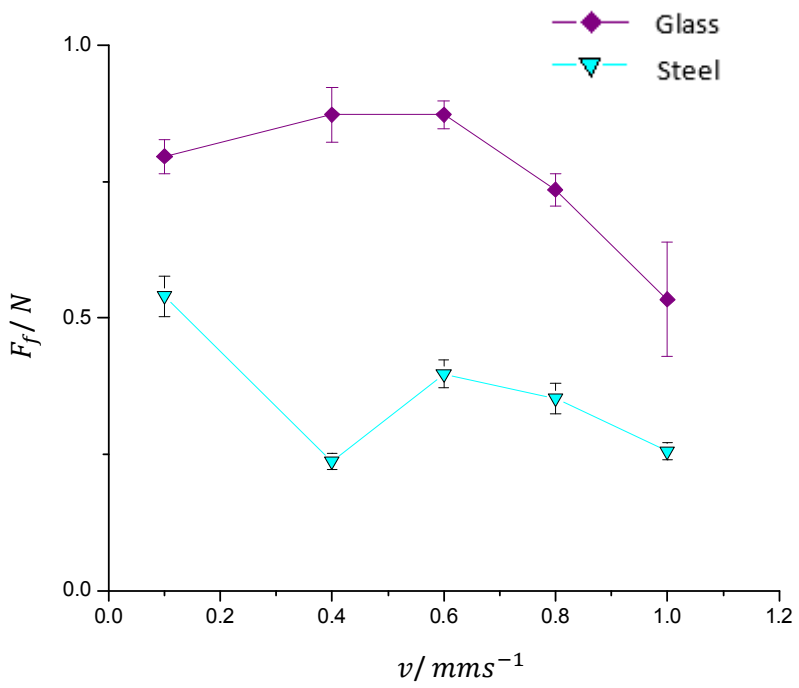

Figure 4-36: Lubricated sliding friction of ENR-0 against glass and steel surfaces.

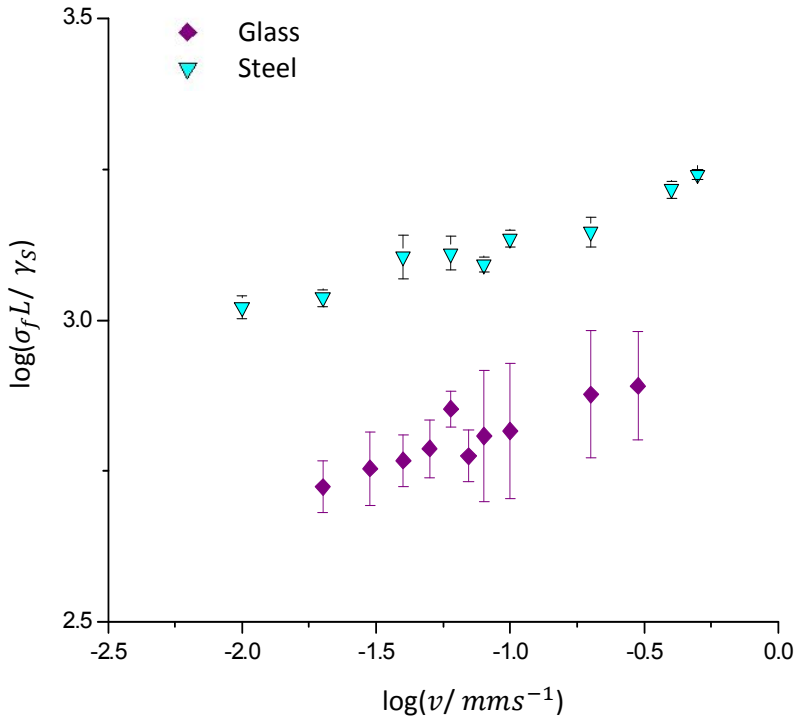

Figure 4-37: Sliding data minus average lubricated F_f and normalised by contact length and surface energy for ENR-0.

When considering the application of the box asperity model to sliding results, it can be seen that, from equation 4-10, the gradients of the curves of the log graph would correspond to the term $\frac{1}{(2\alpha+1)}$ so that α can be found from the results:

$$\alpha = \frac{\left(\frac{1}{m}-1\right)}{2} \qquad 4\text{-}15$$

In Table 4-5, the values of α obtained from the two different sliding tests, with cylindrical and hemispherical asperities, are compared to rolling results. It can be seen that there is relatively good agreement between the two for all surface combinations with NR-0, with the plastics giving an α value of around 3 and glass and steel surfaces around 2.5 and 1.3 respectively. The corresponding values received from sliding results using the ENR-0 rubber compare well to one another. Comparing the α values obtained from sliding results to those obtained from rolling results there seems to be good agreement for all surfaces with both rubbers and asperities except for those of the steel surface with NR-0. It is also important to note that the theoretical analysis follows from a plane strain basis; this means that,

rather than rows of asperities the theory assumes a continuous asperity across the sample surface. This can be mitigated by applying to calculated σ_f a factor equal to the ratio contact to sample width which is equal to the asperity spacing perpendicular to sliding (S_a) over asperity contact length ($\frac{L}{S_a}$).

Table 4-5: Summary of fit parameters and α values from friction curves.

Test	Rubber	Surface	m (2dp)	c (2dp)	α (2dp)
Cylinder Asperities	NR-0	PMMA	0.15	-1.41	2.90
		PP	0.14	-1.72	3.01
		PE	0.14	-1.34	3.14
		Glass	0.17	-1.25	2.42
		Steel	0.29	-1.29	1.20
Hemispherical Asperities	NR-0	PMMA	0.14	0.18	3.02
		PP	0.15	0.33	2.89
		PE	0.14	0.41	3.02
		Glass	0.16	0.37	2.59
		Steel	0.27	0.28	1.38
	ENR-0	Glass	0.13	-0.26	3.27
		Steel	0.14	-0.35	3.19
Rolling	NR-0	PMMA	0.30	1.64	3.34
		PE	0.34	1.56	2.97
		PP	0.31	1.19	3.21
		Glass	0.35	1.76	2.89
		Steel	0.34	1.83	2.98
	ENR-0	Glass	0.31	1.78	3.18
		Steel	0.31	1.55	3.22

The similarity between the rolling and sliding tests suggests that a peeling mechanism is therefore very likely to be occurring during the sliding experiments, one which follows the velocity dependence outlined by the box asperity model, with the exception perhaps of steel with NR-0. It is possible, considering the relaxation spectrum of the rubber, that the frequency of the peeling event with rubber against steel is significantly different to that of other surfaces, shifting the range into an area of different viscoelastic response. There is difference in α values seen between NR-0 and ENR-0. This should be expected when considering their respective T_g and therefore relaxation spectra which show that the two would operate in slightly different viscoelastic regimes. Whilst predicting the velocity dependence well for a majority of surface combinations the box asperity has mixed success in predicting the frictional shear stress itself.

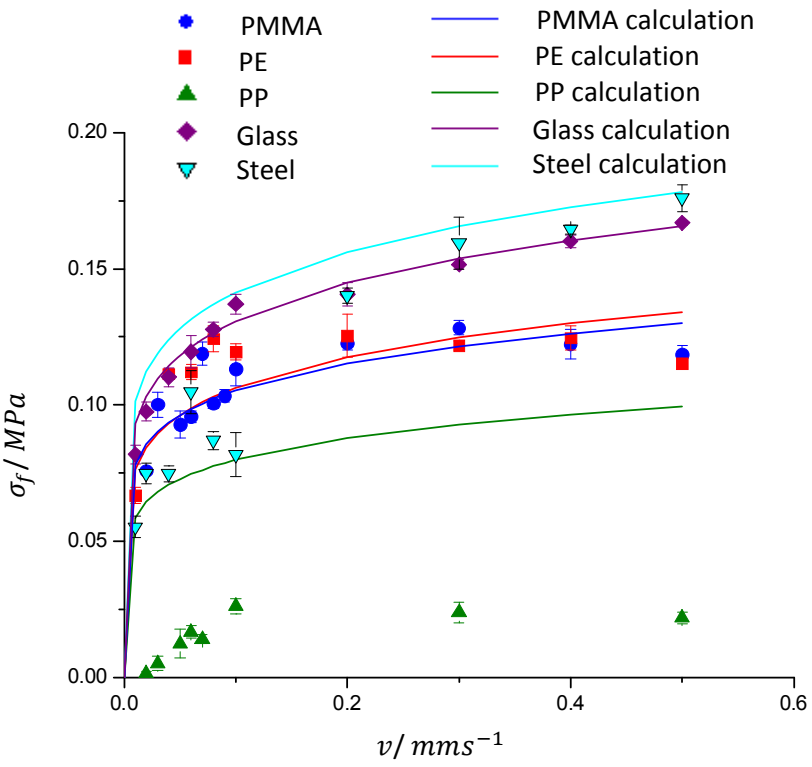

Figure 4-38: Cylindrical asperity experimental results minus lubricated average friction.

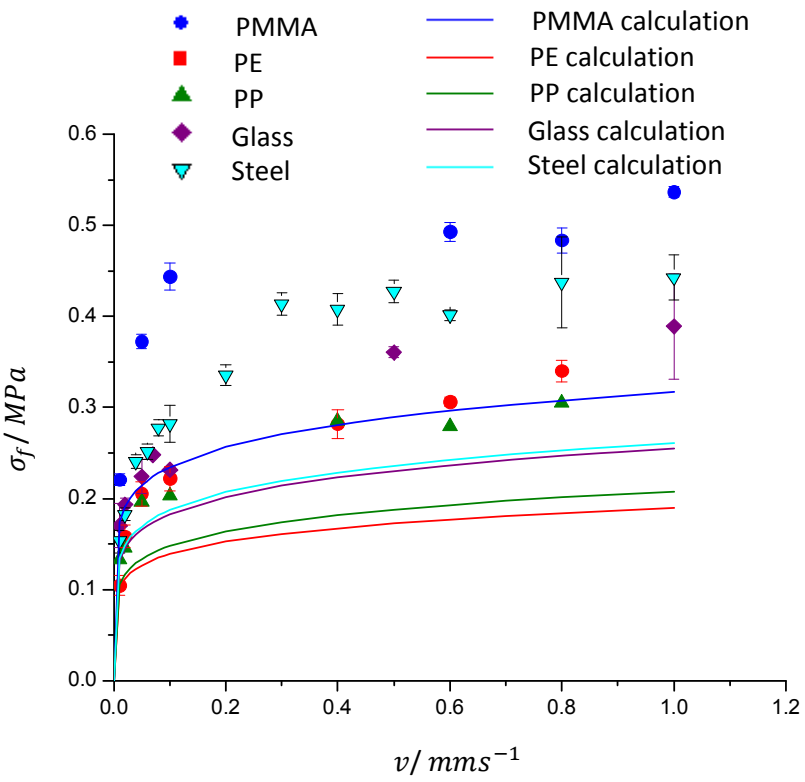

Figure 4-39: hemispherical asperity experimental results for NR-0 compared to box asperity model prediction.

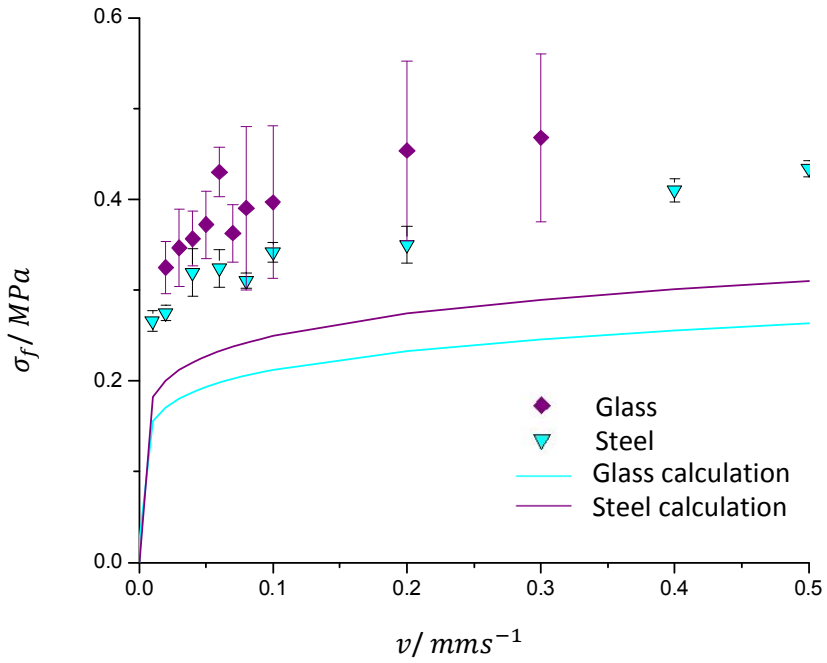

Figure 4-40: ENR-0 hemispherical asperity friction compared to box asperity model prediction.

Figure 4-38 shows that the prediction of the box asperity model gives a very good fit to the cylindrical asperity data for NR-0 against glass and a good fit to PMMA data, a good fit to steel data at high velocities, and moderately good for PE whilst over predicting σ_f for PP results. The reason for the discrepancy between α values for steel between rolling and sliding appears to be due to the low velocity behaviour of the steel. It is possible that the peeling behaviour's frequency operates on a slightly different range for steel; this would likely be seen most clearly at lower velocities judging by the relaxation spectrum of the rubber (Figure 4-13), as the velocity range of the sliding tests touches on the plateau at high τ. At higher velocities, the peeling event frequency enters the linear region of the relaxation spectrum and the behaviour approaches that expected. The sliding friction results against steel of ENR show good agreement to rolling tests in terms of α; this suggests that for the viscoelastic behaviour of ENR the peeling event frequencies for both tests remain in the ENR region of linear relaxation behaviour. The fit of the model to the data is worst for the surfaces with the highest roughness, with PP having both the highest measured average surface roughness and the worst corroboration between model and data; this suggests an effect on the accuracy of the predictions from the roughness of the surfaces. Surface roughness may lower the amount of adhesion or conversely increase it at low roughness levels (Fuller &

Tabor 1975). Counter-surface roughness could even cause a significant change in the dominant friction mechanics, with hysteretic and capstan effects becoming more predominant (Grosch 1963; Busfield et al. 2010). The influence of these effects is likely the cause of the inaccuracy of the predicted σ_f for PP and to a lesser extent PE in comparison to the smoother surfaces of glass, steel, and PMMA. Surface roughness will likely affect rolling and sliding differently; as with the change in mechanics governing adhesion contribution, counter-surface asperities interact differently in both (Scaraggi & Persson 2015; Fuller & Roberts 1981). Roughness does not seem to affect the viscoelastic dependence of sliding tests significantly however, as similar α values are seen for all three plastics with each other and with rolling results despite having quite varied levels of roughness. For hemispherical asperities, Figure 4-39 and Figure 4-40, calculations are about half that of experimental data, although σ_f magnitudes for surfaces relative to each other are well reflected in the calculated σ_f curves with the exception of PE for which σ_f is surprisingly low. This is also seen in the comparison of calculated values to results obtained for ENR-0. The difference between experimental and expected results suggests some unforeseen factor affecting the adhesion force that is not taken into account. There are some differences between the cylindrical asperity and hemispherical asperity tests, the geometry clearly being one of them. The geometric approximation of the box asperity model of the asperity shape to that of a rectangular shape is a source of loss of accuracy; the analysis relies on the evaluation of the strain energy of deformation during the peeling process which is dependent on the shape of the asperity. The box asperity approximation will be increasingly inaccurate for a curved asperity profile as the contact size decreases. this approximation may affect the two differently as F_N per asperity was higher with the cylindrical asperities than hemispherical asperities. Further, in the derivation of the σ_f equation the width (w) of the geometry is assumed constant with peel length (c) which is a good approximation to the cylindrical asperity geometry but not to the circular contact of the hemispherical asperity geometry. To improve accuracy this aspect of the model was subjected to a finite element analysis to improve the accuracy of the strain energy term of the analysis by more closely approximating asperity geometry, this is discussed in section 4.5. As was mentioned, another difference was F_N per asperity between tests on the two asperity geometries; the overall sample F_N however was greater with the

hemispherical asperity tests as the number of asperities was a factor of 10 greater than for the cylindrical asperity samples. Possible factors that could be affecting adhesion levels include the potential effect of surface flaws, which may affect rolling and sliding in different ways, and environmental factors temperature, humidity, and dust particles. Temperature during testing was kept between 21.5-23℃ however overnight temperatures, when $0.01mms^{-1}$ tests were typically run, could reach up to 25℃. Humidity was maintained at about 40% although again this could rise to about 60% overnight. There is little available data to compare obtained results to. The data obtained does however, compare well to data from Arnold et al. (1987) with a power law relationship between sliding velocity and frictional shear stress also observed there. The similarity in α values obtained from both rolling and sliding tests is also a feature of both data sets.

4.3.6 Conclusion

The frictional behaviour of sliding of rough rubber surfaces over smooth counter-surfaces was examined. Results obtained over five different surfaces with two different asperity geometries and with two different types of rubber strongly suggest the occurrence of a peeling behaviour with a characteristic velocity dependence as described by the derived box asperity model theory based on fracture mechanics. This is evidenced by the matching α values for both rolling and sliding tests found for all surface combinations excepting NR-0 on steel. the value of α is seen to be largely independent of the counter-surface and has been linked convincingly to the form of the relaxation spectrum for NR-0. This suggests that the peeling parameter α and thus the velocity dependence is predominantly dependent on the viscoelastic properties of the rubber, which should be expected. The box asperity model describes σ_f well when smooth surfaces are used with a cylindrical asperity geometry; surface roughness has the effect of decreasing adhesion and this ensures a good fit is not found for PMMA and particularly PP surfaces. When hemispherical asperity geometry is examined the level of σ_f of surfaces relative to one another is well predicted however it is seen that predicted σ_f underestimates the experimental data. The following section examines the effect of the approximated asperity geometry in the theoretical analysis.

4.4 Simulation and Modelling of Rubber Asperities

Results of sliding friction tests have so far been compared to the geometrically simple box asperity model in the previous section. Possible sources of error have been discussed; among them is the geometric approximation the box asperity model makes. In order to examine in detail the effect of the geometry on σ_f the strain energy evolution with crack propagation, which will be dependent on the geometry of the surrounding feature, needs to be examined. To study this geometric effect, ABAQUS models were created to simulate specific model geometries. A model for the cylindrical asperity type was created and will be henceforth referred to as the ABAQUS cylindrical asperity model. A model was also created for the hemispherical asperity type; this is referred to as the ABAQUS hemispherical model asperity.

4.4.1 Asperity Peel Modelling

The shapes of the specific asperity geometries used are different from that of the step profile assumed in the theory. This means that the elastic deformation energy (E_{el}) from the shearing of the asperity using the simple geometric profile that was used to derive the theory is only an approximation of the real deformation behaviour. It is necessary therefore to examine the limitations of this approximation especially in relation to the fracture mechanics of the peeling of the asperity by modelling the real behaviour using a more realistic approximation of the real geometries used in this investigation. Limitations might arise as the simple linear relationship of the tearing energy to the length of crack might not necessarily be applicable to these more complex asperity geometries. Thus, the change in elastic energy of deformation as a function of crack (peel) length was also examined.

The actual energy of deformation or strain energy is investigated for the asperity geometries studied using finite element analysis. The simulations were conducted in ABAQUS software. This method requires the change in the strain energy against deformation to be evaluated for different crack lengths. Then an expression for the dependence of the strain energy lost due to peeling (E_t) on the peeled length (c) can be found. Using this approach it is possible to explore the effect of a change in the compressed height (h) or the contact area (A_c) on the strain energy release

rate. From this an equation was constructing that related the energy available for peeling at a given peeled length under specific conditions.

4.4.2 Cylindrical Asperity Modelling

The shape of these asperities, an approximately constant cross-section extended across the whole surface perpendicular to sliding direction, is such that the geometry can be approximated as plane strain with a 2D profile. Thus, the simulation is conducted in 2D simple strain as a simplification. It is very useful to make such simplifications to reduce the simulation run time. The model is simplified further through taking the substrate as analytically rigid. The resulting model is then seen in Figure 4-41.

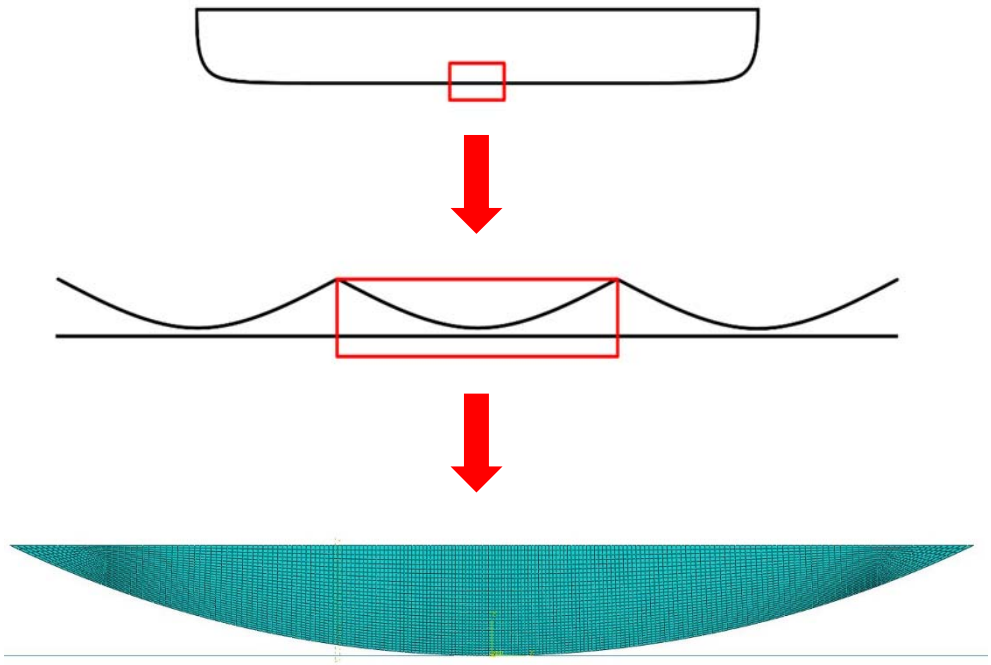

Figure 4-41: Image of the 2D cylindrical asperity CAE model.

The material properties were set to match those of the unfilled natural rubber used in experiments with the Poisson's ratio set to 0.495 and the modulus was assumed linear with a value of 1.2MPa. The mass density was set to 1.2E-9. It was not possible to model the rubber as completely incompressible as explicit techniques

were used. Explicit solvers use the dilational wave-speed of a material which is calculated from the bulk modulus. While an explicit step was not always necessary it was decided to maintain consistency in the material properties. The elements used were quad linear hybrid with distortion and hourglass control and a structured generation was used to provide regular-shaped elements, particularly around the area of contact. The mesh was made finer in this area as well to improve accuracy of the simulations and a mesh refinement study was conducted to check the accuracy and convergence of the solution.

The simulation process is shown in Figure 4-42. In the first step a normal displacement is applied to bring the two surfaces into contact. The contact interaction between the two surfaces in this step is frictionless so that the contact between the two will be Hertzian. A second step is employed to apply the lateral displacement after the compression is completed. The contact interaction between the two is switched to rough friction with zero separation so that the two surfaces are essentially tied together as with the first set of simulations. Simulations for varying peel lengths were then conducted. This was done by applying a vertical partition to the asperity splitting the contact surface into two. One part of the surface was given the rough interaction, i.e. the surfaces are stuck in this area, while the other is given a zero-friction interaction, to represent the part of the contact that has peeled. A series of simulations were conducted with the position of the partition modified to alter the peeled length between simulations. This process is detailed in Figure 4-43.

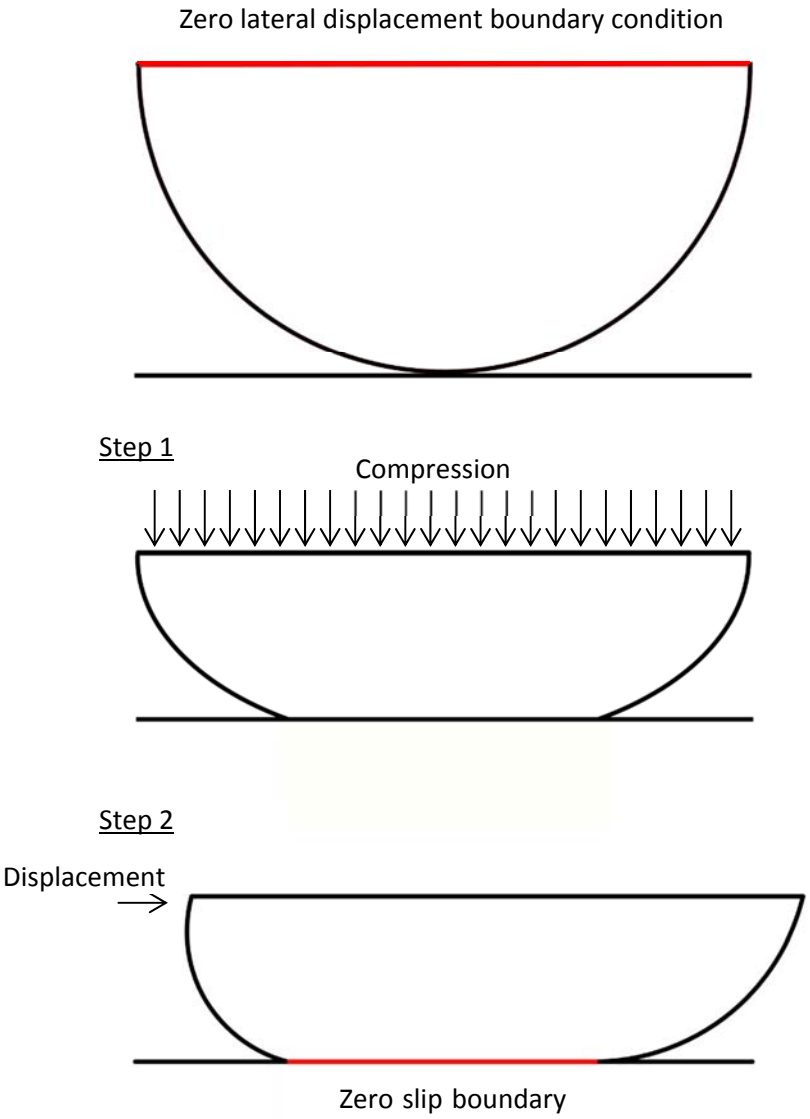

Figure 4-42: Diagram of the simulation sequence.

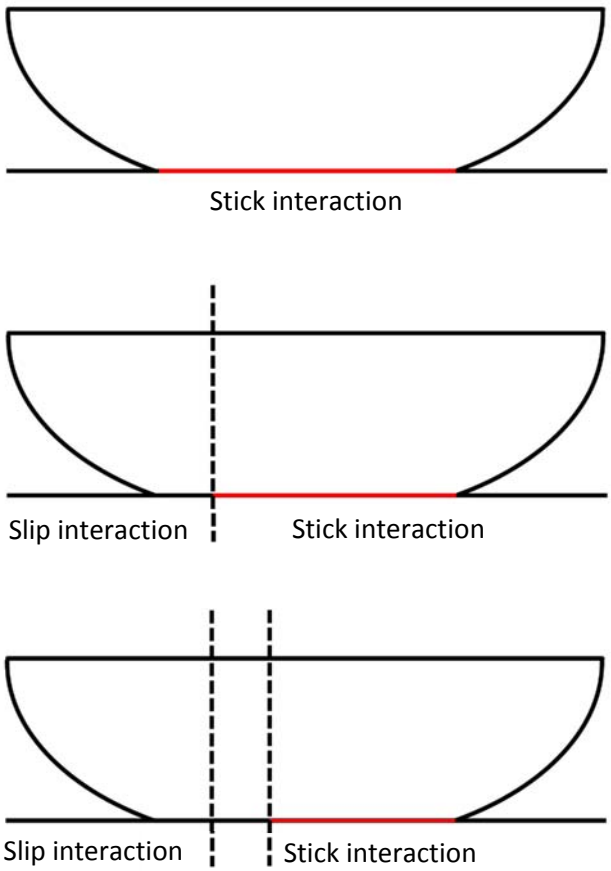

Figure 4-43: Diagram of incremental crack length change between simulations

4.4.3 Hemispherical Asperity Modelling

A similar process was followed with a 3D model asperity this time. The model this time is half a hemisphere; the symmetry of the problem being exploited to simplify the simulation. Again, the substrate was taken as analytically rigid. The resulting model can be seen in Figure 4-44.

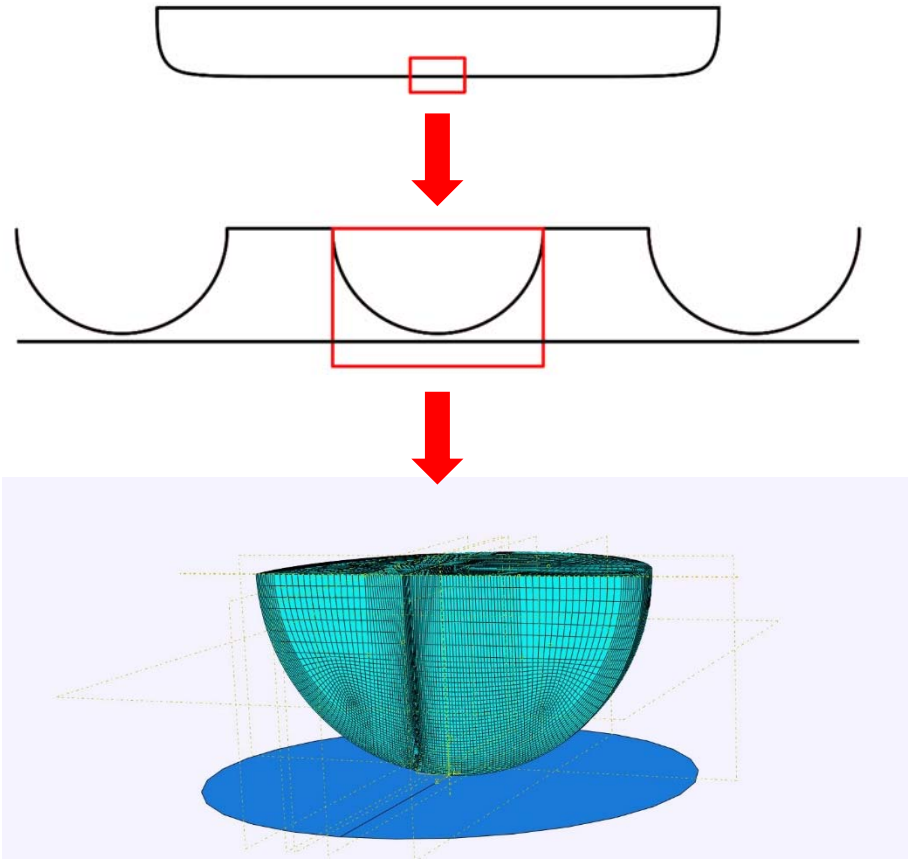

Figure 4-44: Image of the 3D hemispherical asperity CAE model.

The properties of the asperity were of linear elasticity with a Poisson's ratio of 0.495. Hex elements were used, again with a structured generation and an increasing density towards the contact area. It became necessary to employ anti-element distortion techniques hourglass and distortion control for the model which increased the artificial energy of the simulations. It also became necessary to run the shear step as dynamic implicit rather than static. This allows increased sampling of each increment, increasing the simulation computational time but causing rapid changes in element values not to derail the simulation. Care was taken to ensure that there were not high levels of artificial energy present in the model as a consequence.

4.4.4 Results & Discussion

The results obtained from the cylindrical asperity ABAQUS model are detailed next.

The strain energy lost per width (E_{loss}) at a certain crack length (c_n) was calculated by finding the difference between the strain energy (E_{el}) at $c = 0$ (E_0) and $c = c_n$ (E_n).

$$E_{loss} = E_0 - E_n \quad \text{4-16}$$

This could be found at various lateral displacements to give the dependence of E_{loss} against strain. The dependence of the strain energy on the length of peel could be found at different amounts of compression or normal force. The total elastic energy within the asperity model (E_t) is simply found from E_{loss}:

$$E_t = E_{loss} w \quad \text{4-17}$$

Where w is the width of the asperity.

Figure 4-45 shows the resulting dependence of E_{loss} on the lateral displacement (δ). A relation is found of the form:

$$E_{loss} = C_\delta \delta^2 \quad \text{4-18}$$

Where C_δ is a co-efficient dependent on the peel length or peeled area as well as the compression.

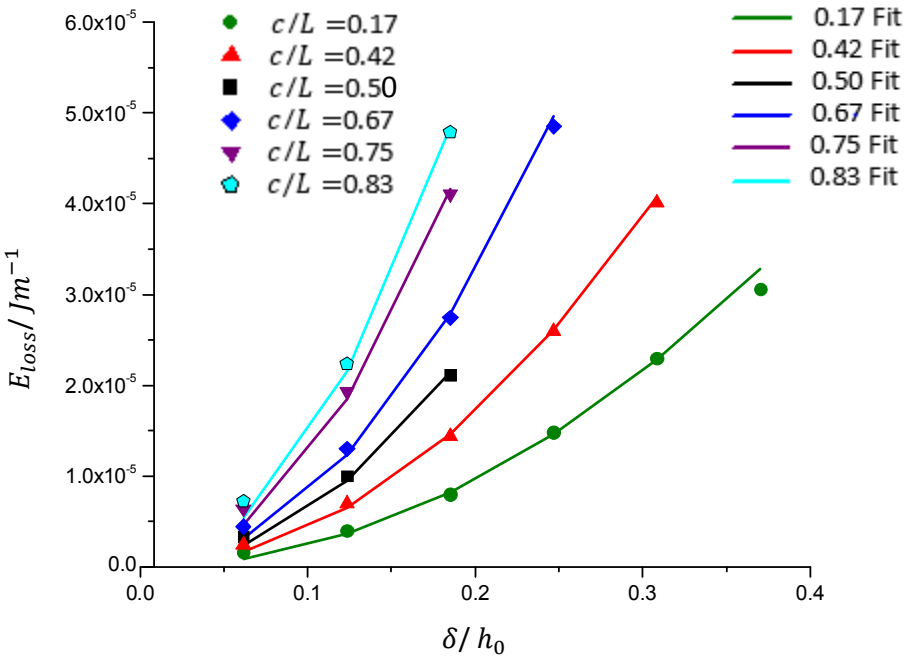

Figure 4-45: Energy lost due to peeling at $\frac{h}{h_0} = 0.025$ compression for a modelled cylindrical NR-0 asperity at various peel lengths with fit curves.

Figure 4-46 plots the coefficients against the peeled area (A_c). This gives a relatively linear trend of the form:

$$C_\delta = C_A A_c$$

Where C_A is the co-efficient of the C_δ against A_c curves.

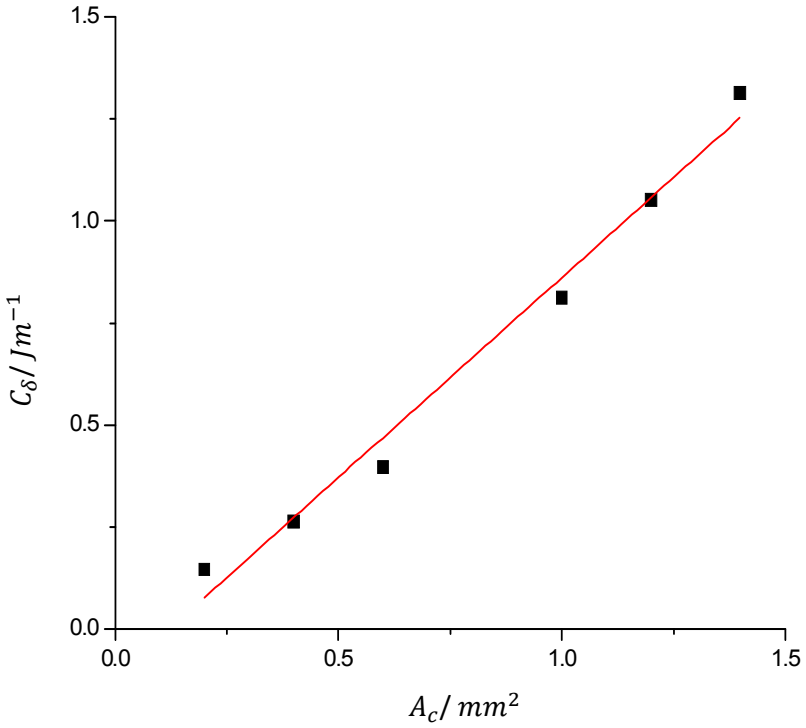

Figure 4-46: Dependence of C_E on A_c for a modelled cylindrical NR-0 asperity with a linear fit applied.

Finally, the effect of the amount of initial compression needs to be taken into account. This is seen in Figure 4-47, where a power law is fitted to the data. This gives the dependence of E_{loss} on all the changing parameters in the model:

$$E_{loss} \propto h^n A_c \delta^2 \qquad 4\text{-}19$$

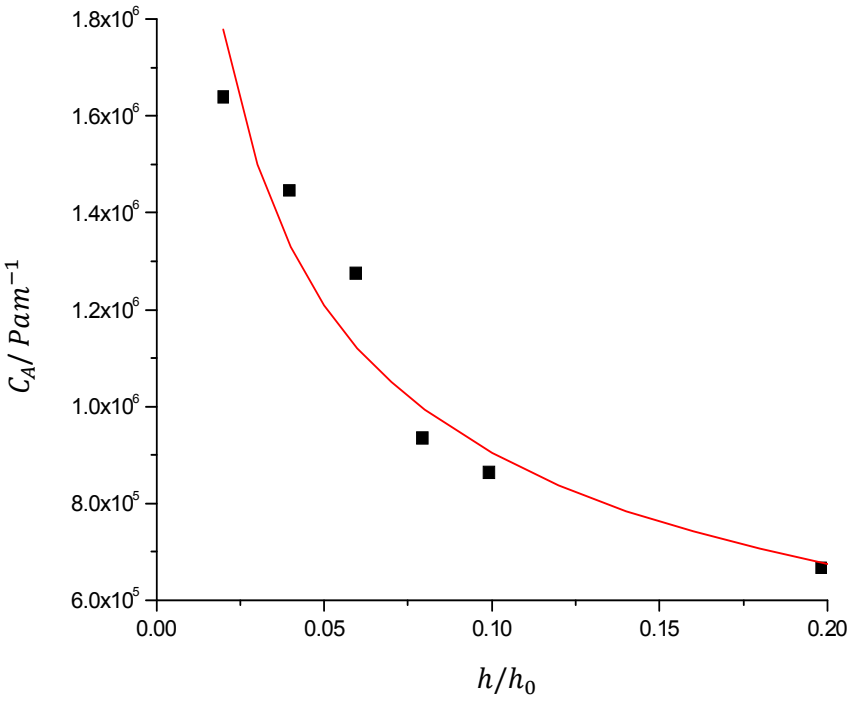

Figure 4-47: Coefficients from A_c versus energy loss coefficients curves against compression for a modelled cylindrical NR-0 asperity, with best fit line in red in the form $y = mx^n$.

Here, the modulus of the material was assumed a constant value consistent with low strain linear elasticity, giving E_t a linear dependence on the modulus. The expression was kept dimensionally correct by normalising the parameters h and δ with a fixed parameter of the asperity geometry, h_0, the height of the un-deformed asperity. The final equation for E_t is thus:

$$E_t = m_c G \left(\frac{h}{h_0}\right)^{n_c} A_c \left(\frac{\delta}{h_0}\right)^2 w \qquad 4\text{-}20$$

Where m_c and n_c are fitting constants found to be 5.75×10^{-9}(2dp) and 0.2 respectively.

In a similar fashion to section 4.2, E_p is defined as the strain energy release rate and is equated to the change in strain energy over the change in crack area so that the fracture mechanics expression 2-17 is invoked to define the peeling energy:

$$E_p = \frac{dE_t}{dA_c} \qquad 4\text{-}21$$

Thus, the expression for E_t is differentiated with respect to A_c to give:

$$E_p = m_c G \left(\frac{h}{h_0}\right)^{n_c} \left(\frac{\delta}{h_0}\right)^2 w \qquad 4\text{-}22$$

The same process as that of section 4.2 in deriving the box asperity model expression for σ_f can be followed. Given equation 4-4:

$$\frac{dc}{dt} = A\left(m_c G \left(\frac{h}{h_0}\right)^{n_c} \left(\frac{vt}{h_0}\right)^2 w\right)^{\alpha} \qquad 4\text{-}23$$

Integrating from $c = 0$ at $t = 0$ to $c = L$, the asperity contact length, at $t = t_1$, the time taken to peel the entire asperity:

$$L = \frac{A\left(m_c G \left(\frac{h}{h_0}\right)^{n_c} \left(\frac{\delta}{h_0}\right)^2 w\right)^{\alpha} t_1^{(2\alpha+1)}}{2\alpha+1}$$

$$t_1 = \left((2\alpha+1)\frac{L}{A}\frac{1}{\left(m_c G\left(\frac{h}{h_0}\right)^{n_c}\left(\frac{v}{h_0}\right)^2 w\right)^{\alpha}}\right)^{\left(\frac{1}{2\alpha+1}\right)} \qquad 4\text{-}24$$

From equations 4-7 and 4-8:

$$\bar{\sigma} = \frac{1}{Lvt_1 A^{\frac{1}{\alpha}}} \int_0^{t_1} \left(\frac{dc}{dt}\right)^{\left(1+\frac{1}{\alpha}\right)} dt$$

$$= \frac{1}{Lvt_1 A^{\frac{1}{\alpha}}} \int_0^{t_1} \left(A\left(m_c G \left(\frac{h}{h_0}\right)^{n_c} \left(\frac{vt}{h_0}\right)^2 w\right)^{\alpha}\right)^{\left(1+\frac{1}{\alpha}\right)} dt$$

$$= \frac{Av^{(2\alpha+1)}}{L}\left(m_c G \left(\frac{h}{h_0}\right)^{n_c} \left(\frac{vt}{h_0}\right)^2 w\right)^{(\alpha+1)} \frac{t_1^{(2\alpha+2)}}{(2\alpha+3)} \qquad 4\text{-}25$$

Substituting equation 4-24 into equation 4-25:

$$\bar{\sigma} = \frac{\left((2\alpha+1)^{\frac{(2\alpha+2)}{(2\alpha+1)}}\right)}{(2\alpha+3)} \left(\frac{L}{A}\right)^{\frac{1}{(2\alpha+1)}} \left(m_c G \left(\frac{h}{h_0}\right)^{n_c} \frac{w}{h_0^2}\right)^{\frac{(\alpha+1)}{(2\alpha+1)}} v^{\frac{1}{(2\alpha+1)}} \qquad 4\text{-}26$$

This equation provides the form of the frictional shear stress for the specific shape of the cylindrical asperity and is henceforth referred to as the ABAQUS cylindrical asperity model. In this way, a more accurate calculation of $\bar{\sigma}$ can be made. It can be noted that the predicted velocity dependence is the same as that found for the box asperity model; the change in the expression occurs in the term involving the asperity height.

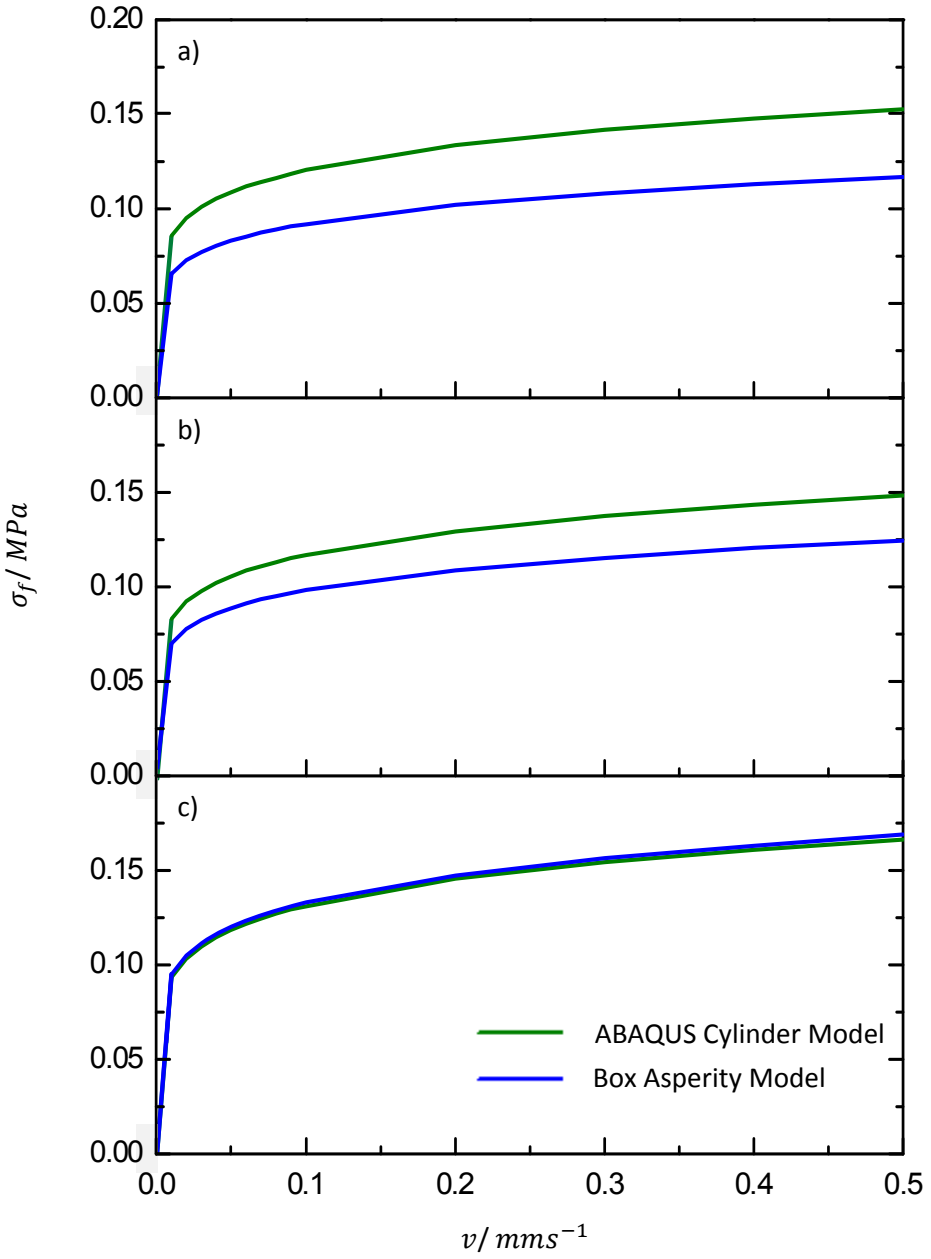

Figure 4-48: Frictional shear stress calculated from the ABAQUS cylindrical model compared to the box asperity model using glass and NR-0 as the materials at loads of: a) 0.1875kg, b) 5kg, and c) 10kg.

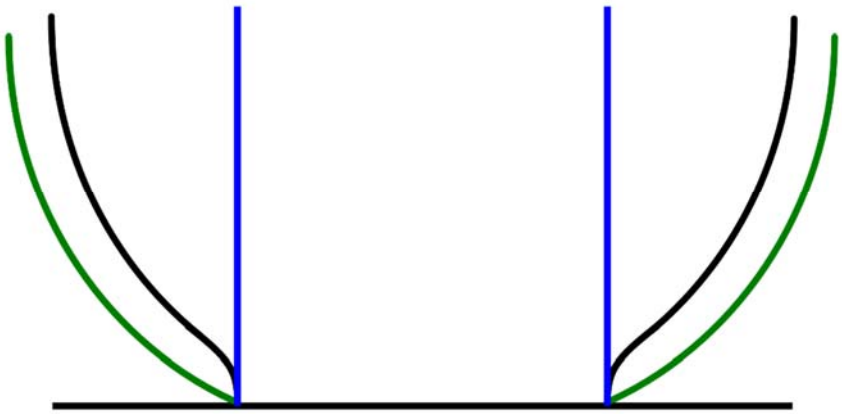

Figure 4-49: Diagram of asperity profiles; black- adhesive profile at rest, blue- box asperity model, green- ABAQUS asperity model.

It is seen in Figure 4-48 that the ABAQUS cylindrical asperity model predicts a slightly larger σ_f than the box asperity model but that the two approach each other at high normal loading. This anticipated as the ABAQUS cylindrical asperity model, as shown in Figure 4-49, models the geometry more faithfully and as such, includes a larger area in the deformation for the calculation of the strain energy than the box asperity model. At higher normal forces, the shapes of the profiles of the two approach each other and so do the values obtained from the two.

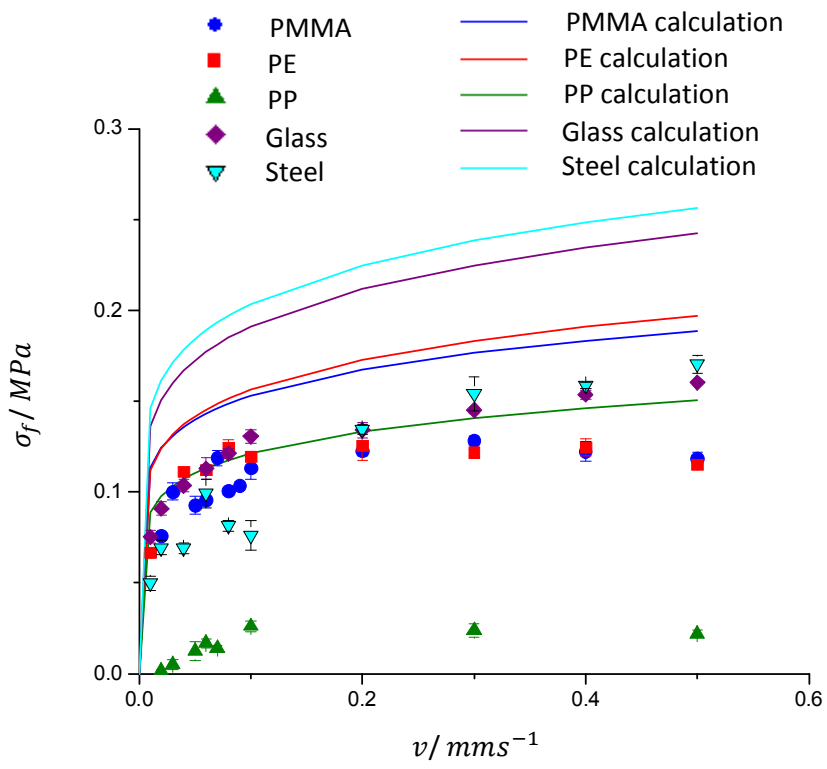

Figure 4-50: Cylindrical asperity experimental results minus lubricated average friction compared to abacus cylindrical model.

Figure 4-50 compares the ABAQUS cylindrical asperity model to sliding results and it is seen that it over predicts σ_f from experiment. The fact that the box shape provides a better approximation to the form of the strain energy function could be due to the elongated profile of the cylindrical asperity geometry studied. With a base length an order of magnitude greater than its height it's likely that the deformation is concentrated towards the centre of the shape and decreases towards the corners of the asperity.

In a similar fashion as to the cylindrical model, the form of the strain energy loss due to peeling may be found from the results of hemispherical asperity modelling. E_{loss} once again has a relationship with δ of the form of equation 4-18, seen in Figure 4-51. The dependence on A_c on C_δ values, from Figure 4-52, is approximated to a linear relationship to simplify the analysis. The dependence on compression of the asperity, Figure 4-53, was found to be approximately linear so that W_p could be expressed as:

$$W_p = G(m_h + n_h h)A_c \left(\frac{\delta}{h_0}\right)^2 \qquad 4\text{-}27$$

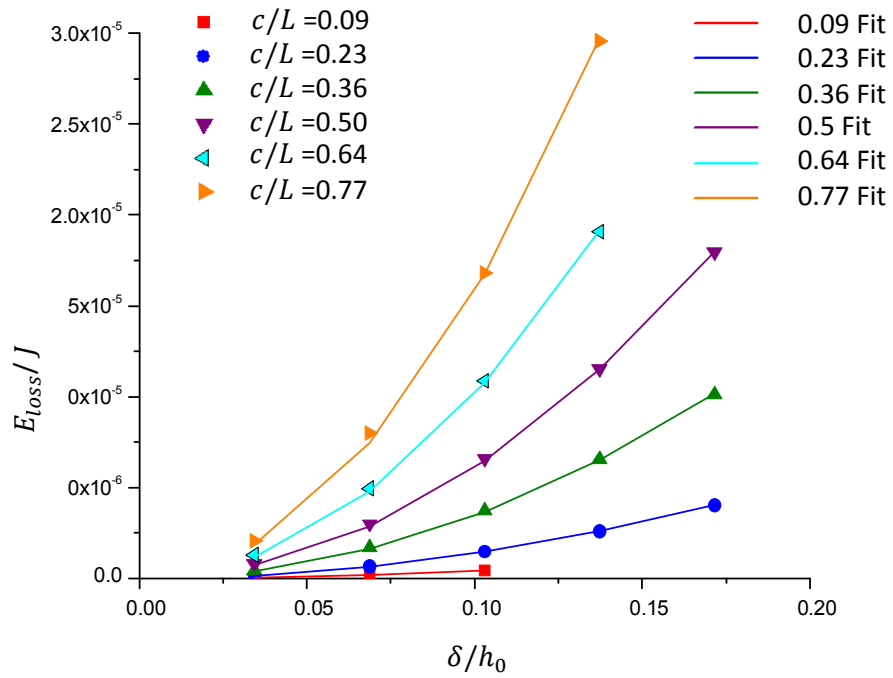

Figure 4-51: Energy lost due to peeling at $\frac{h}{h0} = 0.08$ compression for a modelled hemispherical NR-0 asperity over a range of peel lengths, c.

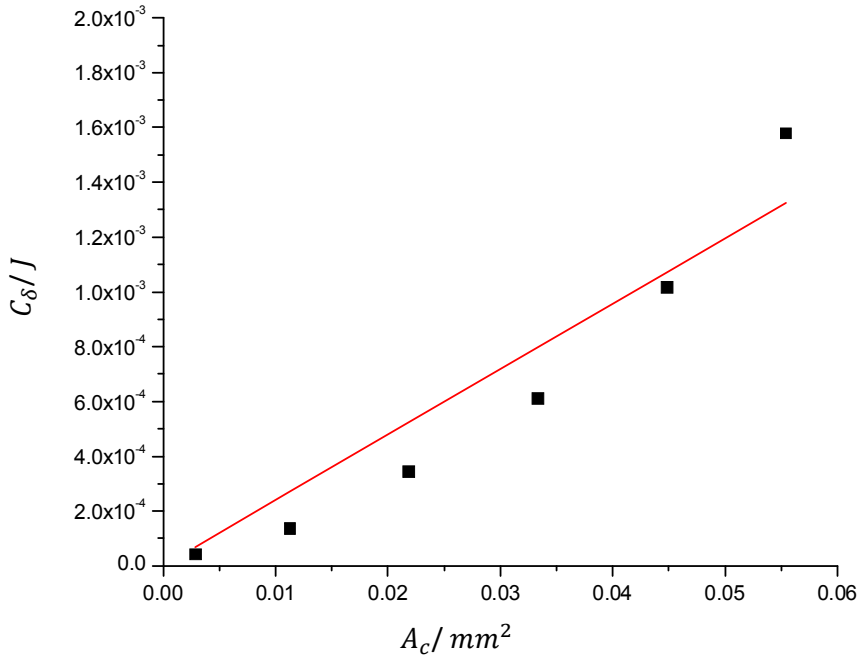

Figure 4-52: Dependence of the coefficients of the energy loss curves on the peeled area for a modelled hemispherical NR-0 asperity.

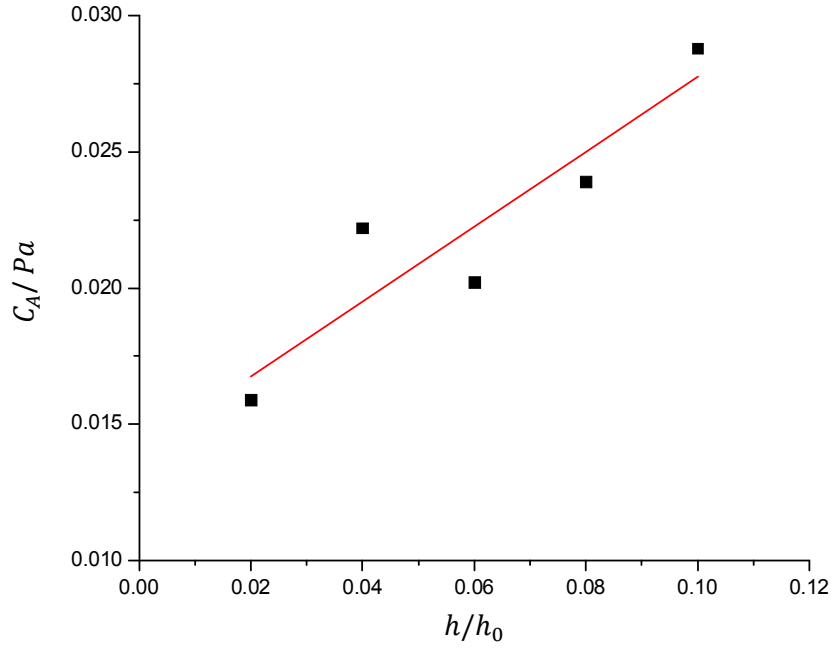

Figure 4-53: Coefficients from A_c versus energy loss coefficients curves against compression for a modelled hemispherical NR-0 asperity, with a linear fit line in red.

The expression for E_p is found as with the cylindrical asperity:

$$E_p = \frac{dW_p}{dA_c} = G(m_h + n_h h)\left(\frac{\delta}{h_0}\right)^2 \qquad 4\text{-}28$$

And subsequently, in the same manner:

$$\frac{dc}{dt} = A\left(G(m_h + n_h h)\left(\frac{\delta}{h_0}\right)^2\right)^{\alpha}$$

$$L = A\left(G(m_h + n_h h)\left(\frac{v}{h_0}\right)^2\right)^{\alpha}\frac{t_1^{(2\alpha+1)}}{(2\alpha+1)}$$

$$t_1 = \left((2\alpha+1)\left(\frac{L}{A}\right)\frac{1}{\left(G(m_h+n_h h)\left(\frac{v}{h_0}\right)^2\right)^{\alpha}}\right)^{\frac{1}{(2\alpha+1)}} \qquad 4\text{-}29$$

Where the solution differs to that of the cylinder asperity model, is that the incremental increase in peeled area is not constant in the displacement direction; the work done equations therefore take the following forms:

$$W_p =$$

$\int_0^c wE_p dc$ 4-30 $W_p =$

$\bar{\sigma} A_t V t_1$ 4-31

Where $A_t = \pi a^2$ is the total contact area. Equation 4-30 can be rewritten as:

$$W_p = \int_0^{A_t} E_p dA_c \quad 4\text{-}32$$

A_c can be expressed as a function of c:

$$A_c = 2a^2 \sin^{-1}\left(\frac{\sqrt{2ac}}{2a}\right) \quad 4\text{-}33$$

Given that, from equation 4-4, the expression of peel rate as a function of E_p , and 4-28:

$$c = \frac{AC_E^{\alpha} v^{2\alpha} t^{(2\alpha+1)}}{(2\alpha+1)}$$

$$C_E = \frac{G(m_h + n_h h)}{h_0^2} \quad 4\text{-}34$$

From equations 4-33 and 4-34:

$$t = \left(\frac{(2\alpha+1)\left(2\sin\left(\frac{A_c}{2a^2}\right)\right)^2}{2aAC_E^{\alpha} v^{2\alpha}}\right)^{\frac{1}{(2\alpha+1)}} \quad 4\text{-}35$$

Substituting equations 4-28 and 4-35 into equation 4-32:

$$W_p = \int_0^{A_t} C_E v^2 \left(\frac{(2\alpha+1)\left(2\sin\left(\frac{A_c}{2a^2}\right)\right)^2}{2aAC_E^{\alpha} v^{2\alpha}}\right)^{\frac{2}{(2\alpha+1)}} dA_c$$

$$= C_E v^2 \left(\frac{2a(2\alpha+1)}{AC_E^{\alpha} v^{2\alpha}}\right)^{\frac{2}{(2\alpha+1)}} a^2 \sqrt{\pi} \frac{\Gamma\left(\frac{(2\alpha+5)}{2(2\alpha+1)}\right)}{\Gamma\left(\frac{(2\alpha+3)}{(2\alpha+1)}\right)} \quad 4\text{-}36$$

Thus, an expression for the frictional shear stress is found from equations 4-31 and 4-36:

$$\bar{\sigma} = \left(\frac{\sqrt{\pi}}{\pi}\right) \frac{\Gamma\left(\frac{(2\alpha+5)}{2(2\alpha+1)}\right)}{\Gamma\left(\frac{(2\alpha+3)}{(2\alpha+1)}\right)} (2a)^{\frac{1}{(2\alpha+1)}} \left(\frac{(2\alpha+1)}{A}\right)^{\frac{1}{(2\alpha+1)}} C_E^{\frac{(\alpha+1)}{(2\alpha+1)}} v^{\frac{1}{(2\alpha+1)}} \quad 4\text{-}37$$

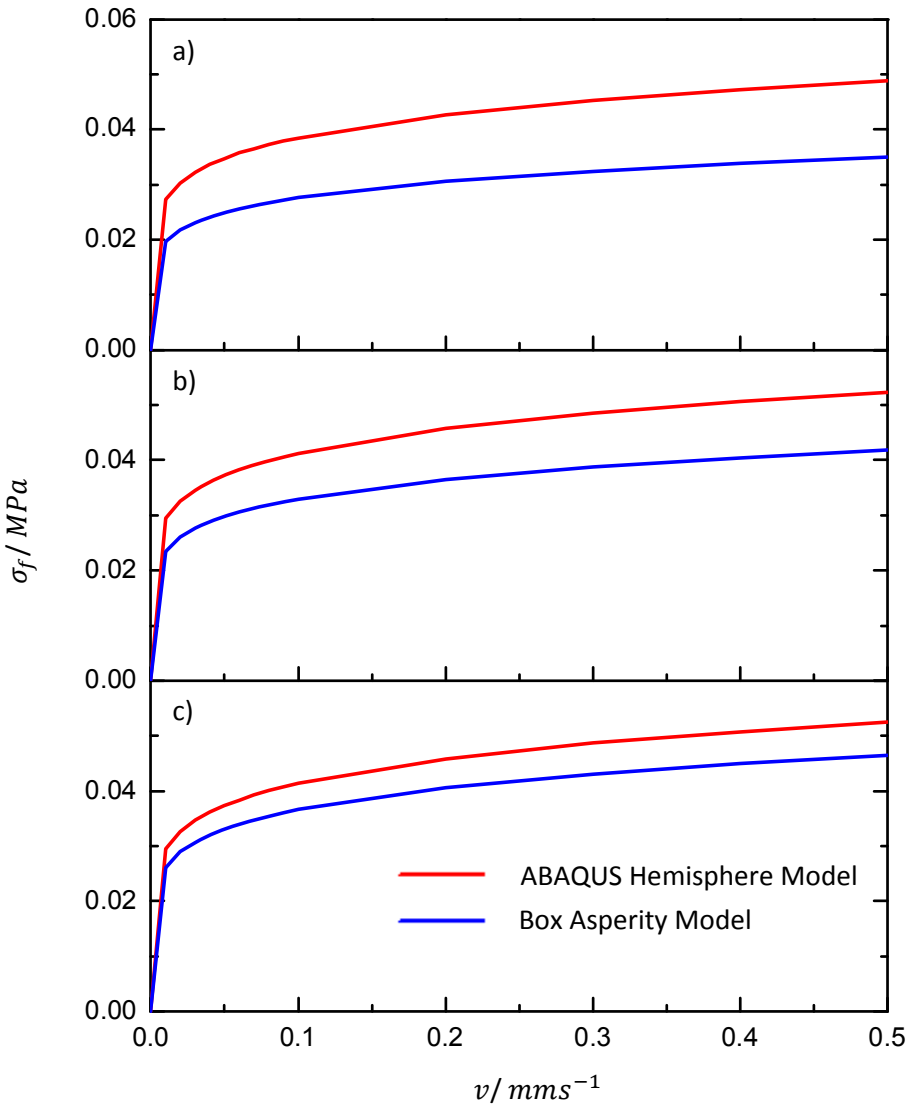

Figure 4-54: ABAQUS hemispherical asperity model compared to the box asperity model using glass and NR-0 as the materials at a load of; a) 0.43kg, b) 5kg, and c) 10kg.

This equation shall be referred to as the ABAQUS hemispherical asperity model. Figure 4-54 compares this model calculation to the box asperity model under the same conditions. It shows that, in a similar fashion to the comparison for the ABAQUS cylindrical asperity model, the ABAQUS hemispherical asperity model predicts a higher σ_f but the two approach each other as the normal load is increased, as is expected.

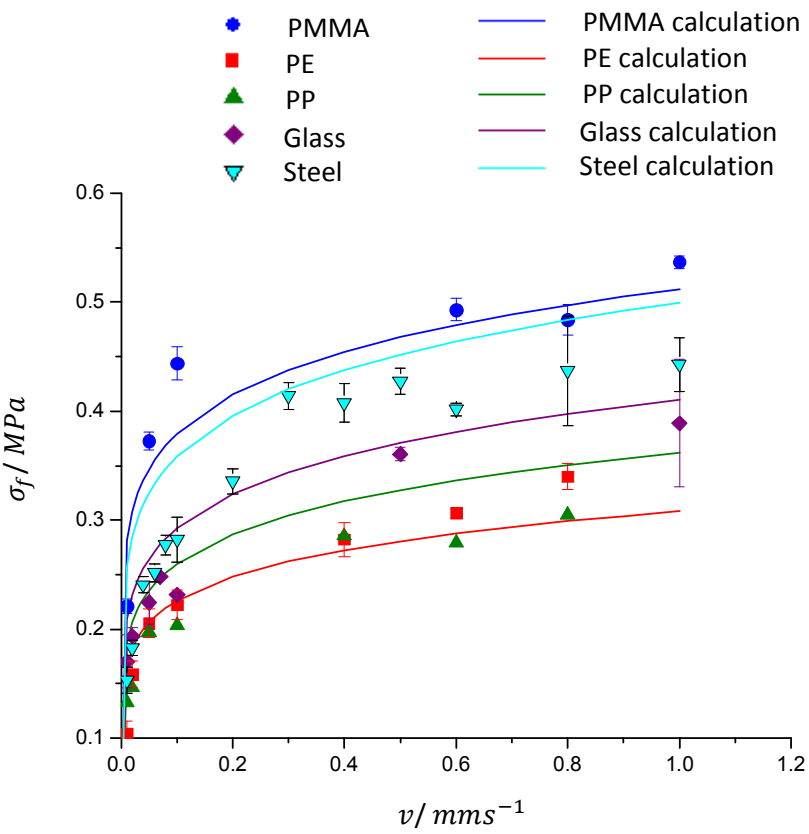

Figure 4-55: Hemispherical asperity experimental results minus lubricated average friction compared to the ABAQUS hemispherical model results for NR-0.

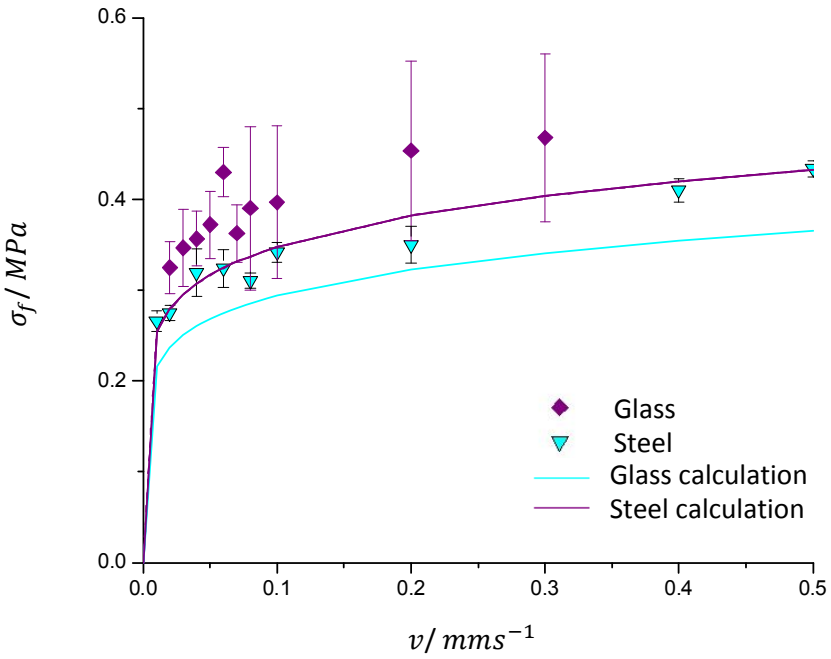

Figure 4-56 Hemispherical asperity experimental results minus lubricated average friction compared to Abacus hemispherical model for ENR-0.

Figure 4-55 and Figure 4-56 give the σ_f values obtained in using the ABAQUS hemispherical model and show that the fit to experimental results is much better. A good fit is found for PMMA, PE and glass surfaces whilst σ_f for steel and PP surfaces is overpredicted slightly. Reasonable agreement is found with ENR-0 results although experimental data is undercut slightly. This would suggest that the accuracy of the theory is much improved with the ABAQUS hemispherical asperity model and that the strain energy involved in the peeling process particular to this geometry was not adequately approximated by the box asperity model.

4.5 Conclusion

A strong dependence on rubber asperity geometry of the theory presented in this section necessitated improved approximation of the effect of asperity contact geometry on peeling energy. A method for tailoring the theoretical analysis for the friction of a rough rubber surface against a smooth rigid surface to a specific asperity geometry using ABAQUS modelling is described. This method evaluates the strain energy of deformation at various peel lengths and normal loadings without having to define a peel rate or ultimate deformation of peeling. For both geometries modelled it gives a higher value of σ_f than the box asperity model which

is as would be expected as a larger geometry, more closely approximating the actual asperity geometry, is modelled. The predictions from the ABAQUS models approach that of the box asperity geometry at high loads as is expected as the shapes of the two would approach one another. For the cylindrical asperity used in experimentation the approximation of asperity geometry as a box provides a more agreeable prediction of frictional shear stress with experiment; this is probably due to the long flat shape of the asperity cross-section somewhat restricting the deformation at or towards the edges of the geometry, thus providing a strain energy lower than that expected for this geometry. The ABAQUS hemispherical asperity model closely matches frictional shear stress values obtained from experiment and thus accounts for the significant discrepancy between calculation and experiment seen with the box asperity model. This suggests that asperity geometry is a significant factor in the peeling process as a consequence of the effect on the strain energy distribution; care must be taken when applying the theory although simply approximating asperity geometry to a cubic shape may be adequate when high loads or long asperity profiles are studied. The theory developed is therefore able to estimate the frictional shear stress between a rubber surface with asperities of known geometry against a smooth surface.

5 Jamming of Soft Frictional Particles

Most often, in engineering applications, rubber components are required to share a boundary with another material. Recently however, the rise in jamming based systems for soft robotic applications has lead to a demand for studies to be conducted on the particles to be used in such systems. One material which may hold significant benefits to such systems is rubber due to it's low modulus but strong frictional properties. This section first discusses work examining the behaviour of jammed systems of rubber particles and then studies individual particle interactions that would occur in such systems.

5.1 Monolayer Jamming

5.1.1 Introduction

The study of packings of particles is complicated by the difficulty in controlling its orientation and arrangement and monitoring of individual particles. To enable a more controlled and observable study it was decided to conduct tests on monolayer arrangements of particles. This entailed constructing a setup to enable a single layer of particles and allow deformation of the layer in one plane.

5.1.2 Results & Discussion

An external pressure gauge was attached in series to the system described in section 3.9 to independently measure the pressure to the pump however, the sensitivity of the instrument was such that the fluctuation of the pressure made obtaining a reading difficult. It was considered likely regardless that there would be losses of pressure within the system, such as losses over the membrane, such that the pressure exerted on the particles would not be that registered by the pump. Instead, the pressure of the packing was estimated by measuring the average contact between particles and using contact mechanics to calculate the pressure the compliant particles (with known elastic properties) were experiencing. The contact length between particles in the packing was measured at various pressure levels as measured by the vacuum pump using a digital microscope. Using this measurement, the average pressure acting on a particle can be found by using equation 2-66 to give a relationship between the contact and the inter-particle force and therefore pressure. The results of this can be seen in Figure 5-1, which shows clearly that the measured pressure is not equal to the pressure calculated at

the particles. This disagreement indicates that there are indeed losses to be accounted for and that care should be taken when considering pressure.

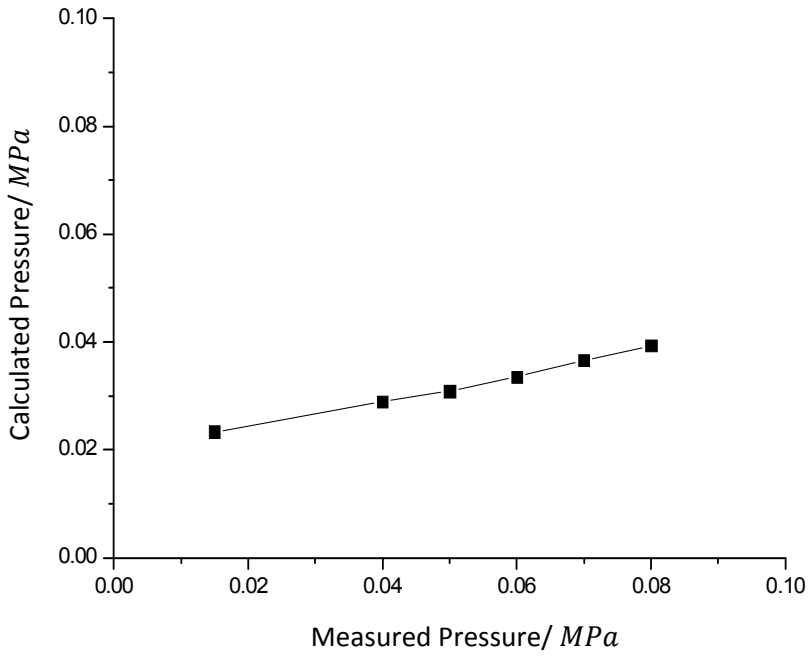

Figure 5-1: Measured pressure compared to pressure calculated from inter-particle contact for a packing of 10mm diameter NR-0 particles.

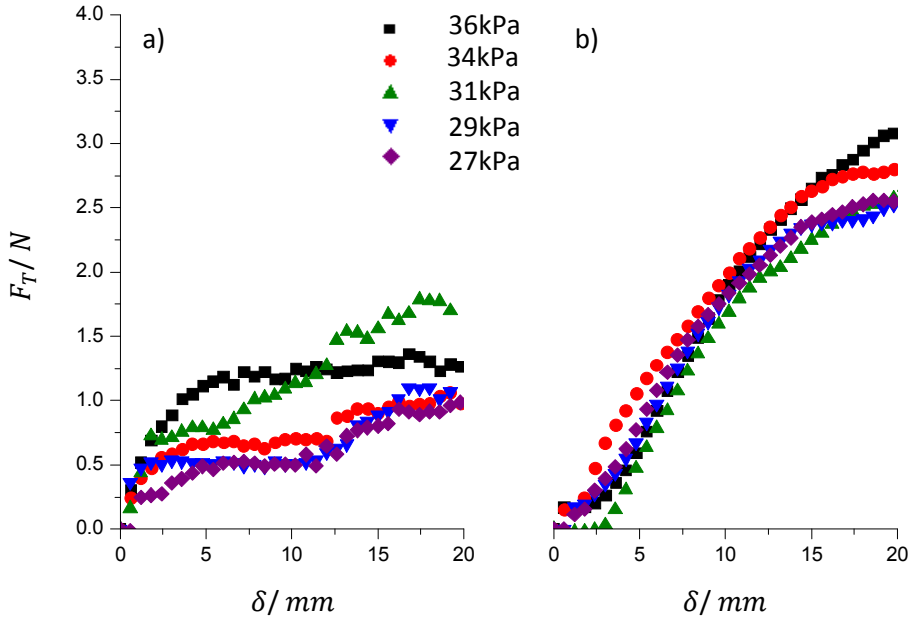

Figure 5-2: Bending tests conducted at different pressures for a random configuration of 10mm particles of a) steel, and b) NR-0.

The results in Figure 5-2 immediately highlight the difference between the particles used in the test. Whilst the pressure, calculated pressure acting on particles, was varied between runs it would seem to have little correlation with the stiffness of the packing for either particle type; a lot of variation is seen in the steel particle packing, but not correlating with pressure change, and there being minimal variation in the rubber packing.

Pressure between tests was not varying significantly so the results do not show a strong correlation with the pressure however, there is a clear difference between the packings of the two particles. A random close packing was used in tests with no fixed pattern of initial particle arrangement which means the arrangement of the particles differed between tests. The variation in structure is seen to have a large effect on the rigid steel particles but not on the NR-0 particles. Particle arrangement is likely to influence the threshold displacement required to cause a form of plastic yield in the steel particle packing. From geometric considerations, particle rearrangement can be seen to occur suddenly in rigid particles, and at a random level of displacement with random particle configurations; the resistance to a lateral force is seen to depend on the angle of contact of the particle with its neighbours (Andreotti et al. 2013). This explains the variation and sudden fluctuations seen in the steel packing force response, seen in work such as Jiang et al. (2012). With the deformable frictional rubber, large contact areas are formed between particles, seen in comparison to a rigid particle in Figure 5-3, and deformation of the particles can occur in response to an applied force; allowing for deformation of the packing without relative movement of particles. This strongly limits the possibility of rearrangement (a particle changing neighbouring contacts) of particles within the packing. The friction between particles may help maintain contact throughout the deformation tested. Particle intrusion and hopping, mechanisms of particle rearrangement, are suppressed (Loeve et al. 2010). Thus, the packing behaves in response to an applied load as a continuous material. The plastic behaviour of stiff particles can be seen in other studies such as Cheng et al. (2010).

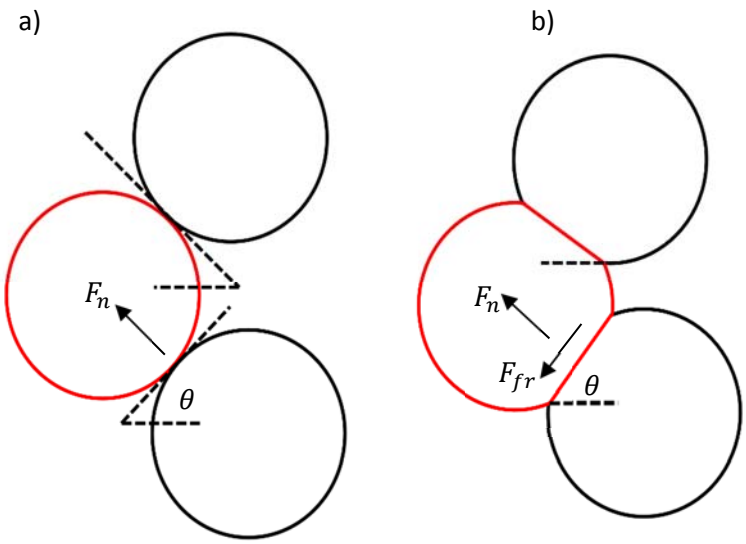

Figure 5-3: Diagram of particle arrangement for; a) rigid particles, b) deformable frictional particles.

Further tests were conducted this time with a pre-arranged particle organisation. The particles were arranged into a hexagonal pattern at the beginning of every test. Results for a bending test are shown in Figure 5-4, for three particle materials, NR-0, acrylonitrile butadiene rubber (NBR), and steel, summarised in Table 5-1. Again, there are key differences between the rubber particles and the steel particles. The stiffness of the packings ranks with the moduli of the particle materials as expected (taking a low-strain modulus for the steel packing). A distinction can be made between the variation of the results for the three materials. The steel packing gives much more repeatable results with a specified initial particle configuration however the variation over the deformation range tested still exceeds that of the two rubber packings. The stiffer NBR rubber shows higher variance out of the two rubbers. As with Figure 5-2, the large initial modulus is seen for the steel packing, decreasing with increased strain. A sudden and distinct yield is not seen as in Figure 5-2, where this occurred at relatively low displacement, the curve instead tends towards a plateau as seen for rigid particles in previous studies (Cheng et al. 2010; Steltz et al. 2009). In contrast the NR-0 and NBR display a lower modulus than the initial steel modulus but a quasi-linear response to applied load over the strain range tested and the NBR matching the steel at the higher strains.

Table 5-1: Summary of monolayer jamming test materials.

Material	Young's Modulus MPa (3sf)
NR-0	1.21
NBR	3.50
Steel	210000

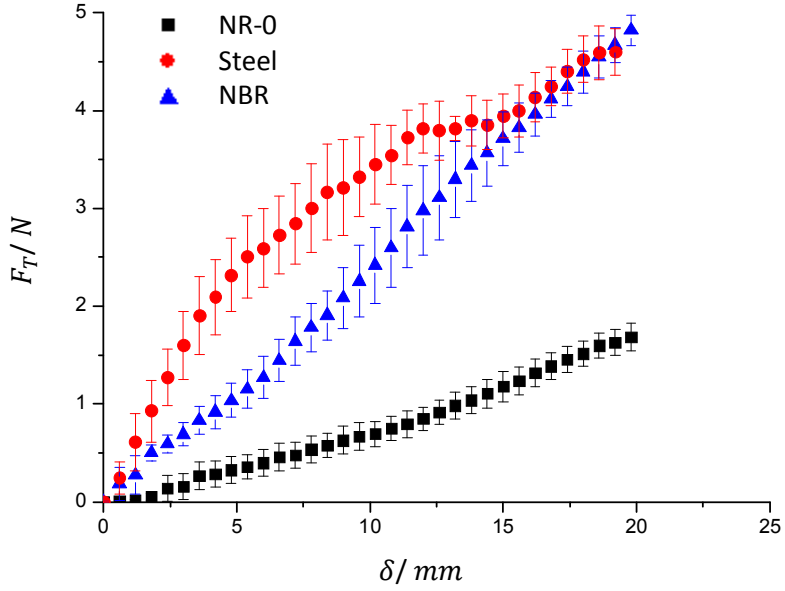

Figure 5-4: Bending forces graph for ordered hexagonal packing of 10mm diameter particles of various stiffnesses.

Cyclic shear tests were carried out by deforming the packing, returning the indenter to the initial position, and repeating a number of times. Results of shear experiments are shown in Figure 5-5. The return path for each different particle type was averaged over each cycle. The results are given as a nominal shear stress (σ'), defined as F_T over the packing width, againts strain (ε). The cyclic shear graph shows a large amount of hysteresis loss for the steel particle packing. The amount of loss is lower for the NBR and much lower in the NR-0 curve. A similar result is seen in the work by Jiang et al. (2012) where rubber particles were seen to show lower hysteresis than rigid spheres (although the rubber particles used were

cubes). The variation is again highest in the steel packing. Each cycle was initiated immediately upon the termination of the previous cycle, such that the recovery of the packings was limiited by the rate of recovery. The difference in starting and ending points of each curve will be termed permanent set. It can be seen that the permanent set is largest for the steel packing, decreasing through NBR down to the NR-0 which has very low permanent set.

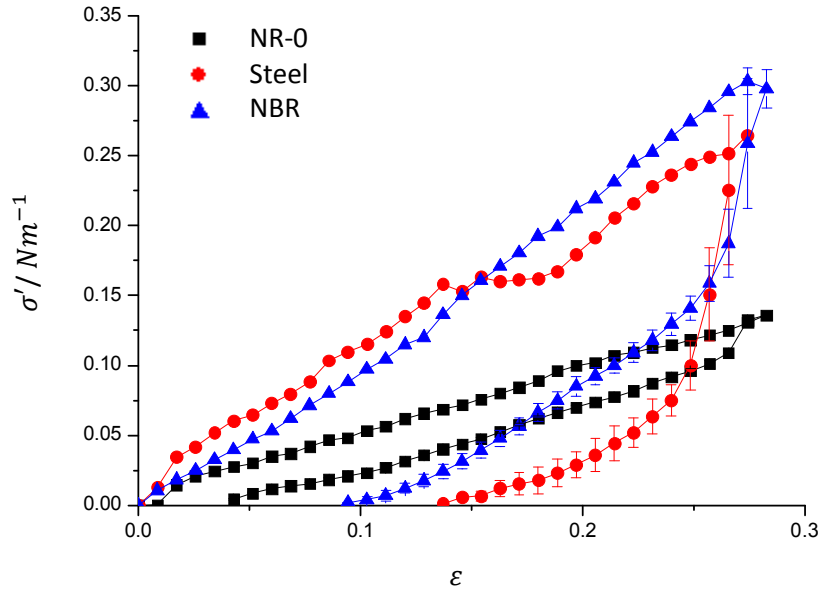

Figure 5-5: Cyclic shear test results on a monolayer packing of 10mm monodisperse spheres for three particle materials of various stiffnesses.

The test was repeated with a packing of lubricated NR-0. Figure 5-6 compares the lubricated NR-0 results against those of the unlubricated NR-0. The graph shows very little change in the loading path however there is a large difference in the unloading where the lubricated NR-0 shows a greater amount of energy loss than the unlubricated NR-0 and a significant level of permanent set. This is highlighted by comparing the hysteretic energy loss from the cycles recorded, shown in Figure 5-7. Consecutive cycles were conducted with a small recovery time between cycles of 10 seconds. It would seem that the deformability of the particles prevent sudden and large shifts in packing particle arrangement however, clearly a substantially greater amount of slippage occurs between the lubricated particles in comparison to the unlubricated. This slippage means that the packing arrangement is altered from the initial arrangement after the external load is removed. This can be seen in the large hysteresis and permanent set in the lubricated curve. This is a result that,

to my knowledge, is novel, the friction interaction between particles has not been shown to contribute independently of the interlocking of particles to the behavioural response of a jammed system.

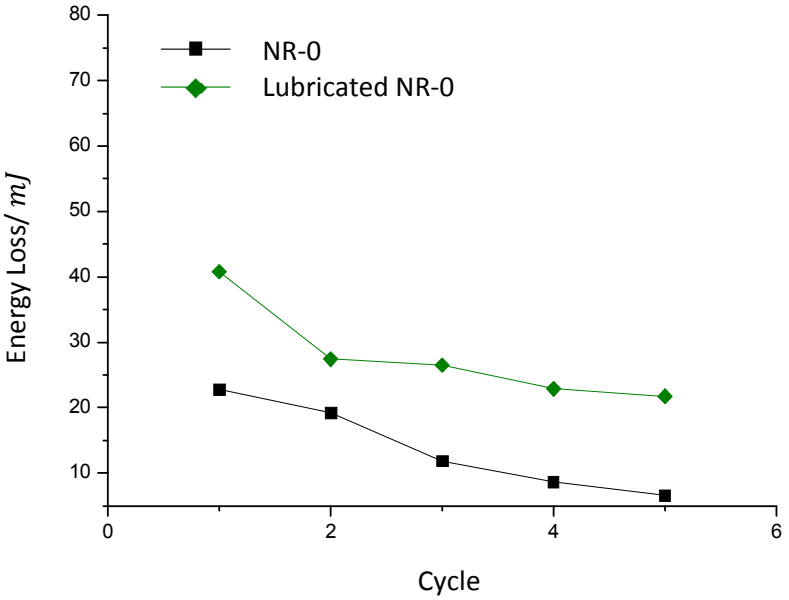

Figure 5-6: Comparison of cyclic shear test results on a monolayer packing of 10mm monodisperse spheres of NR-0 dry and lubricated

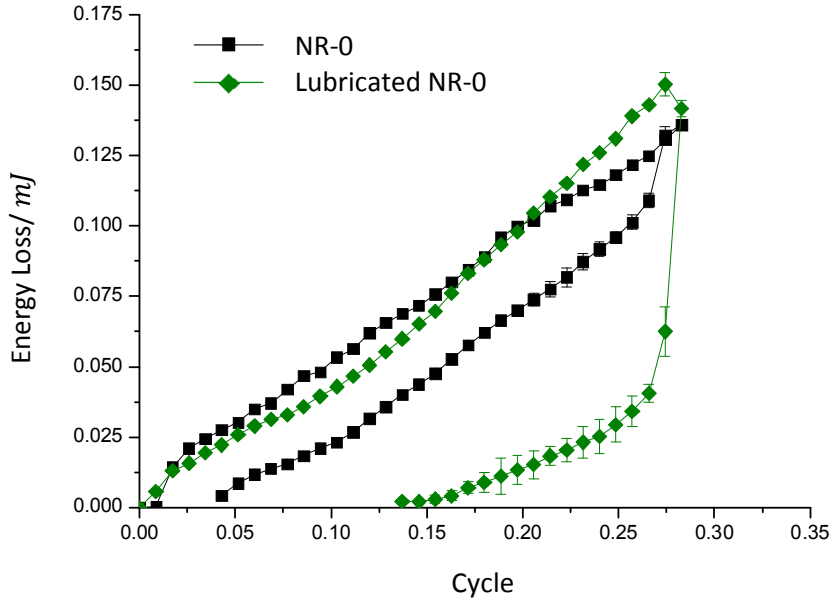

Figure 5-7: Energy loss calculated from the difference between loading and unloading curves in Figure 5-6.

5.1.3 Conclusion

Due to their deformability, easily modified properties, and widescale availability among other advantages, rubber particles, previously not studied to any great degree, could be advantageous to use in soft robotic jamming based systems. The response of monolayer jamming systems of monodisperse rubber particles to externally applied loads was studied and compared to results for steel particles using a monolayer setup newly developed for this purpose. Data was obtained for particles of two different types of particles. The soft frictional particles display markedly different behaviour in force response in comparison to rigid frictionless particles and soft frictionless particles. At a cost to the packing stiffness, the deformability of the particles allows the packing of soft particles to display characteristics of a continuous material in contrast to the steel particle packings that achieved relatively low levels of deformation before structural changes within the packing cause significant fluctuation in the packing stiffness. A relatively constant level of stiffness is maintained to high levels of deformation for the rubber packings. It has been shown that the role of particle interlocking and inter-particle friction may differ. The large inter-particle contacts prevent sudden and dramatic structural changes to the particle arrangement under constant applied load however, slippage and rearrangement may still occur when the direction of applied load is changed suddenly. Inter-particle friction allows little to no slip to occur between particles meaning the structure of packings of deformable frictional particles retain consistent properties after being subjected to multiple loading cycles. The constancy of particle arrangement is what ensures low variation in response, low hysteresis in cyclic loading, and continuous behaviour as oppose to rigid particle packings which show characteristics of fragile matter. These characteristics suggest a strong suitability to soft robotic systems where continuous properties and predictable behaviour would be advantageous. The use of rubber particles specifically is beneficial as rubber is a widely used and available mechanical material, the production of which could be tailored to give desired material properties, such as modulus, to suit specific applications. Effect of the influence of the flexible membrane on results was reduced by maintaining a constant number of particles throughout experimentation however, due to the deformability of the rubber particles and the high level of friction in the interaction in comparison to steel particles, it is clear that membrane influence would not likely to be consistent between the two. For this reason, the displacements reached were

kept relatively low so that the flexible membrane would not build up significant stresses of its own.

5.2 Frictional Interactions Between Rubber Particles

5.2.1 Introduction

In the previous section it has been seen how a packing of rubber particles behaves as a continuous system to applied external forces however, it is very difficult to isolate the forces occurring on individual particles from this work due to the influence of the flexible membrane, friction of the packing with constraining surfaces, and slight imperfections in particle arrangements. In order to better understand how the overall system behaviour develops it is first essential to study the interactions between the individual particles. This section will focus on these interactions between rubber particles.

To examine the development of the contact interactions and the inter-particle forces between them, a simple experimental configuration was developed. This utilised three rubber hemispheres where one hemisphere was displaced relative to the other two using a rheometer. The hemispheres would be attached, at an equal radius to the outer edges of the rheometer plates with two attached to the bottom plate with zero clearance between them and one on the top plate. The movement relative to each other was assumed to be approximately linear over the range of displacements examined. The lateral shearing force acting on the hemispheres was calculated from the torque measured by the instrument by division by the radius at which the centre of each of the hemispheres were located. The normal force on the hemispheres was measured by the rheometer. This value was later observed to be inaccurate and the contact between hemispheres was instead used to calculate normal force using contact mechanics. The simple base unit of three particles was also modelled using a MATLAB code based simulations. This geometry and important contact parameters are detailed in Figure 5-8.

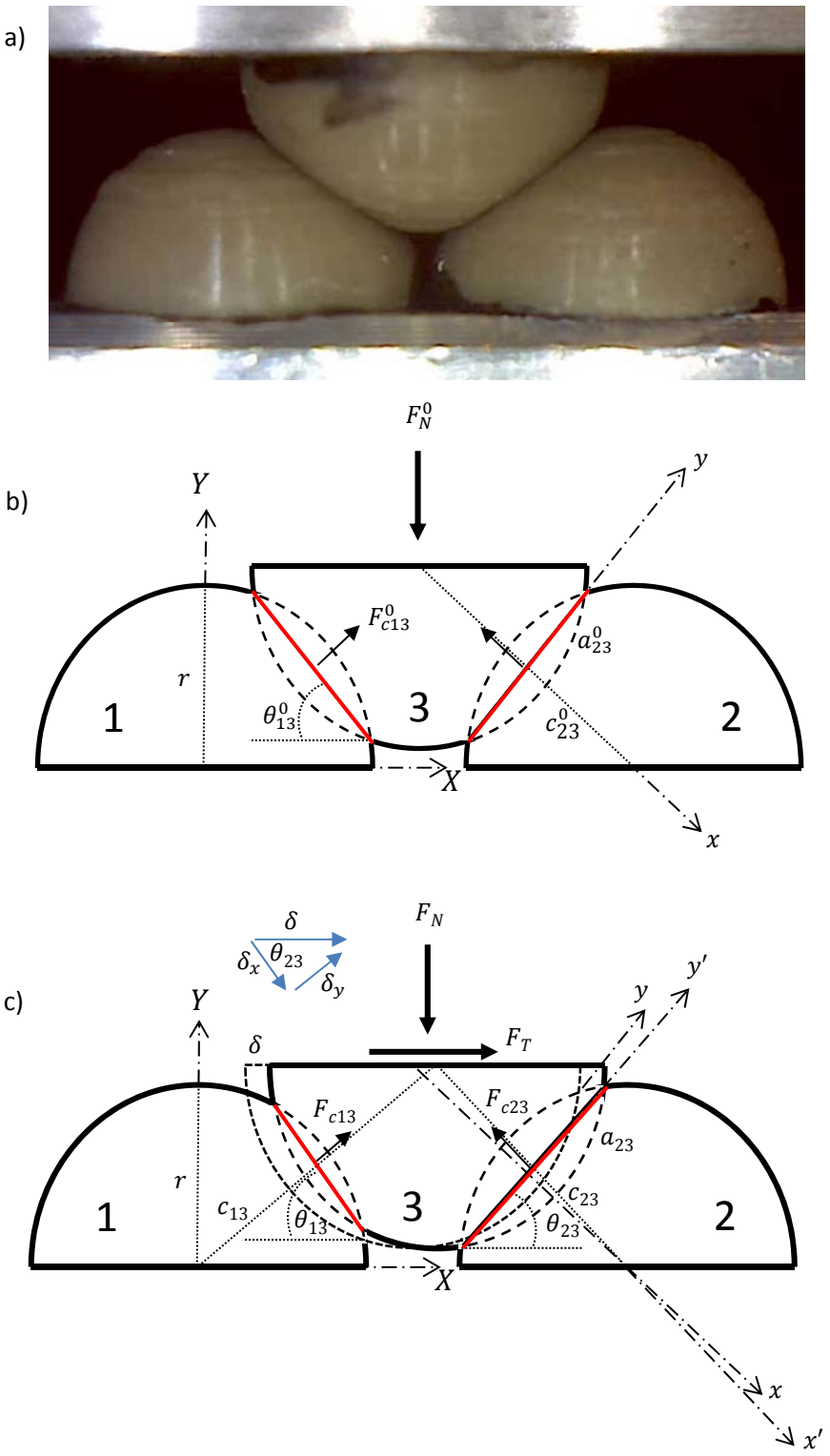

Figure 5-8: a) image of experimental geometry, schematic diagram of the test geometry b) at rest and c) with displacement δ.

5.2.2 Results & Discussion

Tests were done to examine the rate dependency of the hemisphere interactions of the experimental setup. It is seen in Figure 5-9 that there was very little variation

due to angular velocity of the plate actuation implying an approximate rate independence of the interactions at the observed velocities.

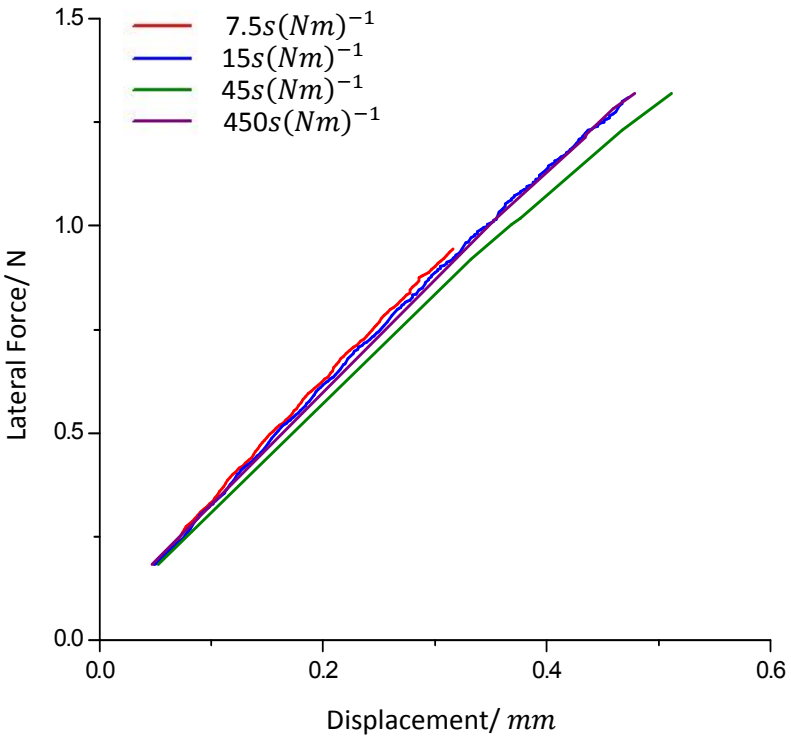

Figure 5-9: Effect of speed of torque application on rheology results.

Slight variation in the results from Figure 5-9 are likely due to small differences in initial conditions. The variation in initial conditions was examined with results shown in Figure 5-10. It was noted that on the initial tests, the hemispheres having been initially brought into contact, the curves of displacement against lateral force display a waver at low displacements which is present independent of an increase in normal force but that develops at increasing displacements.

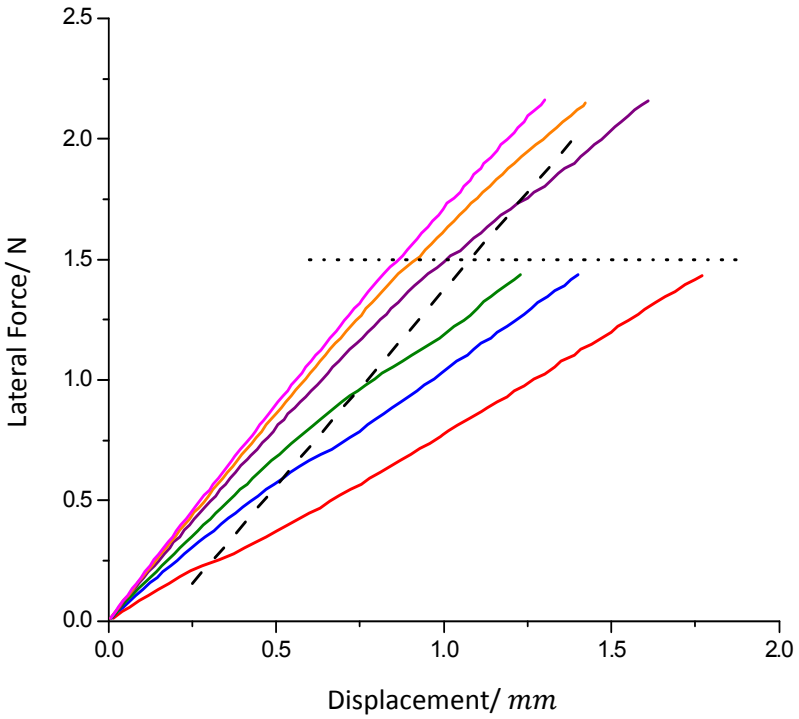

Figure 5-10: A graph showing the first tests for a range of initial normal forces; dashed line- highlighting initial kinks in the curves, dotted line- highlighting a shift in curves at high torque.

This kink disappears in all subsequent tests which are then highly repeatable; showing little variation between them, whilst the first test is prominent in its difference from the rest of the curves. It would seem that in initially bringing the hemispheres together the top hemisphere will contact one before the other and the adhesion between them will mean that the top particle will maintain this initial preferential anti-symmetrical contact position. After being displaced from the first test the hemispheres initial contact with the particles has been broken and thus the top hemisphere resettles into a position of equilibrium between the two bottom hemispheres. A second kink is observed at later displacements which can be seen in those tests allowed to progress to a higher force(torque). These kinks occur at a similar torque level each time and correspond to the initiating of a cooling system activating in the rheometer when high levels of torque are reached. Thus, results from rheometer testing will henceforth be presented as an average of a minimum of five tests after an initial test and will progress up to 4000μNm.

Figure 5-11 shows force-displacement data for three different initial normal forces. As would be expected the lateral shearing force (F_T) increased with increasing

initial normal force (F_N^0). The force-displacement curves were almost linear. However, there was a small initial decrease in gradient, similar to that observed in the rubber stress-strain curves (Suphadon et al. 2009). The standard deviation of the results was derived but it can be seen to be relatively small.

Contact parameters for the contact problem are denoted with subscripts that refer to the contact between hemispheres with the hemisphere numbering system as defined in Figure 5-8. The superscript 0 is used to identify an initial value of a parameter, before displacement has been applied. The contact length (L) and angle (θ), which is defined as the angle between the contact plane and the horizontal, were measured carefully from footage taken of the tests with a digital microscope and are plotted as a function of the deformation (δ) in Figure 5-11 and Figure 5-12 respectively. The curves for contact lengths and angles seem to share similar trends between the different normal forces, offset by the initial contact. The contact angles for θ_{13} are seen to increase with δ within measurement error whereas θ_{23} decreases with δ. Similarly, L_{13} increases whereas L_{23} decreases with δ. This is expected with the increasing contact of hemispheres 2-3 and the decreasing contact of hemispheres 1-3. The scatter in this data was relatively large as it was not always easy to make accurate measurements from the video images however, as anticipated, a broadly monotonic trend was found. Slight discrepancy between initial contact parameters can be seen which indicates that the initial contact was not always exactly at the neutral starting point. It is also interesting to note that, unlike the L^0 values which increase with increased F_N^0 as expected, the values of θ^0 did not show a clear trend with F_N^0. This may in part be due to the difference seen in the θ^0 values at the highest F_N^0. The curves displayed in Figure 5-13 show a similar trend for the change in θ with δ between the different F_N^0. A linear trend was easier to observe for θ_{23} with a greater number of data points but was a reasonable approximation for θ_{13} as well. Furthermore, plotting the slope (C_θ) of these curves against F_N^0 displays a curve that can be found for both hemisphere interactions, as is shown in Figure 5-14. Therefore, the dependence of θ on δ can be approximated from θ^0 which can be approximated as previously discussed from F_N^0:

$$\theta_{13} = \theta^0 + \left(BF_N^{0\beta}\right)\delta \quad 5\text{-}1$$

$$\theta_{23} = \theta^0 - \left(BF_N^{0\beta}\right)\delta \quad 5\text{-}2$$

Where B and β are constants found to be 5.67 and -0.14 (3sf) respectively. This trend is found from data at six different F_N^0 values however Figure 5-11, Figure 5-12, and Figure 5-13 show data for three of these, with a wide range of F_N^0 values, to provide a clearer picture. These three tests are then compared to model results.

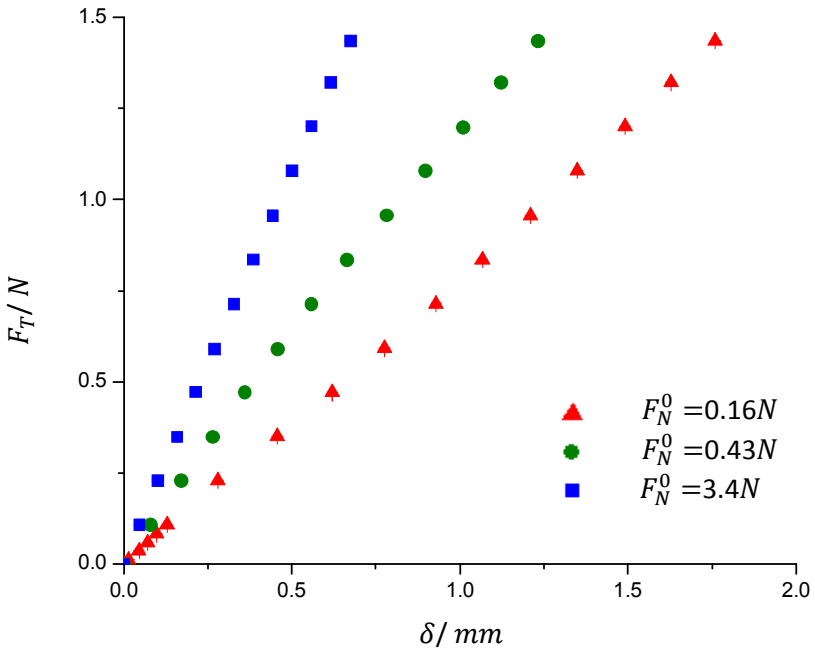

Figure 5-11: Force-displacement curves for three different F_N^0 values.

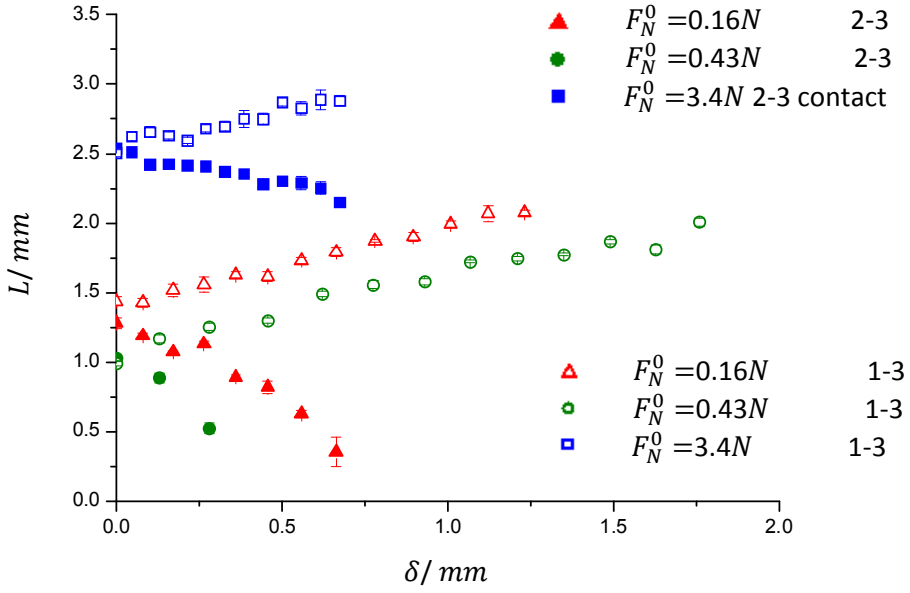

Figure 5-12: Contact length-displacement curves for tests at different F_N^0 values.

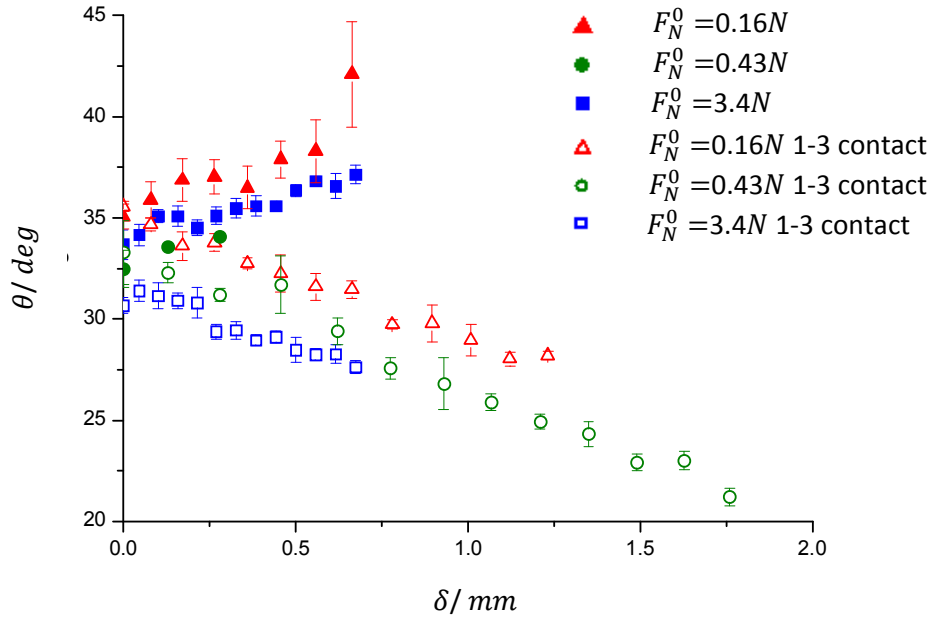

Figure 5-13: Contact angle-displacement curves for tests at different F_N^0 values.

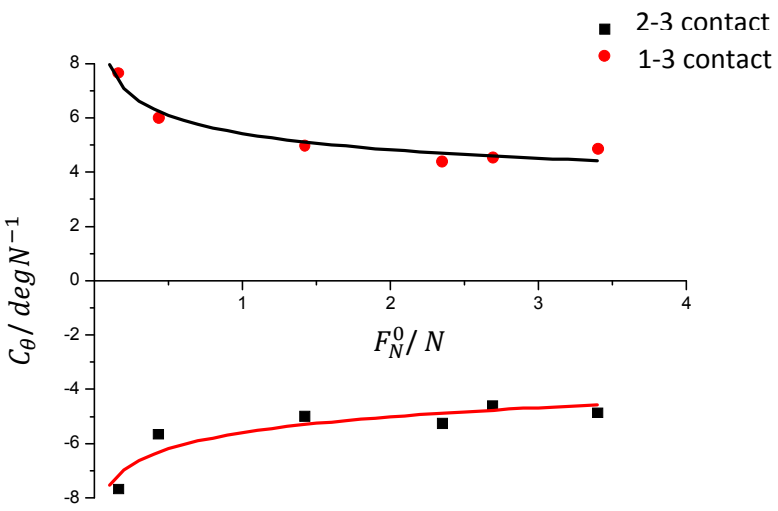

Figure 5-14: The dependence of C_θ to the initial normal force with fit lines.

The force displacement curve up to larger displacements is shown in Figure 5-15. For any given family of tests, it was important not to shear the hemispheres past each other completely as it was very difficult to set up an identical set of initial conditions. A very low initial normal force had to be used to allow the maximum torque to remain within the capabilities of the rheometer. The measured behaviour was continuous and showed no signs of stick-slip, rather a sudden failure corresponding with the plateau in the torque or lateral force. This behaviour, and the video observation of the test, both give an indication of the large amount of shear encountered during the test. The curve displays a lengthy linear region in between two areas of changing gradient. At the highest shear values with a high δ, F_T levels off due to θ_{23} approaching zero which ensures an ever-decreasing contribution of F_{c23} to F_T. Eventually it reaches a point where only the frictional force at the interface is being used to maintain contact. At this point however, the friction will not have much scope to increase as the contact area will have reached or approached to a maximum (Denny 1953). This point of no return could occur sooner or later in terms of applied displacement depending on the strength of the adhesion between the hemispheres.

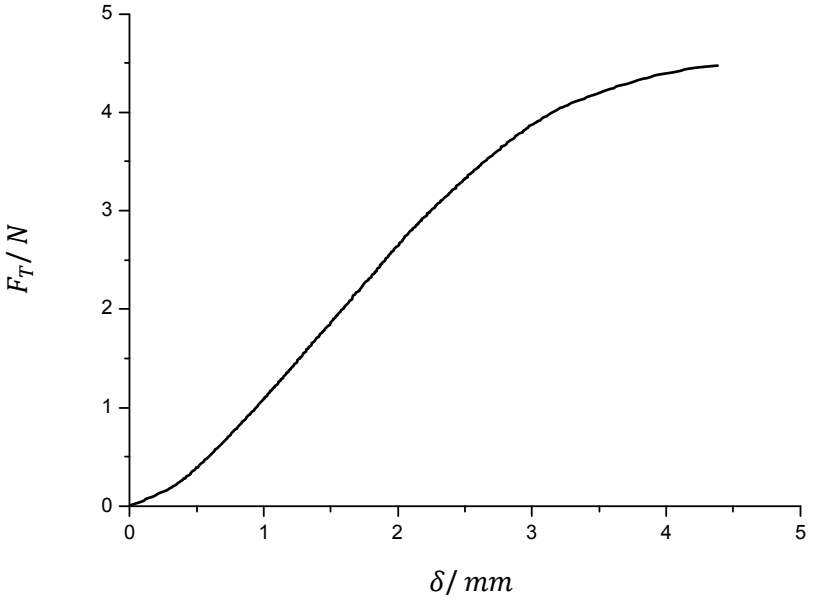

Figure 5-15: Force-displacement curve from early rheometer testing at nominally 0.05N normal force showing the results of having a torque ramp increasing until the hemispheres slip out of contact.

Figure 5-16 shows a repeated test using hemispheres lubricated using talcum powder, which has been applied to their surfaces and which can be compared to a test on the clean hemispheres. The graph shows a large difference between the two cases; the lubricated curve's modulus drops below that of the dry curve above approximately $0.1mm$ displacement. The curve then tends towards a plateau whereas, at a comparable displacement, the clean test curve is still displaying a relatively linear response. The difference between the two behaviours highlights the effect of friction on the inter-particle forces; clearly with minimal interfacial friction the hemispheres are able to slip in contact and thus, despite the interlocking of the particles, the contact points are transitional, with a much-reduced resistance to any applied force.

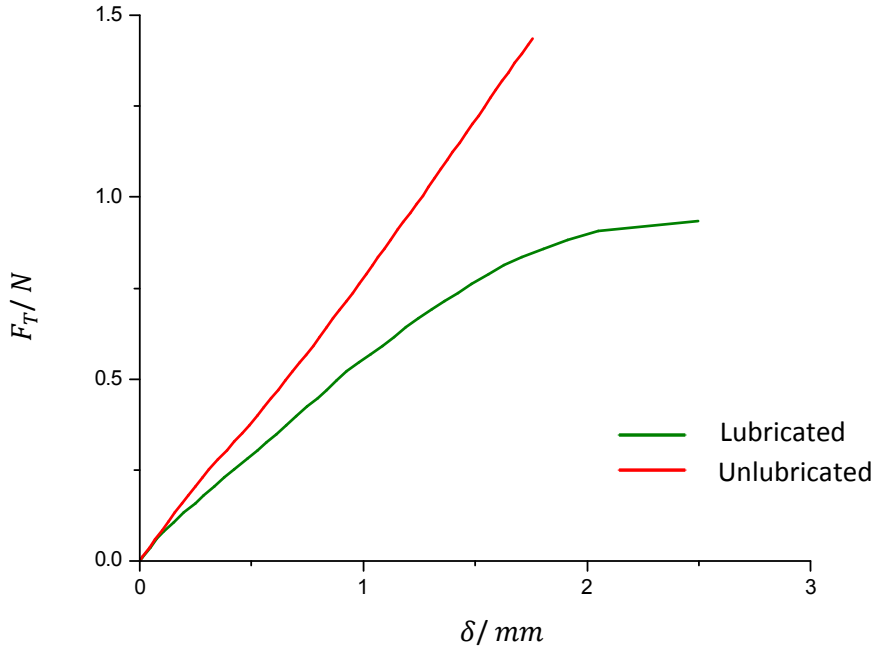

Figure 5-16: Lubricated hemispheres compared to unlubricated at ~0.05N F_N^0; red line- unlubricated, green line- lubricated.

5.2.3 Modelling Inter-Particle Forces

5.2.3.1 Introduction

To model the behaviour observed in the inter-particle force evolution tests measured using the rheometer, a series of analytical approximations that can describe the relative movement of the particles, the deformation of the particles, and the resultant forces was needed. The resulting expressions were encoded using MATLAB to evaluate the effect of specific parameters on the resulting behaviour. The code was designed around the geometric configuration of hemispheres studied with the rheology testing. The aim of this code was primarily to enable prediction of the types of forces experienced by rubber particles in a typical packing. However, the simulation was tailored to match the rheometer testing (with zero dilation and a discontinuous normal force) so that simulation results could be compared directly with the rheometry testing. Then, the simulation was extended to the case with the same geometry but with a constant normal force which allowed the dilation of the particles as would be present within a packing of particles.

Figure 5-8 shows a schematic of the geometry of the hemispheres detailing the parameters used to describe the effect of displacement on the contact between

the hemispheres with the hemisphere numbering system which will be henceforth adopted. It is assumed that the initial contact parameters are equal for both 1-3 and 2-3 contacts so that $F_{c13}^0 = F_{c23}^0,\ a_{13}^0 = a_{23}^0,\ \theta_{13}^0 = \theta_{23}^0,\ c_{13}^0 = c_{23}^0$. When discussing formulas applicable to both contacts the subscripts (13), (23) is dropped to indicate that the parameter for both 1-3 and 2-3 can be found in the same way. The aim was to find the required lateral force F_T to produce a lateral displacement δ. To do this requires insight into how the contact angle between the hemispheres changes with δ.

The contact between the hemispheres can, as a first approximation, be defined using a combination of contact mechanics and geometric considerations. The use of contact mechanics implies the assumption of a small and linear contact area relative to the hemisphere dimensions.

The initial contact between hemispheres depends on the initial interfacial contact force normal to the contact plane (F_c^0):

$$F_c^0 = \left(\frac{F_N^0}{2}\right)\cos\theta^0 \qquad 5\text{-}3$$

Assuming symmetric contacts and zero relaxation of the rubber or other sources of energy loss from the initial normal force, F_{N0}, from geometric considerations. F_N^0 is the initial normal force acting on hemisphere 3 and θ^0 is the initial contact angle, defined with respect to the x axis. It was found that the difference between the Hertzian contact approximation and an approximation that included additional JKR adhesional interactions was minimal with respect to the accuracy of measurement used to measure actual contact lengths in the experiments. This is described in more detail later in this section. However, the minimal difference between the two is partly due to the size of the particles. As the particle size or the normal force decreases then the ratio of the adhesion stress to compressive stress becomes larger (Johnson et al. 1971). The initial contact radius without interfacial adhesive forces (a_H^0) found using Hertzian contact mechanics can be used to find the initial displacement normal to the contact interface for a point far from the contact region (δ_c^0) using equation 2-35 whilst the initial contact radius is found using equation 2-66:

$$a_H^0 = \left(\frac{RF_c^0}{K}\right)^{\frac{1}{3}} \quad 5\text{-}4$$

$$a^0 = \left(\left(\frac{R}{K}\right)\left(F_c^0 + 3\lambda\pi R + (6\lambda\pi R F_c^0 + (3\lambda\pi R)^2)^{\frac{1}{2}}\right)\right)^{\frac{1}{3}} \quad 5\text{-}5$$

Where $K = \frac{2}{3\pi k}$; $k = \frac{(1-\nu^2)}{\pi E}$, ν is the Poisson's ratio and E the Young's modulus of the material and $R = \frac{r}{2}$.

δ_c^0 may be found as:

$$\delta_c^0 = \frac{(a_H^0)^2}{R} \quad 5\text{-}6$$

The centre to centre distance of the hemispheres can be found geometrically from this:

$$c^0 = 2r - \delta_c^0 \quad 5\text{-}7$$

θ^0 for both contacts 1-3 and 2-3 must initially be at 30^0 for a perfectly symmetrical hexagonal packing. However, if the distance between particles 1 and 2 is fixed, θ^0 is dependent on F_N^0. The angle may be found geometrically, assuming no shear of the particles occurs in the initial loading phase, in terms of the particle radius r and the initial centre to centre distance c^0:

$$\theta^0 = \sin^{-1}\left(\frac{r}{c^0}\right) \quad 5\text{-}8$$

An iterative process is used to find the initial parameters from these expressions.

The next step is to calculate geometrically the movement of particle 3 relative to particle 1 and 2. Here we model all particles as 2D hemispheres. We define δ as the horizontal displacement of particle 3 relative to axes parallel and perpendicular with the base of the hemispheres. Another pair of axes, $x - y$, are defined parallel and perpendicular with the contact between particles 2 and 3 as shown in Figure 5-8. δ in the X direction can be split into components δ_x and δ_y, in line with these axes, knowing θ^0.

From the geometry of the particles the post-displacement centre to centre distance (c) can be found geometrically from initial parameters:

$$c_{13} = \frac{c^0 \cos\theta^0}{\sin\left((90-\theta^0)-sin^{-1}\left(\frac{\delta x}{c^0}\right)\right)} \quad 5\text{-}9$$

$$c_{23} = \left(\delta_y^2 + (c^0 - \delta_x)^2\right)^{\frac{1}{2}} \quad 5\text{-}10$$

The indentation (δ_c) of the particles normal to the plane of contact is found from:

$$\delta_c = 2r - c \quad 5\text{-}11$$

The Hertzian contact radius is given by:

$$a_H = \sqrt{\left(\frac{\delta_c}{R}\right)} \quad 5\text{-}12$$

The post-deformation contact angle, θ, is found geometrically:

$$\theta_{13} = \theta^0 + \sin^{-1}\left(\frac{\delta_x}{c^0}\right) \quad 5\text{-}13$$

$$\theta_{23} = \theta^0 - \tan^{-1}\left(\frac{\delta_y}{(c^0-\delta_x)}\right) \quad 5\text{-}14$$

The contact forces are found from the contact radii using contact mechanics. The contact force is split into horizontal and vertical components, F_T and F_N respectively, to give the lateral and normal forces acting on the particles at the given displacement.

$$F_c = \frac{a_H^3 K}{R} \quad 5\text{-}15$$

JKR mechanics are then used iteratively to find F_c with the inclusion of adhesive forces.

$$F_N = F_{c23} cos\theta_{23} + F_{c13}\cos\theta_{13} \quad 5\text{-}16$$

$$F_T = F_{c23} sin\theta_{23} - F_{c13} sin\theta_{13} \quad 5\text{-}17$$

This model provides a basic interaction between particles, with no friction between the particles; the hemispheres deforming in compression with zero shear. This model is henceforth referred to as Model 1. The model was constructed in MATLAB so that parameters could be solved for iteratively.

The shear of the hemispheres was expected to be substantial due to the high level of friction between the hemispheres, ignored in the above consideration. The model is augmented to include shear effects in the discussion section.

5.2.3.2 Results and Discussion

5.2.3.2.1 Model 1

Figure 5-17 shows the experimental data gathered compared to the result from the No Shear model. The modelled lateral force is seen to decrease in gradient to a plateau at $\delta \cong 1.25mm$. This decrease is due to the decrease in the contact angle with displacement which decreases the component of the contact force acting in the horizontal direction. When compared to the lateral force minus a shearing force, approximated from shear observed in optical measurements, the simulation hovers about the same area as this curve. The similarity seen suggests that the difference between the model and test results can be attributed almost entirely to the presence of shear. This shear is of course an expected result of the strong friction between hemispheres. It is seen that the test data parts from the model even at very low displacements despite the reasonable mapping of the contact lengths and angles of the model. The influence of shear in the test therefore begins to occur at low displacements. An approximate shearing force (F_S) was calculated from deformation measured from digital microscope images. The deformation (Δ_h) was measured as the change in distance from hemisphere 3's peak to its edge, and F_S was found by taking the stress to be acting over an area equal to the hemisphere cross-section. In this way the contribution to F_T of shearing was approximated and a lateral force without shearing contribution (F_T^*) could be given as:

$$F_T^* = F_T - F_S$$

$$F_S = \left(\frac{\Delta_h}{r}\right) G \left(\frac{r^2\pi}{2}\right) \quad 5\text{-}18$$

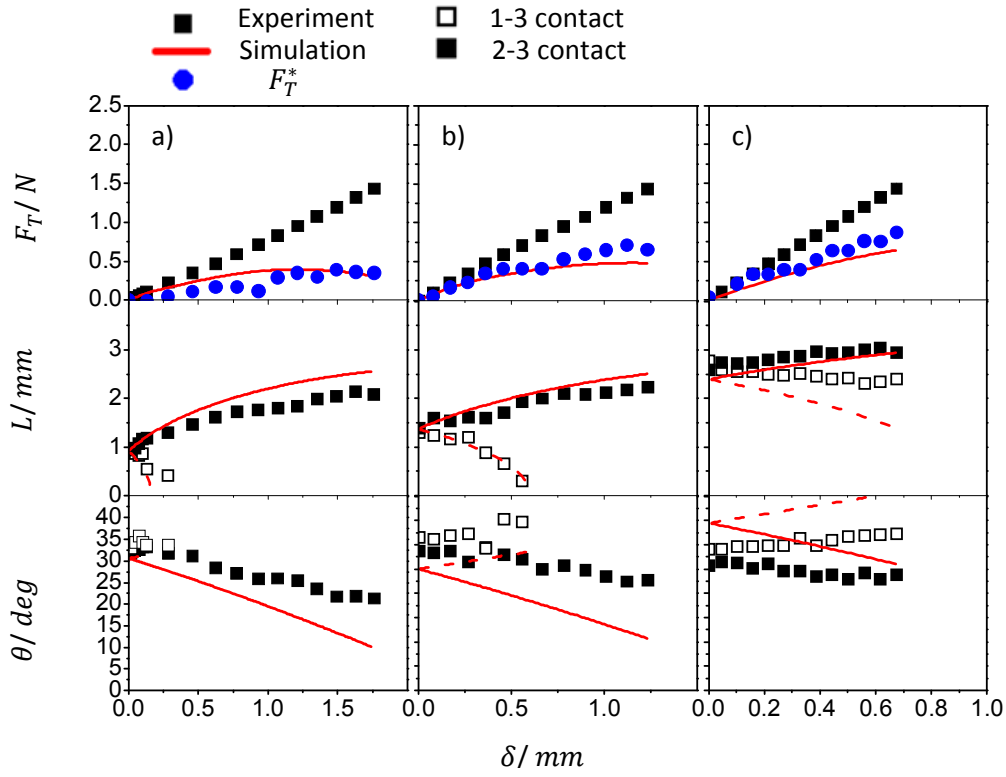

Figure 5-17: Comparison of experimental results with Model 1 for a) $F_N^0 = 0.16N$, b) $F_N^0 = 0.43N$, c) $F_N^0 = 3.4N$.

Contact lengths are in good agreement especially for the higher initial loading, although the initial contact is not as well matched at the highest loading. The trend of the contact angles given by the model is very similar to the test data, however, initial contact angle is not well predicted. The θ^0 predicted is lower for $F_N^0 = 0.16$ and $0.43N$ and for the highest loading θ^0 is overestimated. This discrepancy may be due to a small amount of shear that is also incurred from the initial bringing of the hemispheres together although the shearing of the hemispheres, not considered in the modelling, ought to increase θ^0 contrary to what is observed in the results. The initial angle of contact can be approximately considered to be constant, contrary to expectation, at a value of about $34°$C irrespective of the initial normal force. The closer fit of the model to the highest loading suggests that, as may be expected, the shearing that had occurred at that initial normal force is much lower than at the lower loading tests.

5.2.3.2.2 Model 2

Walton's contact method for oblique contact is used within the model to give the tangential traction (Q) at the interface:

$$Q = \frac{8R^{\frac{1}{2}}}{3\pi(2B+C)} u w^{\frac{1}{2}} \quad \text{5-19}$$

Where $B \cong C \cong \frac{1}{4\pi G}$ for incompressible materials (Walton 1978), a good assumption for rubber. The displacements normal and tangent to the contact plane, w and u respectively, are defined as:

$$w_{13} = \delta_{c13}$$

$$w_{23} = \delta_{c23}$$

$$u_{13} = 0$$

$$u_{23} = \delta_y \quad \text{5-20}$$

Where u and w are the lateral and vertical displacements respectively of a point away from the contact. It is assumed that there are no lateral tractions present due to the initial loading of the hemispheres and that there is no traction from the reducing 1-3 contact. The normal stress distribution is modelled in the same manner with Hertzian normal contact. The lateral force is defined by:

$$F_T = F_{c23} sin\theta_{23} - F_{c13} sin\theta_{13} + Q_{23} cos\theta_{23} - Q_{13} cos\theta_{13} \quad \text{5-21}$$

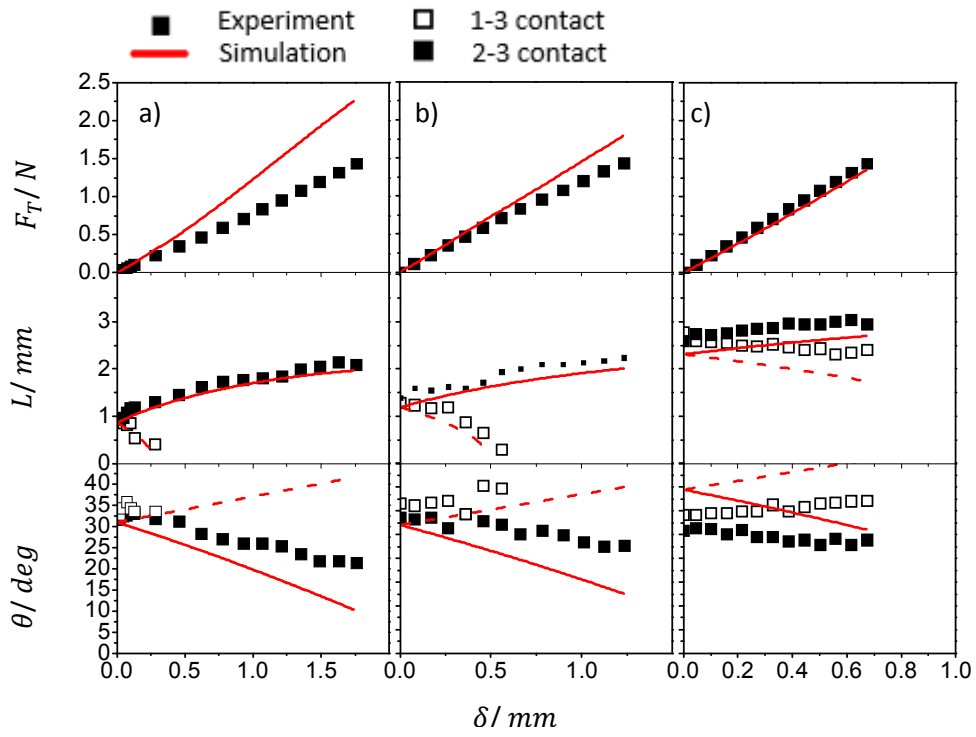

Figure 5-18: Comparison of experimental results with Model 2 a) $F_N^0 = 0.16N$, b) $F_N^0 = 0.43N$, c) $F_N^0 = 3.4N$.

The model using Walton oblique contact mechanics is shown compared to experimental data in Figure 5-18. The predicted F_T is much closer to the experimental data than when Model 1 is employed, especially for the highest initial normal force. Again, contact length is predicted quite well, there should be little difference between the two models in this aspect due to both employing Hertzian pressure. θ from the model is found in the same was as model 1. The method of determining the initial angle was kept the same although a constant θ^0 value was also tried with little difference in the resulting F_T calculated by the model. The model gives a better prediction of F_T with increasing F_N^0, however, it deviates from experimental data with increasing δ for the lowest F_N^0. Whilst there is good agreement at a high initial normal load it seems that the high amounts of shear seen at lower levels of loading prove difficult to map. The discrepancy may be because the contact mechanics are appropriate for, and indeed rely on the assumption of, stresses contained to a region close to the contact. This assumption will be less and less accurate for lower loadings where shear is present throughout the hemispheres. The normal or Hertzian pressure still predicts contact size reasonably well and this may be due to a higher compressive modulus compared to shear modulus meaning the compressive deformation is contained closer to the

contact region. It is also pertinent to note the increasing rotation of the contact plane at lower F_N^0 , which is considered to have negligible effect on the displacements (Walton 1978).

5.2.3.2.3 Model 3

To take into account the influence on F_T of the shearing of the hemispheres an estimation of the shear is used in conjunction with the purely geometric consideration of Model 1 to produce Model 3. A shearing force (F_e) is taken as proportional to this shear. A model was constructed that calculated the shearing deformation of hemispheres 2 and 3 based on the magnitude of δ. The shearing is characterized by a shearing angle (θ_e) which is a measure of the level of shear deformation of the hemispheres. This is taken as the difference in the change in contact angle ($\Delta\theta$) between the normal to the contact plane before and after deformation with and without shearing; visualised in Figure 5-19. If the interface is defined with zero slip, the shearing of the hemispheres will introduce an additional change to the angle of the contact plane. With a no-slip condition at the interface, the distance between two points at the interface (λ_f) remains fixed; the strain in the hemisphere is assumed to be concentrated towards the edge of the contact. The extension (λ_e) is proportional to the displacement and the strain in this region is approximately equal to λ_e over c.

$$\lambda_e \approx \delta \qquad 5\text{-}22$$

$$\varepsilon \approx \frac{\lambda_e}{c} \qquad 5\text{-}23$$

This gives a method for approximating the shear taking place. The strain can also be approximated by the tangent of θ_e.

$$\varepsilon = 2tan\theta_e \qquad 5\text{-}24$$

The fit to experimental data of θ (equation 5-2) can be used to give θ_{23} and the difference between this angle and the angle where the interface is allowed to slip (θ_s) (such as that found using Model 1) can be used to give θ_e. Shear for model 3 is found from equation 5-24 using the fit to data.

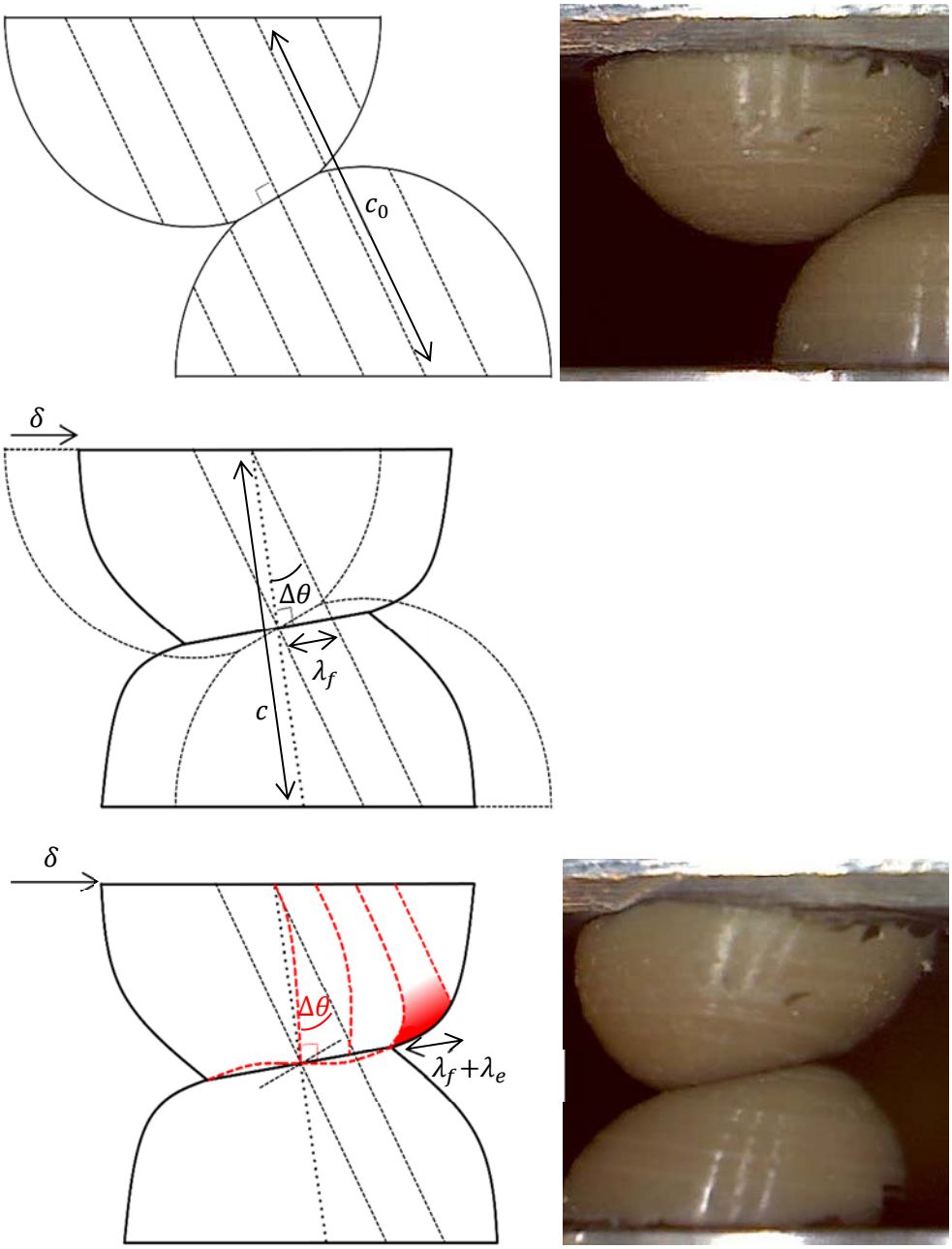

Figure 5-19: Diagram of shear deformation of hemispheres.

A shearing force is calculated from the approximated shear strain. It was seen to give good correlation with experimental results assuming the area over which the shear stress is taken as the 2D un-deformed cross section of the hemispheres. The factor of two is due to there being two hemispheres in shear.

The shear force, F_e, is thus:

$$F_e = \varepsilon G \left(\frac{\pi r^2}{2}\right) \quad 5\text{-}25$$

Where $G \approx \frac{E}{3}$, is the shear modulus (Roberts 1990).

The position of the contact is amended to take into account the shearing of the hemispheres in an iterative process. The reaction forces at the contacts, F_{c23} and F_{c13} are found as before from the contact lengths (equation 5-15). Thus, the total F_T is considered to be the summation of the effects of the shear force and the compression force.

$$F_T = F_{c23} \sin\theta_{23} - F_{c13} sin\theta_{13} + F_e \quad 5\text{-}26$$

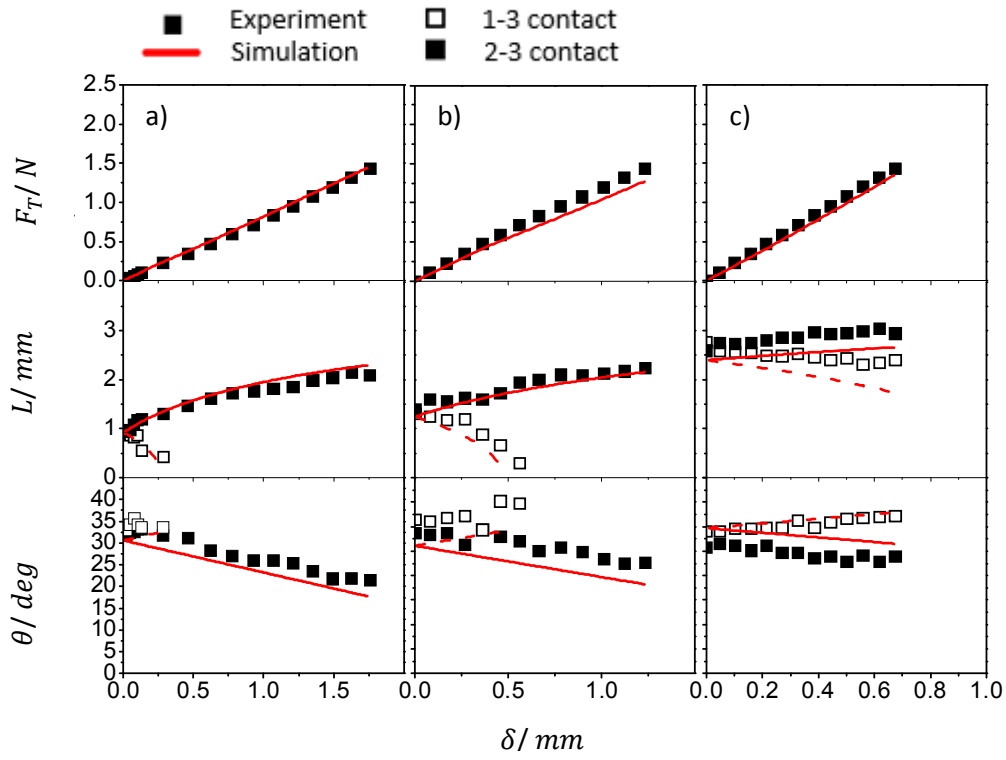

Figure 5-20: Comparison of experimental results with Model 3 a) $F_N^0 = 0.16N$, b) $F_N^0 = 0.43N$, c) $F_N^0 = 3.4N$.

Figure 5-20, comparing the Model 3 output to experimental data, shows a good fit to the data. The contact lengths fit in a similar fashion to the previous models, with the same undercutting of the highest loading and the 1-3 contact for 0.43N initial load. The contact angle slightly undercuts the test data for all but the 3.4N initial normal force, which overpredicts for the 2-3 angle slightly. The degree to which the model matches the experimental data, especially at the lowest loading, seems to

suggest that the approximation for the shearing of the hemispheres is acceptable. The measurements of the contact parameters may involve quite large error due to the measurement method. A high level of human error is possible. Measurements are also dependent on the angle of observation which is not constant during testing due to the actuation of the plates. Discrepancy between results and models may also be caused in part by the inhomogeneity between initial contacts. It would appear that an unaccounted facet of either the initial bringing together of the hemispheres or the test cycle causes θ^0 to be approximately independent of F_N^0 , causing θ^0 to be overestimated. This may affect the accuracy of the model. The model is compared to a few more results at different F_N^0 values in Figure 5-21. The model predicts all of these quite well and the greatest disparity occurs for $F_N^0 = 0.34N$. Occurring as it does in the centre of the F_N^0 range it is likely that this data set suffered from a larger degree of human error than the rest, most probably in the determination of the magnitude of the initial normal force.

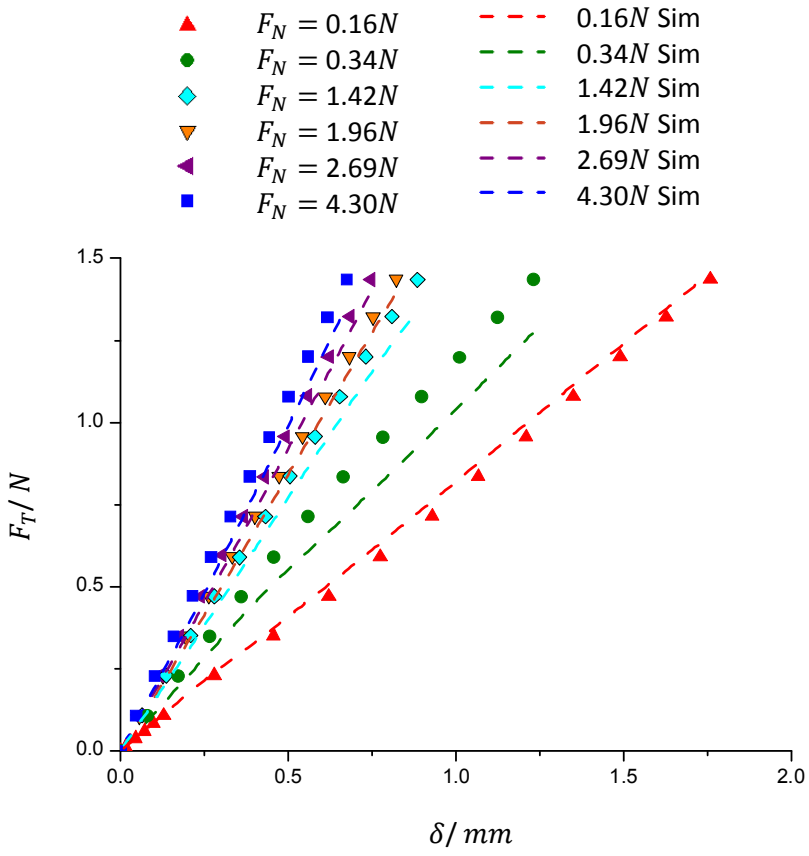

Figure 5-21: Comparison of F_T for multiple F_N^0 to model 3 simulations.

5.2.4 Conclusion

The evolution of contact interactions between rubber hemispheres in a three-hemisphere geometry was investigated to provide insight into the individual interactions within a jammed system of deformable frictional particles under deformation. The novel approach taken showed that the relatively large friction between the surfaces induced shear deformation of the hemispheres. The deformation of the spheres strongly affects the contact forces. This effect is more pronounced at lower F_N^0 due to the larger displacements reached for the same magnitude of F_T with respect to higher initial loadings. The strain is large and occurs throughout the hemispheres at lower initial loading. Work on the mechanics of oblique contact by Walton (1978) fails to give a good fit to the experimental data for low F_N^0. This discrepancy may be due to the elastic half plane assumption failing to approximate well the tangential traction as the relatively low modulus of the rubber leads to large deformations with respect to contact size, especially at low F_N. The large deformations also lead to significant rotation of the contact plane which is assumed negligible in the Walton contact mechanics. The model using Walton contact theory may be successfully put to use when the ratio of displacement to contact size in low such as cases with high F_N^0 or modulus. A novel method to model the interactions is developed by approximating the amount of shear the hemispheres undergo due to the lateral displacement with a shearing angle; good agreement is seen with the experimental results. This approach could be extended to model the behaviour of a packing of soft frictional particles. The model can be altered to better represent the conditions of particles within a packing by setting F_N as a constant and solving for a vertical displacement component instead.

6 Conclusions and Future Work

The work presented in this thesis has examined adhesive interactions involving rubber important for engineering components and soft robotics and contributed novel experimental methods, results, and models.

The characteristic behaviour governing the adhesive friction interaction for a rough rubber surface against a smooth rigid surface was investigated. Little work on such an interaction is currently available in literature and the case could be of interest for applications where it is desirable to control the level of friction or where such an interaction is occurring. A novel theoretically derived constitutive expression for the frictional shear stress of sliding dependent on sliding velocity, asperity geometry, and material dependent peeling parameters is constructed in terms of a peel behaviour based on a fracture mechanics approach. This theory correctly predicts the velocity dependence of the frictional shear stress for a rough rubber against a rigid smooth surface and it is seen that this velocity dependence originates directly from the viscoelastic properties of the rubber. Good agreement to experimental results is found when the geometry of the asperities is adequately approximated. A method for approximating the effect of asperity geometry on the strain energy function required to calculate peeling energy has been developed using a finite element analysis approach; it is important to adequately model asperity geometry to correctly calculate friction. Results strongly support the basis of the theory of a peel behaviour as the dominant mechanism in sliding of rough rubber surfaces over smooth rigid surfaces.

The behaviour of jammed macroscopic rubber particles was examined using a monolayer packing structure. It was found that in response to externally applied loads the packing would exhibit relatively linear response with no yielding in the deformation range studied. The packing response was found to be very consistent in comparison to packings of particles with much greater stiffness, attributed to the resistance of the packing to particle rearrangement and slippage. The rearrangement of particles is inhibited by a geometric interlocking of the particles provided by the deformation of the particles; this ensures a relatively constant packing modulus at moderate strains. The friction between particles prevents slip which affects particle arrangement primarily with a change in direction of applied load. A novel finding is these independent roles the inter-particle interlocking and

inter-particle friction have on the response to applied load. These facets contribute to give rubber packings the properties of a continuous material. It is concluded that rubber particles would be a good candidate for soft robotic applications. Inter-particle forces were studied using a novel approach that isolated the interactions between three particles approximating packing interactions. Experimental results were modelled using a MATLAB simulation which highlighted that a high level of shearing in the spheres contributed to the lateral shearing force. Conventional contact mechanics were found unable to adequately map this force at low initial normal loads as high levels of particle shearing occurred. A novel model was developed that provides good agreement with experimental data by approximating the shearing of the particles from a difference in angle of incidence to the contact plane for zero shear displacement to that when the shearing of particles occurs.

Improvement in the experimental techniques can be implemented to improve the accuracy of friction measurements; temperature, humidity, and dust are all important influences on friction measurements, so a big improvement could be enacted by conducting experiments in a well environmentally controlled space. The monolayer packing experiments could be improved in terms of observing purely the packing response due to particles by minimising friction to holding apparatus and the influence of the flexible membrane. If this was achievable, tests could be conducted to greater strains in order to evaluate the levels of stress and strain required to reach a yield stress for such packings without incurring large strains in the membrane. The rheometry tests could be improved by using a rheometer that allowed for vertical dilation to better approximate packing conditions of particles as well as one that could be used to obtain higher levels of torque. The model should be developed to more accurately approximate the shear strain and extend it to higher deformations.

The work conducted in this thesis highlights many interesting and useful mechanisms of rubber adhesive interactions and paves the way for interesting studies to look at the phenomena more extensively, apply similar ideas in different contexts, and uncover the mechanics of related interactions. A continuation on the work presented herein could study the theory developed for rough rubber friction in assessing less controlled surface geometries, with the eventual goal to be capable of adapting the theory to model any realistic engineering surface of a

rubber surface. It was seen that surface roughness of the counter-surface strongly affected results, as would be expected; the exact manner of the effect of the level of roughness of the counter-surface could be examined. A peeling effect can still be present on rough surfaces the mechanism of which is likely altered by geometry of the rough surface; peeling propagation would be altered as well as degree of contact, so the mechanism involved will likely change with roughness and may even be present when other friction contributions become more dominant. The theoretical analysis could also potentially be expanded to encompass a wider range of sliding velocities. Currently, the rough rubber-smooth rigid surface friction theory works within a specific section of the relaxation spectrum so that if peeling frequencies depart from a specific range the theory would no longer hold. This becomes important for rubbers with high T_g which may have rapidly changing viscoelastic properties at peeling velocities or filled rubbers which have less distinct relaxation curves. Furthermore, the theoretical basis of the model, that of evaluating the strain energy of deformation of a specific surface geometry to evaluate a peeling mechanism could be extended and adopted to other friction problems with such characteristics such as analysing adhesive friction contribution to smooth rubber on rough surfaces. The asperity interaction modelling could be improved by increasing the complexity of the model to give improved representation of not just the asperity but the bulk of a sample as well so that the asperity top would not simply be a rigid boundary condition. Such improvement may enable better accuracy of the evaluation of the dependence of asperity contact geometry on peeling energy. A theoretical approximation to the modelling of the peeling energy dependence on asperity contact geometry would remove the need for modelling in order to apply the asperity peel theory to different geometry types entirely. This may be difficult to apply to a wide range of geometries to any degree of accuracy however. Monolayer experiments could be conducted with packings of more values of particle modulus in order to examine the range of packing behaviour and the cross-over in behaviour from a continuous-like packing to fragile matter-like behaviour. Experiments using different shaped particles could be conducted to view in more detail the effects of the interlocking of particles and the relationship between that and the inter-particle friction; some particles may be able to geometrically avoid structural change and slippage from changes to applied forces and it would be interesting to see if the role of friction is significant regardless.

Development of an experimental setup that would remove the need of a fully enveloping flexible membrane would remove the influence on the packing of the flexible membrane, isolating the response of the particles; this could be done by using a vertical setup with a ribbon to constrain cylindrical particles if significant friction with constraining boundaries can be avoided. Rheometry experiments could be extended to a system with more particles and particle interaction being tested although this would require a high level of precision to ensure initial interactions are uniform and a strong rheometer, capable of achieving high levels of torque, may be necessary to achieve high displacements. Tests to higher displacements would enable observation of behaviour over a wider range of displacements. The behaviour on the approach to a maximum in lateral force may be interesting to observe, particularly when considering different levels of frictional interaction between particles. Future work could also concern itself with the time dependence of adhesion, an interesting phenomenon which could be a significant factor at very low sliding velocities and for static friction. One approach might be based on a statistical model of Brownian motion of rubber surface molecules and give a probability function for Van der Waals type bonds developing over a contact area with time.

Bibliography

Adams, G.G. & Nosonovsky, M., 2000. Contact modeling - forces. *Tribology International*, 33(5), pp.431–442.

Aleshin, V. & Van Den Abeele, K., 2009. Preisach analysis of the Hertz-Mindlin system. *Journal of the Mechanics and Physics of Solids*, 57(4), pp.657–672.

Amontons, G., 1699. Mémoires de l'Acadèmie Royale. *Histoire de l'Academie Royale des Sciences avec les Memoires de Mathematique et de Physique*, 206, pp.1706–1709.

Andreotti, B., Forterre, Y. & Pouliquen, O., 2013. *Granular Media*, Cambridge: Cambridge University Press.

Andrews, E.H. & Kinloch, A.J., 1973. Mechanics of Adhesive Failure. II. *Proceedings of the Royal Society A: Mathematical, Physical and Engineering Sciences*, 332, pp.401–414.

Arnold, S.P., Roberts, A.D. & Taylor, A.D., 1987. Rubber Friction Dependence on Roughness and Surface Energy. *Journal of Natural Rubber Research*, 2(1), pp.1–14.

Barquins, M., 1988. Adherence and Rolling Kinetics of a Rigid Cylinder in Contact with a Natural Rubber Surface. *The Journal of Adhesion*, 26(June), pp.1–12.

Bateman, L., 1963. *The Chemistry and Physics of Rubber-like Substances* L. Bateman, ed., London.

Best, B., Meijers, P. & Savkoor, A.R., 1981. The formation of schallamach waves. , 65, pp.385–396.

Boast, D. & Coveney, V.A., 1999. *Finite Element Analysis of Elastomers* D. Boast & V. A. Coveney, eds., Bury St-Edmunds: Professional Engineering Publishing Limited.

Boussinesq, M.J., 1885. *Applications des Potentiels à l'Étude de l'Équilibre et du Mouvement des Solides Élastiques* G. Villars, ed., Paris: Gauthier-Villars.

Briggs, G.A.D. & Briscoe, B.J., 1977. The effect of surface topography on the adhesion of elastic solids. *Journal of Physics D: Applied Physics*, 10, pp.2453–

2466.

Brown, E. et al., 2010. Universal robotic gripper based on the jamming of granular material. *Proceedings of the National Academy of Sciences*, 107(44), pp.18809–18814.

Bui, Q. V. & Ponthot, J.P., 2002. Estimation of rubber sliding friction from asperity interaction modeling. *Wear*, 252(1–2), pp.150–160.

Busfield, J.J.C., Thomas, a. G. & Gabriel, P., 2010. Influence of interface geometry on rubber friction. *Wear*, 268(5–6), pp.747–750.

Cattaneo, C., 1939. Sul Contatto di Due Corpi Elastici: Distribuzione Locale Degli Sforzi. , pp.342–356.

Cerruti, V., 1882. *Ricerche Intorno all'Equilibrio de'Corpi Elastici Isotropi: Memoria*, Rome: Salviucci.

Chaudhury, M.K. et al., 1996. Adhesive contact of cylindrical lens and a flat sheet. *Journal of Applied Physics*, 80(1), pp.30–37.

Cheng, N.G. et al., 2010. Manipulator Enabled by Jamming of Granular Media. *Proceedings of 2012 IEEE International Conference on Robotics and Automation (ICRA)*.

Denkov, N.D. et al., 2009. Jamming in Sheared Foams and Emulsions, Explained by Critical Instability of the Films between Neighboring Bubbles and Drops. *Physical Review Letters*, 103(11), pp.1–4.

Denny, D.F., 1953. The Influence of Load and Surface Roughness on the Friction of Rubber-Like Materials. *Proceedings of the Physical Society. Section B*, 66, pp.721–727.

Derjaguin, B. V, Muller, V.M. & Toporov, Y.P., 1975. Effect of Contact Deformations on the Adhesion of Particles. , pp.131–143.

Drelich, J., 2013. Guidelines to measurements of reproducible contact angles using a sessile-drop technique. *Surface Innovations*, 1(4), pp.248–254.

Dupre, M.A., 1869. *Theorie Mechanique de la Chaleur*, Paris: Gauthier-Villars.

El-Saftawy, A., 2013. *Regulating the Performance Parameters of Accelerated Particles*. Zagazig University.

Elata, D., 1996. On the oblique compression of two elastic spheres. *Journal of Applied Mechanics*, 63(3), pp.1039–1041.

Engelbach, R., 1923. *The Problem of the Obelisks*,

Etsion, I., 2010. Revisiting the Cattaneo–Mindlin Concept of Interfacial Slip in Tangentially Loaded Compliant Bodies. *Journal of Tribology*, 132(2), p.20801.

Evesque, P., 2000. The jamming surface of granular matter Determined from soil mechanics results. *Poudres & Grains*, 11(4), pp.58–59.

Ferry, J.D., Grandine, L.D. & Fitzgerald, E.R., 1953. The relaxation distribution function of polyisobutylene in the transition from rubber-like to glass-like behavior. *Journal of Applied Physics*, 24(7), pp.911–916.

Flory, P.J., 1944. Network structure and the elastic properties of vulcanized rubber. *Chemical Reviews*, 35(1), pp.51–75.

Fowkes, F.M., 1964a. Attractive Forces At Interfaces. *Industrial & Engineering Chemistry*, 56(12), pp.40–52.

Fowkes, F.M., 1964b. Attractive Forces At Interfaces. *Industrial & Engineering Chemistry*, 56(12), pp.40–52.

Fuller, K.N.G. & Roberts, A.D., 1981. Rubber rolling on rough surfaces. *Journal of Physics D: Applied Physics*, 14(2), p.221.

Fuller, K.N.G. & Tabor, F.R.S., 1975. The Effect of Surface Roughness on the Adhesion of Elastic Solids. *Proceedings of the Royal Society of London A: Mathematical, Physical and Engineering Sciences*, 345(1642), pp.327–342.

Le Gal, A., Yang, X. & Klüppel, M., 2005. Evaluation of sliding friction and contact mechanics of elastomers based on dynamic-mechanical analysis. *Journal of Chemical Physics*, 123(1).

Gao, J. et al., 2004. Frictional Forces and Amontons ' Law : From the Molecular to the Macroscopic Scale. *Journal of Physcial Chemistry B*, 106(11), pp.3410–3425.

Greensmith, H.W. & Thomas, a. G., 1956. Rupture of Rubber. III. Determination of Tear Properties. *Rubber Chemistry and Technology*, 29(2), pp.372–381.

Greenwood, J.A., Minshall, H. & Tabor, D., 1961. Hysteresis Losses in Rolling and Sliding Friction. *Proceedings of the Royal Society of London A: Mathematical, Physical and Engineering Sciences*, 259(1299), pp.480–507.

Grosch, K.A., 1963. The Relation between the Friction and Visco-Elastic Properties of Rubber. *Proceedings of the Royal Society A: Mathematical, Physical and Engineering Sciences*, 274(1356), pp.21–39.

Grosch, K.A. & Schallamach, A., 1966. Relation Between Abrasion and Strength of Rubber. *Rubber Chemistry and Technology*, 39(2), pp.287–305.

Heinrich, G. & Klüppel, M., 2008. Rubber friction, tread deformation and tire traction. *Wear*, 265(7–8), pp.1052–1060.

Hertz, H., 1882. Über die Berührung Fester Elastischer Körper. *Journal fur die Reine und Angewandte Mathematik*, 1882(92), pp.156–171.

Höhler, R. & Cohen-Addad, S., 2005. Rheology of liquid foam. *Journal of Physics: Condensed Matter*, 17(41), pp.R1041–R1069.

Huijben, F., Herwijnen, F.V.A.N. & Nijsse, R., 2009. Vacuumatics 3D-Formwork Systems: Customised Free-Form Solidification. *International Conference on Textile Composites and Inflatable Structures*, (figure 1), pp.1–4.

Isaksson, P. & Stahle, P., 2002. Prediction of shear crack growth direction under compressive loading and plane strain conditions. *International Journal of Fracture*, 113(2), pp.175–194.

Jayasinghe, P., 2002. Bulletin oftlie Rubber Research Institute of Sri Lcrnkcu (2002) 44,12-13. , pp.12–13.

Jiang, A. et al., 2012. Design of a Variable Stiffness Flexible Manipulator with Composite Granular Jamming and Membrane Coupling. , pp.2922–2927.

Jiang, A. et al., 2014. Robotic Granular Jamming: Does the Membrane Matter? *Soft Robotics*, 1, p.140623112217004.

Johnson, K.L., 1985. *Contact Mechanics*, Cambridge: Cambridge University Press.

Johnson, K.L., 1982. One Hundred Years of Hertz Contact. *Proceedings of the Institution of Mechanical Engineers*, 196(1), pp.363–378.

Johnson, K.L., Kendall, K. & Roberts, A.D., 1971. Surface Energy and Contact of Elastic Solids.

Kaliske, M. & Heinrich, G., 1999. An Extended Tube-Model for Rubber Elasticity: Statistical-Mechanical Theory and Finite Element Implementation. *Rubber Chemistry and Technology*, 72(4), pp.602–632.

Kendall, K., 1975. Rolling friction and adhesion between smooth solids. *Wear*, 33(2), pp.351–358.

Kendall, K., 1975. Thin-Film Peeling - The Elastic Term. *Journal of Physics D: Applied Physics*, 8, pp.1449–1452.

Klüppel, M., 2009. Evaluation of viscoelastic master curves of filled elastomers and applications to fracture mechanics. *Journal of physics. Condensed matter : an Institute of Physics journal*, 21(3), p.35104.

Klüppel, M. & Heinrich, G., 2000. Rubber Friction on Self-Affine Road Tracks. *Rubber Chemistry and Technology*, 73(4), pp.578–606.

Kraynik, A.M., 1988. Foam Flows. *Annual Review of Fluis Mechanics*, 20, pp.325–327.

Kraynik, A.M. & Hansen, M.G., 1987. Foam rheology: a model of viscous phenomena. *Journal of Rheology*, 31(2), pp.175–205.

Kuhn, W., 1934. Über die Gestalt fadenförmiger Moleküle in Lösungen. *Kolloid-Zeitschrift*, 68(1), pp.2–15.

Lake, G., 1995. Fatigue and Fracture of Elastomers. *Rubber Chemistry and Technology*, 68, pp.435–460.

Lechenault, F. et al., 2007. Critical scaling and heterogeneous superdiffusion across the jamming/rigidity transition of a granular glass. , 46003, p.4.

Lee, L.H., 1999. *Fundamentals of Adhesion and Interface* L. P. DeMejo, D. S. Rimai, & L. H. Sharpe, eds., Amsterdam: Gordon and Breach Science Publishers.

Lespiat, R., Cohen-Addad, S. & Höhler, R., 2011. Jamming and flow of random-close-packed spherical bubbles: An analogy with granular materials. *Physical Review Letters*, 106(14), pp.1–4.

Liu, A.J. & Nagel, S.R., 1998. Nonlinear dynamics: Jamming is not just cool any more. *Nature*, 396(6706), pp.21–22.

Loeve, A.J. et al., 2010. Vacuum packed particles as flexible endoscope guides with controllable rigidity. *Granular Matter*, 12(6), pp.543–554.

Lorenz, B. et al., 2013. Rubber friction for tire tread compound on road surfaces. *Journal of physics. Condensed matter : an Institute of Physics journal*, 25(9), p.95007.

Machado, M. et al., 2012. Compliant contact force models in multibody dynamics: Evolution of the Hertz contact theory. *Mechanism and Machine Theory*, 53, pp.99–121.

Maegawa, S. & Nakano, K., 2010. Mechanism of stick-slip associated with Schallamach waves. *Wear*, 268(7–8), pp.924–930.

Majidi, C., 2014. Soft Robotics: A Perspective—Current Trends and Prospects for the Future. *Soft Robotics*, 1(1), pp.5–11.

Marckmann, G. & Verron, E., 2006. Comparison of Hyperelastic Models for Rubber-like Materials. *Rubber Chemistry and Technology*, 79(5), pp.835–858.

Maugis, D., 1992. Adhesion of spheres: The JKR-DMT transition using a dugdale model. *Journal of Colloid And Interface Science*, 150(1), pp.243–269.

McFarlane, J.S. & Tabor, D., 1950. Relation Between Friction and Adhesion. *Proceedings of the Royal Society of London. Series A, Mathematical and Physical Sciences.*, 202(1069), pp.244–253.

Meyer, K.H. & Ferri, C., 1935. The Elasticity of Rubber. *Rubber Chemistry and Technology*, 18(3), pp.570–589.

Milliken, W., Klitgard, B. & Baracat, A., 2009. Hevea Brasiliensis. *Plants of the World Online*.

Mindlin, R.D., 1949. Compliance of Elastic Bodies in Contact. *Journal of Applied*

Mechanics, 16, pp.250–268.

Mooney, M., 1940. A theory of large elastic deformation. *Journal of Applied Physics*, 11(9), pp.582–592.

Muhr, A.H. & Roberts, A.D., 1992. Rubber abrasion and wear. *Wear*, 158(1–2), pp.213–228.

Mukhopadhyay, S. & Peixinho, J., 2011. Packings of deformable spheres. *Physical Review E*, 84(1), pp.2–6.

Ogden, R.W., 1972. Large Deformation Isotropic Elasticity- on the Correlation of Theory and Experiment for Incompressible Rubberlike Solids. *Proceedings of the Royal Society of London A: Mathematical, Physical and Engineering Sciences*, 326, pp.565–584.

Ovcharenko, A., Halperin, G. & Etsion, I., 2008. In situ and real-time optical investigation of junction growth in spherical elastic-plastic contact. *Wear*, 264(11–12), pp.1043–1050.

Owens, D.K. & Wendt, R.C., 1969. Estimation of the Surface Free Energy of Polymers. *Journal of Applied Poilymer Science*, 13, pp.1741–1747.

Paris, P.C., Gomez, M.P. & Anderson, W.E., 1961. A rational analytic theory of fatiuge. *The Trend in Engineering*, 13(4), pp.9–14.

Pernell, C.W. et al., 2000. Measurement of the yield stress of protein foams by vane rheometry. *Journal of Food Science*, 65(1), pp.110–114.

Persson, B.N.J., 2001. Theory of rubber friction and contact mechanics. *The Journal of Chemical Physics*, 115(8), p.3840.

Persson, B.N.J. & Brener, E.A., 2005. Crack propagation in viscoelastic solids. *Physical Review E*, 71(3), p.36123.

Persson, B.N.J. & Volokitin, a I., 2006. Rubber friction on smooth surfaces. *The European physical journal. E, Soft matter*, 21(1), pp.69–80.

Pocius, A. V, 2007. *Physical Properties of Polymers Handbook* J. E. Mark, ed., New York: Springer.

Pollock, H.M., Maugis, D. & Barquins, M., 1978. The force of adhesion between solid surfaces in contact. *Applied Physics Letters*, 33(9), p.798.

Prior, A. & Cadge, D., 1999. *Finite Element Analysis of Elastomers* D. Boast & V. A. Coveney, eds., Bury St-Edmunds: Professional Engineering Publishing Limited.

Rhee, S.K., 1977. Surface energies of silicate glasses calculated from their wettability data. *Journal of Materials Science*, 12(4), pp.823–824.

Rivlin, R.S. & Thomas, a. G., 1953. Rupture of rubber. I. Characteristic energy for tearing. *Journal of Polymer Science*, 10(3), pp.291–318.

Roberts, A.D., 1990. *Natural rubber science and technology*,

Roberts, A.D., 1988. *Natural Rubber Science and Technology*,

Roberts, A.D. & Thomas, A.G., 1975. The adhesion and friction of smooth rubber surfaces. *Wear*, 33(1), pp.45–64.

Rulison, C., 1999. So you want to measure surface energy. *Kruss USA*, 49(40). Available at: http://scholar.google.com/scholar?hl=en&btnG=Search&q=intitle:So+You+Want+to+Measure+Surface+Energy+?#0.

Savkoor, A.R. & Briggs, G.A.D., 1977. The Effect of Tangential Force on the Contact of Elastic Solids in Adhesion. *Proceedings of the Royal Society of London. Series A, Mathematical and Physical Sciences.*, 356, pp.103–114.

Scaraggi, M. & Persson, B.N.J., 2015. Friction and universal contact area law for randomly rough viscoelastic contacts. *Journal of Physics: Condensed Matter*, 27(10), p.105102.

Schallamach, A., 1966. A Theory of Dynamic Rubber Friction. *Rubber Chemistry and Technology*, 39(2), pp.320–327.

Schallamach, A., 1969. Friction and Frictional Rise of Wedge Sliders on Rubber. *Wear*, 13, pp.13–25.

Schallamach, A., 1971. How does rubber slide? *Wear*, 17(4), pp.301–312.

Schallamach, A., 1953. The velocity and temperature dependence of rubber

friction. *Proceedings of the Physical Society. Section B*, 386.

Schrader, M.E., 1995. Young- Dupre Revisited. *Langmuir*, 11(6), pp.3585–3589.

Shartsis, L. & Smock, A.W., 1947. Surface Tensions of Some Optical Glasses. *Journal of the American Ceramic Society*, 30(4), pp.130–136.

Southern, E. & Thomas, A.G., 1979. Studies of Rubber Abrasion. *Rubber Chemistry and Technology*, 52(5), pp.1008–1018.

Steltz, E. et al., 2010. Jamming as an enabling technology for soft robotics. In *Spie*. p. 764225.

Steltz, E. et al., 2009. JSEL: Jamming skin enabled locomotion. *2009 IEEE/RSJ International Conference on Intelligent Robots and Systems, IROS 2009*, pp.5672–5677.

Sundaram, N., Farris, T.N. & Chandrasekar, S., 2012. JKR adhesion in cylindrical contacts. *Journal of the Mechanics and Physics of Solids*, 60(1), pp.37–54.

Suphadon, N., Thomas, A.G. & Busfield, J.J.C., 2009. Viscoelastic Behaviour of Rubber Under a Complex Loading. *Journal of Applied Poilymer Science*, 113(2), pp.693–699.

Tabor, D., 1977. Surface forces and surface interactions. *Journal of Colloid And Interface Science*, 58(1), pp.2–13.

Thomas, A.G., 1958. Rupture of rubber. V. Cut growth in natural rubber vulcanizates. *Polymer Chemistry*, 31(123), pp.467–480.

Thomas, a. G., 1955. Rupture of rubber. II. The strain concentration at an incision. *Journal of Polymer Science*, 18(88), pp.177–188.

Thomas, S. et al. eds., 2014. *Natural Rubber Materials: Volume 1: Blends and IPNs*, Cambridge: The Royal Society of Chemistry.

Trappe, V. et al., 2001. Jamming phase diagram for attractive particles. *Nature*, 411(June), pp.0–3.

Treloar, L.R.G., 1943a. The elasticity of a Network of Long-Chain Molecules-I. *Transactions of the Faraday Society*, 39, pp.36–41.

Treloar, L.R.G., 1943b. The Elasticity of a Network of Long-Chain Molecules-II. *Transactions of the Faraday Society*, 39, pp.241–246.

Wall, F.T., 1942. Statistical Thermodynamics of Rubber II. *The Journal of Chemical Physics*, 10, pp.485–488.

Walton, K., 1987. The effective elastic moduli of a random packing of spheres. *Journal of the Mechanics and Physics of Solids*, 35(2), pp.213–226.

Walton, K., 1978. The Oblique Compression of Two Elastic Spheres. *Journal of the Mechanics and Physics of Solids*, 26, pp.139–150.

Warren, D., 1987. *Brazil and the Struggle for Rubber: A Study in Environmental History*, Cambridge: Cambridge University Press.

Whelan, A. & Lee, K.S. eds., 1979. *Developments in Rubber Technology- 1*, London: Applied Science Publishers LTD.

Williams, M.L., Landel, R.F. & Ferry, J.D., 1955. The Temperature Dependence of Relaxation Mechanisms in Amorphous Polymers and Other Glass-forming Liquids. *Journal of American chemical society*, 77(14), pp.3701–3707.

Wolf, H. & Wolf, R., 1936. *Rubber- A Story of Glory and Greed*, New York: Covici-Friede.

7 Appendix

7.1 List of Conference Papers

2014- International Rubber Conference, Beijing, *Adhesive Rubber Friction*.

2014- American Chemical Society, Nashville, *Adhesive Rubber Friction*.

2015- Tyre Technology, Cologne, *Adhesive Rubber Friction*.

2015- Tyre Colloquium, Prague, *Adhesive Rubber Friction*.

2015- European Conference on Constitutive Models for Rubber, *Jamming of Rubber Particles*.

7.2 FEA Input File Used in Section 4.5

7.2.1 Cylindrical Asperity Model

*Heading

** Job name: Cyl Model name: Model-1

** Generated by: ABAQUS/CAE 6.14-5

*Preprint, echo=NO, model=NO, history=NO, contact=NO

**

** PARTS

**

*Part, name=Hem

*Node

[…]

*Element, type=CPE4RH

[…]

*Nset, nset=Set-1, generate

```
  1,  5813,    1
*Elset, elset=Set-1, generate
  1,  5610,    1
** Section: Section-1
*Solid Section, elset=Set-1, material=Rubber
,
*End Part
**
*Part, name=Part-3
*End Part
**
**
** ASSEMBLY
**
*Assembly, name=Assembly
**
*Instance, name=Hem-1, part=Hem
      0.,    0.054564,         0.
      0.,    0.054564,         0.,         0.,    0.054564,         -1.,         90.
*End Instance
**
*Instance, name=Part-3-1, part=Part-3
     -0.2,         0.,         0.
```

```
*Node
     1,  0.200000003,          0.,          0.
*Nset, nset=Part-3-1-RefPt_, internal
1,
*Surface, type=SEGMENTS, name=m_Surf-3
START,         -0.3,          0.
 LINE,          0.7,          0.
*Rigid Body, ref node=Part-3-1-RefPt_, analytical surface=m_Surf-3
*End Instance
**
*Nset, nset=Set-3, instance=Part-3-1
 1,
*Nset, nset=Set-5, instance=Hem-1
[…]
*Elset, elset=Set-5, instance=Hem-1
[…]
*Nset, nset=Set-6, instance=Hem-1
[…]
*Elset, elset=Set-6, instance=Hem-1
[…]
*Nset, nset=Set-7, instance=Hem-1
[…]
*Elset, elset=Set-7, instance=Hem-1
```

[…]

*Nset, nset=Set-8, instance=Hem-1

[…]

*Elset, elset=Set-8, instance=Hem-1

[…]

*Nset, nset=Set-9, instance=Hem-1

[…]

*Elset, elset=Set-9, instance=Hem-1

[…]

*Nset, nset=Set-10, instance=Hem-1

[…]

*Elset, elset=Set-10, instance=Hem-1

[…]

*Nset, nset=Set-11, instance=Hem-1

[…]

*Elset, elset=Set-11, instance=Hem-1

[…]

*Nset, nset=Set-12, instance=Hem-1

[…]

*Nset, nset=Set-13, instance=Hem-1

[…]

*Elset, elset=Set-13, instance=Hem-1

[…]

*Nset, nset=Set-14, instance=Hem-1

[…]

*Elset, elset=Set-14, instance=Hem-1

[…]

*Nset, nset=Set-15, instance=Hem-1

[…]

*Elset, elset=Set-15, instance=Hem-1

[…]

*Nset, nset=m_Set-16, instance=Part-3-1

1,

*Nset, nset=s_Set-16, instance=Hem-1

8,

*Elset, elset=_s_Surf-4_S2, internal, instance=Hem-1

5130,

*Elset, elset=_s_Surf-4_S1, internal, instance=Hem-1, generate

5131, 5145, 1

*Surface, type=ELEMENT, name=s_Surf-4

_s_Surf-4_S2, S2

_s_Surf-4_S1, S1

*Elset, elset=_s_Surf-6_S2, internal, instance=Hem-1

5130,

*Elset, elset=_s_Surf-6_S1, internal, instance=Hem-1, generate

5131, 5145, 1

*Surface, type=ELEMENT, name=s_Surf-6

_s_Surf-6_S2, S2

_s_Surf-6_S1, S1

*Elset, elset=_s_Surf-10_S1, internal, instance=Hem-1

[…]

*Elset, elset=_s_Surf-10_S2, internal, instance=Hem-1

[…]

*Surface, type=ELEMENT, name=s_Surf-10

_s_Surf-10_S1, S1

_s_Surf-10_S2, S2

*Elset, elset=_s_Surf-11_S2, internal, instance=Hem-1

5385,

*Elset, elset=_s_Surf-11_S1, internal, instance=Hem-1, generate

5386, 5400, 1

*Surface, type=ELEMENT, name=s_Surf-11

_s_Surf-11_S2, S2

_s_Surf-11_S1, S1

*Elset, elset=_s_Surf-12_S1, internal, instance=Hem-1

[…]

*Elset, elset=_s_Surf-12_S2, internal, instance=Hem-1

[…]

*Surface, type=ELEMENT, name=s_Surf-12

_s_Surf-12_S1, S1

_s_Surf-12_S2, S2

*Elset, elset=_s_Surf-13_S2, internal, instance=Hem-1

5385,

*Elset, elset=_s_Surf-13_S1, internal, instance=Hem-1, generate

5386, 5400, 1

*Surface, type=ELEMENT, name=s_Surf-13

_s_Surf-13_S2, S2

_s_Surf-13_S1, S1

*Elset, elset=_s_Surf-14_S1, internal, instance=Hem-1

[…]

*Elset, elset=_s_Surf-14_S2, internal, instance=Hem-1

[…]

*Surface, type=ELEMENT, name=s_Surf-14

_s_Surf-14_S1, S1

_s_Surf-14_S2, S2

*Elset, elset=_s_Surf-15_S1, internal, instance=Hem-1

[…]

*Elset, elset=_s_Surf-15_S2, internal, instance=Hem-1

[…]

*Surface, type=ELEMENT, name=s_Surf-15

_s_Surf-15_S1, S1

_s_Surf-15_S2, S2

*Elset, elset=_s_Surf-16_S2, internal, instance=Hem-1

5385,

*Elset, elset=_s_Surf-16_S1, internal, instance=Hem-1, generate

5386, 5400, 1

*Surface, type=ELEMENT, name=s_Surf-16

_s_Surf-16_S2, S2

_s_Surf-16_S1, S1

*Elset, elset=_s_Surf-17_S2, internal, instance=Hem-1

5385,

*Elset, elset=_s_Surf-17_S1, internal, instance=Hem-1, generate

5386, 5400, 1

*Surface, type=ELEMENT, name=s_Surf-17

_s_Surf-17_S2, S2

_s_Surf-17_S1, S1

*Elset, elset=_s_Surf-18_S1, internal, instance=Hem-1

[…]

*Elset, elset=_s_Surf-18_S2, internal, instance=Hem-1

[…]

*Surface, type=ELEMENT, name=s_Surf-18

_s_Surf-18_S1, S1

_s_Surf-18_S2, S2

*Elset, elset=_s_Surf-19_S2, internal, instance=Hem-1

5385,

*Elset, elset=_s_Surf-19_S1, internal, instance=Hem-1, generate

5386, 5400, 1

*Surface, type=ELEMENT, name=s_Surf-19

_s_Surf-19_S2, S2

_s_Surf-19_S1, S1

*Elset, elset=_s_Surf-20_S1, internal, instance=Hem-1

[…]

*Elset, elset=_s_Surf-20_S2, internal, instance=Hem-1

[…]

*Surface, type=ELEMENT, name=s_Surf-20

_s_Surf-20_S1, S1

_s_Surf-20_S2, S2

*Elset, elset=_s_Surf-21_S2, internal, instance=Hem-1

5385,

*Elset, elset=_s_Surf-21_S1, internal, instance=Hem-1, generate

5386, 5400, 1

*Surface, type=ELEMENT, name=s_Surf-21

_s_Surf-21_S2, S2

_s_Surf-21_S1, S1

*Elset, elset=_s_Surf-22_S2, internal, instance=Hem-1

5385,

*Elset, elset=_s_Surf-22_S1, internal, instance=Hem-1, generate

5386, 5400, 1

*Surface, type=ELEMENT, name=s_Surf-22

_s_Surf-22_S2, S2

_s_Surf-22_S1, S1

*Elset, elset=_s_Surf-23_S4, internal, instance=Hem-1, generate

1, 1291, 30

*Elset, elset=_s_Surf-23_S2, internal, instance=Hem-1

[…]

*Elset, elset=_s_Surf-23_S1, internal, instance=Hem-1

[…]

*Surface, type=ELEMENT, name=s_Surf-23

_s_Surf-23_S4, S4

_s_Surf-23_S2, S2

_s_Surf-23_S1, S1

*Elset, elset=_s_Surf-25_S2, internal, instance=Hem-1

5385,

*Elset, elset=_s_Surf-25_S1, internal, instance=Hem-1, generate

5386, 5400, 1

*Surface, type=ELEMENT, name=s_Surf-25

_s_Surf-25_S2, S2

_s_Surf-25_S1, S1

*Elset, elset=_s_Surf-26_S4, internal, instance=Hem-1, generate

1321, 3841, 30

*Elset, elset=_s_Surf-26_S2, internal, instance=Hem-1

5385,

*Elset, elset=_s_Surf-26_S1, internal, instance=Hem-1, generate

5386, 5400, 1

*Surface, type=ELEMENT, name=s_Surf-26

_s_Surf-26_S4, S4

_s_Surf-26_S2, S2

_s_Surf-26_S1, S1

*Elset, elset=_s_Surf-27_S4, internal, instance=Hem-1, generate

1, 3841, 30

*Elset, elset=_s_Surf-27_S2, internal, instance=Hem-1

[…]

*Elset, elset=_s_Surf-27_S1, internal, instance=Hem-1

[…]

*Surface, type=ELEMENT, name=s_Surf-27

_s_Surf-27_S4, S4

_s_Surf-27_S2, S2

_s_Surf-27_S1, S1

*Elset, elset=_s_Surf-28_S4, internal, instance=Hem-1, generate

1321, 3841, 30

*Elset, elset=_s_Surf-28_S2, internal, instance=Hem-1, generate

3900, 5100, 30

*Surface, type=ELEMENT, name=s_Surf-28

_s_Surf-28_S4, S4

_s_Surf-28_S2, S2

*Elset, elset=_s_Surf-29_S4, internal, instance=Hem-1, generate

1321, 3841, 30

*Elset, elset=_s_Surf-29_S1, internal, instance=Hem-1

[…]

*Elset, elset=_s_Surf-29_S2, internal, instance=Hem-1

[…]

*Surface, type=ELEMENT, name=s_Surf-29

_s_Surf-29_S4, S4

_s_Surf-29_S1, S1

_s_Surf-29_S2, S2

*Elset, elset=_s_Surf-30_S4, internal, instance=Hem-1, generate

1321, 3841, 30

*Elset, elset=_s_Surf-30_S1, internal, instance=Hem-1

[…]

*Elset, elset=_s_Surf-30_S2, internal, instance=Hem-1

[…]

*Surface, type=ELEMENT, name=s_Surf-30

_s_Surf-30_S4, S4

_s_Surf-30_S1, S1

_s_Surf-30_S2, S2

*Elset, elset=_s_Surf-31_S4, internal, instance=Hem-1, generate

1321, 3841, 30

*Elset, elset=_s_Surf-31_S2, internal, instance=Hem-1

5385,

*Elset, elset=_s_Surf-31_S1, internal, instance=Hem-1, generate

5386, 5400, 1

*Surface, type=ELEMENT, name=s_Surf-31

_s_Surf-31_S4, S4

_s_Surf-31_S2, S2

_s_Surf-31_S1, S1

*Elset, elset=_s_Surf-32_S4, internal, instance=Hem-1, generate

[…]

*Elset, elset=_s_Surf-32_S1, internal, instance=Hem-1

[…]

*Elset, elset=_s_Surf-32_S2, internal, instance=Hem-1

[…]

*Surface, type=ELEMENT, name=s_Surf-32

_s_Surf-32_S4, S4

_s_Surf-32_S1, S1

_s_Surf-32_S2, S2

*Elset, elset=_s_Surf-33_S4, internal, instance=Hem-1, generate

[…]

*Elset, elset=_s_Surf-33_S2, internal, instance=Hem-1

[…]

*Elset, elset=_s_Surf-33_S1, internal, instance=Hem-1

[…]

*Surface, type=ELEMENT, name=s_Surf-33

_s_Surf-33_S4, S4

_s_Surf-33_S2, S2

_s_Surf-33_S1, S1

*Elset, elset=_s_Surf-34_S4, internal, instance=Hem-1, generate

 1321, 3841,   30

*Elset, elset=_s_Surf-34_S2, internal, instance=Hem-1

[…]

*Elset, elset=_s_Surf-34_S1, internal, instance=Hem-1, generate

 5386, 5400,   1

*Surface, type=ELEMENT, name=s_Surf-34

_s_Surf-34_S4, S4

_s_Surf-34_S2, S2

_s_Surf-34_S1, S1

*End Assembly

*Amplitude, name=Ramp

          0.,   0.,   1.,   1.

**

** MATERIALS

**

*Material, name=Rubber

*Density

1.2e-06,

*Elastic

1.2, 0.495

**

** INTERACTION PROPERTIES

**

*Surface Interaction, name=Slip

1.,

*Friction

0.,

*Surface Behavior, pressure-overclosure=HARD

*Surface Interaction, name=Stick

1.,

*Friction, rough

*Surface Behavior, no separation, pressure-overclosure=HARD

*Time Points, name=TimePoints-1

0., 0.05, 0.1, 0.15, 0.2, 0.25, 0.3, 0.35

0.4, 0.6, 0.8, 1.

**

** INTERACTIONS

**

** Interaction: Slip

*Contact Pair, interaction=Slip, type=SURFACE TO SURFACE

s_Surf-33, Part-3-1.m_Surf-3

** Interaction: Stick

*Contact Pair, interaction=Stick, type=SURFACE TO SURFACE

s_Surf-34, Part-3-1.m_Surf-3

** --

**

** STEP: Comp

**

*Step, name=Comp, nlgeom=YES, inc=100000000

*Static

0.1, 1., 1e-30, 1.

**

** BOUNDARY CONDITIONS

**

** Name: Comp Type: Displacement/Rotation

*Boundary, amplitude=Ramp

Set-15, 1, 1

Set-15, 2, 2, -0.05

** Name: Fix Base Type: Symmetry/Antisymmetry/Encastre

*Boundary

Set-3, ENCASTRE

**

** INTERACTIONS

```
**
** Interaction: Stick
*Model Change, type=CONTACT PAIR, remove
s_Surf-34, Part-3-1.m_Surf-3
**
** OUTPUT REQUESTS
**
*Restart, write, frequency=0
**
** FIELD OUTPUT: F-Output-1
**
*Output, field
*Node Output
RF, U
*Element Output, directions=YES
ENER, NE, S
*Contact Output
CDISP, CSTRESS
**
** HISTORY OUTPUT: H-Output-1
**
*Output, history, variable=PRESELECT, time points=TimePoints-1
*End Step
```

```
** ----------------------------------------------------------------
**
** STEP: Shear
**
*Step, name=Shear, nlgeom=YES, inc=10000000
*Static
0.001, 1., 1e-30, 1.
**
** BOUNDARY CONDITIONS
**
** Name: Comp Type: Displacement/Rotation
*Boundary, amplitude=Ramp
Set-15, 1, 1, 0.05
**
** INTERACTIONS
**
** Interaction: Stick
*Model Change, type=CONTACT PAIR, add
s_Surf-34, Part-3-1.m_Surf-3
**
** OUTPUT REQUESTS
**
*Restart, write, frequency=0
```

**

** FIELD OUTPUT: F-Output-1

**

*Output, field

*Node Output

RF, U

*Element Output, directions=YES

ENER, NE, S

*Contact Output

CDISP, CSTRESS

**

** HISTORY OUTPUT: H-Output-1

**

*Output, history, variable=PRESELECT, time points=TimePoints-1

*End Step

7.2.2 Hemispherical Asperity Model

*Heading

h=0.49, disp=0.25

** Job name: CompShear Model name: Model-1

** Generated by: ABAQUS/CAE 6.14-5

*Preprint, echo=NO, model=NO, history=NO, contact=NO

**

** PARTS

**

*Part, name=Hem

*Node

[…]

*Element, type=C3D8R

[…]

*Nset, nset=m_Set-13, instance=Sub-1

1,

*Elset, elset=_s_Surf-25_S2, internal, instance=Hem-1

[…]

*Elset, elset=_s_Surf-25_S4, internal, instance=Hem-1

[…]

*Elset, elset=_s_Surf-25_S1, internal, instance=Hem-1

[…]

*Elset, elset=_s_Surf-25_S6, internal, instance=Hem-1

[…]

*Elset, elset=_s_Surf-25_S5, internal, instance=Hem-1

[…]

*Elset, elset=_s_Surf-25_S3, internal, instance=Hem-1

[…]

*Surface, type=ELEMENT, name=s_Surf-25

_s_Surf-25_S2, S2

_s_Surf-25_S4, S4

_s_Surf-25_S6, S6

_s_Surf-25_S1, S1

_s_Surf-25_S5, S5

_s_Surf-25_S3, S3

*Elset, elset=_s_Surf-26_S2, internal, instance=Hem-1

[…]

*Surface, type=ELEMENT, name=s_Surf-26

_s_Surf-26_S2, S2

*Elset, elset=_s_Surf-27_S2, internal, instance=Hem-1

[…]

*Elset, elset=_s_Surf-27_S4, internal, instance=Hem-1

[…]

*Elset, elset=_s_Surf-27_S6, internal, instance=Hem-1, generate

135261, 136089, 12

*Surface, type=ELEMENT, name=s_Surf-27

_s_Surf-27_S2, S2

_s_Surf-27_S4, S4

_s_Surf-27_S6, S6

*End Assembly

**

** ELEMENT CONTROLS

**

*Section Controls, name=EC-1, second order accuracy=YES

1., 1., 1.

```
**
** MATERIALS
**
*Material, name=NR-0
*Density
 1.2e-06,
*Elastic
 1.2, 0.495
**
** INTERACTION PROPERTIES
**
*Surface Interaction, name=IntProp-1
1.,
*Friction
0.,
*Surface Behavior, pressure-overclosure=HARD
*Surface Interaction, name="Shear Phase"
1.,
*Friction, rough
*Surface Behavior, no separation, pressure-overclosure=HARD
*Time Points, name=TimePoints-1
0., 0.2, 0.4, 0.6, 0.8, 1.
**
```

```
** BOUNDARY CONDITIONS
**
** Name: Fix Base Type: Symmetry/Antisymmetry/Encastre
*Boundary
Set-18, ENCASTRE
**
** INTERACTIONS
**
** Interaction: Int-1
*Contact Pair, interaction=IntProp-1, type=SURFACE TO SURFACE
s_Surf-27, Sub-1.m_Surf-1
** Interaction: Shear
*Contact Pair, interaction="Shear Phase"
s_Surf-26, Sub-1.m_Surf-1
** ----------------------------------------------------------------
**
** STEP: Comp
**
*Step, name=Comp, nlgeom=YES, inc=1000000
*Static
0.01, 1., 1e-10, 1.
**
** BOUNDARY CONDITIONS
```

```
**
** Name: BC-2 Type: Displacement/Rotation
*Boundary
Set-27, 1, 1
Set-27, 5, 5
Set-27, 6, 6
** Name: Comp Type: Displacement/Rotation
*Boundary
Set-28, 2, 2, -0.02
Set-28, 3, 3
**
** INTERACTIONS
**
** Interaction: Shear
*Model Change, type=CONTACT PAIR, remove
s_Surf-26, Sub-1.m_Surf-1
**
** OUTPUT REQUESTS
**
*Restart, write, frequency=0
**
** FIELD OUTPUT: F-Output-1
**
```

```
*Output, field
*Node Output
U,
*Element Output, directions=YES
ENER, NE, S
*Contact Output
CDISP, CSTRESS
**
** HISTORY OUTPUT: H-Output-1
**
*Output, history, variable=PRESELECT
*End Step
** ----------------------------------------------------------------
**
** STEP: Shear6
**
*Step, name=Shear6, nlgeom=YES, inc=10000000
*Dynamic
0.01,1.,0.0001
**
** BOUNDARY CONDITIONS
**
** Name: Comp Type: Displacement/Rotation
```

*Boundary

Set-28, 2, 2, -0.02

Set-28, 3, 3, 0.05

Set-28, 4, 4

Set-28, 5, 5

Set-28, 6, 6

**

** INTERACTIONS

**

** Interaction: Shear

*Model Change, type=CONTACT PAIR, add

s_Surf-26, Sub-1.m_Surf-1

**

** OUTPUT REQUESTS

**

*Restart, write, frequency=0

**

** FIELD OUTPUT: F-Output-1

**

*Output, field, frequency=1

*Node Output

U,

*Element Output, directions=YES

ENER, NE, S

*Contact Output

CDISP, CSTRESS

**

** HISTORY OUTPUT: H-Output-1

**

*Output, history, variable=PRESELECT, time points=TimePoints-1

*End Step

7.3 MATLAB Code Used in Section 3.2

```
plot( Logt , LogH4 , 'ro')

corrcoef( Logt , LogH4 )

[p,ErrorEst] = polyfit( Logt , LogH4 ,10)

LogH4_fit = polyval( p , Logt , ErrorEst );

plot( Logt , LogH4 ,'+green', Logt , LogH4_fit,'-black');
```

7.4 MATLAB Code Used in Section 4.3

```
R=0.000644062

K=2151078.406;

S=0.083875471;

L=0.01;

P0=0.80410;%5kg

P=0;

ax=0;

ai=0.01

err=0.000000000001
```

```
while P<P0;

a = ax + ai;

P=((pi*K*a^2)/(3*R)-((8/3)*K*pi*a*S)^(1/2))*L;

if abs(P-P0)<err;

   break

end

if P>P0;

   a=a-ai;

   ai=ai/10;

   P=0;

end

ax=a;

end
```

7.5 MATLAB Scripts Used in Section 5.2.3

7.5.1 Initial Variable Solver

```
clc;

clear all;

r = 0.0025;%input('r = ?'); m

E = 1200000;%input('E = ?'); Pa

v = 0.5;%input('v = ?');

Fext0 =0.16;%input'Fext0=?'); N

%filename = input ('output file name?');

Se = 2*49.28*10^(-3);%J/m^2
```

```
G = E/3;

B = 1/(4* pi * G );

R = r/2;

k = (1- v^2)/( pi*E );

K = 4/( 3*pi*2*k);

%a0 = ( ( ( 2 / (3^(1/2)) )*R*( Fext0 /2) ) / K )^(1/3);

P = (( (3^(1/2)) /2 )* Fext0 )/2;

a0 = (( R * P )/ K );%(( R/ K )*( P +3* Se * pi * R + (6* Se * pi * R * P +(3* Se * pi * R )^2)^(1/2) ))^(1/3);

dc0 = a0 ^2/ R

c0 = 2* r - dc0 %2*( r^2 - a0^2)^(1/2);

A0 = asind( r / c0 ); %For hex = 30deg, but for point contact rheo hems not constant with applied load.

H0 = ( c0 /2) * cosd(30); %Initial vertical height from centre of contact plane to hemisphere base/top.

Al = 0;

err = 0.0001;

dc = 0;

dcx =0;

dcy =0;

dc1 = 10;

while abs(Al - A0 )>err

  if Al>0;

   A0 = Al;
```

```
  end

  P = (cosd(A0)* Fext0 )/2;

  a0 = (( R * P )/ K )^(1/3);%(( R/ K )*( P +3* Se * pi * R + (6* Se * pi * R * P +(3* Se
* pi * R )^2)^(1/2) ))^(1/3);

  dc0 = a0 ^2/ R;

  c0 = 2* r - dc0; %2*( r^2 - a0^2)^(1/2);

  Al = asind( r / c0 ); %For hex = 30deg, but for point contact rheo hems not constant
with applied load.

end
```

7.5.2 Model 1

```
output = { 'dX', 'Fx', 'Fext', 'a', 'ap2', 'A', 'O' };

row = 1;

%Particle 1 is the particle in the direction the particle to which force is applied is

%moving towards.

for dx = 0:0.00001:n

            if dx > c0 *cosd(60)

         break

      end

   dx2 = dx * sind(A0);%Relating dx and dy movement to new revolved co-ords.

  dy2 = dx * cosd(A0);

    x = -(( dy2^2+( c0 - dx2 )^2)^(1/2))/2;

y = ( r^2 - ( dy2^2 + ( c0 - dx2 )^2)/4)^(1/2); %Calculating the circle intersection
points on a rotated axis related back to the initial position which is related back to
initial configuration.

a =  abs( y );  %Magnitude of the contact between particles.
```

```
A = A0 - atand( dy2 /( c0 - dx2 ));  %The angle from the original config.

c = 2*( r^2 - a^2)^(1/2);

%2nd particle contact parameters, for 3 particle configuration.

O = A0 + asind( dx2 / c0 ); %Angle of the plane of contact to the horizontal(A for particle 2).

o =atand( dy2 /( c0 + dx2 ))

cp2 =( c0 *sind(90+ A0 ))/ sind( 90 - A0 - o );

ap2 = ( r^2 - ( cp2 /2)^2)^(1/2)

if cp2 > 2*r;

   ap2 = 0;

end

Fn1 = ( a^3 * K )/ R;    %Force normal to contact of particle 1.

 Fn2 = ( ap2^3 * K )/ R;  %Force normal to contact of particle 2.

 if cp2 > 2* r

    Fn2 = 0

 end

 Fext = (Fn1 *cosd( A )) + ( Fn2 *cosd( O ));

  Fx = Fn1 *sind( A ) - Fn2 *sind( O );

Fxd = (((3^(3/4))/(2^(1/2)))* r )* G *2* dx

  dx = dx *1000;

     row = row+1;

   output{row, 1} = dx;

   output{row, 2} = Fx;

   output{row, 3} = Fext;
```

```
output{row, 4} = a;

output{row, 5} = ap2;

output{row, 6} = A;

output{row, 7} = O;

   dx = dx /1000;

a = a /1000;

ap2 = ap2 /1000;

    end
```

7.5.3 Model 2

```
output = { 'dX', 'Fx', 'Fext', 'N', 'Q', 'A', 'O', 'a', 'ap2' };

row = 1;

%Particle 1 is the particle in the direction the particle to which force is applied is

%moving towards.

%No shear geometry and shear geometry given by angle fit from data used to

%find lateral displacement and this is used with Waltons eq'n to give shear

%force. A factor of 2 is included in the Fn eq'ns as B is seen to be equal

%to k and Hertz normal(which should be the same) has 2k in eq'n.

for dx = 0.00001:0.00001:0.00174

    %%%%%%%%%%%%%%%%%%%%%%%%%No shear geometry.

      dx2s = dx * sind( A0 );%Relating dx and dy movement to new revolved co-
ords.

  dy2s = dx * cosd( A0 );

   %No friction parameters

  xs = -(( dy2s^2+( c0 - dx2s )^2)^(1/2))/2;
```

ys = (r^2 - (dy2s^2 + (c0 - dx2s)^2)/4)^(1/2); %Calculating the circle intersection points on a rotated axis related back to the initial position which is related back to initial configuration.

cs = (dy2s^2 +(c0 - dx2s)^2)^(1/2);

dcs =2* r - cs;

as = (dcs * R)^(1/2) %as = abs(ys); %Magnitude of the contact between particles.

As = A0 - atand(dy2s /(c0 - dx2s)); %The angle from the original config.

%%%%%%%%%%%%%%%%%%%%%%%%%

if dx > c0 *cosd(60)

break

end

dc = dcs;

a = as;

A = As;

dy2 = dy2s;

dx2 = dx2s;

N = (4* r ^(1/2)* dc ^(3/2))/(3* pi *2* B);

Q = ((8* R ^(1/2))/(3* pi *3* B))*(dy2)* dc ^(1/2);%Was using sheared position but Walton should not.

O = A0 + asind(dx2 / c0);%O = A0 - atand((dy2 - dy0)/(c0 +(dx2 - dx0)));%O = A0 + CoEfA *(dx *1000); %Angle of the plane of contact to the horizontal(A for particle 2).%O = A0 - atand((dy2 - dy0)/(c0 +(dx2 - dx0))); %Angle of the plane of contact to the horizontal(A for particle 2).

o =atand(dy2 /(c0 + dx2))

cp2 =(c0 *sind(90+ A0))/ sind(90 - A0 - o);%cp2 = ((c0 +(dx2 - dx0))^2 +(dy2 - dy0)^2)^(1/2); %Centre-centre distance post deformation.

```
dcp2 = 2* r - cp2;

ap2 = ( dcp2 * R )^(1/2);

N2 = (4* r ^(1/2)* dcp2 ^(3/2))/(3* pi *2* B );

Q2 =0;%2* a *( G /(2- v ))* dyp2;

if dcp2 <0;

   ap2 = 0;

   N2 = 0;

   Q2 = 0;

end

 Fn1 = N;    %Force normal to contact of particle 1.

 Fn2 = N2;  %Force normal to contact of particle 2.

 if N2 < 0

    Fn2 = 0;

    Q2 = 0;

 end

 Fext = (Fn1 *cosd( A )) + ( Fn2 *cosd( O ));

  Fx = Fn1 *sind( A ) - Fn2 *sind( O )+ Q *cosd( A ) - Q2 *cosd( O ) ;

Fxd = (((3^(3/4))/(2^(1/2)))* r )* G *2* dx

  dx = dx *1000;

a = a *1000;

ap2 = ap2 *1000;

      row = row+1;

   output{row, 1} = dx;
```

```
output{row, 2} = Fx;

output{row, 3} = Fext;

output{row, 4} = N;

output{row, 5} = Q;

output{row, 6} = A;

output{row, 7} = O;

output{row, 8} = a;

output{row, 9} = ap2;

dx = dx /1000;

a = a /1000;

ap2 = ap2 /1000;

    end
```

7.5.4 Model 3

```
output = { 'dx', 'Fx', 'Fn1', 'Fext', 'a', 'ap2' };

row = 1;

a = a0;

ap2 = a0;

A = A0;

CoEfA = 5.67* Fext0 ^(-0.142);

err = 0.000001;

dc = 0;

dcx =0;

dcy =0;

dc1 = 10;
```

```
m = 2;

for dx = 0.00001:0.00001:0.0047;

%%%%%%%%%%%%%%%%%%%%%%%%%No shear geometry.

    dx2s = dx * sind(A0)+ dcx;%Relating dx and dy movement to new revolved co-ords.

  dy2s = dx * cosd(A0)+ dcy;

    %No friction parameters

   xs = -(( dy2s^2+( c0 - dx2s )^2)^(1/2))/2;

ys = ( r^2 - ( dy2s^2 + ( c0 - dx2s )^2)/4)^(1/2); %Calculating the circle intersection points on a rotated axis related back to the initial position which is related back to initial configuration.

as =  abs( ys );  %Magnitude of the contact between particles.

As = A0 - atand( dy2s /( c0 - dx2s ));  %The angle from the original config.

cs = 2*( r^2 - as^2)^(1/2);

%%%%%%%%%%%%%%%%%%%%%%%%%

%Strain:

AE = -CoEfA *( dx *1000) + A0; %x1000 because data from which trend was taken was in mm not m.

% Strain angle effect on contact angle (initial contact angle - strain angle)(Rangle, the leading angle):

Aee = AE - As;%Strain angle as the difference between no shear and shear contact angles.

es = 2*tand( Aee );

e = es;

Fs = e * G *(( r^2 * pi )/2); %Force for shearing to strain using area as = semicircle. Seemed to give a relatively reasonable value from rheometer data.
```

```
dxp = 0;

dxs = 0.00001;

% To obtain the contact length at the strain angle. I can then find the

% shearing force and the force to produce the change in

% contact(compression).

while abs( A - AE )> err;

   dxi = dxp + dxs;

  dx2 = dxi * sind(A0)+ dcx;%Relating dx and dy movement to new revolved co-ords.

  dy2 = dxi * cosd(A0)+ dcy;

      x = -(( dy2^2+( c0 - dx2 )^2)^(1/2))/2;

  y = ( r^2 - ( dy2^2 + ( c0 - dx2 )^2)/4)^(1/2); %Calculating the circle intersection points on a rotated axis related back to the initial position which is related back to initial configuration.

   a =  abs( y );  %Magnitude of the contact between particles.

   A = A0 - atand( dy2 /( c0 - dx2 ));  %The angle from the original config.

c = 2*( r^2 - a^2)^(1/2);

if A < AE

   dxi = dxp - dxs;

   dxs = dxs /10;

end

dxp = dxi;

end

if A > 0;

   Amx = 0;
```

```
   amx = a;

   cmx = c;

end

%2nd particle contact parameters, for 3 particle configuration.

dx2 = dx * sind(A0);%Relating dx and dy movement to new revolved co-ords.

  dy2 = dx * cosd(A0);

O = A0 + CoEfA *( dx *1000); %Angle of the plane of contact to the horizontal(A for
particle 2).

cp2 = ( c0 * sind(90+A0))/ sind(90-A0 - asind( dx2 / c0 )) %Centre-centre distance
post deformation.

ap2 = ( r^2 - ( cp2 /2)^2)^(1/2)

 Fn1 = ( a^3 * K )/ R;    %Force normal to contact of particle 1.

 Fn2 = ( ap2^3 * K )/ R;  %Force normal to contact of particle 2.

 if cp2 > 2* r

    Fn2 = 0

    ap2 = 0

 end

Fext = (Fn1 *cosd( A )) + ( Fn2 *cosd( O ));


Fc = Fn1 *sind( A ) - Fn2 *sind( O );

Fx = Fc + Fs; %Total force, thought to be a combination of the force into both types
of deformation

Fad = m * Fext;

Fadx = Fad /cosd( A );
```

```
if Fx > Fadx;
   break
end
if A <0;
   Fn1 = ( amx^3 * K )/ R;
   Fc = Fn1 *sind( Amx ) - Fn2 *sind( O );
   %Fah = Fa *cosd( Amx );
   %h = r -( r^2 - amx^2)^(1/2);
   Fx = Fc + Fs;
   %d = ((2* Ec )/ E)^(1/2)* H;
end
dx = dx *1000; %Total deformation, indenting + shear.
     row = row+1;
   output{row, 1} = dx;
   output{row, 2} = Fx;
   output{row, 3} = Fn1;
   output{row, 4} = Fext;
   output{row, 5} = a;
   output{row, 6} = ap2;
dx = dx /1000;
       end
```